Fine-tuned silica nanohelices as platforms for chiral organization of gold nanoparticles : synthesis, characterization and chiroptical analysis

Jiaji Cheng

université de BORDEAUX

THÈSE PRÉSENTÉE

POUR OBTENIR LE GRADE DE

DOCTEUR DE

L'UNIVERSITÉ DE BORDEAUX

ÉCOLE DOCTORALE DES SCIENCES CHIMIQUES

SPÉCIALITÉ : Physico-Chimie de la Matière Condensée

Par **Jiaji CHENG**

Fine-tuned Silica Nanohelices as Platforms for Chiral Organization of Gold Nanoparticles : Synthesis, Characterization and Chiroptical Analysis

Sous la direction de : Reiko ODA

Soutenue le : **18 Décembre 2015**

Membres du jury:

Mme M.-H. DELVILLE Directeur de Recherche, CNRS, ICMCB, Bordeaux	**Président**
M. B. PICHON Maitre de Conférence, IPCMS, Strasbourg	**Rapporteur**
M. M.IN Directeur de Recherche, CNRS, LCC, Montpellier	**Rapporteur**
M. M. PAULY Maitre de Conférence, ICS, Strasbourg	**Examinateur**
M. P. BAROIS Directeur de Recherche, CNRS, CRPP, Bordeaux	**Examinateur**
M. E. DUJARDIN Directeur de Recherche, CNRS, CEMES, Toulouse	**Examinateur**
Mme R. ODA Directeur de Recherche, CNRS, CBMN, Bordeaux	**Directrice de thèse**
Mme E. POUGET Chargé de recherche, CNRS, CBMN, Bordeaux	**Co-encadrante**

– Acknowledgement –

This work was performed in the collaboration among the laboratory of Chimie & Biologie des Membranes et des Nanoobjets (CBMN), Centre de Recherche Paul Pascal (CRPP) and Institut de Chimie de la matière condensée de Bordeaux (ICMCB). I would like to thank their directors Erick DUFOURC, Philippe RICHETTI and Mario MAGLIONE as well as Jean-Louis MERGNY director of Institut Européen de Chimie et Biologie (IECB) and Patrick MAESTRO director of laboratory of the future (LOF) for the provided opportunity to work in their laboratories.

To start with, I would like to express my special thanks of gratitude to all the jury members and specially Dr. Martin IN and Dr. Benoît PICHON who kindly agreed to be reviewers for this manuscript.

Besides, I would like to express my sincere gratitude to my supervisors Dr. Emilie POUGET and Dr. Reiko ODA for their insightful comments and encouragement, but also for the hard question which incented me to widen my research from various perspectives. Additionally, I would like to personally thank Dr. Emilie POUGET for the continuous support of my Ph.D study and related research, for her patience, motivation, and immense knowledge. I would also like to personally thank Dr. Reiko ODA, who introduces me how to be a good scientific researcher and also how to learn and be a good man. Her guidance helped me in all the time of research and writing of this thesis. I could not have imagined having a better advisor and mentor for my Ph.D study.

There are a number of people who shared their pearls of wisdom with us and provided expertise that greatly assisted the research during the course of this research. I would like to thank them all and in particular: Dr. Marie-Hélène DELVILLE (ICMCB) who did a lot of help on the characterizations of nanoparticles and also advisory suggestions; Dr. Virginie PONSINET (CRPP) who provided scattering measurements and theoretical supports; Dr. Ovidiu Ersen and Dr. Simona MOLDOVAN (IPCMS) who performed electron tomography;

Dr. Jacques LENG (LOF) who introduced microfluidics technique to me; and Dr. Matthias PAULY and Dr. Gero DECHER(ICS) who worked on the 2D assembly of silica nanohelices.

Furthermore, I have to express my appreciation to all the engineers of IECB, ICMCB and CBMN who helped me with the equipment and personally to Etienne HARTE from CBMN for deepening my knowledge and improving my skills of the FTIR-ATR experiments. I am also immensely grateful to Elisabeth SELLIER from CREMEM for the help with HRTEM and SEM. Also I would like to thank Sisareuth TAN and Marion DECOSSAS-MENDOZA from CBMN for the help with FEI-120kv TEM.

I would like to thank all the people whom I was working with during these three years: Ibrahim BILEM, Dr. Zhe Annie CHENG, Dr. Alexandre CUNHA, Dr. Rajat Kumar DAS, Dr. Dima DEDVETS, Dr. Marie-Christine DURRIEU, Jie GAO, Dr. Yi-Shiang Huang, Gregor KEMPER, Dr. Guillaume LE SAUX, Dr. Alla MALINENKO, Dr. Sylvain NLATE, Yutaka OKAZAKI, Laurence PADIOLLEAU, Dr. Loic PICHAVANT, Dr. Laurent PLAWINSKI, Caroline ROYER, Dr. Naoya RYU, Dr. Rumi TAMOTO, Dr. Xiaoqian Xu and Dr. Omar F. ZOUANI. In particular, I am grateful to Dr. Guillaume LE SAUX for enlightening me the first glance of this research, Gregor KEMPER who did lot of generous help for my French, and Dr. Rajat Kumar DAS and Dr. Dima DEDVETS for their instructive help and their friendship. Thank you for all the suggestion you gave to me, for all the problems I was able to share with you, for all the invaluable happiness and joy we made together. You are all the best friends in my life!

Last but not least, I would like to thank my family: my parents and my brother and sister for supporting me spiritually throughout writing this thesis and my life in France. Thank you for making my life colorful!

– Résumé –

Dans cette thèse, nous proposons une approche simple et unique pour créer des matériaux nano-photoniques chiraux à l'échelle nanométrique en utilisant des nanohélices inorganiques (silice) comme structures directrices pour le greffage de nanoparticules d'or (structures hybrides appelées dans ce manuscrit Goldhelix). Les nanohélices de silice sont synthétisées grâce à la chimie du sol-gel sur des auto-assemblages organiques chiraux utilisés comme « moules ». Plus précisément, ces auto-assemblages organiques sont des surfactants Gemini cationiques non chiraux complexés par des contre-ions chiraux. La chiralité des contre-ions induit une chiralité à l'échelle macromoléculaire qui amène à la formation de nano-rubans hélicoidaux (hélices) ou torsadés. La réplication de ces structures en silice permet ensuite de figer les structures et d'obtenir des nanohélices et rubans de silice aux morphologies très bien contrôlées. Dans un deuxième temps, la surface de ces hélices de silice peut être modifiée chimiquement afin d'y greffer des particules plasmoniques (ici des nanoparticules d'or), créant ainsi les Goldhelices. L'aspect 3D chiral ainsi que la taille nanométrique des Goldhelices permet d'envisager de nouvelles applications telles que la formation de matériaux à indice de réfraction inhabituels, des capteurs chiro-optiques, des polarisateurs circulaires ou même des métamatériaux chiraux dans le domaine du visible. Ces propriétés pour être accrues grâce à une organisation hiérarchique en 2 ou 3 dimensions. Dans ce projet, nous montrons la preuve qu'il est possible d'aligner les hélices de silice par deux techniques : la pulvérisation en incidence rasante et l'évaporation contrôlée par microfluidique

Dans le premier chapitre de ce manuscrit, une étude bibliographique sur les nanoparticules métalliques plasmoniques et leur auto-assemblage chiral est présentée, mettant en avant les propriétés de contrôle de l'interaction lumière/matière. Des exemples d'applications dans des domaines de technologies de pointes sont présentées (spectroscopie, pinces optiques, capteur biologique ou imagerie optique. Ensuite, le concept de l'utilisation de nanoparticules métalliques plasmoniques pour obtenir des propriétés optiques inhabituelles –

indice de réfraction proche de zéro, voire négatif, est introduit en présentant les « métasurfaces » obtenues jusqu'à présent.

Dans le deuxième chapitre, nous présentons une introduction générale du travail proposé dans ce manuscrit. Nous proposons d'utiliser une approche originale pour créer des structures nano-photoniques chirales en utilisant les nanohélices de silice comme échafaudage pour le greffage de nanoparticules d'or de diamètres bien calibrés (formation des Goldhelices). L'organisation hélicoidale des nanoparticules d'or présente des propriétés plasmoniques nouvelles de dichroism circulaire. D'autre part, le diamètre des nanohélices étant inférieur à 100 nm, la réalisation des Goldhelices fournira des matériaux photoniques pour des applications dans le domaine du visible. L'organisation des Goldhelices en deux ou trois dimensions sera également proposée via des techniques de pulvérisation en incidence rasante ou de microfluidique. Dans la dernière partie de ce chapitre, nous présenterons quelques exemples typiques de techniques de caractérisation qui seront utilisées pour ces travaux.

Dans le troisième chapitre, nous avons d'abord étudié la possibilité de créer des nanohélices organiques avec une plus grande taille en augmentant la longueur de la chaîne hydrophobe de carbone des tensioactifs Gemini. Une étude détaillée a comparé des Gemini au chaines hydrophobes composées de 16 carbones, 18 carbones ou 20 carbones (Gemini 16-2-16, 18-2-18 et 20-2-20). Une étude plus poussée a montré que la concentration et la température d'incubation sont essentielles pour un bon contrôle morphologique des nanohélices. Nous avons également remarqué la formation d'hélices que nous appelons « mauvaises hélices » qui montrent une morphologie originale et probablement très intéressante pour les applications envisagées. Ensuite, la transcription inorganique en silice des différentes hélices organiques étudiées ici a été effectuée. Enfin, une étude sur la fragmentation des hélices de silice par ultrasons sera présentée. Des paramètres tels que la nature du solvant, la puissance de traitement aux ultrasons, le pH et le séchage de pré-traitement ont été étudiés pour déterminer une approche pour individualiser les nanohelices de silice avec une longueur contrôlée.

Dans le chapitre 4, trois types de nanoparticules d'or de différentes tailles et stabilisées par différentes molécules ont été synthétisées et caractérisées par spectroscopie UV-visible, spectroscopie FTIR-ATR, microscopie électronique, analyse XPS et mesure du potentiel zeta. Ainsi, des nanoparticules d'or stabilisées par des molécules chargées positivement ont été utilisées pour interagir avec des nanohélices de silice brutes qui, selon le pH, peuvent être chargées négativement. D'autre part, des nanoparticules d'or stabilisées par des molécules chargées négativement réagissent avec des hélices de silice dont la surface a été modifiée avec des fonctions amines, chargées positivement selon le pH. Des études sur l'importance de paramètres physico-chimiques tels que le pH et la concentration sur l'adsorption des nanoparticules d'or ont été menées. Les propriétés optiques des Goldhelices formées ont également été étudiées par dichroisme circulaire. Les effets de taille et optimisations basées sur pH et la concentration ont été optimisées pour obtenir la meilleure activité optique (dichroisme circulaire induit au niveua de la bande plasmon). Des analyses de tomographie en microscopie électronique ont également été menées. À la fin de ce chapitre, une expérience préliminaire basée sur la diffusion de lumière en temps résolu (mis en place par Virginie Ponsinet et Philippe Barois au CRPP) a été menée pour étudier les propriétés magnétiques des Goldhelices en suspension. Les résultats préliminaires ont montré l'existence de dipôle magnétique induit et ont prouvé que cette technique pourrait être une approche réalisable.

Dans le dernier chapitre, en vue d'organiser les Goldhelices en deux ou trois dimensions, des expériences ont été réalisées avec des nanohélices de silice afin de prouver la faisabilité du concept. Deux techniques innovantes ont été utilisées : la pulvérisation en incidence rasante et l'évaporation contrôlée par microfluidique. La pulvérisation en incidence rasante a montré des résultats très encourageants pour l'alignement des nanohélices sur une surface avec un paramètre d'ordre supérieur à 0,73. Un grand nombre de paramètres tels que la concentration, le pH, la chimie de surface du substrat, angle de pulvérisation peuvent encore être optimisés pour améliorer ce résultat. En parallèle, une organisation 3D compacte des nanohélices de silice a été obtenue par évaporation contrôlée par microfluidique. Ces deux

techniques ont montré la possibilité d'obtenir un alignement intéressant des nanohélices qui pourrait par la suite être applicables aux Goldhelices.

Mots-clés: auto-assemblage, chiralité, Gemini tensioactifs, nanoparticules plasmoniques, chimie sol-gel, silice, dichroïsme circulaire, métamatériaux chiraux, diffusion de la lumière, pulvérisation en incidence rasante, microfluidique.

Titre : Nanohélices de silice de morphologie contrôlée utilisées comme plateforme pour l'organisation chirale de nanoparticules d'or: synthèse, caractérisation et analyses chiro-optiques.

– Abstract–

In this thesis, we proposed a simple and unique approach to create nanoscale chiral nano-photonics materials by using inorganic chiral (silica) nanohelices as scaffold for the GNPs grafting (hybrid structures named here Goldhelix). To fulfil this goal, chiral superstructures of organic assemblies formed via bottom-up approach are employed as templates for the fabrication of inorganic silica materials through sol–gel chemistry, where the combination of cooperative self-assembly and the chiral templating process favors the formation of inorganic chiral materials with highly ordered meso-structures. Specifically, organic self-assembly of achiral Gemini surfactant with chiral counterions was used for the synthesis of organic helical fibers. Afterwards, silica replicas were templated by using the as-synthesized organic helices as molds. Then, with proper surface functionalization, plasmonic GNPs are grafted on the silica surface to obtain chiroptical properties. Furthermore, hierarchically assembly of Goldhelix to create 2D or 3D structures was investigated based on proof-of-concept attempts on the alignment of silica nanohelices by using grazing incidence spraying (GIS) and controlled evaporation microfluidics techniques. The three dimensional aspect and the nanometric size of the Goldhelix enabled novel applications such as new unusual refractive index materials, chiro-optical sensors circular polarizers, heterogonous catalysts and even metamaterials.

In the first Chapter of this work, a bibliographic study on the plasmonic metal nanoparticles and chirality in self-assemblies was presented in order to set a theoretical and practical background on controlling light and matter interactions. To establish the argument, the plasmonic properties of metal nanoparticles are introduced via cutting edge applications on areas such as SERS, optical tweezers, biological sensors and optical imaging. Afterwards, the concept of using plasmonic metal nanoparticles to obtain unusual optical properties--close to zero or even negative refractive index was explained and a perspicacious example--split-ring resonator was introduced not only to prove the realization of negative refractive index materials in IR or microwave range, but also to point out the possibility and challenge on fabricating negative refractive index materials in visible frequencies. Then, a

literature overview on studies of chirality, especially on chiral self-assemblies in aqueous medium was provided to illustrate the unprecedented capability of chiral self-assemblies to polarize incident light and its promising potential in applications such as circular polarizers, optical sensors and chiral metamaterials.

In the second Chapter, we first introduced the purpose of this work, in which we proposed an original approach to create chiral nano-photonics structures by using silica nanohelices as scaffold for well-calibrated gold nanoparticles (GNPs) grafting (hereafter named as Goldhelix). The helicoidal organization of the GNPs presents new plasmonic circular dichroism properties interesting for the super-lensing or chiral sensing applications. Moreover, since the diameter and helical pitch of proposed Goldhelix structures are all smaller than 100nm, the realization of Goldhelix will provide a new approach for negative refraction in visible frequencies. Then, experimental methods are suggested for the fabrication of Goldhelix via soft templating. Then, in order to make such objects appealing in the context of materials, 2D and 3D uniaxial assembly of Goldhelix were also planned by using grazing incidence spraying and controlled evaporation microfluidics techniques. In the last part of the Chapter, we presented some typical examples of cutting edge characterization techniques that can be used to study the physicochemical properties of the synthesized nanostructures.

In the third Chapter, we first studied the possibility to create organic nanohelices with larger size by increasing the hydrophobic carbon chain length of Gemini surfactants. Detailed study showed that comparing to 16-2-16 Gemini tartrate, 18-2-18 and 20-2-20 Gemini tartrates exhibited greater diameters and pitch length, which is favorable for the synthesis of nanohelices with controlled manner. Further study showed that the concentration and incubation temperature are critical for the formation of nanohelices. In the meantime, an intermediate state, which is noted as “bad helices”, was observed which shows an interesting morphology that exists during the self-assembly of longer chain Gemini tartrate. Afterwards, inorganic silica transcription was investigated on 18-2-18 and 20-2-20 Gemini tartrate with different parameters in order to make more homogenous nanohelices. Finally, fragmentation

of as-synthesized silica nanohelices was done by tip sonication. Parameters such as the nature of solvents, sonication power, pH and drying pre-treatment were studied to figure out an approach for individualizing the silica nanohelices with controlled length. Additionally, the fragmented individualized silica nanohelices were surface functionalized with APTES and characterized by XPS analysis and zeta potential for further usage.

In Chapter 4, three types of GNPs with different sizes and stabilizers were synthesized, ligand exchanged if needed, and characterized via UV-vis spectroscopy, FTIR-ATR spectroscopy, TEM, XPS analysis, zeta potential measurement. Depending on the surface electronegativity, positively charged APTES-GNPs were used to interact with bare silica nanohelices which are negatively charged in general, while negatively charged $NaBH_4$-GNPs and TA-GNPs were used to graft on the amine functionalized silica nanohelices that are positively charged in aqueous solution. In case of APTES-GNPs, study on parameters such as pH and concentration showed that the most homogenous adsorption of such GNPs was when 0.42mg of APTES-GNPs (10.88μm) mixed with 0.05mg silica helical ribbons (0.5mg/ml) at pH>7. However, due to the size of this type of GNPs is too small, we do not observe chiral activity in CD measurement. In case of $NaBH_4$-GNPs and TA-GNPs, when directly mixing the GNPs with silica nanohelices, inhomogeneous adsorptions were observed. Afterwards, if a ligand exchange reaction with SH-PEG_7-COOH was applied the overall adsorptions could be homogeneous and strong plasmonic CD activities in UV range were observed in Goldhelix with GNPs larger than 5nm. Therefore, size effects and optimizations based on pH and concentration were investigated with respect to induced plasmonic CD activity. During the investigation, comprehensive characterization and complementary analysis were provided via electron tomography, extinction spectroscopy, electronic CD and vibrational CD. In the end of this Chapter, a tentative experiment based on time-resolved light scattering (set up by Group Barois from CRPP) was conducted to study the magnetic properties of Goldhelix suspension. The preliminary results showed the existence of induced magnetic dipole and proved this technique could be a feasible approach for studying on magnetic issues of assembled nanoparticles.

– Abstract–

In the last Chapter, in order to fabricate Goldhelix in the context of material, proof-of-concept experiments were performed based on two innovative techniques: grazing incidence spraying and controlled evaporation microfluidics. On a 2D flat surface, grazing incidence spraying was proved successful for the alignment of silica helical ribbons with nematic order parameter greater than 0.73. Spraying time effect was compared to show the possibility to control the gap between nanohelices with steady nematic order parameter, showing that other parameters such as concentration, pH, surface chemistry of the substrate, spray angle should also be crucial for the fine control of the alignment and this technique has great potential for the fabrication of chiral film structures with intrinsically chiral building blocks. In parallel, an overview concerning microfluidics was presented and preliminary experiments on the 3D alignment of silica nanohelices via controlled evaporation microfluidics were done and found practical for condensed uniaxial packing of silica twisted ribbons, which may be the result of phase transition from random to oriented (like an isotropic-nematic phase transition). Both of the two techniques showed the possibility to deliver well-controlled alignment of silica nanohelices and potentials for the alignment of Goldhelix into macroscopic materials with enhanced optical properties.

Keywords: self-assembly, chirality, Gemini surfactant, plasmonic nanoparticles, sol-gel chemistry, silica, circular dichroism, negative index materials, chiral metamaterials, time-resolved light scattering, grazing incidence spraying, microfluidics.

– List of used abbreviations –

A_{LCP}- absorbance of left circularly polarized light

A_{RCP}- absorbance of right circularly polarized light

APTES - (3-Aminopropyl)triethoxysilane

APTES-GNPs- GNPs capped by (3-Aminopropyl)triethoxysilane

APTMS- (3-Aminopropyl)trimethoxysilane

ATR- Attenuated total reflectance spectroscopy

CD - Circular dichroism

CNTs – Carbon Nanotubes

D_2O - Deuterium oxide

DDA- discrete dipole approximation

DETAS- (3-trimethoxysilylpropyl)diethylenetriamine

DMF- dimethylformamide

DMSO-d6 - Dimethyl sulfoxide (Deuterated)

ED- electronic dipole

EQ- electric quadrupole

FT-IR- Fourier Transform Infrared spectra

GI- grazing incidence

GIS- grazing incidence spraying

GNPs- Gold nanoparticles

Goldhelix- Silica nanohelices grafted with GNPs

HOOC-PEG/$NaBH_4$-GNPs- $NaBH_4$-GNPs ligand exchanged with HS-PEG_7-COOH

HOOC-PEG/TA-GNPs- TA-GNPs ligand exchanged with HS-PEG_7-COOH

HS-PEG_7-COOH- O-(2-Carboxyethyl)-O'-(2-mercaptoethyl)

LbL - Layer-by-layer deposition

LSPR- localized surface plasmon resonance

MD- magnetic dipole

NMR - Nuclear magnetic resonance

$NaBH_4$-GNPs-GNPs stabilized by tri-sodium citrate but reduced by sodium borohydride

Nanohelices-NH_2- amine functionalized silica helical ribbons and twisted ribbons

PDMS- polydimethylsiloxane

PEI- poly(ethylene immine)

SERS- Surface Enhanced Raman spectroscopy

SEM - Scanning electron microscopy

Silica nanohelices- silica helical ribbons and silica twisted ribbons

TA-GNPs- GNPs capped by both tri-sodium citrate and tannic acid potassium

TEM - Transmission electron microscopy

TEOS - Tetraethoxysilane

TFE - Trifluoroethanol

T_k - Krafft temperature

TMOS- Tetramethoxysilane

UV-vis spectroscopy- Ultraviolet–visible spectroscopy

XPS- X-ray photoelectron spectroscopy

– Outline –

– General introduction –

In photonics, hot topics in modern optics such as photonic crystals, optical sensors and solar cells are now attracting more and more researchers' eyes, it is however undeniable that the origin of these advanced technologies are all inspired from the fundamental light and matter interactions. Based on this idea, noble metal nanoparticles have attracted significant interests due to their unique physical properties in both fundamental science and nanotechnology. When assembled close to each other, their localized surface plasmon resonances are coupled together, resulting in the enhancement of the electric field in the gap between the adjacent nanoparticles. Such systems, therefore, are attractive candidates for the amplification of optical signals for numerous applications. On the other hand, Chirality in nanoscience may offer new opportunities for applications beyond the traditional fields of chirality, such as controlling the flow of an electromagnetic wave inside of matter. If this optical activity can be enhanced, the refractive index may become negative for one circular polarization, even if the electric permittivity ϵ and magnetic permeability μ are both positive. Therefore, to obtain a chiral self-assembly of metal nanoparticles such as gold and silver onto nanometric templates with precisely controlled position and specific chiral arrangements which could exhibit interesting optical properties raises researchers' interests, and to establish a sustainable and feasible approach for the applications such as biomedical materials and metamaterials is overwhelmingly on top of calendar.

Herein, we present a new template–assisted method to fabricate a collection of self-assemblies of GNPs onto the surface of a helical silica substrate, denoted as Goldhelix, in which plasmonic chirality can be transcribed by the elaborate arrangement of the nanoparticles. We expect that this assembly strategy will carve out a way to rationally design a variety of superstructures based on nanoparticles to discover a better view towards metamaterials and spark the originality towards "bottom-up" approaches in nanoscience.

Chapter 1. Literature review

References – page 40

1. Introduction

While hot topics in modern optics such as photonic crystals[1-3], solar cells[4-8], quantum dots[9-13] are now attracting more and more researchers' eyes, it is undeniable that the origin of these advanced technologies are all inspired from the fundamental light and matter interactions. With centuries of development, many basic theories have been developed to understand such common but complex interactions which would direct to numerous applications. Controlling light-matter interaction is scientifically challenging and can help broadening the limits of modern optics and relate to the most paradoxical concept— a material called metamaterials[14-16] also known as negative index materials, which indeed raised tremendous interests. The knowledge on such novel materials helps developing many interdisciplinary fields which makes the realization of brand-new materials. Typically, the emerging area of plasmonics[17, 18], for example, is closely related to refractive index manipulation particularly at optical frequencies, where the very mechanism and designs of negative effective parameter media at optical frequencies are intimately related to the excitation of these plasmons in the nano-metallic particles. Recent studies showed that chiral media [19-21] with positive constitutive parameters can be also used to achieve near-zero or negative refraction. These findings opened the floodgates to new experiments on innovative materials, pushing researchers to reevaluate the origin of electromagnetic response between light and matter so as to discovering newly released areas in materials' design by essentially manipulating light and matter interactions.

Due to the complexity on manipulation of light and matter interaction, it is recommended for the uninitiated readers to check the appendix part of this thesis for the classic theories on light-matter interaction.

In this Chapter, reviews on plasmonic metal nanoparticles and chirality in self-assemblies will be presented in order to set a theoretical and practical background on controlling light and matter interaction towards applications on 3D resonators such as super-lensing, optical sensors and circular polarizers.

2. Plasmonic metal nanoparticles

2.1. Why plasmonic metal nanoparticles?

The “simple” fact that we “see” anything is all based on the interaction of light on matter. However, there is a fundamental limitation on the use of light defined by their wavelength that light cannot be focused down to a spot smaller than about half their wavelength. As the wavelength of visible light ranges from about 400 to about 800 nm, it seems to greatly confine nanoscience and nanotechnologies to the world of optics.

Meanwhile, the invention of metal nanoparticles in nanoscience revolutionized the field and allows us to go beyond such limit. When a metal nanoparticle is irradiated by light, its electric field separates negatively charged electrons and positively charged cores of the particle. As they attract each other, they would oscillate with a certain frequency. If the frequency of the incident light matches this natural resonance frequency, it will produce large oscillations of all of the free electrons in the metal and large electric fields are produced within the nanoparticles and these fields themselves act on the electrons, reinforcing the oscillations. This coupled excitation, between oscillating charges inside the particle and oscillating electromagnetic fields immediately outside the particle, is known as a plasmon resonance (or, often, as a localized surface plasmon or a particle plasmon),[22] and the response time of free electrons’ movement under applied electric field becomes comparable to the period of the electromagnetic wave resulting in a strong coupling between electromagnetic fields and electron motion that we refer to as plasmons.

Plasmon resonances of metal nanoparticles quickly give impetus to the development of optic applications in the areas like broadcast, reception and transmission of radiowaves and microwaves. The phase velocity depends strongly on the shape of the particle, when plasmons propagate through metal surface. For macroscopic objects, whose sizes are comparable to or larger than the wavelength of incident light, this phase mismatch means that incident light does not naturally excite plasmons with high efficiency while in nanoscale objects, which are very small and comparable to the optical wavelength, the confinement does not exist anymore,

and the coupling between light and plasmon resonances can be greatly enhanced.[22]

Due to the plasmon resonance in metal nanoparticles, it becomes possible for nanoscale optics which allows ordinary light fields to produce strong evanescent waves. More specifically, plasmons in gold and silver nanoparticles are of great interest because of their great amount of conduction electrons. When these electrons involved in a plasmon oscillation, there will be stronger electrostatic restoring forces and thus the greater the resonance frequency. While the losses in silver and gold are relatively low, for other metals with high losses, these resonances are rapidly dissipated and get very weak although they can also provide plasmon resonances at optical frequencies. Compared to silver, which has the strongest plasmon resonance among all the metals, gold is often the metal of choice due to its stability and relatively strong plasmon resonance so it is often used instead of silver. Note that some metals like aluminum, can produce plasmon resonances at ultraviolet frequencies, and some semiconductors can has plasmon resonances at infrared frequencies, nonetheless with skyrocketing interest about optical resonances, modern optics are basically focused on gold and silver.[22] Gold and silver nanoparticle can be fabricated with various sizes, dimensions and morphologies, allowing us to utilize their plasmonic properties within optical frequencies. In general, asymmetric shape and high aspect ratios result in lower restoring forces and thus lower resonance frequencies, closely packed nanoparticles can couple together when the interparticle distance is comparable to their sizes, leading to red shifts of the resonance and further concentration of fields to small volumes. To study the surface plasmon resonance of particles, a theoretical calculation was introduced by Mie as described in the last section. By solving Maxwell's equations, the interaction of small spheres with an electromagnetic field was illustrated to be related to the size of the particles and surrounding environment. While in terms of arbitrary geometries, in modern physics, a number of numerical methods have been developed as well. Among the most commonly used are the finite-difference time domain (FDTD) method[23], the discrete dipole approximation (DDA)[24, 25], Greens-function[26] approaches similar in spirit to the DDA, the multiple multipole (MMP) method[27], multiple scattering techniques, transfer-matrix approaches[28], plane wave expansions[29], and

boundary element methods (BEM)[30]. In sum, with the support of proper model and theory, the enhancement of the electric field as the intensity of the surface plasmon resonance absorption increases can be exploited as potentials in many applications.

2.2. Metal nanoparticles in optics

In light of the surface plasmon, many applications became possible due to the large enhancement of the surface electric field on the metal nanoparticles surface. Metal nanoparticles generate enhanced electromagnetic fields that affect the local environment. The field is determined by the geometry of the nanoparticle and can enhance fluorescence of the metal itself, the Raman signal of a molecule on the surface, and the scattering of light. These optical properties of noble nanoparticles enable many applications in the fields of sensing, detection, nano-photonics, metamaterials and many others.

Among many types of nanoparticle assembly, dimers are arguably the simplest structure and can be considered as the building block of each cluster. For this reason, dimers are also widely used as a model to analyze and interpret more complex experimental results. Reported by Le Ru and Etchegoin in their book ‘‘*Principles of Surface-Enhanced Raman Spectroscopy”*[31] gap-plasmon resonances and the local SERS enhancement factors (EF) at the interparticle junction of dimers formed by two identical spheres (radius a = 25 nm, either Ag or Au) are very sensitive to the gap distance. (Figure 1.1) The decrease of the interparticle distance in the dimer leads to stronger local enhancements but with an increasing degree of spatial localization.

References – page 40

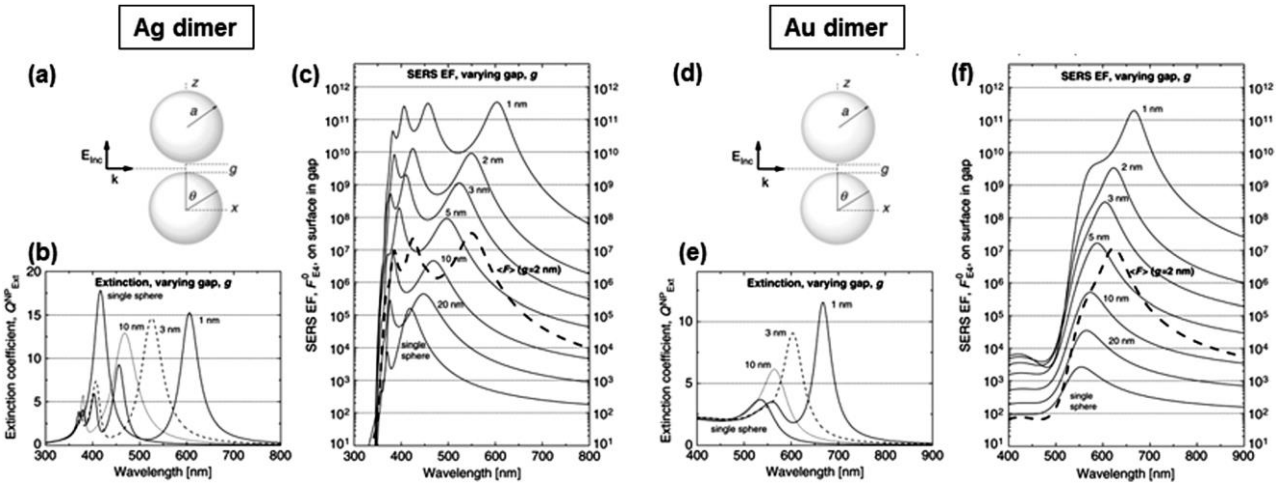

Figure 1.1-(a, d) Schematic configuration of dimers formed by two Ag (a) or Au (d) spheres of radii a = 25 nm and separated by a gap g. The incoming wave is polarized along z (axis of the dimer) and with wave-vector k along x. (b, e) Extinction coefficients, Qext, for varying gaps as functions of incident wavelength for Ag (b) and Au (e) dimers. (c, f) SERS EF at the hot-spot for Ag (c) and Au (f) dimers. Also shown (thick dashed line) is the average SERS EF in the case of a g = 2 nm gap.[31]

Later on S. K. Kleinman et al reported that by using a pair of molecules that have contrasting isotopic vibrational signatures, it is possible to distinguish signals that originate from either of the adsorbates, even at very low concentrations. Rhodamine 6G and crystal violet were both characterized separately using this approach by comparing 50:50 mixtures of their isotopologues (H vs D-terminated; Figure 1.2a-c). For each spectrum, only the vibrational signature of either the deuterated or non-deuterated samples was predominantly detected, confirming the single molecule SERS (SMSERS) nature of the experiment.[32, 33]

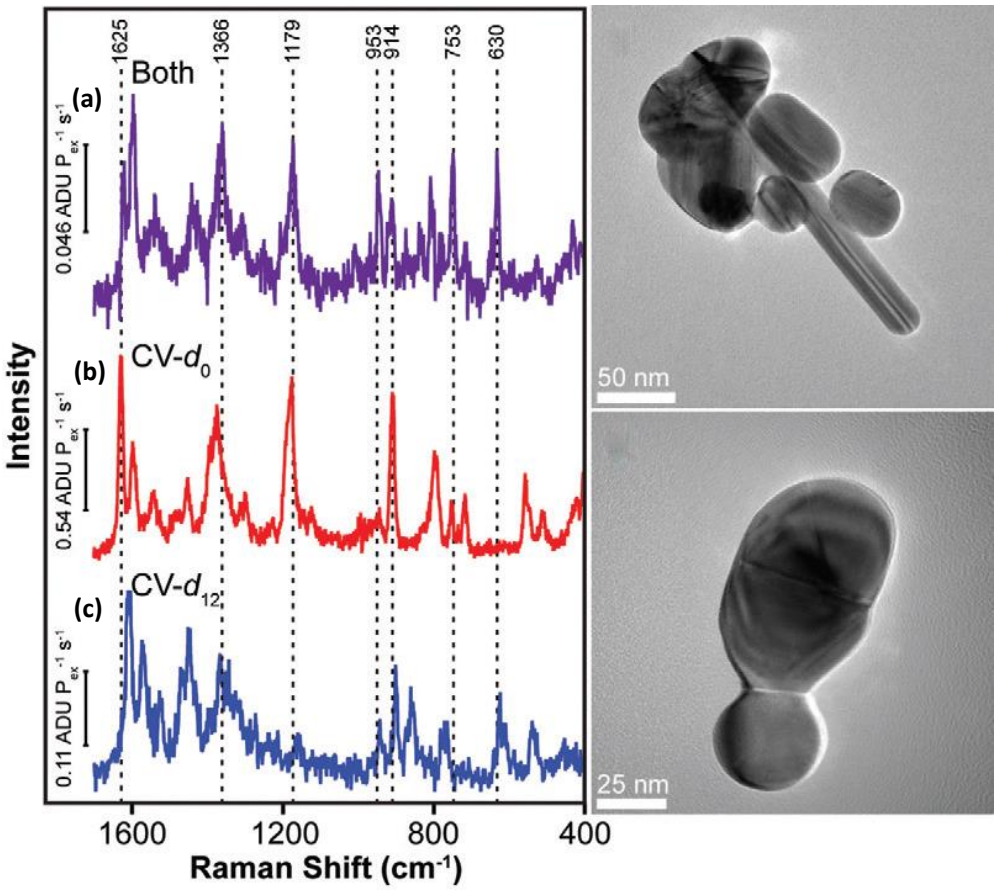

Figure 1.2-Representative SMSERS spectra of crystal violet isotopologues. (a) both deuterated and undeuterated, (b) undeuterated, (c) deuterated, (d-e) TEM images of Ag colloid aggregates which support SMSERS.[32]

Another important application of GNPs is in the field of optical tweezer. The conventional approach to increase the gradient force to hold the particles is normally by increasing the laser intensity, however very strong intensities will damage the trapped particles such as live cells and other delicate biological objects. But coupling light to plasmonic metal nanoparticles can lead to near fields that vary over just a few nanometers, producing optical gradients that are much greater than otherwise possible.[34] Moreover, the fields can vary rapidly in three dimensions, as illustrated in Figure 1.3. This is a key advantage over conventional optical tweezers, where the optical gradient and thus the trapping force, is always weaker in the beam-propagation direction than in the transverse directions.[35, 36]

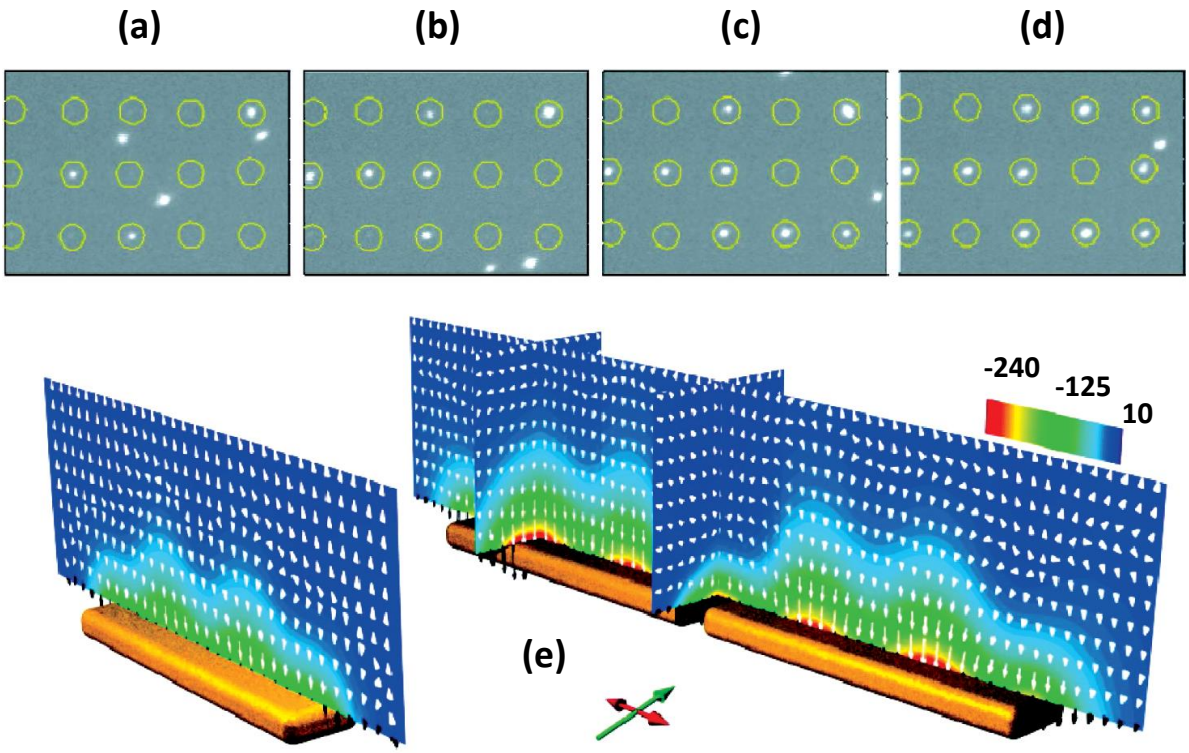

Figure 1.3-Optical trapping due to localized near fields above a pair of gold nanoparticles. (a–d) Sequence of images recorded above an array of 15 nanoparticle pairs, showing trapping of 200-nm polystyrene particles in water. The circles indicate the positions of the metal particles, and the bright spots are the polystyrene particles. (e) Calculated optical force acting on the particles above individual nanoparticles and pairs of nanoparticles. The arrows show the strength and direction of the force.[36]

H.Duan and his coworkers have proved that GNPs can be also used in cancer cell targeting and traceable intracellular drug delivery. They pointed out that amphiphilic nanoparticles carrying mixed polymer brush coatings with distinctly different hydrophobicity can self-assemble into vesicles with the functional nanoparticles embedded in the shell formed by the hydrophobic brushes and the hydrophilic brushes extending into aqueous environment to stabilize the structures. This new type of plasmonic assemblies enables plasmonic imaging probes to specifically label targeted cancer cells, when tagged with cancer-targeting ligands. (The schematic illustration is shown in Figure 1.4) .[37]

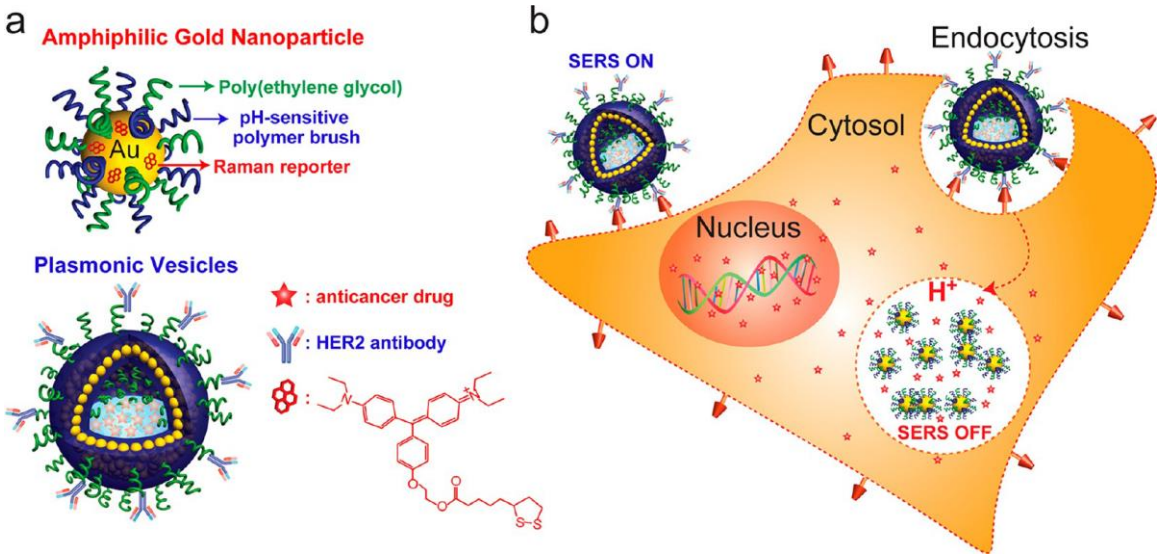

Figure 1.4-(a) Schematic illustration of the amphiphilic gold nanoparticle coated with Raman reporter BGLA and mixed polymer brushes of hydrophilic PEG and pH-sensitive hydrophobic PMMAVP grafts and the drug-loaded plasmonic vesicle tagged with HER2 antibody for cancer cell targeting. (b) The cellular binding, uptake, and intraorganelle disruption of the SERS-encoded pH-sensitive plasmonic vesicles.[37]

Nanoparticle–sample interaction can provide new modes of high-resolution imaging. L. Novotny et al reported that metal nanoparticle tip can strongly modify the amount of light absorbed by and emitted by a luminescent sample. This modification occurs only within the nanometer-scale volume next to the nanoparticle where local fields are strongly enhanced, so that scanning the particle over the sample produces a luminescence image with nanometer-scale resolution (Figure 1.5).[38] The resolution of the luminescence image decreases as the separation between the nanoparticle and the sample increases; on the other hand, if the nanoparticle is too close to the sample, quenching dominates over plasmon-enhanced emission, and the luminescence image is degraded. At optimal separations, spherical gold nanoparticles provide a lateral resolution of approximately 20 nm, and even better resolution should be achievable using nanorods or other anisotropic nanoparticles.[39]

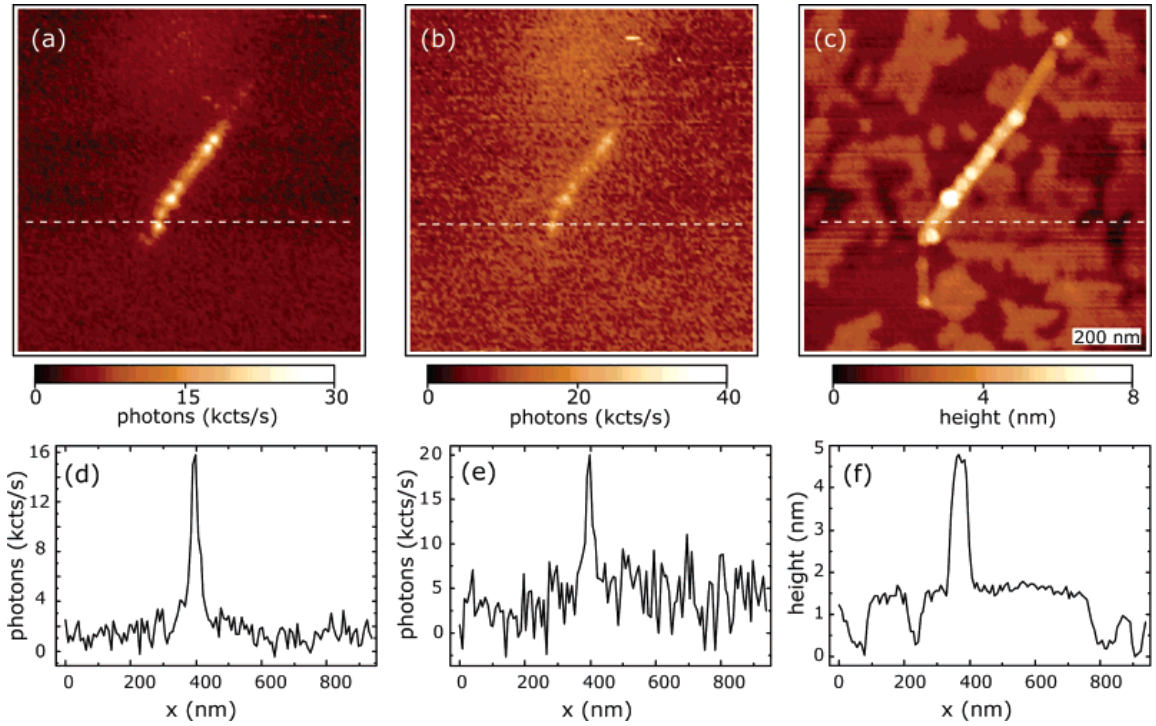

Figure 1.5-Near-field PL (a), Raman (b), and topography image (c) detected simultaneously for micelle-encapsulated SWNTs. (d), (e), and (f) are optical and topographic cross sections taken along the dashed lines in (a), (b), and (c), respectively. [38]

Not only on 2D surfaces, R. ODA et al[40] also showed the SERS spectrum of benzenethiol (BT) used as molecular probe adsorbed on the nanostructures consisting of GNPs assembled on a 3D surface of a fibrous silica template. They found that in the absence of hybrid nanosilica fiber-GNPs, no signal was detected even at concentrations as high as 10^{-2} M for BT, but highly enhanced Raman signals were observed when GNPs were assembled on the silica surface, and this phenomenon is highly size dependent as it shows in Figure 1.6.

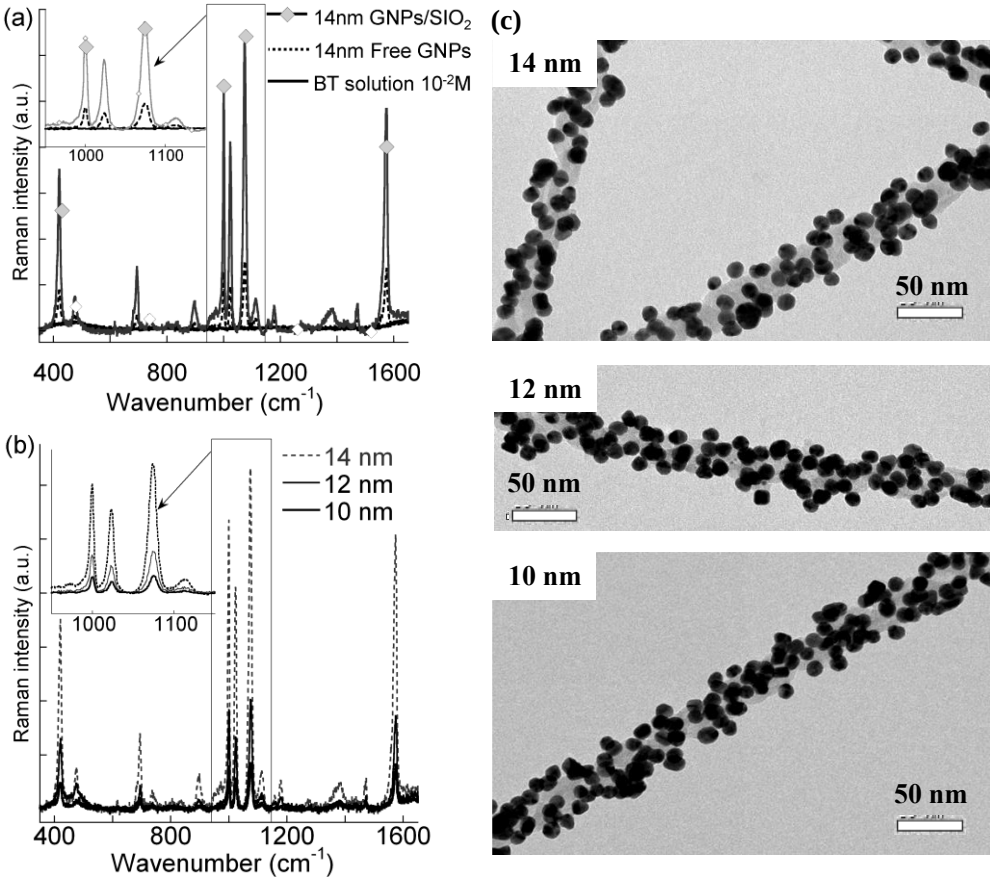

Figure 1.6- Raman and SERS spectra of Benzenethiol and corresponding TEM images. a) Comparing the Raman spectrum of 10-2 M BT aqueous solution, the SERS spectrum of 10-6 M BT in 14nm GNPs colloid solution, and that of 10-6 M BT in the presence of GNPs/silica-nanohelices hybrid structures; b) SERS spectra of 10-6 M BT adsorbed on GNPs/silica-nanohelices hybrid structures with different diameters (10, 12, 14 nm). λex = 633 nm; c) TEM images of GNPs/silica-nanohelices hybrid structures with different diameters (10, 12, 14 nm). Scale bar=50nm.[40]

Among all these promising applications and perspectives based on interactions of light and metals, rarely has witnessed an explosion of interest on a given topic like negative refractive index materials, which is also equivalently known as metamaterials or double negative media (negative ε and μ). Indeed, after we steer the knowledge on basic physics and classical electromagnetics discussed in previous section, a very special issue attracted scientists' attention concerning "is it possible to obtain negative refractive index, and if so, what can we do with it?" First explored by Veselago[41] in 1968, metamaterials has revolutionized researchers' empirical knowledge in optics, electromagnetics, materials science, mathematics, and physics.

Basically, the index of refraction n is expressed as a function of the product of the

permittivity and the permeability as the Maxwell relation states

$$n = \sqrt{\varepsilon\mu}\,.$$

Hence, it is not immediately obvious that negative permittivity and negative permeability can achieve negative refraction. But, like often in electromagnetics, one has to look at the lossy situation in order to extrapolate the conclusions to lossless media.[42]

Upon including losses, the permittivity and permeability are written in the polar coordinate system as

$$\varepsilon = |\varepsilon| e^{i\theta_\varepsilon}, \quad \mu = |\mu| e^{i\theta_\mu}.$$

The index of refraction thus becomes

$$n = \sqrt{|\varepsilon||\mu|}\, e^{i\frac{1}{2}(\theta_\mu + \theta_\varepsilon)}.$$

In isotropic and homogeneous media, our convention (using $i = \sqrt{-1}$ to denote the imaginary number) imposes that $\varepsilon'' > 0$ (the imaginary part of the permittivity to be positive) and $\mu'' > 0$, so that $\theta_\varepsilon \in [0, \pi]$ and $\theta_\mu \in [0, \pi]$ (Shown in Figure 1.7).

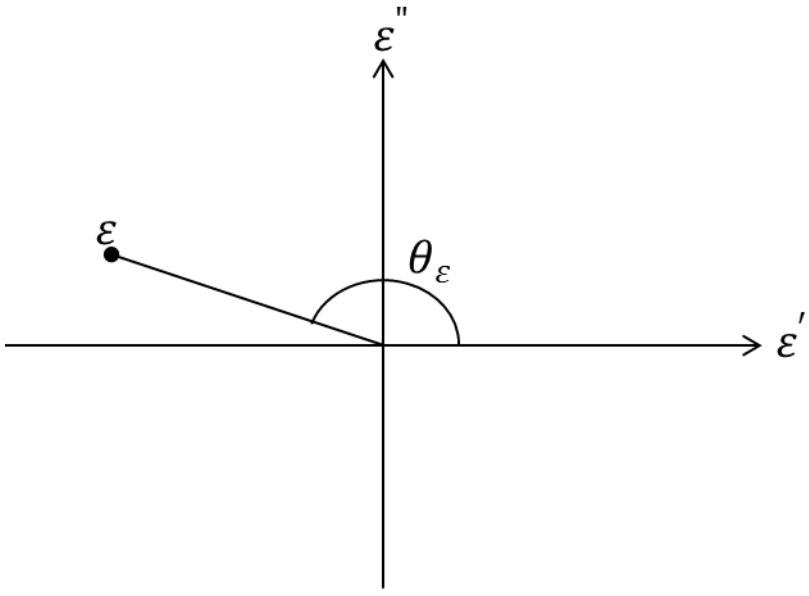

Figure 1.7- Representation of permittivity in the polar coordinate system. [42]

Consequently, the angle of the index of refraction is $(\theta_\varepsilon + \theta_\mu)/2 \in [0, \pi]$. This range is reduced to $\left[\frac{\pi}{2}, \pi\right]$ in the situation when $\varepsilon' < 0$ and $\mu' < 0$, so that the real part of the index of refraction is negative ($n' < 0$). In particular, the lossless limit is obtained as $\theta_\varepsilon \to \pi$ and $\theta_\mu \to \pi$ which produces:

$$n = \sqrt{|\varepsilon||\mu|}e^{i\pi} = -\sqrt{|\varepsilon||\mu|}.$$

Under the assumption of an isotropic medium, this index of refraction can be directly written as- $n = \sqrt{|\varepsilon||\mu|}e^{i\pi} = -\sqrt{|\varepsilon||\mu|}$ introduced into Snell's law and is seen to reverse the refraction direction based on phase matching of the wave-vector.[42]

Another situation inducing $n' < 0$ exists theoretically but with limited practical interest. As a matter of fact, a negative index of refraction is obtained as soon as $(\theta_\varepsilon + \theta_\mu) > \pi$. This can be obtained when $\theta_\varepsilon > \frac{\pi}{2}$ and $\theta_\mu > \frac{\pi}{2}$, which is the situation of a standard left-handed medium described above, or for example if we let $\theta_\varepsilon = \frac{\pi}{2} + \delta_\varepsilon$, where $\delta_\varepsilon \in \left[0, \frac{\pi}{2}\right]$. In this latter situation, a negative n' is obtained when $\theta_\mu > \frac{\pi}{2} - \delta_\varepsilon$:

1. When $\delta_\varepsilon \to \frac{\pi}{2}$, a situation can be selected where the permittivity has a negative real part and small losses ($\theta_\varepsilon \to \frac{\pi}{2}$) and the permeability has a positive real part and small losses ($\theta_\mu \to 0$). With the proper combination of angles, a negative refraction can be obtained.
2. When $\delta_\varepsilon \to 0$, the permittivity has a small negative real part and high losses which, combined with a permeability with a small positive real part and high losses, can also yield a negative refraction.

In both cases, however, the resulting complex *n* has a negative real part, but also a very large imaginary part. This configuration therefore corresponds to a medium with high losses where

electromagnetic waves are strongly evanescent, and has a limited practicality except for some very specific near-field applications.[42]

Then, we will discuss about metal nanoparticles in negative permittivity. Similarly to what we have discussed in Lorentz model and Drude model before, we assume the free electrons in the metal is much smaller than the ion cores and then, we can subsequently obtain the relative dielectric permittivity as

$$\varepsilon(\omega) = 1 - \frac{Ne^2/(\varepsilon_0 m)}{\omega(\omega + i\gamma)} = 1 - \frac{\omega_p^2}{\omega(\omega + i\gamma)},$$

Where the plasma frequency is defined as $\omega_p \equiv \sqrt{(Ne^2)/(\varepsilon_o m)}$.

The real part of dielectric permittivity is negative when $\omega < \omega_p$, this means when the incident light has a frequency which is smaller than plasmon frequency, the dissipation can be negligible especially for metals like gold and silver, indicating that gold and silver could be idea candidate for negative dielectric materials. On the other hand, when $\omega > \omega_p$, the medium behaves as an ordinary dielectric medium.

The manufacturing of artificial magnetics can be achieved with metals that induced loop shaped current, which in return will produce a strong magnetic moment.[43]

Pendry, for example, proposed the resonant loop-shaped conductors with a gap inserted to realize the negative permeability.[44] The gap in the structure introduces capacitance and gives rise to a resonant frequency determined only by the geometry of the element. It is also known as the split-ring resonator (SRR) as shown in Figure 1.8, which could be described as

$$\mu(\omega) = 1 - \frac{F\omega^2}{\omega(\omega + j\Gamma_m) - \omega_{0m}^2},$$

Where F, Γ_m, and ω_{0m} are the filling fraction, resonant damping, and resonant frequency, respectively. By simply assuming that the metal making up the SRR is a perfect conductor, it appears possible to fabricate SRRs with resonances at optical frequencies by simply by making them smaller. However, in spite that the fabrication of such a structure in very small scale is difficult, this assumption is no longer valid when it is at high frequencies. At high

frequencies, the response time of the electrons becomes comparable to the period of the electron-magnetic wave, and the charge lags behind the applied fields, indicating the strength of the magnetic Mie resonance of the nanoparticles will decrease due to the increasing losses in the metal.[45]

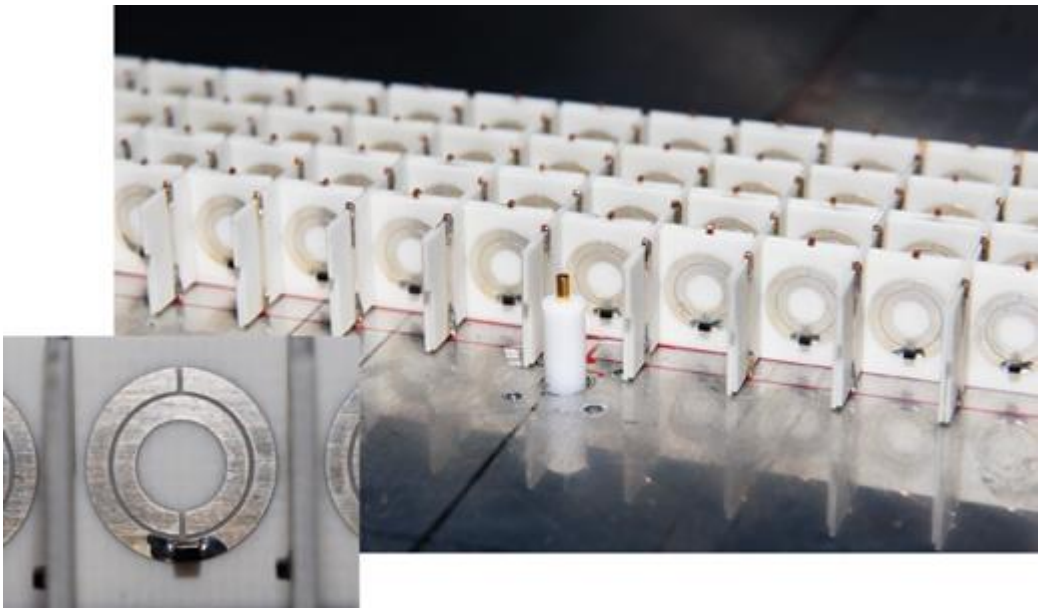

Figure 1.8- An illustrative view of a split ring structure.[46]

To overcome this difficulty, the usage of metal nanoparticles, *e.g.* side-by-side pairs of metal nanorods (Figure 1.9), can greatly enhance the magnetic resonance due to the hybrid mode of Mie resonance as we discussed. Different from bulk metals, every plasmonic nanoparticle can be considered as an LC circuit, which can attribute to a magnetic dipole moment. Furthermore, increasing the number of coupled metal nanoparticles can lead to new hybrid modes at higher frequencies and this phenomenon is greatly related to the symmetry of the assembly. More importantly, the inclusion of nanoscale particles as the building blocks can make it possible for negative effective parameters at optical or visible frequencies, because both experimentally and theoretically, the periodicity of the metamaterials requires the size of the materials to be at least 10 times smaller than the wavelength of incident light[47] suggesting if we want to have negative index of refraction at optical or visible frequencies (400nm-800nm), the size of the periodical units should be at nanometer scale.[45]

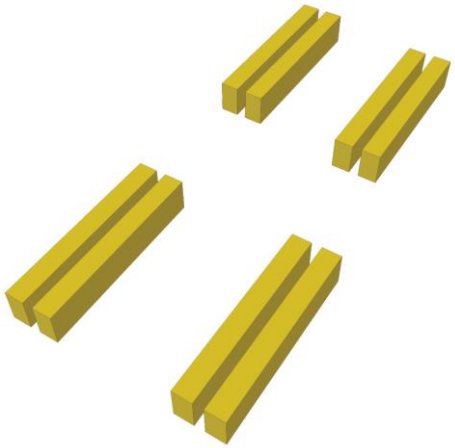

Figure 1.9- Illustration of side-by-side pairs of metal nanorods exhibiting magnetic resonances.[48]

In general, metamaterials are materials that are able to rotate visible light as it passes through them. If the effect is strong enough, it can lead to the material having a negative index of refraction. To completely control the flow of an electromagnetic wave inside of matter, one needs the ability to manipulate both the electric and magnetic components of light with microscopic electric and magnetic dipoles, respectively.[19] The realization of negative permittivity can be obtained by using metal nanoparticles-(nanowires or some kind of nanorods or nanospheres), and for the negative permeability,[17] the shape and the organization of the materials plays a critical role. Such material does not exist in nature and no atom in a natural material can have such a level of control. Artificial materials and structures are needed to approach to such a purpose.

As stated in this part, the booming development of plasmonics, especially in gold/silver nanoparticles has paved a way in materials selection. The self-assembly of these nanoparticles has been identified as an important process where the building blocks spontaneously organize into ordered structures. Among them, chiral self-assemblies of small objects are of great interest due to not only the conformational anisotropy that chirality brought in but also the optical properties and potential applications whereas more detailed information will be discussed in the following paragraph.

3. Chiral self-assemblies in optical nanoscience

3.1 Why chiral self-assembly?

Chirality can be defined as "An object or a system is chiral if it is distinguishable from its mirror image; that is, it cannot be superposed onto it" since the identification of chirality was first introduced in 1848.

Chirality in nanostructures could potentially provide a new scope of interactions of chiral objects with their surrounding environment like chiral molecules, creating a new dimension of mechanical and optical applications in nanodevices. Needless to say, as the rapid development in material science, the requirement of structural diversity will inevitably lead us to synthesize asymmetric, anisotropic or even chiral materials at nanoscale. Janus (two-sided) particles,[49-51] for instance, has been demonstrated that simply having two different faces on a particle can help in designing multiple functionalities[52, 53] and developing more controllable assembly methods.[54, 55] Therefore, it is well believed that further breaking of symmetry by imparting chirality in nanostructures will open new possibilities in syntheses and applications.

Nanoscale chiral self-assembly finds applications in biological and optical functional materials. As it can be seen in proteins or DNA, helices or helical structures can result from the packing of 1D molecular chain. In a protein α-helix, an amino acid residue is strongly bonded via H-bonding to a residue that is four units earlier (Figure 1.10a). The consistent molecular chirality of the different amino acids (L) was critical in ensuring the same turning direction of the peptide backbone, giving a right-handed helix in terms of the secondary structure. The structure can thus maximize the number of intra-molecular H-bonds. DNA double helices are also right-handed (Figure 1.10b). The consistent chirality of the sugar moiety (D) turns the backbones towards the same directions and the packing model maximizes the H-bonding between complementary nucleotides and the $\pi - \pi$ stacking between neighboring ''rungs''. In both cases, the molecular packing or bonding was the origin

of the axial contraction (coiling) of the 1D molecule like packing of a wire into a cylindrical space as Figure 1.10c shows.[56]

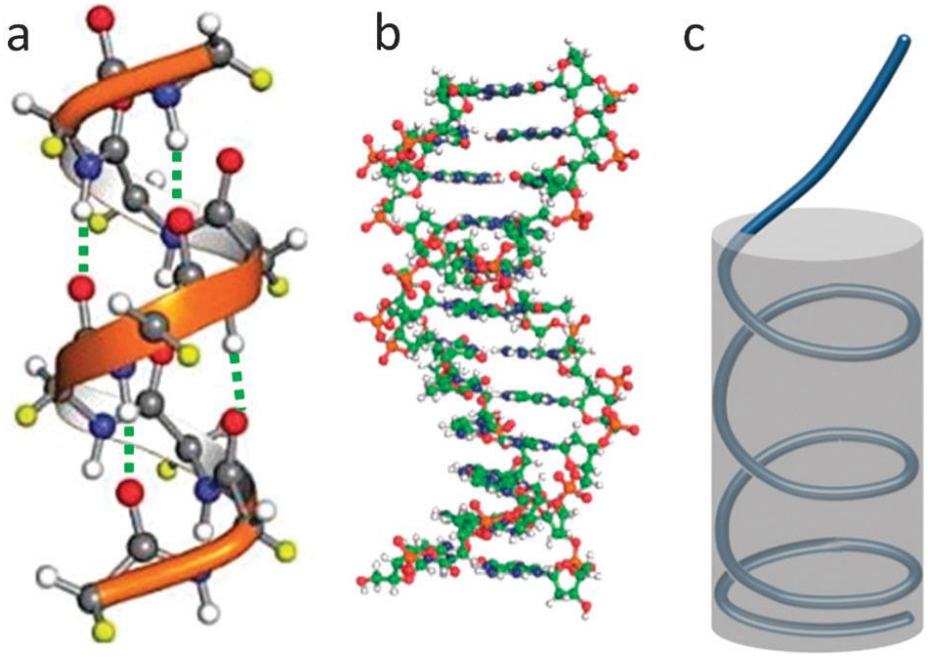

Figure 1.10- Schematics illustrating: (a) peptide a-helix (with green dashed lines indicating the H bonds), (b) DNA double helix, and (c) packing of a wire into a cylindrical space.[56]

The origin of helices was often studied by using *Bauhinia* pod and related natural plant structures. Armon et al.[57] showed that a single component, namely a flat strip of *Bauhinia* pod with a saddle-like intrinsic curvature, is sufficient to generate a wide variety of helical shapes, where the flat valves were turned into helices of opposite chirality. Forterre and Dumais illustrated the same chirality-creating mechanism using paper model and proved that the generic approach of Armon should be applicable to all of these different situations, as it does not rely on the specific knowledge of the microscopic interaction. The Bauhinia seed pod and its mechanical analogs clearly show how chiral shapes can emerge from global geometrical constraints without bulk chirality at the microscopic level. (Figure 1.11).[58]

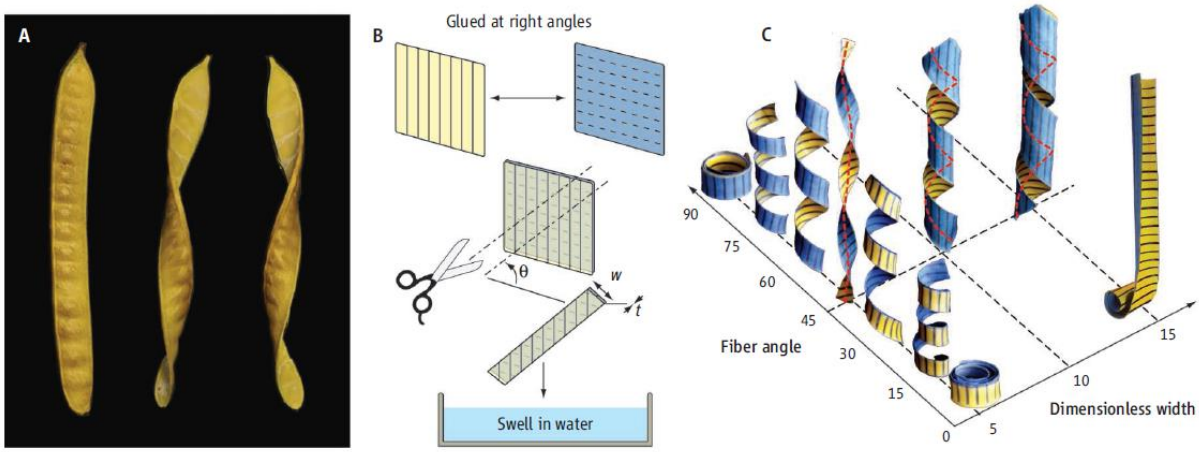

Figure 1.11- The coiling of pods and paper models, following the model of Armon *et al*., is illustrated. (A) An initially straight seed pod was split to show the strong curvature stored in the two valves. (B) The protocol used to prepare paper models, which reproduces the coiling behavior of plant structures. (C) The geometry of paper models for various values of the two control parameters: the dimensionless width and the fiber angle. Note the reversal of the blue and yellow faces for fiber angles exceeding 45 ° and the transition from helicoid to cylindrical ribbons as the width is increased.[58]

The application of chirality in nanoscience is quite promising, however many mechanistic understandings and concepts are still unclear, for example, molecular chirality could be the cause for morphological chirality; but it is also possible that molecular chirality may arise as a consequence of the morphological chirality. Just like in any other field, advancement in fabrication capabilities is a must for improving known properties and exploring new ones.[56]

In contrast to traditional areas for the application of chirality such as catalysts[59-61] and molecular recognition[62, 63], the application of chirality in plasmon has stretched to novel areas like photovoltaics[64], optical sensing[22] and even negative index materials. E. Plum and coworkers, for example, have fabricated a chiral structure, in which both the electric and magnetic components of light excite strong electric and magnetic dipoles[20]. At microwave frequencies this structure has an effective negative index of refraction. This means that the phase velocity of the wave is opposite to the electromagnetic energy flow. S. Zhang and colleagues[21] described a closely related structure that can operate at THz frequencies. If these structures could be further engineered to work in optical and visible frequency ranges, strong optical activity might enable novel types of optical devices. To understand these

promising fields, one has to first understand how chiral materials could cause polarization of incident light or linearly polarized wave to gradually rotate. It is known that the interaction of circularly polarized light with chiral matter depends on the relative handedness between the two. However, the microscopic origin of this effect is magnetic dipoles that are excited by the electric component of the light and vice versa [65-68]. In a plane wave, the incident electric and magnetic vector components are perpendicular to each other. If the magnetic component induces an electric dipole parallel to the magnetic field vector, the resulting net local electric field vector will be rotated a bit. It can be shown that reciprocity demands that, likewise, magnetic dipoles are excited by the electric vector component. Hence the magnetic field vector rotates as well. The relations between the relevant components of the electromagnetic fields in the macroscopic Maxwell equations then become[66, 68]

$$D = \varepsilon_0 \varepsilon E + i\kappa / c_0 H \quad \text{and} \quad B = \mu_0 \mu H - i\kappa / c_0 E \,.$$

Here, κ is the dimensionless chirality parameter. The refractive index, *n*, for right- (+) and left-handed (-) circular polarization becomes $n_{\pm} = \sqrt{\varepsilon\mu} \pm \kappa$. For such three-dimensional chiral materials, it is of great interest for it gives an opportunity to control the refractive index towards to unusual values such as largely positive, near-zero or even negative refractive index for one circular polarization, even if the electric permittivity ϵ and magnetic permeability μ are both positive.[19]

3.2 An overview of current self-assembled chiral nanosystems

As chirality can be found everywhere in daily life from big macroscopic objects to small micro- or even submicro- particles, and novel self-assembling systems involving chirality based on noncovalent bonding interactions, such as hydrogen bonding, π–π stacking, ion-dipolar, electrostatic interactions, and their combinations are now emerging rapidly, it would be beyond the scope of this thesis to summarize all the chiral self-assembled systems. Hereby in this part we will typically introduce very recent achievements in chiral self-assembled nanosystems in aqueous medium. Common biomolecules and organic

molecular self-assemblies with different bonding interactions will be briefly discussed first, then induced chirality in inorganic self-assembled systems composed of metals, oxides and ions will be presented as followed. The basic idea of this part is to set up a fundamental concept on chiral self-assemblies and broaden the view of modern physical chemistry and materials sciences in optics.

3.2.1 Fabrication of chiral organic self-assembled nanostructures

The discovery of double helical structures of DNA in 1953 did revolutionize people's view and point out one feasible origin of chirality. But, afterwards more and more interests are focusing on the chiral assembly of small organic molecules such as amino acids[69], sugars[70], lipids[71], and their analogues. This allows researchers to freely design self-assemblies without much confinement.

One of the examples is reported by E. W. Meijer and Albertus P. H. J. Schenning, who synthesized oligo(p-phenylenevinylene) (OPV)-substituted hexaarylbenzene and showed that they can self-assemble via a highly cooperative fashion into right-handed chiral superstructures in apolar solvents by π-stacked aggregates as shown in Figure 1.12. These properties will make this star-shaped molecule a potential candidate in supramolecular electronics.[72]

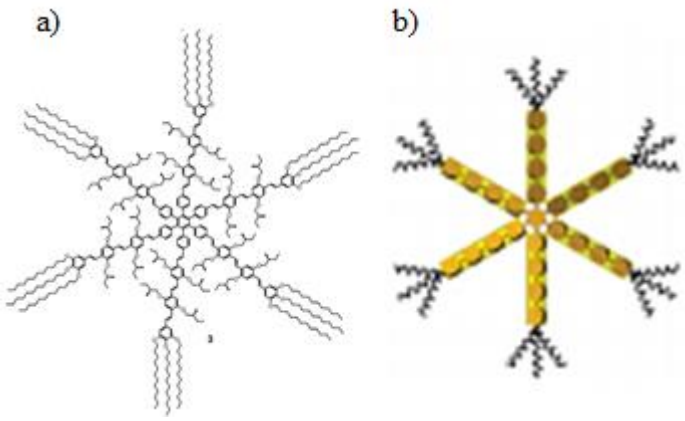

References – page 40

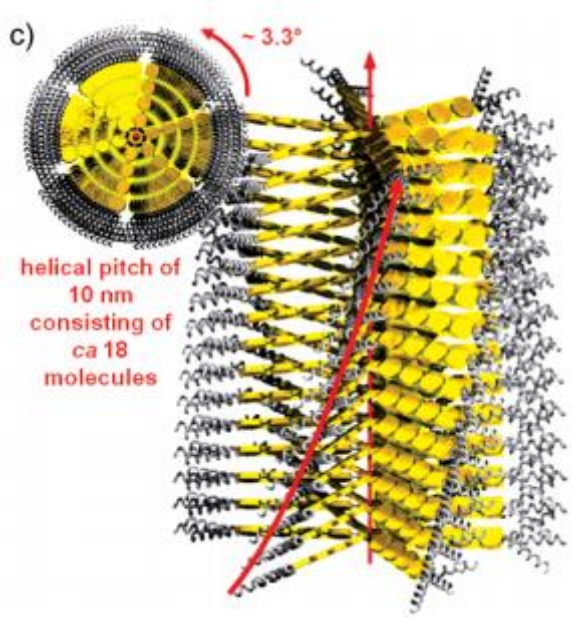

Figure 1.12- (a) molecular structure of OPV-substituted hexaarylbenzene, (b) schematic representation of (a), and (c) schematic illustration of the helical columnar packing.[72]

More recently, Z. He et al, reported that based on the hierarchical self-assembly of a ferrocene (Fc)-modified dipeptide, ferrocene-L-Phe-L-Phe-OH (Fc-FF), it is able to rationally design the chiral self-assembly and the formation of well-defined chiral nanostructures composed of helical twisted β sheets, where the strong hydrophobic interaction of the Fc moiety was suggested to have a key role in this kinetically controlled self-assembly process. They also proved that the realization of precisely controlling the helical pitch, diameter, and handedness of the self-assembled chiral nanostructures could be done by subtle controls in counterions, temperature, and solvents as it is illustrated in Figure 1.13 below.[73]

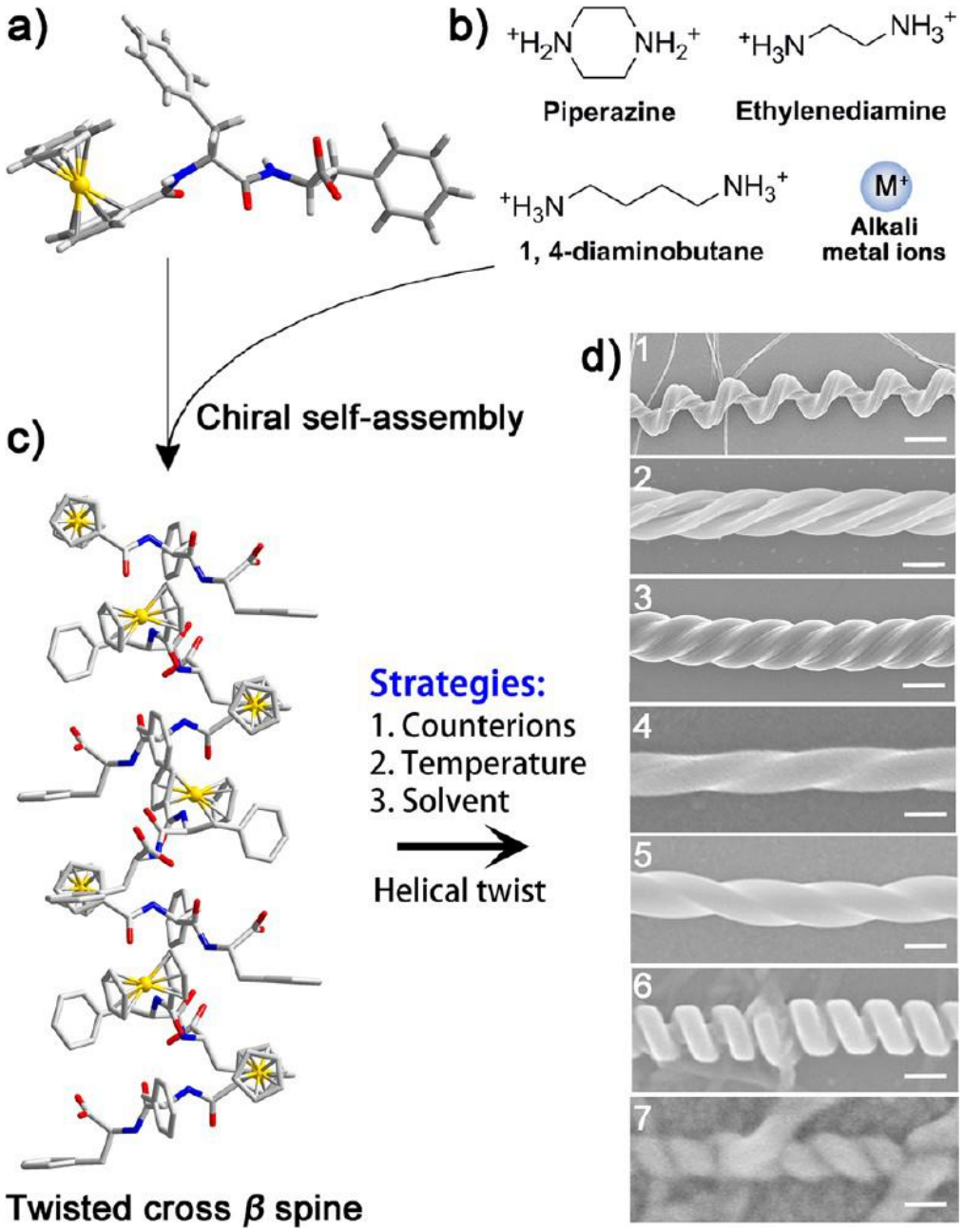

Figure 1.13-a) Molecular structure of Fc-FF from the single crystal structure determination (grey: carbon red: oxygen, blue: nitrogen, white: hydrogen). b) Counterions used to direct the chiral self-assembly of Fc-FF. c) Single-crystal structure of Fc-FF showing the cross *β* spine of a twisted *β* sheet in Fc-FF. d) Rationally designed hierarchical chiral nanostructures with unprecedented levels of diversity and precision (top-down) Chiral nanostructures in d) 1−5 were self-assembled with piperazine counterions via precise control of the temperatures, solvents and pH. The rigid nanosprings in d)6 were grown with ethylenediame or 1,4-diaminobutane in less polar solvents. The tubelike helical ribbons in d)7 were self-assembled in the presence of alkali metal ions (Na^+ or K^+) in less polar solvents.[73]

Alternatively, J.-M. Lehn introduced “helicate” as early as 1987 to describe helical metal complexes that contain organic strands intertwining around the metal centers[74]

(Figure 1.14). They reported that the ether-linked 6,6′ -methyl- 2,2′ -bipyridine oligomers can instantly self-assemble to form double-stranded helical metal complexes with Cu+ ions. The helical structures were determined by the geometrical preferences of the metal centers as well as the structures of the organic ligand strands, so that a rational design of a double-helical structure is possible, thereby enabling the introduction of some properties into helicates by functionalization.

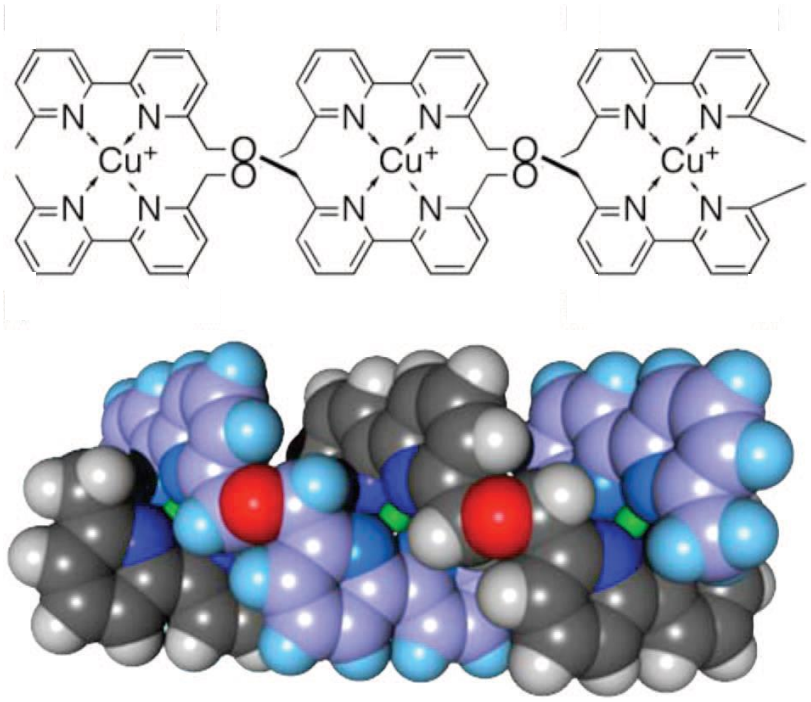

Figure 1.14-Structural formulas of the Cu(I) helicates and its schematic helical illustration. [74]

E. Yashima et al reported that the hydrogen-bonding interaction is an exploitable and versatile tool for constructing supramolecular assemblies. They reported a double- helical oligomer (**3**) that consists of two complementary molecular strands (**1** and **2**) bound together through amidinium-carboxylate salt bridges (Figure 1.15). The duplex, (R)- or (S)-**3**, was spontaneously formed from the (R)- or (S)-**1** and achiral **2** in chloroform through the two identical amidinium-carboxylate salt bridges, which have been widely used as a joint for constructing various supramolecular assemblies for their nature of double hydrogen bonding and high association constants even in polar media.[75]

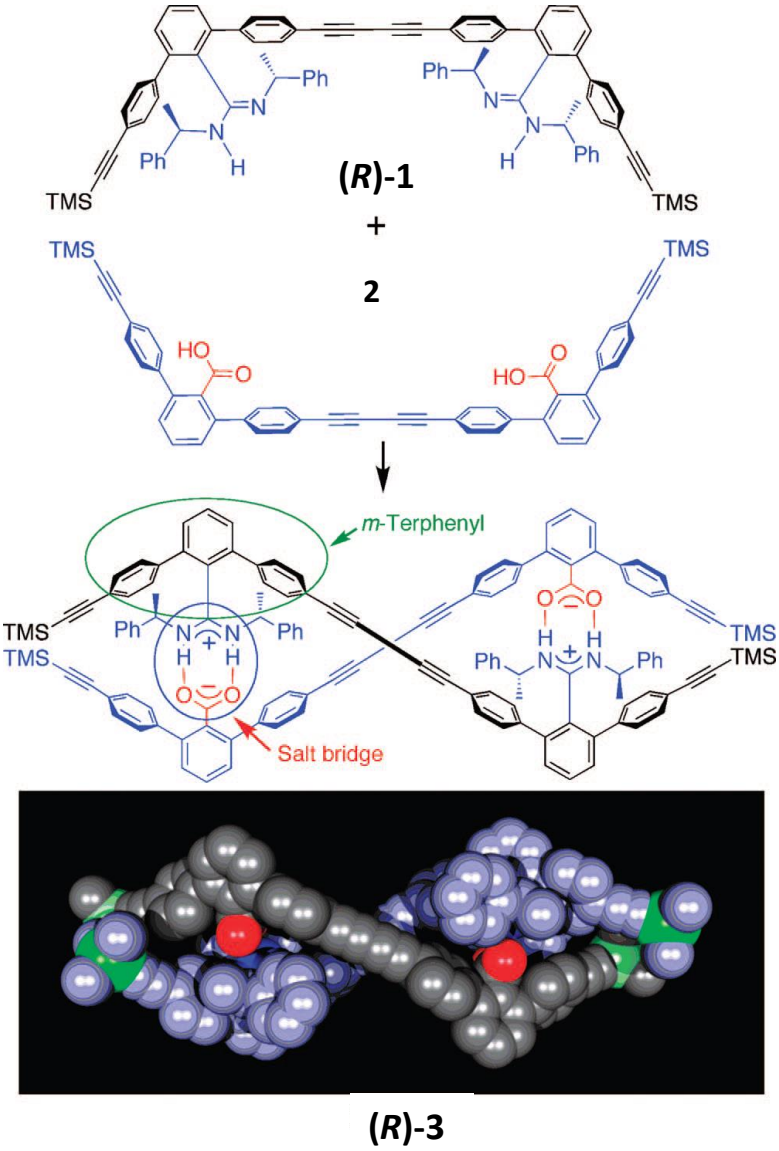

Figure 1.15-Schematic illustration of complementary double-strand helix formation and crystal structure of (R)-3.[75]

Later on they reported that helicity can be also induced to polymers. One typical example is the poly (methyl methacrylate) (st-PMMA), which folded into a preferred-handed helix assisted by a chiral alcohol **4** in toluene accompanied by gelation, and at the same time, fullerenes, such as C_{60}, were encapsulated within its helical cavity to form a robust, processable peapod-like crystalline complex as shown in Figure 1.16. The interesting point is that after removal of **4**, the induced helicity can be still memorized by the st-PMMA. The st-PMMA gel complexed with C_{60} exhibited apparent VCD and ICD signals in the PMMA IR regions and in the encapsulated C_{60} chromophore regions, respectively, although C_{60} itself is achiral.[76]

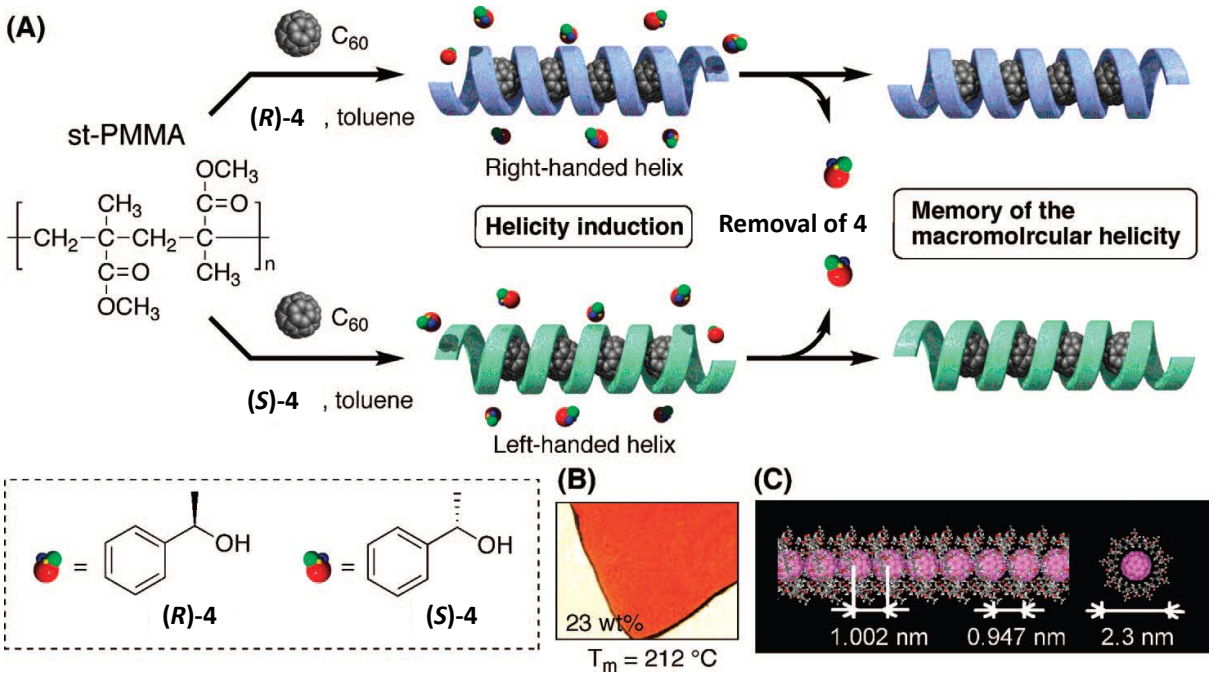

Figure 1.16-(A) Helicity induction in st-PMMA in the presence of C_{60} with (S)- or (R)-4 and memory of the induced helicity after removal of 4, (B) polarized optical micrograph (POM) of a st-PMMA-C_{60} film, and (C) a possible structure of st-PMMA-C_{60} complex.[76]

Katz et al. found that π-donor–acceptor interactions between the nonracemic helicene **5** and quinone residues makes the mixture self-assembles into one-handed helical columns in apolar solvents, where the molecules are stacked along their helix axes (Figure 1.17).[77] They asserted that donor-acceptor interactions between electron-rich rings of one molecule and electron-poor rings of the adjacent molecules stabilize columnar stacks.[78]

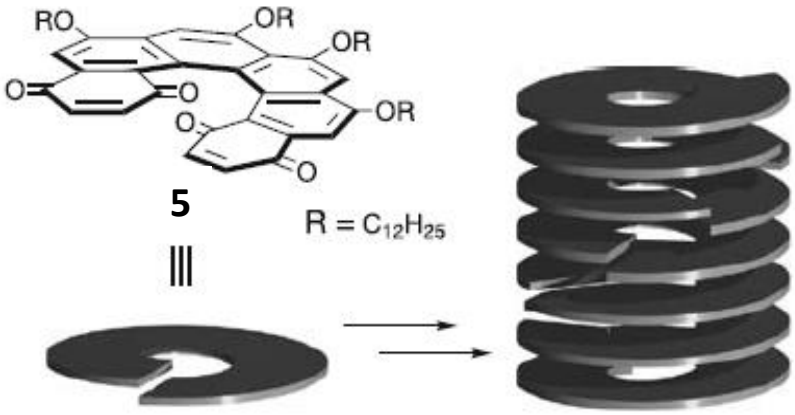

Figure 1.17-Schematic illustration of aggregation of nonracemic helicene 5 into helical columns. [77, 78]

The G-quartet is a well-known structural motif found in biological systems, in which a tetrameric cyclic arrangement of guanosine derivatives is formed through hydrogen bonding

(Figure. 1.18a),[79] and initially it was found that G-quartets of oligomeric deoxyguanosines stack to form helical columnar structures in water via the coordination effect of potassium ions.[80, 81] But later on S. Matile et al reported that long helical columns are formed through ion–dipolar interactions when the concentration of potassium is increased (Figure 1.18b).[82]

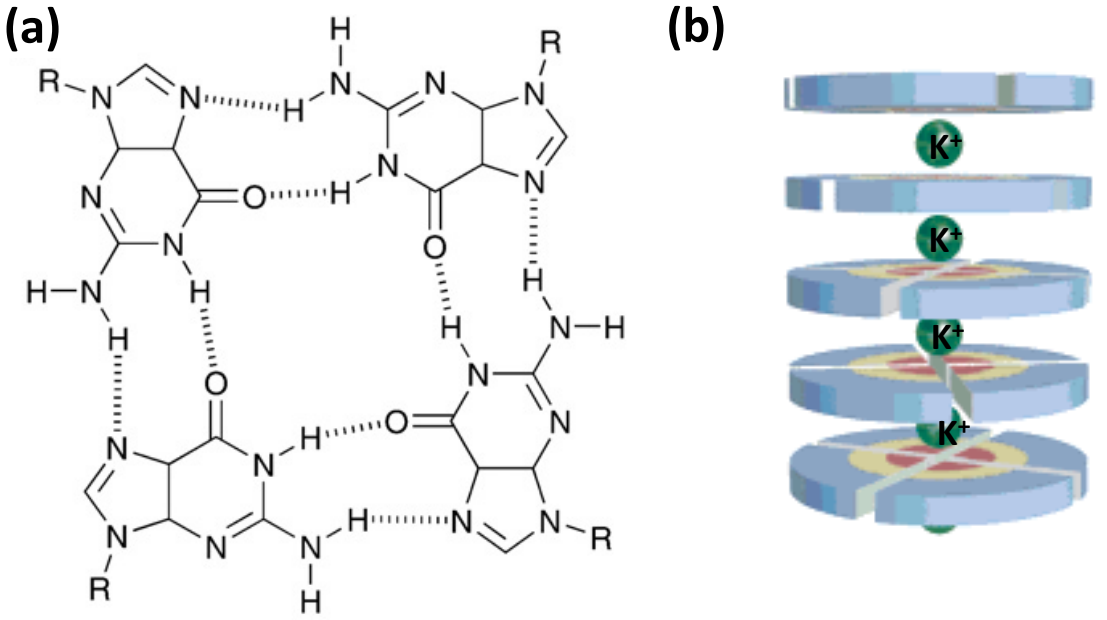

Figure. 1.18-a) The tetrameric cyclic arrangement in a G-quartet structural motif formed by guanosine units, and b) a schematic representation of the helical columnar aggregate formed by the tetramers in the presence of potassium ions.[82]

While using chiral molecules to obtain chirality in the self-assemblies has become a very popular method, assembling achiral molecules can sometimes express chirality for the overall structures. Study of D. M. Walba reported that a smectic liquid-crystal phase made from achiral molecules **1** and **2** (Figure 1.19) was found to have fluid layers that exhibit two spontaneous symmetry-breaking instabilities: polar molecular orientational ordering about the layer normal and molecular tilt. These instabilities combine to form a chiral layer structure with a handedness that depends on the sign of the tilt.[83]

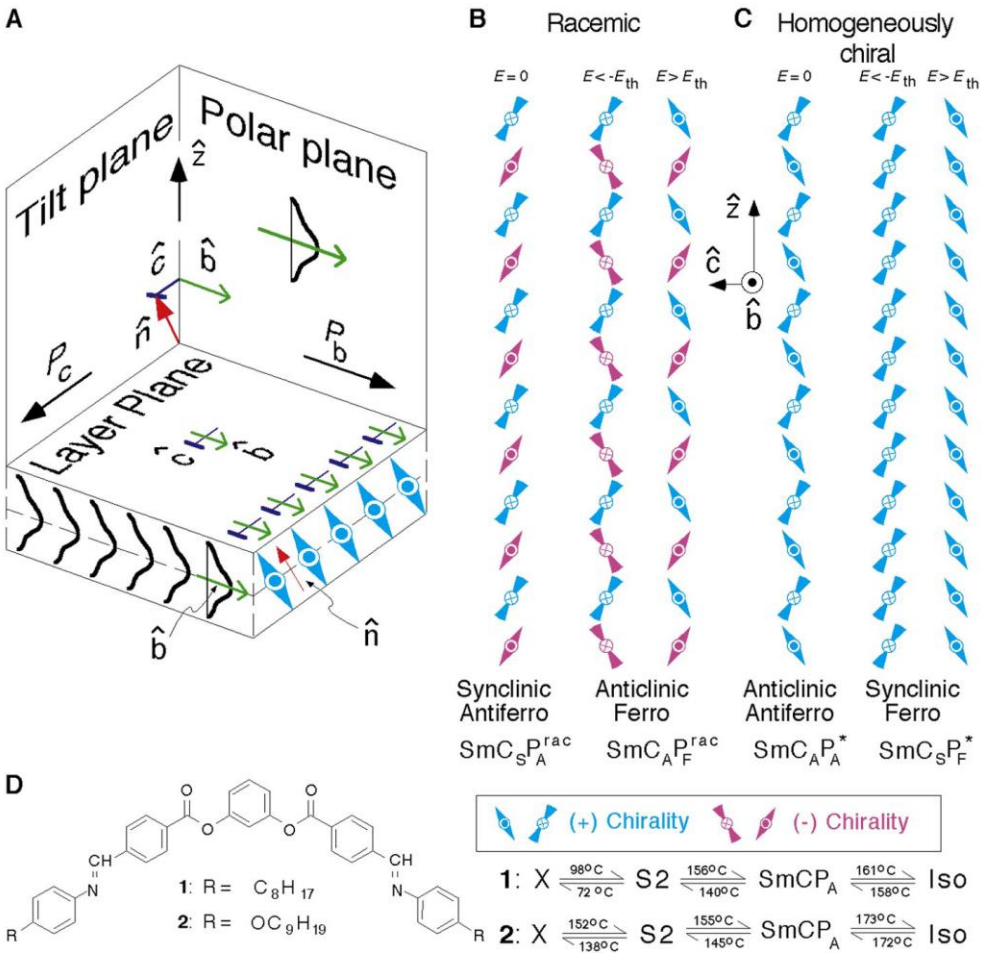

Figure 1.19- (A) Geometry of the $SmCP_A$ phase, showing the layer, tilt, and polar planes, the result of three distinct symmetry-breaking events: the formation of fluid Sm layers normal to z, the tilt of the molecular bows in the direction given by c, and the polar ordering of the molecular bows along the "arrow" b. (B and C) Layer organization in the $SmCP_A$ phase showing the antiferroelectric racemic and homogeneously chiral states at zero applied electric field (E=0) and the corresponding ferroelectric states for fields beyond the threshold E_{th}. (D) Compounds 1 and 2, and their phase diagrams.

It was previously shown by Oda's group that non-chiral dicationic n-2-n Gemini amphiphiles complexed with chiral tartrate anions can be used to fabricate twisted and helical ribbons consisting of bilayers of gemini surfactants.[84] Such systems express the chirality of the tartrate at a supramolecular level resulting in the right-handed (L-Tartrate) or left-handed (D-Tartrate) nanostructures formation (Figure 1.20), where the self-assembling mechanism can be associated to the H-bonding between the network of tartrate ions even though the organization of the aggregates has rarely been elucidated at the molecular level. In fact, hydrogen bonding and chirality are not sufficient to explain the formation of the fibers, and head-group connection between the ammonium ions also plays acritical role.[85] Later on

they showed that essential features of the self-assembly include interdigitation of alkyl chains within each bilayer and networks of ionic and hydrogen bonds between cations, anions, and water molecules between bilayers in the X-ray studies. These features in the molecular packing following the symmetry leading to homochiral monolayer, heterochiral bilayer, and heterochiral adjacent bilayers conserved through large morphology transitions from racemic flat multilayered ribbons to chirally twisted and helical ribbons as well as tubules of the pure enantiomer which is likely at the origin of the expression of molecular chirality at a mesoscopic scale in this system (Figure 1.21).[86]

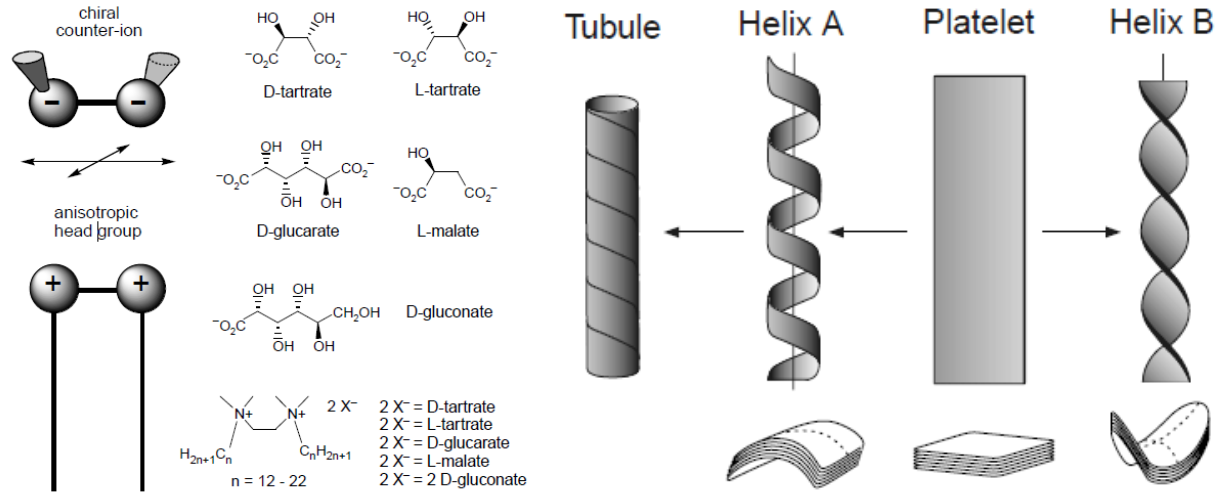

Figure 1.20-Cationic gemini amphiphiles having chiral counterions. Shown in the left are the structures of ethylene-1,2-bis(dimethylalkylammonium) surfactants with various chiral anions. Shown in the right is the schematic representation of helical and twisted ribbons. Top, platelet or flat ribbon. Helical ribbons (helix A), precursors of tubules, feature inner and outer faces. Twisted ribbons (helix B), formed by some n-2-n tartrate surfactants, have equally curved faces. Bottom, the consequences of cylindrical and saddle-like curvatures in multilayered structures. In a stack of cylindrical sheets, the contact area from one layer to the next varies. This is not the case for saddle-like curvature, which is thus favored when the layers are coordinated.[84]

References – page 40

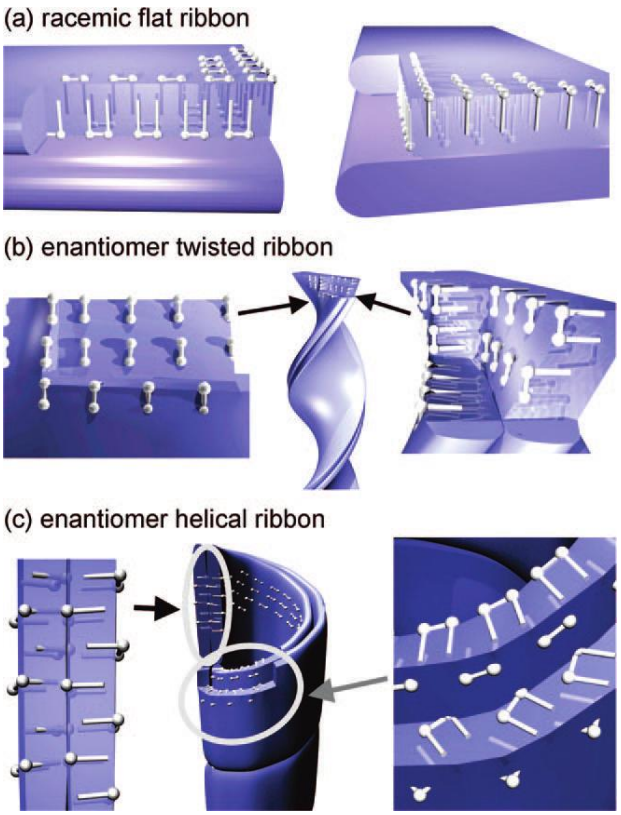

Figure 1.21-Schematic representation of the orientation of gemini molecules with respect to the ribbons in (a) flat, (b) twisted, and (c) helical structures.[86]

In sum, many organic systems have involved into the fabrication of chiral self-assemblies and other systems such as co-assemblies of hybrids[87, 88] are also widely used to design chiral nanostructures and already showed promising applications as well. However, the interests about the origins of chirality and how scientists can manipulate this property prompts research-oriented discoveries on the induced chirality from inorganics and other intrinsically chiral systems.

3.2.2 Fabrication of chiral inorganic self-assembled nanostructures

Inorganics nanomaterials such as metals, oxides and ions can also be used to achieve chiral nanostructures which could exhibit completely different underlying principle to the organics. Due to the revolutionary progressing in plasmon and especially in metal nanoparticles of material designs as stated above, herein we will mainly focus on the chiral self-assemblies of inorganic metal nanoparticle systems with plasmon and exciton resonances.

First and foremost, one efficient way to synthesize inorganic chiral self-assemblies is to

use the existing chiral organic structures as the template, and then deposits inorganic units onto such chiral template which in return, induces chirality to the inorganic assemblies.[89] Govorov[90, 91] and Rosi[92, 93], for example, showed that DNA- and peptide-based assemblies for the controlled arrangement of metal nanoparticles in complex and also chiral geometries can be realized by "bottom up" technology (Figure 1.22). The induced chirality was characterized by plasmonic circular dichroism spectrometer and further simulations were provided by using discrete dipole approximation (DDA) method. The experimental results are well in line with the modelling systems indicating DNA origami or peptides can be a valuable addition to the existing tools for precisely arranging nanoparticles into assemblies with desired electric or magnetic properties.

References – page 40

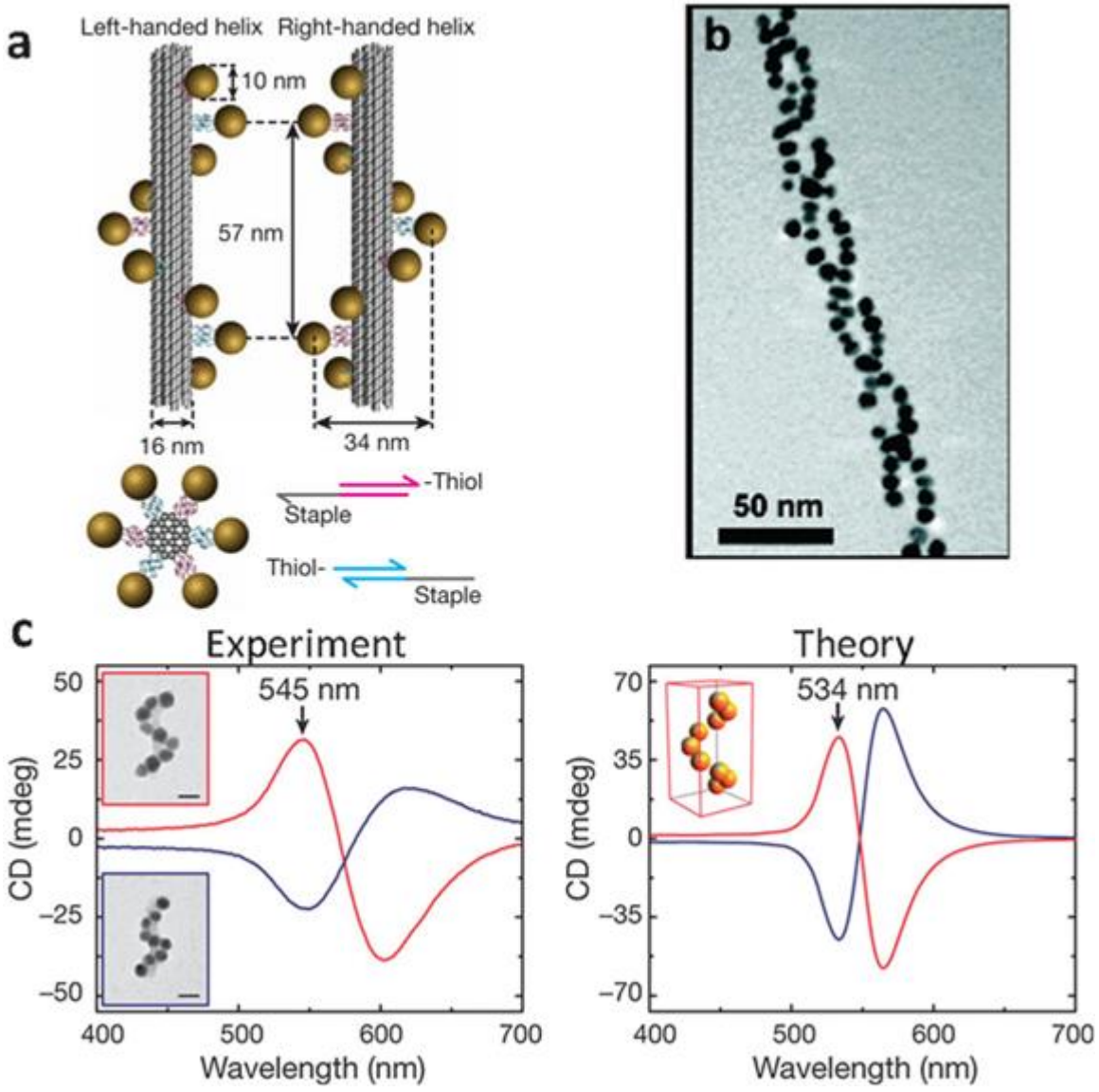

Figure 1.22- Chiral NP configurations: (a) and (b) helical configuration held by peptide molecules. (c) Strongly interacting helical gold NPs held by DNA Origami and exhibiting strong chiroptical activity together with a model calculation.[91-93]

Chirality induction can be realized in a similar but different system consisting of achiral plasmonic nanoparticles and self-assembled chiral molecules. R. L. Whetten et al[94], for instance, showed that when monodispersed gold clusters capped with L-glutathione, the system can induce CD signal at surface plasmon resonance excitations. The induced CD on small metal clusters capped with chiral ligands apparently showed different mechanism from the optical activity in the DNA-metal nanoparticles systems which are often much weaker in presence of larger size of NPs. Different models were used to study the CD induction

mechanism in this case. i) Near-field (dipolar) plasmonic CD induction model which described the CD activity as a sum of $CD_{molecule}$+$CD_{plasmon}$, and this theory was supported by G. Markovich and his coworkers.[95] In their work, dependence of the intensity of the induced CD effect on the metal-chiral molecule separation was found to roughly follow the dipolar model as shown in Figure 1.23. While for metal structures that are about the size of half the wavelength, ii) far-field (electrodynamic) plasmonic CD induction model was used to concern long-range electromagnetic coupling. This method enables us to understand the induced CD activity in cases like chiral shells on achiral particles and vice versa.[96] Moreover, when studying the interaction of plasmons with chiral molecules, one has to consider the local field enhancement of CD signal, indicating enhancement of absorption and CD of chiral molecular species and special chiroptical effects in hot-spots produced by inter-particle junctions.[97]

References – page 40

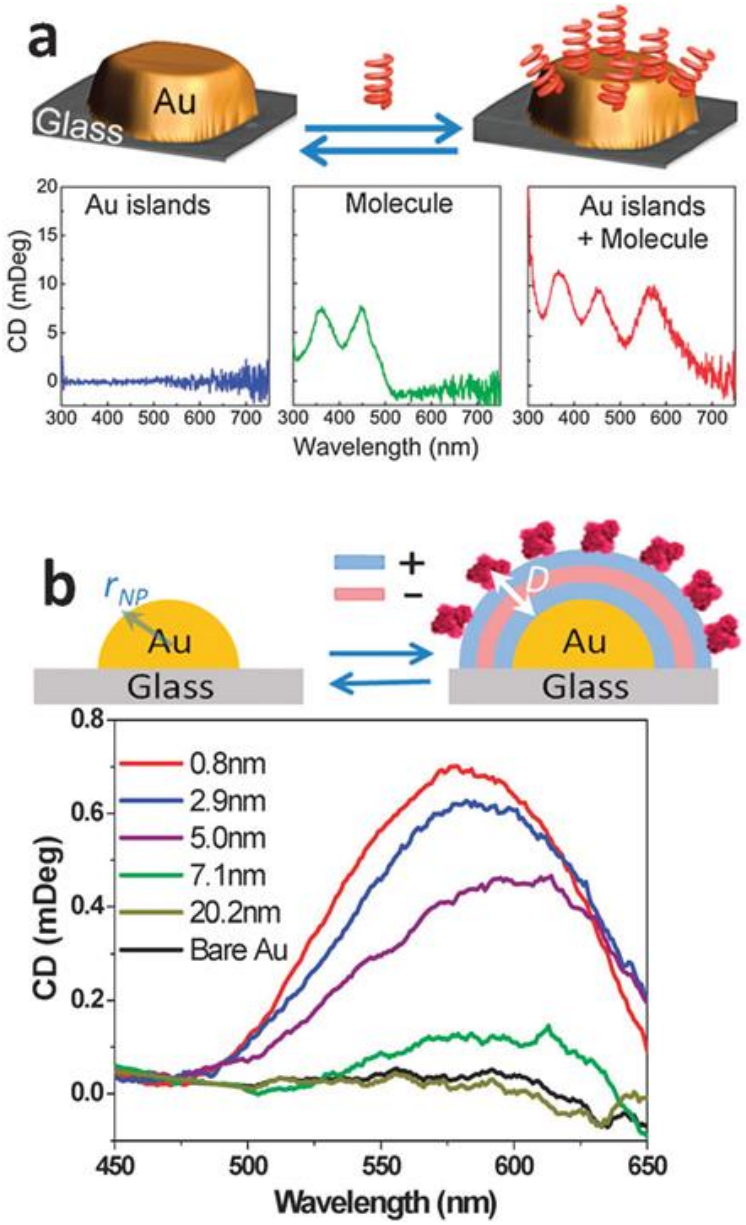

Figure 1.23- (a) A scheme of the experiment on plasmonic CD induction by bringing chiral molecules (riboflavin) in proximity to plasmonic gold islands deposited on a glass substrate. It can be seen that on combining the chiral molecules with the plasmonic particles a new CD line appears at the metal plasmon resonance (570 nm). (b) Observation of the decay of the induced plasmonic CD as a function of achiral spacer layer thickness on which the riboflavin is deposited.[95]

Although self-assemblies of plasmonic particles were believed to typically follow either tetrahedral or helical geometries that require four or more different constituent nanoparticles. N. A. Kotov and his coworkers[98] have proved that smaller number of self-organized particles with different chiral geometries allow better understanding the chiral plasmonic effects. By using single-particle spectroscopy, the chiroptical property is observed in

accordance with the scattering property (Figure 1.24C and D), which represents a new class of stereometamaterials and opens the road to the realization of symmetry broken chiral photonics devices and new techniques of optical manipulation at nanoscale. Though practical models and special considerations are applied to study the induced plasmonic chirality, the CD induction mechanism here as well as induced CD signal of hybrids between DNA-, peptide- and other organics and nanoparticles discussed above is still unclear. Nonetheless, the giant optical activity compared to molecular systems and illustrative contributions to the understanding of interaction of molecules with plasmons steeply raise scientific interests and enables perspective applications such as biosensing and chiral plasmonics.

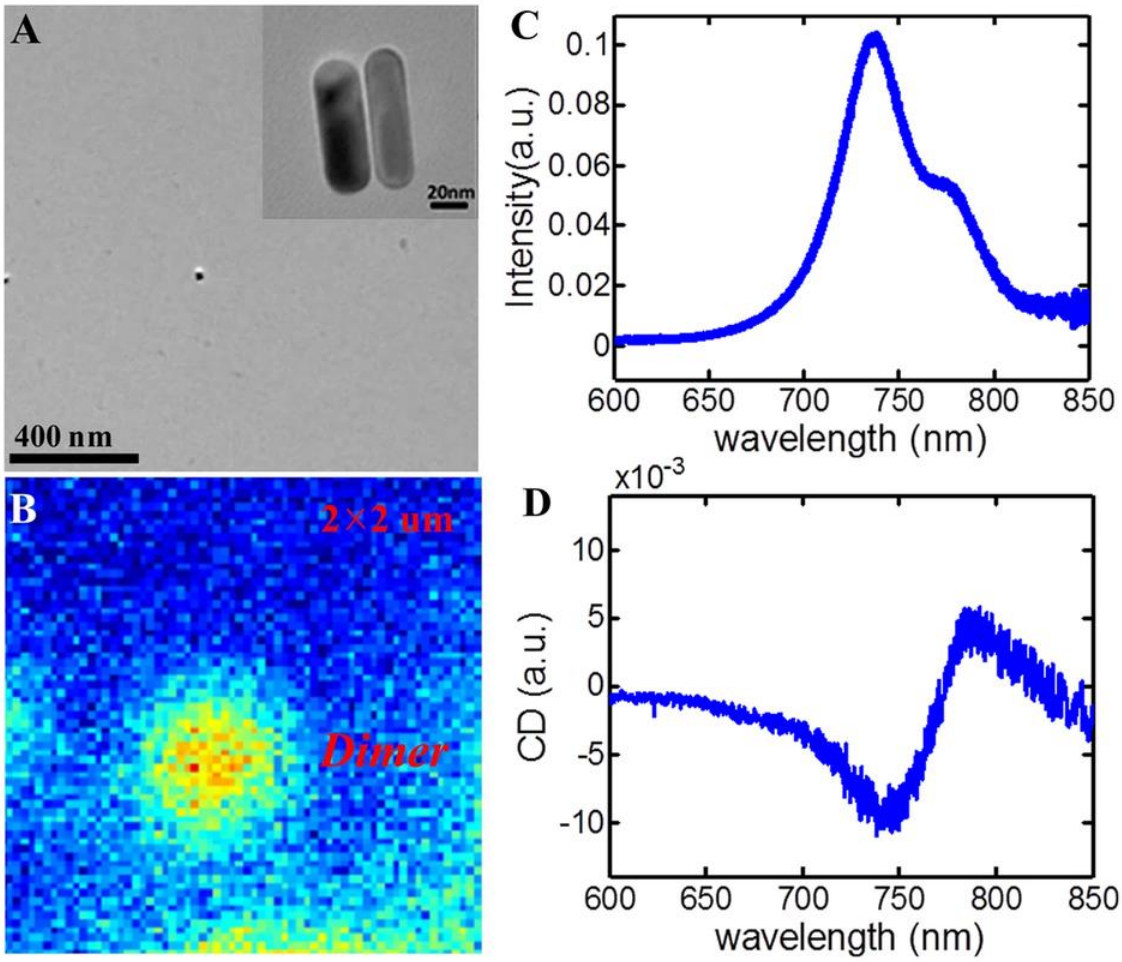

Figure 1.24- (A) TEM images at different magnifications of a single twisted dimer and (B) correlated dark-field scattering image of the same single dimer as in (A). (C, D) Optical properties of a single sodium citrate-assembled NR dimer as characterized by (C) the dark-field scattering spectrum and (D) the circular dichroism spectrum.[98]

References – page 40

Conclusion

In sum, in light of the classic theories on light and matter interaction, material engineers are able to rationally control the light and matter interaction by initiating materials' design from both the building blocks and their intrinsic organizations. Plasmonics, especially gold and silver, are proved to be promising candidates for the design of optical resonators for super-lensing and negative permittivity materials due to the surface plasmon effect which can greatly enhance the resonance effect close to the surface plasmon frequencies. The beauty of asymmetric materials is also discussed and it has been proved that chiral nanostructures have the capability to rotate light propagation planes, indicating uncommon materials such as near-zero or even negative index materials can be realized with positive constitution parameters. These interdisciplinary fields actually inspire the interest of designing chiral metal nanostructures to manipulate and enhance light polarizations in an unusual manner. The realization of such nanomaterials will definitely enrich materials' design and establish a feasible solution to applications such as super-lensing, optical sensors and circular polarizers at optical frequencies.

References – page 40

References:

1. Laskey, R.A. and A.D. MILLS, *Quantitative film detection of 3H and 14C in polyacrylamide gels by fluorography.* European Journal of Biochemistry, 1975. **56**(2): p. 335-341.
2. Kwiat, P.G., et al., *New high-intensity source of polarization-entangled photon pairs.* Physical Review Letters, 1995. **75**(24): p. 4337.
3. Sakoda, K., *Optical properties of photonic crystals*. Vol. 80. 2004: Springer Science & Business Media.
4. Chen, H.-Y., et al., *Polymer solar cells with enhanced open-circuit voltage and efficiency.* Nature Photonics, 2009. **3**(11): p. 649-653.
5. Günes, S., H. Neugebauer, and N.S. Sariciftci, *Conjugated polymer-based organic solar cells.* Chemical Reviews, 2007. **107**(4): p. 1324-1338.
6. Wang, X., L. Zhi, and K. Müllen, *Transparent, conductive graphene electrodes for dye-sensitized solar cells.* Nano Letters, 2008. **8**(1): p. 323-327.
7. Law, M., et al., *Nanowire dye-sensitized solar cells.* Nature materials, 2005. **4**(6): p. 455-459.
8. Green, M.A., *Solar cells: operating principles, technology, and system applications.* 1982.
9. Medintz, I.L., et al., *Quantum dot bioconjugates for imaging, labelling and sensing.* Nature materials, 2005. **4**(6): p. 435-446.
10. Bimberg, D., M. Grundmann, and N.N. Ledentsov, *Quantum dot heterostructures*1999: John Wiley & Sons.
11. Robel, I., et al., *Quantum dot solar cells. Harvesting light energy with CdSe nanocrystals molecularly linked to mesoscopic TiO2 films.* Journal of the American Chemical Society, 2006. **128**(7): p. 2385-2393.
12. Chan, W.C. and S. Nie, *Quantum dot bioconjugates for ultrasensitive nonisotopic detection.* Science, 1998. **281**(5385): p. 2016-2018.
13. Yeom, J., et al., *Chiral templating of self-assembling nanostructures by circularly polarized light.* Nat Mater, 2015. **14**(1): p. 66-72.
14. Zhang, X., *Image resolution depending on slab thickness and object distance in a two-dimensional photonic-crystal-based superlens.* Physical Review B, 2004. **70**(19): p. 195110.
15. Engheta, N. and R.W. Ziolkowski, *Metamaterials: physics and engineering explorations*2006: John Wiley & Sons.
16. Cui, T.J., D.R. Smith, and R. Liu, *Metamaterials*2014: Springer.
17. Sakai, O. and K. Tachibana, *Plasmas as metamaterials: a review.* Plasma Sources Science and Technology, 2012. **21**(1): p. 013001.
18. Alù, A., A. Salandrino, and N. Engheta, *Negative effective permeability and left-handed materials at optical frequencies.* Optics Express, 2006. **14**(4): p. 1557-1567.
19. Wegener, M. and S. Linden, *Giving light yet another new twist.* Physics, 2009. **2**: p. 40

3-6.
20. Plum, E., et al., *Metamaterial with negative index due to chirality.* Physical Review B, 2009. **79**(3): p. 035407.
21. Zhang, S., et al., *Negative Refractive Index in Chiral Metamaterials.* Physical Review Letters, 2009. **102**(2): p. 023901.
22. Pelton, M. and G.W. Bryant, *Introduction to metal-nanoparticle plasmonics*. Vol. 5. 2013: John Wiley & Sons.
23. Miller, E.K., *Time-domain modeling in electromagnetics.* Journal of Electromagnetic Waves and Applications, 1994. **8**(9-10): p. 1125-1172.
24. Draine, B.T. and P.J. Flatau, *Discrete-Dipole Approximation For Scattering Calculations.* Journal of the Optical Society of America A, 1994. **11**(4): p. 1491-1499.
25. Purcell, E.M. and C.R. Pennypacker, *Scattering and absorption of light by nonspherical dielectric grains.* The Astrophysical Journal, 1973. **186**: p. 705-714.
26. Martin, O.J., C. Girard, and A. Dereux, *Generalized field propagator for electromagnetic scattering and light confinement.* Physical Review Letters, 1995. **74**(4): p. 526.
27. Hafner, C. and R. Ballisti, *The multiple multipole method (MMP).* COMPEL-The international journal for computation and mathematics in electrical and electronic engineering, 1983. **2**(1): p. 1-7.
28. Pendry, J. and A. MacKinnon, *Calculation of photon dispersion relations.* Physical Review Letters, 1992. **69**(19): p. 2772.
29. Leung, K. and Y. Liu, *Photon band structures: The plane-wave method.* Physical Review B, 1990. **41**(14): p. 10188.
30. de Abajo, F.G. and A. Howie, *Relativistic electron energy loss and electron-induced photon emission in inhomogeneous dielectrics.* Physical Review Letters, 1998. **80**(23): p. 5180.
31. Blackie, E.J., E.C.L. Ru, and P.G. Etchegoin, *Single-molecule surface-enhanced Raman spectroscopy of nonresonant molecules.* Journal of the American Chemical Society, 2009. **131**(40): p. 14466-14472.
32. Kleinman, S.L., et al., *Single-molecule surface-enhanced Raman spectroscopy of crystal violet isotopologues: theory and experiment.* Journal of the American Chemical Society, 2011. **133**(11): p. 4115-4122.
33. Dieringer, J.A., et al., *A frequency domain existence proof of single-molecule surface-enhanced Raman spectroscopy.* Journal of the American Chemical Society, 2007. **129**(51): p. 16249-16256.
34. Xu, H. and M. Käll, *Surface-plasmon-enhanced optical forces in silver nanoaggregates.* Physical Review Letters, 2002. **89**(24): p. 246802.
35. Juan, M.L., M. Righini, and R. Quidant, *Plasmon nano-optical tweezers.* Nature Photonics, 2011. **5**(6): p. 349-356.
36. Righini, M., et al., *Nano-optical trapping of Rayleigh particles and Escherichia coli bacteria with resonant optical antennas.* Nano Letters, 2009. **9**(10): p. 3387-3391.
37. Song, J., J. Zhou, and H. Duan, *Self-assembled plasmonic vesicles of SERS-encoded amphiphilic gold nanoparticles for cancer cell targeting and traceable intracellular*

drug delivery. Journal of the American Chemical Society, 2012. **134**(32): p. 13458-13469.

38. Hartschuh, A., et al., *Nanoscale optical imaging of excitons in single-walled carbon nanotubes.* Nano Letters, 2005. **5**(11): p. 2310-2313.
39. Eghlidi, H., et al., *Resolution and enhancement in nanoantenna-based fluorescence microscopy.* Nano Letters, 2009. **9**(12): p. 4007-4011.
40. Tamoto, R., et al., *Gold Nanoparticle Deposition on Silica Nanohelices: A New Controllable 3D Substrate in Aqueous Suspension for Optical Sensing.* Journal of Physical Chemistry C, 2012. **116**(43): p. 23143-23152.
41. Veselago, V.G., *THE ELECTRODYNAMICS OF SUBSTANCES WITH SIMULTANEOUSLY NEGATIVE VALUES OF IMG align= ABSMIDDLE alt= ϵ eps/IMG AND μ.* Physics-Uspekhi, 1968. **10**(4): p. 509-514.
42. Ramakrishna, S.A. and T.M. Grzegorczyk, *Physics and applications of negative refractive index materials*2008: CRC press.
43. Schelkunoff, S.A. and H.T. Friis, *Antennas: theory and practice*. Vol. 639. 1952: Wiley New York.
44. Pendry, J.B., et al., *Magnetism from conductors and enhanced nonlinear phenomena.* Microwave Theory and Techniques, IEEE Transactions on, 1999. **47**(11): p. 2075-2084.
45. Capolino, F., *Metamaterials Handbook–Two Volume Slipcase Set: Theory and Phenomena of Metamaterials.* CRC, Boca Raton, 2009.
46. Shadrivov, I., *Nonlinear metamaterials: a new degree of freedom.*
47. Gansel, J.K., et al., *Gold Helix Photonic Metamaterial as Broadband Circular Polarizer.* Science, 2009. **325**(5947): p. 1513-1515.
48. Capolino, F., *Theory and phenomena of metamaterials*2009: CRC Press.
49. Perro, A., et al., *Design and synthesis of Janus micro-and nanoparticles.* Journal of Materials Chemistry, 2005. **15**(35-36): p. 3745-3760.
50. Walther, A. and A.H. Müller, *Janus particles.* Soft Matter, 2008. **4**(4): p. 663-668.
51. Niu, Z., et al., *Synthesis of nano/microstructures at fluid interfaces.* Angewandte Chemie International Edition, 2010. **49**(52): p. 10052-10066.
52. Gu, H., et al., *Heterodimers of nanoparticles: Formation at a liquid-liquid interface and particle-specific surface modification by functional molecules.* Journal of the American Chemical Society, 2005. **127**(1): p. 34-35.
53. Gao, J., H. Gu, and B. Xu, *Multifunctional magnetic nanoparticles: design, synthesis, and biomedical applications.* Accounts of Chemical Research, 2009. **42**(8): p. 1097-1107.
54. Chen, Q., S.C. Bae, and S. Granick, *Directed self-assembly of a colloidal kagome lattice.* Nature, 2011. **469**(7330): p. 381-384.
55. Chen, Q., et al., *Supracolloidal reaction kinetics of Janus spheres.* Science, 2011. **331**(6014): p. 199-202.
56. Wang, Y., et al., *Emerging chirality in nanoscience.* Chemical Society Reviews, 2013. **42**(7): p. 2930-2962.
57. Armon, S., et al., *Geometry and mechanics in the opening of chiral seed pods.* Science, 42

2011. **333**(6050): p. 1726-1730.
58. Forterre, Y. and J. Dumais, *Generating helices in nature.* 2011.
59. Ma, L., C. Abney, and W. Lin, *Enantioselective catalysis with homochiral metal–organic frameworks.* Chemical Society Reviews, 2009. **38**(5): p. 1248-1256.
60. César, V., S. Bellemin-Laponnaz, and L.H. Gade, *Chiral N-heterocyclic carbenes as stereodirecting ligands in asymmetric catalysis.* Chemical Society Reviews, 2004. **33**(9): p. 619-636.
61. Maruoka, K. and T. Ooi, *Enantioselective amino acid synthesis by chiral phase-transfer catalysis.* Chemical Reviews, 2003. **103**(8): p. 3013-3028.
62. Zhang, M., G. Qing, and T. Sun, *Chiral biointerface materials.* Chemical Society Reviews, 2012. **41**(5): p. 1972-1984.
63. Berthod, A., *Chiral recognition mechanisms.* Analytical Chemistry, 2006. **78**(7): p. 2093-2099.
64. Tang, L., et al., *Nanometre-scale germanium photodetector enhanced by a near-infrared dipole antenna.* Nature Photonics, 2008. **2**(4): p. 226-229.
65. Pendry, J.B., *A Chiral Route to Negative Refraction.* Science, 2004. **306**(5700): p. 1353-1355.
66. Tretyakov, S., et al., *Waves and energy in chiral nihility.* Journal of Electromagnetic Waves and Applications, 2003. **17**(5): p. 695-706.
67. Agranovich, V.M. and Y.N. Gartstein, *Spatial dispersion and negative refraction of light.* Physics-Uspekhi, 2006. **49**(10): p. 1029.
68. Tretyakov, S., A. Sihvola, and L. Jylhä, *Backward-wave regime and negative refraction in chiral composites.* Photonics and Nanostructures-Fundamentals and Applications, 2005. **3**(2): p. 107-115.
69. Kira, Y., et al., *Amphiphilic molecular gels from ω-aminoalkylated l-glutamic acid derivatives with unique chiroptical properties.* Amino Acids, 2010. **39**(2): p. 587-597.
70. Clemente, M.J., et al., *Supramolecular hydrogels based on glycoamphiphiles: effect of the disaccharide polar head.* Chemistry of Materials, 2012. **24**(20): p. 3847-3858.
71. Fameau, A.-L., et al., *12-Hydroxystearic acid lipid tubes under various experimental conditions.* Journal of Colloid and Interface Science, 2010. **341**(1): p. 38-47.
72. Tomovic, Z., et al., *Star-shaped oligo (p-phenylenevinylene) substituted hexaarylbenzene: purity, stability, and chiral self-assembly.* Journal of the American Chemical Society, 2007. **129**(51): p. 16190-16196.
73. Wang, Y., et al., *Rational Design of Chiral Nanostructures from Self-Assembly of a Ferrocene-Modified Dipeptide.* Journal of the American Chemical Society, 2015.
74. Lehn, J.-M., et al., *Spontaneous assembly of double-stranded helicates from oligobipyridine ligands and copper (I) cations: structure of an inorganic double helix.* Proceedings of the National Academy of Sciences, 1987. **84**(9): p. 2565-2569.
75. Tanaka, Y., et al., *A modular strategy to artificial double helices.* Angewandte Chemie, 2005. **117**(25): p. 3935-3938.
76. Kawauchi, T., et al., *Encapsulation of fullerenes in a helical PMMA cavity leading to a robust processable complex with a macromolecular helicity memory.* Angewandte Chemie International Edition, 2008. **47**(3): p. 515-519.

77. Nuckolls, C., T.J. Katz, and L. Castellanos, *Aggregation of conjugated helical molecules.* Journal of the American Chemical Society, 1996. **118**(15): p. 3767-3768.
78. Nuckolls, C., et al., *Synthesis and aggregation of a conjugated helical molecule.* Journal of the American Chemical Society, 1999. **121**(1): p. 79-88.
79. Gellert, M., M.N. Lipsett, and D.R. Davies, *Helix formation by guanylic acid.* Proceedings of the National Academy of Sciences of the United States of America, 1962. **48**(12): p. 2013.
80. Mariani, P., et al., *A study of the structure of the lyomesophases formed by the dinucleoside phosphate d (GpG). An approach by X-ray diffraction and optical microscopy.* Journal of the American Chemical Society, 1989. **111**(16): p. 6369-6373.
81. Bonazzi, S., et al., *Four-stranded aggregates of oligodeoxyguanylates forming lyotropic liquid crystals: a study by circular dichroism, optical microscopy, and X-ray diffraction.* Journal of the American Chemical Society, 1991. **113**(15): p. 5809-5816.
82. Sakai, N., et al., *Dendritic folate rosettes as ion channels in lipid bilayers.* Journal of the American Chemical Society, 2006. **128**(7): p. 2218-2219.
83. Link, D.R., et al., *Spontaneous Formation of Macroscopic Chiral Domains in a Fluid Smectic Phase of Achiral Molecules.* Science, 1997. **278**(5345): p. 1924-1927.
84. Oda, R., et al., *Tuning bilayer twist using chiral counterions.* Nature, 1999. **399**(6736): p. 566-569.
85. Oda, R., I. Huc, and S.J. Candau, *Gemini surfactants as new, low molecular weight gelators of organic solvents and water.* Angewandte Chemie International Edition, 1998. **37**(19): p. 2689-2691.
86. Oda, R., et al., *Molecular structure of self-assembled chiral nanoribbons and nanotubules revealed in the hydrated state.* Journal of the American Chemical Society, 2008. **130**(44): p. 14705-14712.
87. Wang, R.-Y., et al., *Chiral assembly of gold nanorods with collective plasmonic circular dichroism response.* Soft Matter, 2011. **7**(18): p. 8370-8375.
88. Yuan, J. and M. Liu, *Chiral molecular assemblies from a novel achiral amphiphilic 2-(heptadecyl) naphtha [2, 3] imidazole through interfacial coordination.* Journal of the American Chemical Society, 2003. **125**(17): p. 5051-5056.
89. Ben-Moshe, A., et al., *Chirality and chiroptical effects in inorganic nanocrystal systems with plasmon and exciton resonances.* Chemical Society Reviews, 2013. **42**(16): p. 7028-7041.
90. Fan, Z., H. Zhang, and A.O. Govorov, *Optical Properties of Chiral Plasmonic Tetramers: Circular Dichroism and Multipole Effects.* The Journal of Physical Chemistry C, 2013. **117**(28): p. 14770-14777.
91. Kuzyk, A., et al., *DNA-based self-assembly of chiral plasmonic nanostructures with tailored optical response.* Nature, 2012. **483**(7389): p. 311-314.
92. Chen, C.L. and N.L. Rosi, *Preparation of Unique 1-D Nanoparticle Superstructures and Tailoring their Structural Features.* Journal of the American Chemical Society, 2010. **132**(20): p. 6902-+.
93. Chen, C.-L., P. Zhang, and N.L. Rosi, *A New Peptide-Based Method for the Design and Synthesis of Nanoparticle Superstructures: Construction of Highly Ordered Gold*

Nanoparticle Double Helices. Journal of the American Chemical Society, 2008. **130**(41): p. 13555-13557.

94. Schaaff, T.G. and R.L. Whetten, *Giant gold-glutathione cluster compounds: Intense optical activity in metal-based transitions.* The Journal of Physical Chemistry B, 2000. **104**(12): p. 2630-2641.
95. Maoz, B.M., et al., *Amplification of chiroptical activity of chiral biomolecules by surface plasmons.* Nano Letters, 2013. **13**(3): p. 1203-1209.
96. Govorov, A.O. and Z. Fan, *Theory of chiral plasmonic nanostructures comprising metal nanocrystals and chiral molecular media.* ChemPhysChem, 2012. **13**(10): p. 2551-2560.
97. Lieberman, I., et al., *Plasmon‐Resonance‐Enhanced Absorption and Circular Dichroism.* Angewandte Chemie International Edition, 2008. **47**(26): p. 4855-4857.
98. Ma, W., et al., *Chiral plasmonics of self-assembled nanorod dimers.* Sci. Rep., 2013. **3**.

References – page 40

Chapter 2. Project description

References – page 65

1. Introduction

In photonics, the fabrication, organization and use of chiral objects of nanometric dimensions is of extreme interest since it can result in super-chiral structures with giant optical activity, and other innovative chiro-optical materials which have promising applications such as chiro-optical sensors, circular polarizers or metamaterials. Many of these potential applications require working at wavelengths corresponding to the visible range, a constraint that means the active structures have typical internal dimensions much smaller than the wavelength of light. Fabricating and organizing nano-elements displaying sufficient chiral activity at such scales is a highly challenging task which has slowed down industrial applications. In this thesis, we propose an original approach to create chiral nano-photonics structures by using silica nanohelices as scaffold for well-calibrated gold nanoparticles (GNPs) grafting (hereafter named as Goldhelix). The helicoidal organization of the GNPs presents new plasmonic circular dichroism properties interesting for the super-lensing or the chiral sensing applications. Further studies are investigated on techniques to hierarchically assemble the Goldhelix with the purpose of creating 2D or 3D structures with properties enhanced into specific directions.

As it shows surface plasmon resonance at the interface with dielectrics, gold is an important material for nano-photonics. Well-calibrated GNPs are of particular interest because their localized surface plasmon resonance is highly dependent on their size and morphology (sphere, rods, etc…). Beyond the control in terms of shape and size, the hierarchical organization of the particles is crucial to reach optical and plasmonic properties.[1, 2] A chiral organization of such GNPs would present new plasmonic circular dichroism properties,[3] and so could be used as new chiral metamaterials.[4-6] Indeed, in nanophotonics, the use of chiral objects could induce out-of-the-common optical properties such as giant optical activity or circular dichroism as well as negative refractive index which would find applications in the super-lensing,[7] the ultra-thin quarter wave plate[8] or the chiral sensing[9] in the visible range thanks to the nanometric dimension of the devices. Actually, such chiral devices can

introduce a magneto-dielectric coupling coefficient κ modifying the index seen by circularly polarized light: $n = \sqrt{\varepsilon\mu} \pm \kappa$ (depending on the actual polarization).[10, 11] This is of extreme interest since it gives access to new strategies to control the refractive index, classically defined as $n = \sqrt{\varepsilon\mu}$, towards hardly accessible values such as largely positive, near-zero or even negative refractive index. Few groups[12-14] have experimentally demonstrated interesting optical properties based on this strategy by patterning periodically arranged chiral motifs on surfaces but no example is yet known of such chiral materials organized in three dimensions at the nanometric level, which would allow working at visible range frequencies.

For several years, our group has been developing a high yield bottom up approach using an organic nanohelical structure (diam. = 30-60 nm) as a template for the silicon oxide growth. Indeed, self-assemblies from chiral molecules can spontaneously form various chiral nanostructures such as twisted or helical ribbons.[15] These structures then give access to well-defined silica nano-structures hardly obtainable with conventional top-down techniques. These silica nanohelices can then be surface functionalized and used as scaffold for the adsorption or grafting of metal nanoparticles.[16] The process of the fabrication of these nanohybrid Goldhelix structures is performed in soft conditions without high temperature, corrosive solvent, or hazardous wastes, giving rise to environmentally friendly fabrication of nanomaterials, a field recently named “green-nano”. The organization/packing of the GNPs along the chiral nanohelices should thus lead to a chiral optically active response around the surface plasmon resonance, which couple from one nanoparticle to the other along the supporting helical direction. These nano-devices can be suspended in bulk solution and their aligned hierarchical 2D or 3D organizations can be envisaged, giving the incomparable advantage to randomly oriented systems. Their elongated structure can give access to their alignment/controlled orientation of these structures by developing grazing incidence spraying or evaporation-based microfluidic systems which permit to guide the self-assembly of nanomaterials.

References – page 65

Method and Methodology

1.1 Inducing chirality in fabrication of nanostructures

As stated in chapter 1, when chirality is introduced into optical applications, one impetus to the manipulation of light and matter interactions came with the realization that one of the circularly polarized states of light could experience a near-zero or even negative refractive index under suitable conditions. Unlike common natural materials, such chiral materials are not necessarily built up from intrinsically chiral building blocks but rather derive their chiral properties from the chiral geometric structure of the basic units. For example, Zhang et al.[17] obtained negative refractive index at terahertz frequencies thanks to micrometer scale periodical surfaces. Pendry et al.[18] theoretically suggested a 3D helix structure for realizing a chiral metamaterial with negative refraction. On the other hand, it is worth noting that Gansel et al.[14] succeeded in obtaining a beautiful lattice of 3D micrometric gold helices with one handedness showing that the structure selectively transmits light with only one of the circular polarization along the helix axis.

The realization of negative refractive index within optical frequency requires designing objects finely controlled at nanometric level. For this approach, it is therefore more preferable to employ “bottom-up” technique via nanoscale building blocks such as gold or silver nanoparticles. To the best of our knowledge, nonetheless, very few known examples of chiral GNPs organization can be efficiently used as functional materials for such applications because of the difficulty to reach chiral organization for GNPs and the vulnerability of the supports usually used to attach the GNPs (generally organic chiral assemblies).

1.2 Directed Self-assembly of GNPs on silica nanohelices

Noble metal nanoparticles such as GNPs with controlled arrangements have attracted significant interests due to their unique physical properties in both fundamental science and nanotechnology.[12, 18-24] When assembled close to each other, their localized surface plasmon resonances are coupled together, resulting in the enhancement of the electric field in

the gap between the adjacent nanoparticles. Such systems, therefore, are attractive candidates for the amplification of optical signals such as Fluorescence,[25, 26] Raman scattering,[27-29] and Circular dichroism.[3, 14, 30-35] Nevertheless, the applications of these nanostructures are very often restricted by the structural complexity and the lack of fine-tunability at nanometer scale (optical wave length).[36, 37] To improve the situation, synthetic methods based on "bottom-up" approaches are often employed to fabricate self-assembled organic systems to obtain a diversity of candidate templates. Recently, new types of systems based on nanoparticles assembled to sophisticated structures such as nanofibers[35, 38], nanohelices[3, 6, 30-34, 39, 40] and films[41] have been introduced as they can be used as bases for alignment of nanoparticles, however, most of these nanostructures are still based on organic scaffolds or isotropic surfaces, which generally suffer from vulnerability and lack of capability to consider structural contribution to optical properties. Herein, we will show that finely controlled platforms as reported in previous literatures [42, 43] will help directed chiral assembling of GNPs onto inorganic twisted or helical ribbons and tubules with precisely controlled position. Thus, these specific chiral arrangements of GNPs within such superstructures will lead to interesting optical properties directing a sustainable and feasible approach for the synthesis and applications such as biosensing, circular polarizers and super-lensing.

1.3 Hierarchical organizations of Goldhelix in 2D or 3D motif

After successful fabrication of Goldhelix in suspension, nature extension will be to align them into 2D surface or 3D objects in order to make such objects appealing in the context of materials. The sky-rocketing developments of grazing angle spraying techniques associated with layer-by-layer (LbL) techniques and microfluidic devices do provide us such possibilities to obtain such systems. With several decades of application in both science and industry, grazing angle spraying techniques together with LbL deposition have proven powerful as material fabrication techniques planting on various practical fields and areas. They are widely used based on many possible mechanisms ranging from simple electrostatic interactions,

hydrogen bonding and base-pair interactions to more complicated charge transfer interactions, stereocomplexation, host-guest interactions, covalent bonding and so forth[44], suggesting that a 2D alignment of silica nanohelices and even Goldhelix would be accomplished by using this technique and if so, the synthesized materials can be quickly involved into applications such as optical polarizers and thin film technology. On the other hand, as a modern technique, microfluidics has also been invited into many fields. R. F. Ismagilov et al, for example, have used microfluidic droplet-based system to fabricate CdS and CdS/CdSe core-shell nanoparticles indicating that microfluidic system may also become useful for synthesis of nano-size drug particles with or without encapsulating layers, and other particles used in pharmaceutical, food, and agricultural industries.[45] Moreover, C. Leroy and M. D. Dickey have showed promising applications of microfluidics in 3D printing which would be a leading technology in contemporary science and engineering.[46, 47] Therefore, employing microfluidic systems with proper parameters will probably give us a feasible method for the fabrication of Goldhelix in a 3D shape and broaden the scope of applications to 3D resonators or even metamaterials.

References – page 65

2. Typical characterization techniques for directed plasmonic assemblies

In materials science, in order to probe into the surface and understand internal structural responses to the outside environment of the sample materials, many advanced techniques are used for the structural, chemical and topological characterization of synthesized nanostructures. Microscopes are often employed to visualize the internal structure or even the chemical composition. With the observation of the sample by microscope, analyzing techniques based on physical or chemical properties can be effectively used to investigate properties of interest, or even *in situ* monitoring the whole reaction. Some correlated techniques below are typically used to study both the morphological and physiochemical properties of anisotropically organized self-assembly of plasmonic nanoparticles.

2.1 Electron microscopy

Fundamentally, electron microscopies, namely Scanning electron microscope (SEM), Transmission electron microscopy (TEM), are widely used in materials sciences, for they provide preliminary and direct information about the surface and interface of specimens with size down to nanometric scale, even though sometimes the sample preparation procedures such as drying and metallization in SEM or staining and drying in TEM could bring in artifacts especially when observed self-assembling components could inherently exist in a solvated state.[48] For example, metallization could sometimes destroy the stability of the sample and staining can even change the sample morphology.[49] To improve the situation, many advanced electron microscopies are derived from basic SEM or TEM. For example, the capabilities of the TEM can be further extended by additional stages and detectors, sometimes incorporated on the same microscope. An electron cryomicroscope (CryoTEM) is a TEM with a specimen holder capable of maintaining the specimen at liquid nitrogen or liquid helium temperatures. This allows imaging specimens prepared in vitreous ice, the preferred preparation technique for imaging individual molecules or macromolecular assemblies.[50] A TEM can be modified into a scanning transmission electron microscope (STEM) by the

addition of a system that rasters the beam across the sample to form the image, combined with suitable detectors. A low-voltage electron microscope (LVEM) is operated at relatively low electron accelerating voltage between 5-25 kV. Some of these can be a combination of SEM, TEM and STEM in a single compact instrument. Low voltage increases image contrast which is especially important for biological specimens. This increase in contrast significantly reduces, or even eliminates the need to stain. Resolutions of a few nanometers are possible in TEM, SEM and STEM modes. The low energy of the electron beam means that permanent magnets can be used as lenses and thus a miniature column that does not require cooling can be used.[51, 52] In parallel, it is also possible to perform cryo-SEM imaging of organic assemblies.[53] Although it is not easy for the sample preparation, it is still a potential technique to use secondary electrons to obtain pseudo 3D images of the specimen.[54] Notably, although microscopy techniques give direct image of the sample, it can only provide part of the local information of the sample and it may induce casual artifacts when using a typical sample image to generalize the overall properties of the whole specimen.

2.2 Spectroscopy

Spectroscopic techniques such as UV-vis spectroscopy, Raman or Surface Enhanced Raman Spectroscopy (SERS), Attenuated total reflectance spectroscopy (ATR), Circular dichroism (CD) give complementary information to microscopies. Since these techniques reflect interaction between the sample and incident light or laser, unlike microscopy, they can provide global information about characteristic properties of the sample especially when they are used together. Yan et al,[38] for instance, employed extinction spectroscopy to monitor the self-assembly of Au/Ag nanoparticles onto silica fibers together with TEM images, they pointed out that the extinction spectrums of the synthesized hybrid nanostructures were broaden and red shifted to higher wavelength as the volume of Au/Ag nanoparticles used for coating increased, and this finding was consistent with the observed TEM image. Moreover, these newly synthesized nanostructures can be used for SERS absorption of 4-mercaptobenzoic acid (4-MBA) molecules which gives a solid proof of dipole-dipole

coupling between NPs (Figure 2.1). Similarly, R. Tamato et al,[42] also showed an enhancement factor of ~10^7 with benzenethiol in SERS measurement, when GNPs with around 14nm in diameter were engineered onto the surface of a helical silica template which could exhibit vibrational CD activity in IR range. The silica template was fabricated via sol-gel chemistry where the organic helical structures were qualitatively characterized by ^{1}H-NMR and ATR.

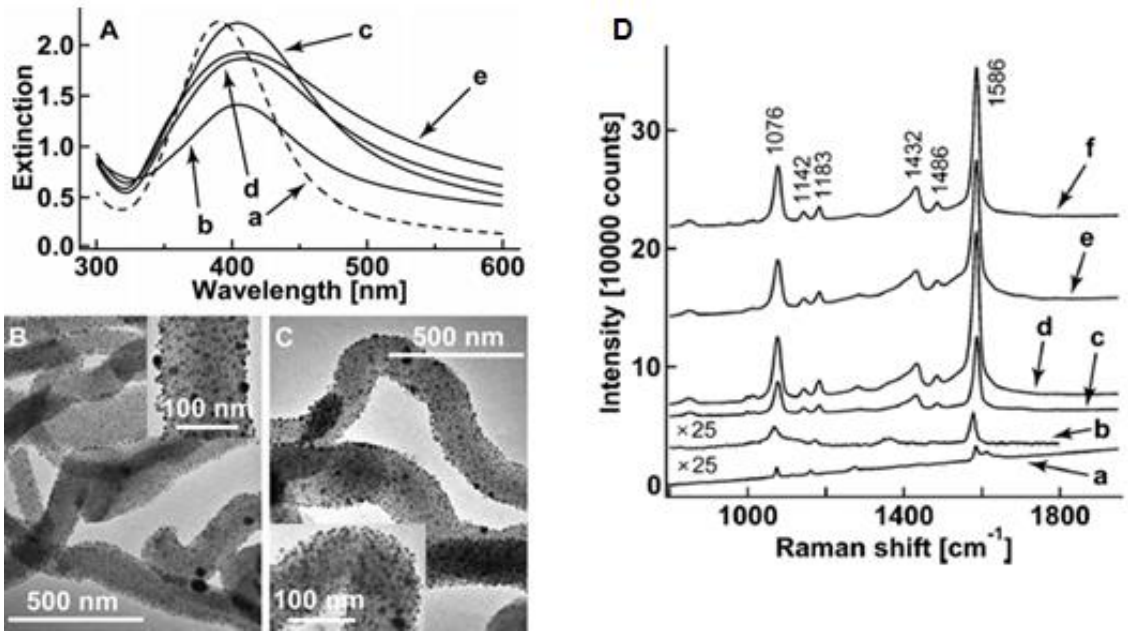

Figure 2.1- A) Extinction spectra of nanofibers coated with varying amounts of spherical Ag nanoparticles. The volumes of the citrate-stabilized Ag nanoparticle solution used for coating were b) 7, c) 21, d) 35, and e) 49 mL. a) The extinction spectrum of the Ag nanoparticle solution. The extinction maxima are at a) 390, b) 404, c) 405, d) 409, and e) 410 nm. The mass of the APTES-functionalized silica nanofibers before coating was 3.5 mg. B), C) TEM images of nanofibers coated with Ag nanoparticles taken from samples c and d in (A), respectively. D) Raman spectra of 4-MBA. a) Dry 4-MBA powders. b) 4-MBA molecules adsorbed on Ag nanoparticles that were deposited on a glass slide. c)–f) 4-MBA molecules adsorbed on Ag-nanoparticle/silica-nanofiber hybrid nanostructures. The extinction spectra of the hybrid nanostructures used as SERS substrates for (c), (d), (e), and (f) are shown by curves b, c, d, and e in A).[38]

The most versatile characterizing tool for studying chirality on molecular assemblies is circular dichroism (CD) spectroscopy, which measures the difference between absorptions of the sample on left and right circularly polarized light. While the difference of the adsorption is considerably small compared to the absorption, it is extremely sensitive to the changes in the

conformation of the molecules or vibration of the chemical bond's direction in the vicinity of the chromophores or bonds. Depending on the absorption frequencies, electronic CD for UV range and vibrational CD (VCD) for IR range are used together with related UV or IR spectrometer. Induced CD (ICD) signal can be observed in chromophores that are remote from any stereogenic centers when the overall structure exhibits chiral morphology, or even in achiral molecules or units that have no chiral centers but organized in a chiral way or conjugated with some sort of chiral ligands.[55] There are still many unknown factors on the mechanism on how morphological chirality is induced and how chirality is transferred from chiral molecules to achiral molecules, which arouse tremendous interest on studying self-assembling of molecules.

One of the advanced usages of CD spectrum is to obtain information on the macroscopic chiral arrangement of supramolecular assemblies by external parameters. The reports by the Aida and Meijer groups describe in detail the origin of CD in achiral systems in which the solute self-assembles into anisometric aggregates that are able to orient in response to fluidic flows. In particular, Spada and his co-workers[56] reported that, in Figure 2.2, while a hydrocarbon solution of achiral **1** without stirring was CD silent, it became optically active upon mechanical rotary stirring. When stirred in a clockwise direction (CW), the sample solution displayed intense CD signals at the Soret absorption bands arising from J-aggregated zinc porphyrin, while no chiroptical activity emerged at the absorption band of unassembled molecules.

References – page 65

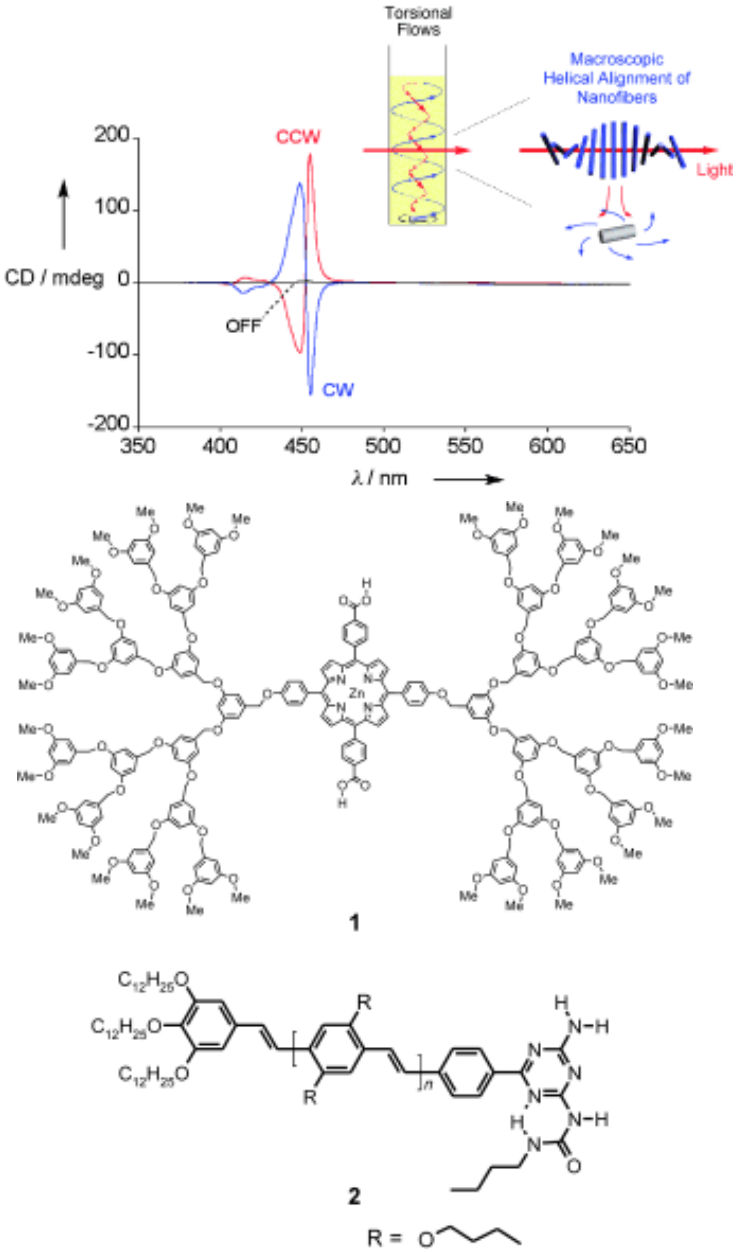

Figure 2.2- Circular dichroism (CD) spectra of a benzene solution of assemblies of 1 upon rotary stirring in clockwise (CW, blue curve) and counterclockwise (CCW, red curve) directions, and without stirring (OFF, black curve). The inset shows a schematic illustration of torsional flows and macroscopic helical alignment of nanofibers generated upon counterclockwise rotary stirring.[56]

Meijer and co-workers[57] point out another possible source of apparent CD in solutions of achiral assemblies. In the temperature-induced self-assembly of achiral **2**, LD and CD signals appear, even in unstirred solutions, when the assemblies reach a certain length; these optical responses, which are enhanced by shaking the solutions, are a consequence of partial alignment of the fibers owing to convective flow as shown in Figure 2.3.

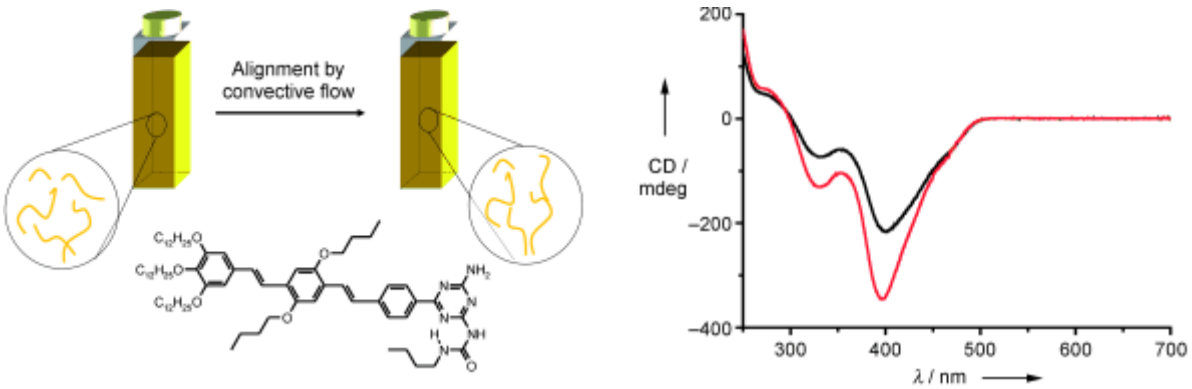

Figure 2.3- CD spectra of a solution of 2 in dodecane after cooling (black) and after shaking the solution (red).[57]

Another interesting example is to study the formation of self-assembly in water via hydrogen bonds. J. G. Stowell and his coworkers[58] pointed out in Figure 2.4 that the supramolecular chirality of folate- and G-quadruplexes in helical rosette nanotubes is studied by CD measurement. The observed CD signal proves the H-bonding effects on the self-assembling procedure therefore the generated supramolecular chirality is most probably the result of helically stacked rosettes and the further TEM and DLS results proved this finding.

References – page 65

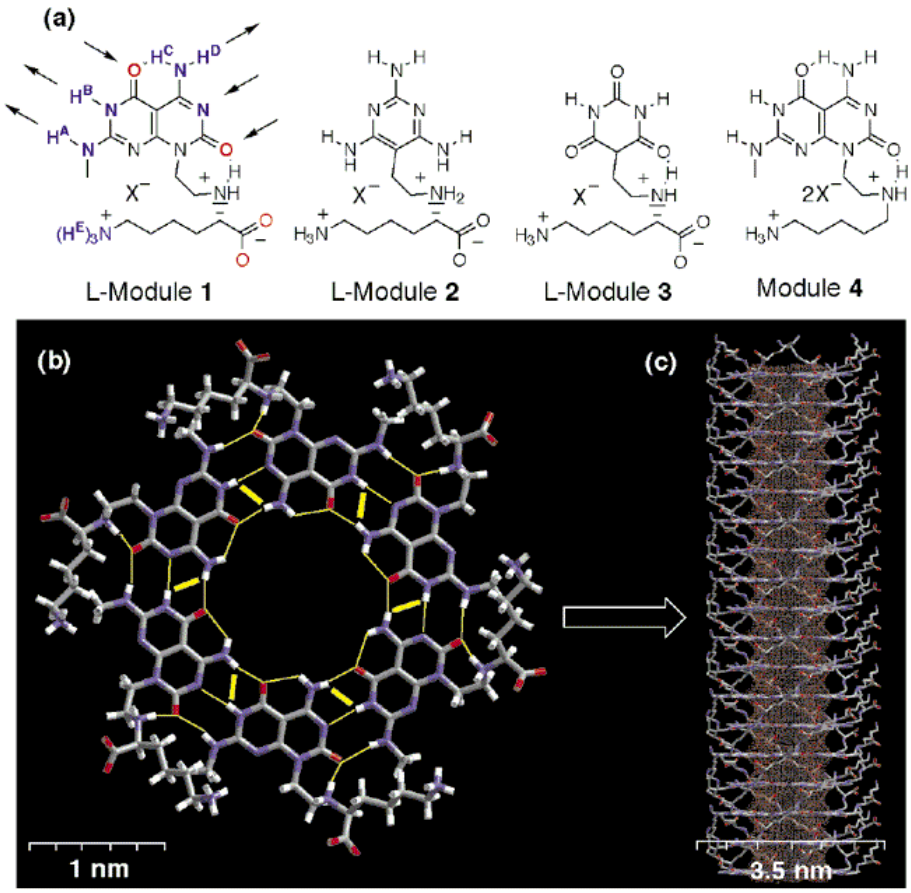

Figure 2.4- Hierarchical self-assembly of rosette nanotubes from L-moldule 1. (a) Modules 1-4 synthesized and investigated. (b) Molecular model of the rosette structure resulting from 1. The thin yellow lines show the hydrogen-bond network. The thick yellow lines highlight unique intermodular NOEs recorded. (c) Molecular model of the proposed nanotube. Eighteen rosettes were arranged in a tubular fashion with a starting interplane distance of 4.5 Å and 30° rotation along the tube's main axis. The inner solvent-accessible surface area of the tube is highlighted in red.[58]

Furthermore, CD spectrometer can be used to study plasmonic transitions of chirality on noble metal nanoparticles. Z. Tang[59] for example, proved that reversible plasmonic circular dichroism responses can be realized based on temperature-dependent assembly and disassembly of Au nanorods and DNA hybrids (Figure 2.5). In this case, the observed plasmonic CD activities are generally believed to originate from the chiral current inside noble metal NPs, which is induced by the dipole of the attached chiral molecules. The chirality is considered to be transferred from the DNA molecules to the Au nanorods, which is confirmed by the extinction spectra of the mixture. Differently, N. L. Rosi[3, 39] and his coworkers successfully synthesized self-assembly of achiral Au nanospheres by using DNA as a template. The synthesized 3D organization exhibited well defined chirality as following

the helicity of the NDA origami. A. O. Govoro and T. Liedl[60] observed such plasmonic CD signals and successfully interpreted these signals to the interactions between the individual gold particles within each helix that create a splitting between the longitudinal and transverse modes of the electromagnetic wave, and these modes typically have opposite chirality.

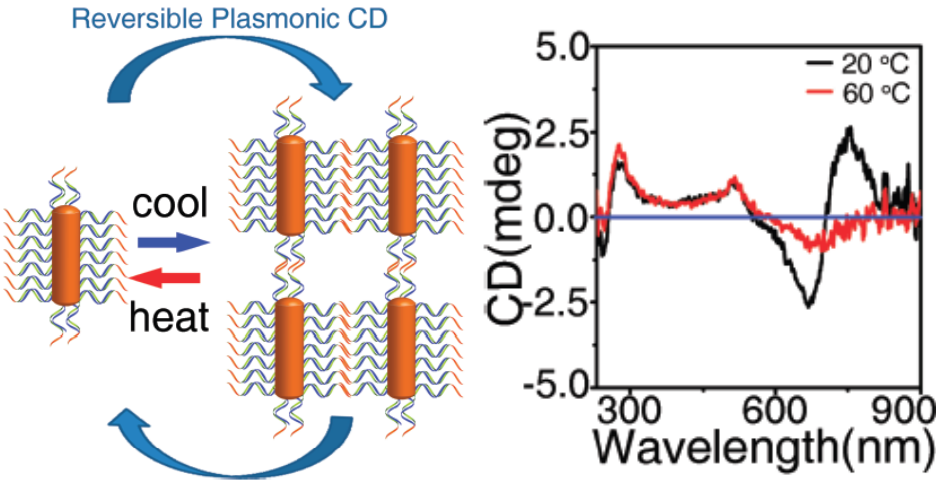

Figure 2.5- Scheme of reversible plasmonic CD responses based on dynamic assembly and disassembly of double-strand DNA modified Au NRs (yellow column) at different temperature. Au NRs are modified with single-strand DNA (blue curves) and its complementary DNA (green curves) with the sticky end (red curves). Reversible plasmonic CD spectra of DNA modified Au NRs at 20 ℃ (black line) and 60 ℃ (red line).[59]

Another frontier application of CD spectrum is vibrational CD (VCD). Unlike electronic CD spectrometer, VCD measures the vibration of bonds in the self-assembly and very often it is cooperatively used with IR or other spectrometers. A good example is provided by R. Oda et al,.[61] They synthesized achiral C_2H_4-α,ω-((CH_3)$_2$N+$C_{16}H_{33}$)$_2$ 16-2-16 tartrate Gemini surfactant in the presence of chiral tartaric acid counterion. Their assembly showed chiral organizations in TEM, exhibiting morphologies like twisted ribbons and helices in nanometric scale. The ECD signal was observed at round 210nm for the absorption of C=O bonds in tartrate anions, however, further study based on VCD revealed another induced CD activity in the symmetric and antisymmetric stretching modes of CH_2 groups of the alkyl chains of the achiral cations. This demonstrates that chirality of the tartrate anions is transferred to the cations which adopt chiral conformations resulting in chiral ribbons.

2.3 Scattering techniques

The interaction of light with matter can reveal important information about the structure and dynamics of the material being examined. If the scattering centers are in motion, then the scattered radiation is Doppler shifted. An analysis of the spectrum of scattered light can thus yield information regarding the motion of the scattering center. Periodicity or structural repetition in the scattering medium will cause interference in the spectrum of scattered light. Thus, the study of the scattered light intensity as a function of scattering angle gives information about the structure, spatial configuration, or morphology of the scattering medium. The most common light scattering techniques are static and dynamic light scattering, which can be used to decide the hydrodynamic radius of spherical particles, layers of the film structures and so forth. More advanced applications such as detection of molar mass distribution based on Batch light scattering or providing structural information about the self-assembly by small-angle X-ray scattering (SAXS) and small-angle neutron scattering (SANS) are widely introduced in variety of scientific topics. S. Mann,[62] for example, used DLS to prove the presence of microemulsion water droplets with a constant hydrodynamic radius around 5.8 ± 0.5nm and the appearance of second component in the microemulsion fluid during the synthesis, where these findings are further supported by SAXS and TEM images. It is noteworthy that light scattering technique can be also used to study the array of electric and magnetic plasmonic particles, which is believed to behave like double-negative particles. F. González and O. J. F. Martin[63] reported that some certain arrays of electric and magnetic particles present a sharp minimum in the backward direction and the shape of the scattering pattern is very similar to that for an isolated particle with $\varepsilon = \mu = -2.01$ shown in Figure 2.6 below. This effect is very robust and could be used to produce double-negative metamaterials using single negative components.

References – page 65

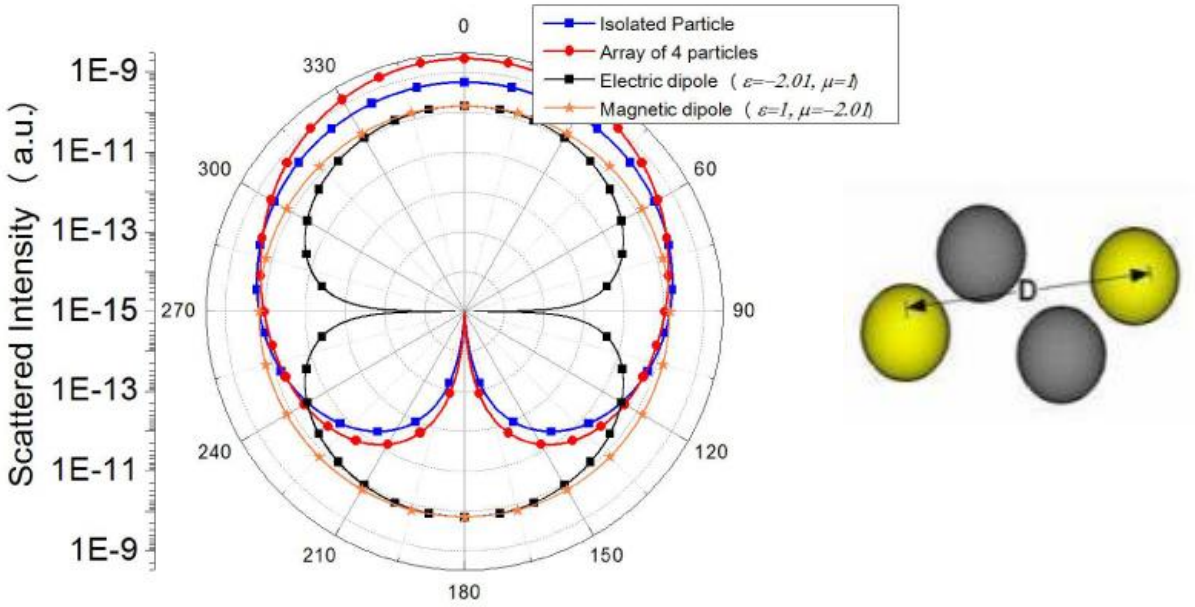

Figure 2.6- Comparison of the scattering patterns for an isolated particle (R = 0.01λ) with optical constants (ε=μ= −2.01) and for an array of electric (ε= −2.01, μ= 1) and magnetic (ε= 1, μ= −2.01) particles (R = 0.01λ, D = 0.5λ) with a spatial distribution indicated as on top. Also the scattering patterns for an electric (ε= −2.01, μ= 1) and a magnetic (ε= 1, μ= −2.01) dipole has been included. The incident wave is polarized with the electric field parallel to the scattering plane (P polarization).[63]

2.4 Ellipsometry

Ellipsometry allows quantitative characterization of surfaces such as porosity and dimension of the coatings on a substrate without the need for assuming the refactive indices of the constituent entities. . R. E. Cohen[64] for example, reported that based on ellipsometry it is able to measure the assemblies of TiO_2 and SiO_2 layers. This technique will, in turn, enable the reverse engineering of the all-nanoparticle multilayer coatings by allowing the determination of the effects of porosity and chemical composition on the functionality of interest. J.R. Henderson[65] also pointed that spectroscopic ellipsometer can be used to investigate the optical properties of nanoparticle thin films. From their results, the refractive indices can be fitting to a Lorentz oscillator dispersion model and the refractive indices of nanoparticles films undergo dramatic variation in the range close to plasmon band which helps interpret the complex refractive index in nanoparticle materials.

Conclusion

In this chapter, we introduced the potential merits and applications of chiral assembly of GNPs and provided a simple and unique way to design 3D Goldhelix. Furthermore, grazing incidence spraying associated with LbL technique and controlled evaporation microfluidics technique are proposed for the realization of hierarchical organizations of Goldhelix in 2D and 3D motif. Instructive interpretations and investigations are suggested based on typical cutting edge characterization techniques. The synthesized Goldhelix will provide an ideal model to create a better theoretical description of induced plasmon CD signals based on calculations and simulations of plasmonic GNPs in 3D helical organizations. Such Goldhelix with strong CD response will develop new applications for fabrication of materials such as super-lens, enhanced circular polarizers in visible range, biosensing and detection based on the importance of SPR effect in biological structures and new generation of chiral metamaterials.

References – page 65

References:

1. Campione, S., et al., *Comparison of electric field enhancements: Linear and triangular oligomers versus hexagonal arrays of plasmonic nanospheres.* Optics Express, 2013. **21**(7): p. 7957-7973.
2. Capolino, F., *Metamaterials Handbook–Two Volume Slipcase Set: Theory and Phenomena of Metamaterials.* CRC, Boca Raton, 2009.
3. Song, C., et al., *Tailorable Plasmonic Circular Dichroism Properties of Helical Nanoparticle Superstructures.* Nano Lett, 2013.
4. Zhu, Y., et al., *A one-step homogeneous plasmonic circular dichroism detection of aqueous mercury ions using nucleic acid functionalized gold nanorods.* Chemical Communications, 2012. **48**(97): p. 11889-11891.
5. Fan, Z.Y. and A.O. Govorov, *Plasmonic Circular Dichroism of Chiral Metal Nanoparticle Assemblies.* Nano Letters, 2010. **10**(7): p. 2580-2587.
6. Govorov, A.O., et al., *Chiral nanoparticle assemblies: circular dichroism, plasmonic interactions, and exciton effects.* Journal of Materials Chemistry, 2011. **21**(42): p. 16806-16818.
7. Fang, N., et al., *Sub–Diffraction-Limited Optical Imaging with a Silver Superlens.* Science, 2005. **308**(5721): p. 534-537.
8. Yu, N., et al., *A Broadband, Background-Free Quarter-Wave Plate Based on Plasmonic Metasurfaces.* Nano Letters, 2012. **12**(12): p. 6328-6333.
9. Hembury, G.A., V.V. Borovkov, and Y. Inoue, *Chirality-sensing supramolecular systems.* Chemical Reviews, 2008. **108**(1): p. 1-73.
10. Zhao, R., *Chiral metamaterials: retrieval of the effective parameters with and without substrate.* Optics Express, 2010. **18**(14): p. 14553.
11. Zhaofeng, L., M. Mehmet, and O. Ekmel, *Chiral metamaterials: from optical activity and negative refractive index to asymmetric transmission.* Journal of Optics, 2013. **15**(2): p. 023001.
12. Walker, D.A., et al., *Geometric curvature controls the chemical patchiness and self-assembly of nanoparticles.* Nature Nanotechnology, 2013. **8**(9): p. 676-681.
13. Soukoulis, C.M. and M. Wegener, *Past achievements and future challenges in the development of three-dimensional photonic metamaterials.* Nat Photon, 2011. **5**(9): p. 523-530.
14. Gansel, J.K., et al., *Gold Helix Photonic Metamaterial as Broadband Circular Polarizer.* Science, 2009. **325**(5947): p. 1513-1515.
15. Oda, R., et al., *Tuning bilayer twist using chiral counterions.* Nature, 1999. **399**(6736): p. 566-569.
16. Delclos, T., et al., *Individualized silica nanohelices and nanotubes: Tuning inorganic nanostructures using lipidic self-assemblies.* Nano Letters, 2008. **8**(7): p. 1929-1935.
17. Zhang, S., et al., *Negative Refractive Index in Chiral Metamaterials.* Physical Review Letters, 2009. **102**(2): p. 023901.
18. Pendry, J.B., *A Chiral Route to Negative Refraction.* Science, 2004. **306**(5700): p.

1353-1355.
19. Wang, Y., et al., *Emerging chirality in nanoscience.* Chemical Society Reviews, 2013. **42**(7): p. 2930-2962.
20. Ben-Moshe, A., et al., *Chirality and chiroptical effects in inorganic nanocrystal systems with plasmon and exciton resonances.* Chemical Society Reviews, 2013. **42**(16): p. 7028-7041.
21. Hutter, E. and J.H. Fendler, *Exploitation of Localized Surface Plasmon Resonance.* Advanced Materials, 2004. **16**(19): p. 1685-1706.
22. Ma, W., et al., *Chiral plasmonics of self-assembled nanorod dimers.* Sci. Rep., 2013. **3**.
23. Ma, W., et al., *Attomolar DNA detection with chiral nanorod assemblies.* Nat Commun, 2013. **4**.
24. Yeom, J., et al., *Chiral templating of self-assembling nanostructures by circularly polarized light.* Nat Mater, 2015. **14**(1): p. 66-72.
25. Aslan, K., J.R. Lakowicz, and C.D. Geddes, *Rapid Deposition of Triangular Silver Nanoplates on Planar Surfaces: Application to Metal-Enhanced Fluorescence.* The Journal of Physical Chemistry B, 2005. **109**(13): p. 6247-6251.
26. Aslan, K., et al., *Fast and Slow Deposition of Silver Nanorods on Planar Surfaces: Application to Metal-Enhanced Fluorescence.* The Journal of Physical Chemistry B, 2005. **109**(8): p. 3157-3162.
27. Freeman, R.G., et al., *Self-Assembled Metal Colloid Monolayers: An Approach to SERS Substrates.* Science, 1995. **267**(5204): p. 1629-1632.
28. Nikoobakht, B. and M.A. El-Sayed, *Surface-Enhanced Raman Scattering Studies on Aggregated Gold Nanorods†.* The Journal of Physical Chemistry A, 2003. **107**(18): p. 3372-3378.
29. Tao, A., et al., *Langmuir−Blodgett Silver Nanowire Monolayers for Molecular Sensing Using Surface-Enhanced Raman Spectroscopy.* Nano Letters, 2003. **3**(9): p. 1229-1233.
30. Sharma, J., et al., *Control of Self-Assembly of DNA Tubules Through Integration of Gold Nanoparticles.* Science, 2009. **323**(5910): p. 112-116.
31. Kuzyk, A., et al., *DNA-based self-assembly of chiral plasmonic nanostructures with tailored optical response.* Nature, 2012. **483**(7389): p. 311-314.
32. Guha, S., M.G.B. Drew, and A. Banerjee, *Construction of Helical Nanofibers from Self-Assembling Pseudopeptide Building Blocks: Modulating the Handedness and Breaking the Helicity.* Small, 2008. **4**(11): p. 1993-2005.
33. Sone, E.D., E.R. Zubarev, and S.I. Stupp, *Semiconductor Nanohelices Templated by Supramolecular Ribbons.* Angewandte Chemie International Edition, 2002. **41**(10): p. 1705-1709.
34. Wang, Y., et al., *Chiral Transformation: From Single Nanowire to Double Helix.* Journal of the American Chemical Society, 2011. **133**(50): p. 20060-20063.
35. Fu, X., et al., *Assemblies of Metal Nanoparticles and Self-Assembled Peptide Fibrils—Formation of Double Helical and Single-Chain Arrays of Metal Nanoparticles.* Advanced Materials, 2003. **15**(11): p. 902-906.

36. Shen, X., et al., *Rolling Up Gold Nanoparticle-Dressed DNA Origami into Three-Dimensional Plasmonic Chiral Nanostructures.* Journal of the American Chemical Society, 2011. **134**(1): p. 146-149.
37. Chen, C.L. and N.L. Rosi, *Preparation of Unique 1-D Nanoparticle Superstructures and Tailoring their Structural Features.* Journal of the American Chemical Society, 2010. **132**(20): p. 6902-+.
38. Zhang, S., et al., *Formation of Gold and Silver Nanoparticle Arrays and Thin Shells on Mesostructured Silica Nanofibers.* Advanced Functional Materials, 2007. **17**(16): p. 3258-3266.
39. Hwang, L., C.L. Chen, and N.L. Rosi, *Preparation of 1-D nanoparticle superstructures with tailorable thicknesses using gold-binding peptide conjugates.* Chemical Communications, 2011. **47**(1): p. 185-187.
40. Chen, C.-L., P. Zhang, and N.L. Rosi, *A New Peptide-Based Method for the Design and Synthesis of Nanoparticle Superstructures: Construction of Highly Ordered Gold Nanoparticle Double Helices.* Journal of the American Chemical Society, 2008. **130**(41): p. 13555-13557.
41. Qi, H., et al., *Chiral Nematic Assemblies of Silver Nanoparticles in Mesoporous Silica Thin Films.* Journal of the American Chemical Society, 2011. **133**(11): p. 3728-3731.
42. Tamoto, R., et al., *Gold Nanoparticle Deposition on Silica Nanohelices: A New Controllable 3D Substrate in Aqueous Suspension for Optical Sensing.* Journal of Physical Chemistry C, 2012. **116**(43): p. 23143-23152.
43. Houmadi, S., et al., *Determination of the elastic properties of SiO2 nanotubes templated from organic amphiphilic self-assemblies through inorganic transcription.* Applied Physics Letters, 2013. **102**(15).
44. Moeller, M. and K. Matyjaszewski, *Polymer Science: A Comprehensive Reference, 10 Volume Set*2012: Newnes.
45. Shestopalov, I., J.D. Tice, and R.F. Ismagilov, *Multi-step synthesis of nanoparticles performed on millisecond time scale in a microfluidic droplet-based system.* Lab on a Chip, 2004. **4**(4): p. 316-321.
46. Kitson, P.J., et al., *Configurable 3D-Printed millifluidic and microfluidic 'lab on a chip'reactionware devices.* Lab on a Chip, 2012. **12**(18): p. 3267-3271.
47. Ladd, C., et al., *3D printing of free standing liquid metal microstructures.* Advanced Materials, 2013. **25**(36): p. 5081-5085.
48. Kölbel, M. and F.M. Menger, *Hierarchical structure of a self-assembled xerogel.* Chemical Communications, 2001(3): p. 275-276.
49. Fuhrhop, J.-H. and J. Köning, *Membranes and molecular assemblies: the synkinetic approach*1994: Royal society of chemistry.
50. Li, Z., et al., *Rotavirus architecture at subnanometer resolution.* Journal of virology, 2009. **83**(4): p. 1754-1766.
51. Vancová, M., *How to observe small biological objects in low voltage electron microscope.* Microscopy and Microanalysis, 2007. **13**(S03): p. 248-249.
52. Drummy, L.F., J. Yang, and D.C. Martin, *Low-voltage electron microscopy of polymer and organic molecular thin films.* Ultramicroscopy, 2004. **99**(4): p. 247-256.

53. Menger, F.M., et al., *Gemini-induced columnar jointing in vitreous ice. Cryo-HRSEM as a tool for discovering new colloidal morphologies.* Journal of the American Chemical Society, 2002. **124**(7): p. 1140-1141.
54. Estroff, L.A. and A.D. Hamilton, *Water gelation by small organic molecules.* Chemical Reviews, 2004. **104**(3): p. 1201-1218.
55. Fages, F. and K. Araki, *Low molecular mass gelators: design, self-assembly, function*. Vol. 256. 2005: Springer Science & Business Media.
56. Spada, G.P., *Alignment by the Convective and Vortex Flow of Achiral Self-Assembled Fibers Induces Strong Circular Dichroism Effects.* Angewandte Chemie International Edition, 2008. **47**(4): p. 636-638.
57. Wolffs, M., et al., *Macroscopic Origin of Circular Dichroism Effects by Alignment of Self-Assembled Fibers in Solution.* Angewandte Chemie, 2007. **119**(43): p. 8351-8353.
58. Fenniri, H., et al., *Helical rosette nanotubes: design, self-assembly, and characterization.* Journal of the American Chemical Society, 2001. **123**(16): p. 3854-3855.
59. Li, Z., et al., *Reversible plasmonic circular dichroism of Au nanorod and DNA assemblies.* Journal of the American Chemical Society, 2012. **134**(7): p. 3322-3325.
60. Kuzyk, A., et al., *DNA-based self-assembly of chiral plasmonic nanostructures with tailored optical response.* Nature, 2012. **483**(7389): p. 311-314.
61. Berthier, D., et al., *From chiral counterions to twisted membranes.* Journal of the American Chemical Society, 2002. **124**(45): p. 13486-13494.
62. Li, M., H. Schnablegger, and S. Mann, *Coupled synthesis and self-assembly of nanoparticles to give structures with controlled organization.* Nature, 1999. **402**(6760): p. 393-395.
63. García-Cámara, B., et al., *Light scattering by an array of electric and magnetic nanoparticles.* Optics Express, 2010. **18**(10): p. 10001-10015.
64. Lee, D., M.F. Rubner, and R.E. Cohen, *All-nanoparticle thin-film coatings.* Nano Letters, 2006. **6**(10): p. 2305-2312.
65. Zhang, H.L., S.D. Evans, and J.R. Henderson, *Spectroscopic Ellipsometric Evaluation of Gold Nanoparticle Thin Films Fabricated Using Layer-by-Layer Self-Assembly.* Advanced Materials, 2003. **15**(6): p. 531-534.

Chapter 3. Controlled fabrication, fragmentation and functionalization of silica nanohelices via soft templating of self-assembled helical Gemini amphiphiles

References – page 118

1. Introduction

As stated in Chapter 1, due to the unique geometrical and physical properties, chiral helical structures can be used to fabricate catalysts, optical polarizers and even metamaterials. Although chiral helical structures are found in many natural products like DNA or peptides, to obtain inorganic materials with tunable helical morphology still remains a challenge. To realize such purpose, methods and techniques like chemical vapor deposition, dip-pen lithography and template synthesis are widely studied based on a variety of materials such as metal oxides, gold, carbon or its derivatives. Among all these inorganic helical materials, silica is the most intensively studied material to fabricate helical silica structures by using soft organic templates due to well established sol-gel chemistry .[1]

To overview all the existing literature devoted to the synthesis of chiral silica structures is far beyond the scope of this thesis, therefore, here we will focus on fabrication methods of a variety of silica helical nanotubes such as mesoporous helical, single-walled helical, double-walled helical, and double-helical structures prepared through organogel-templated approaches by sol–gel reaction. Some typical examples illustrating the basic principle of chirality transfer from organic molecular assemblies to silica materials will be presented and discussed.

Chiral mesoporous silica nanomaterials can be synthesized by cooperative self-assembly of chiral or achiral amphiphiles and the silica precursors, based on the electrostatic interactions between the head groups of amphiphiles and inorganic reagents.[2-9] T. Chen et al[7], for instance, reported that by using achiral cationic surfactant cetyltrimethylammonium bromide (CTAB) as a template, chiral mesoporous silica with a twisted hexagonal rod-like morphology and hexagonally ordered chiral channels with mixture of right handed and left handed helices can be fabricated via sol-gel transcription of tetraethyl orthosilicate (TEOS)[10] as shown in Figure 3.1. Furthermore, C. Lin and his co-workers[11] demonstrated that mesoporous silica helical fibers can be synthesized in high yield in a highly dilute silica solution at pH~2.0-2.5 by using alkyltrimethylammonium-dodecyl sulfate-Pluronic 123

ternary surfactant (C_nTMAB/SDS/P123) as the template. In this one-pot synthesis, different helical structures can be obtained as shown in Figure 3.2, and depending on the alkyltrimethylammonium surfactants, the surfactant compositions that are suitable for the formation of the helical fibers differed. Although it is believed that owing to the chiral configuration, the chiral amphiphiles in the rod-like micelles prefer a helical packing in the formation of the chiral mesoporous silica materials,[12] the exact mechanism for the origin of the helical meso-structure from achiral amphiphiles is still unclear.

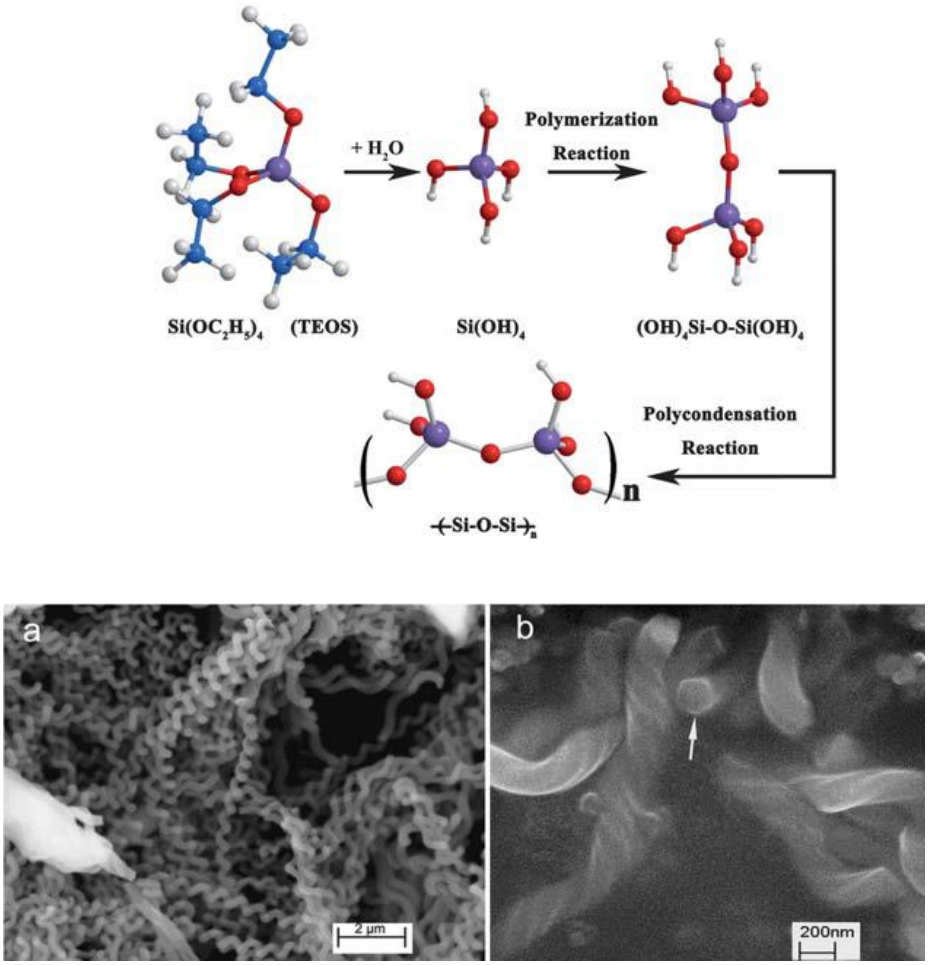

Figure 3.1- Top: schematic illustration of the hydrolytic–polymeric reaction of TEOS. Silicon, purple; oxygen, red; carbon, blue; hydrogen, white. Bottom: SEM image of the nanofibers, a) with low magnification, b) with high magnification. The white arrow indicates the hexagonal cross-section of a fiber end, though not geometrically perfect. Distinguished facets of the nanofibers could be seen.[7, 10]

References – page 118

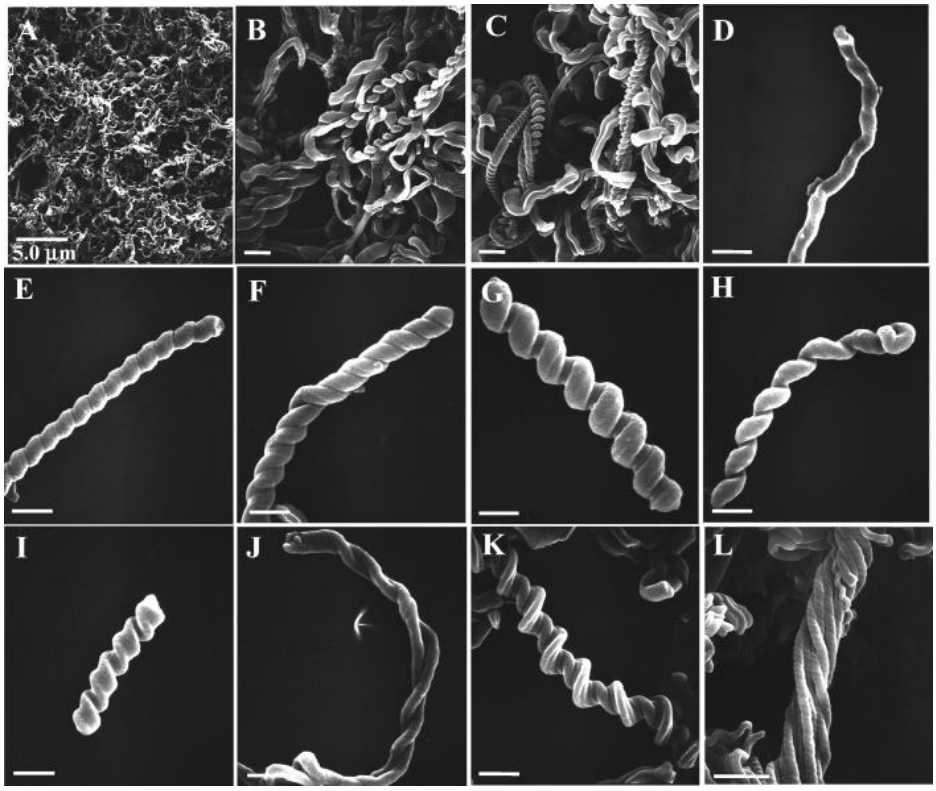

Figure 3.2- SEM images at different magnifications of various shapes of mesoporous silica helical fibers synthesized with the C_{18}TMAB/SDS/P123 template (A) low-magnification image, (B, C) higher-magnification images, (D) single helix, (E) double helix, (F) double helix, (G) double helix, (H) double-helical loop, (I) double-helical ribbon, (J) coupled single-helix strains, (K) triplet helix (one helix winds around a double helix), and (L) multiple strains of helix fibers. Scale bars are 500 nm.[11]

Hanabusa et al. fabricated the mesoporous-type silica nanofibers by using the self-assembled amino acid-based hydrogels in which the synthesized helical nanofibers were bundled with ultrafine nanofibers and they have a pore size of 2nm. The formation mechanism of the hierarchical structure for mesoporous silica nanofibers can be understood by the shearing force generated during the self-assembling process as illustrated in Figure 3.3 where they believed that during the formation of helical bundles of gel fibers from the multiple-strand gel fibers as well as the polycondensation procedure of TEOS onto these multiple-strand fibers, the shearing force was introduced and aligned the overall nanofibers.[13]

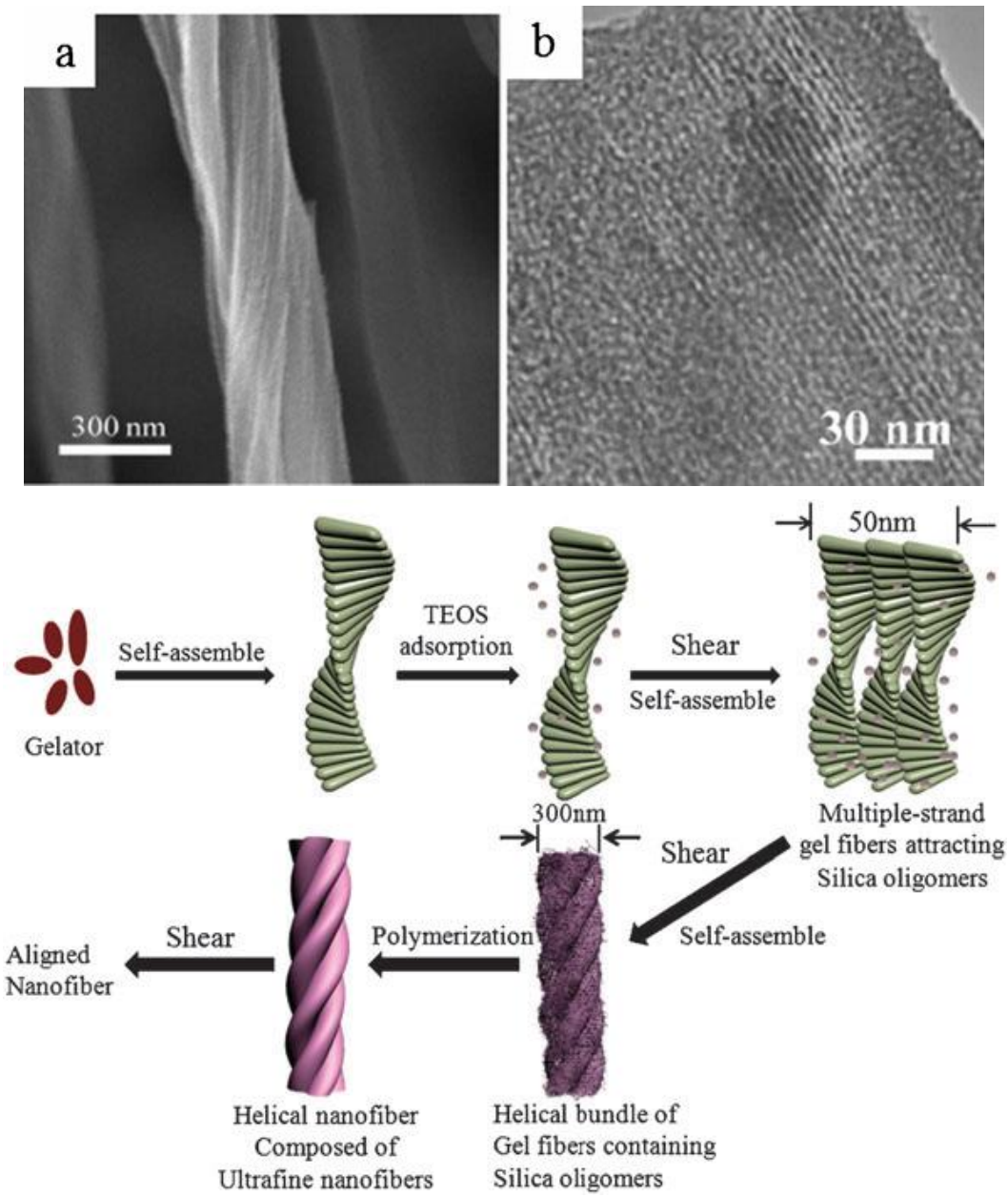

Figure 3.3- (a) SEM and (b) TEM images of the right-handed helical silica nanotube with mesopores. (c) Schematic representation of formation of mesoporous right-handed helical nanofibers and alignment.[13]

Shinkai's group also found that organogel supramolecular structures can be elaborately transcribed into inorganic silica materials by utilizing the template-silanol interaction[14, 15]. Sol-gel polycondensation of TEOS proceeds along the organogel aggregate used as a template fiber, leading to various types of hollow silica. For example, their recent study showed that amphiphilic porphyrin (**1**) bearing four β-D-galactopyranoside groups at its periphery tends to aggregate in a one-dimensional direction, which results in very robust gels in DMF/alcohol mixed solvents. Depending on heating after addition of polycondensation catalyst or not, the

post-transcripted silica fibers can express unimolecular stacks and single-walled helical bundles (Figure 3.4), where they reasoned that the heating process can accelerate the polycondensation of TEOS and suppress the bundle formation of organogels, which explained the formation mechanism of silica-coated porphyrin arrays and single-walled helical bundles.[16]

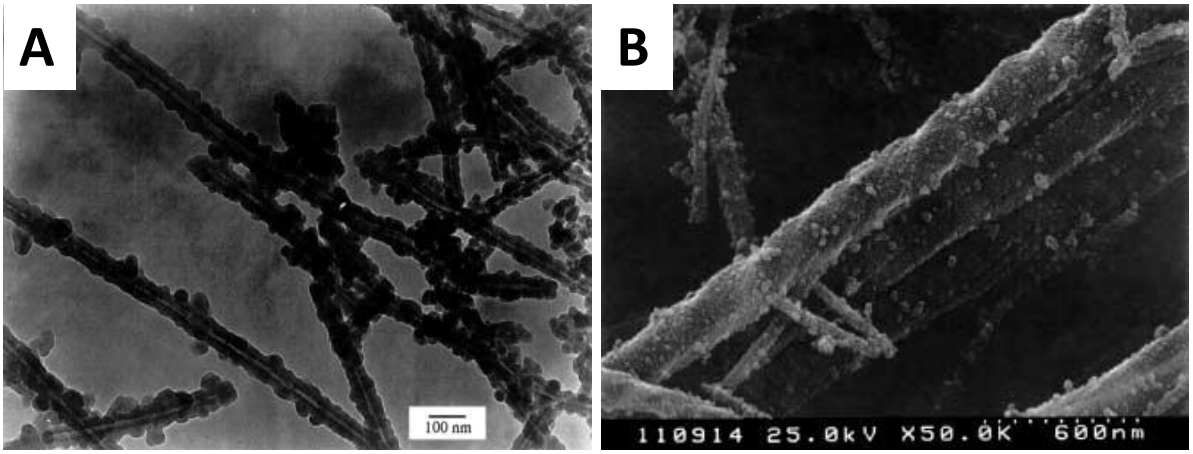

Figure 3.4- A:TEM images of silica-coated porphyrin arrays. B: SEM image of the silica structure prepared by transcription of helically bundled 1 as a template (before calcination).[16]

Moreover, Shinkai *et al* reported that certain amphiphiles can form a tubular structure through the helical ribbon structure in an aqueous solution. They demonstrated that 30-crown-10-appended cholesterol gelator **1** forms a tubular structure in the gel system and this chiral tubular structure can be also transcribed via proper sol-gel transcription as discussed above. But interestingly the silica had double layers with an interlayer distance of 8 to 9 nm (Figure 3.5). These double-walled silica helical fibers indicated that TEOS (or oligomeric silica particles) had been adsorbed onto both surfaces of the double-walled tubules that were 8 to 9 nm thick, meaning the tubular silica had two hollow cavities. [17]

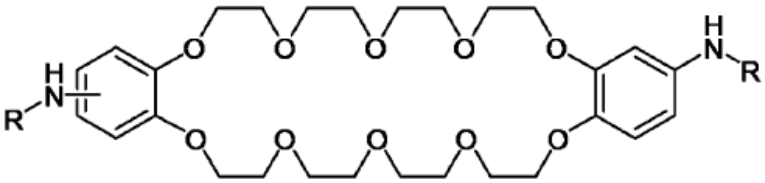

1

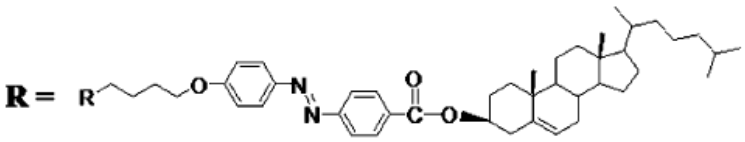

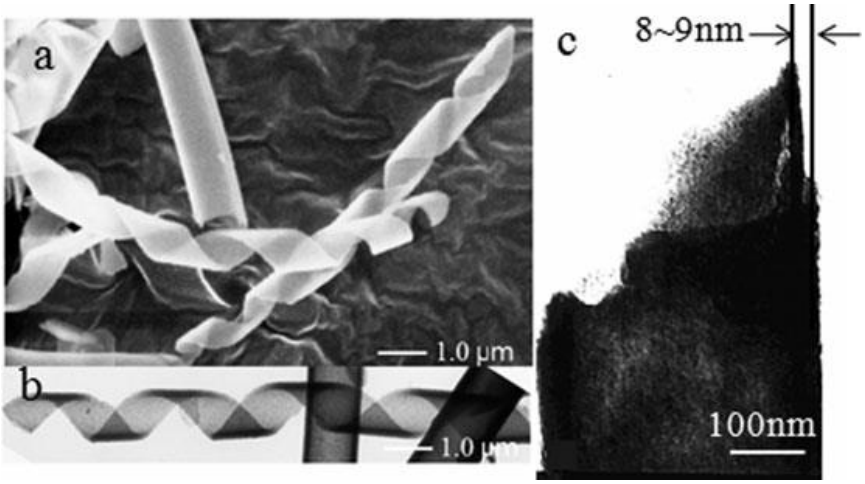

Figure 3.5-(a) SEM and (b and c) TEM images of the double-walled silica nanotubes obtained from organogel 1 after silica transcription.[17]

S. Che *et al.*[18] reported that right- and left-handed excess chiral mesoporous silica nanotubes with a helical channel in the wall can be fabricated by the self-assembly of an achiral surfactant sodium dodecyl sulfate (SDS) in the presence of (R)-(+)- and (S)-(-)-2-amino-3-phenyl-1-propanol ((R)-(+)- and (S)-(-)-APP) chiral molecules.(Figure 3.6) Their further studies showed that the mesoporous silica nanotubes were produced via a specific crystallization route that hollows out the chiral mesoporous silica rod which is different from general mechanisms reported previously.[19-23]

References – page 118

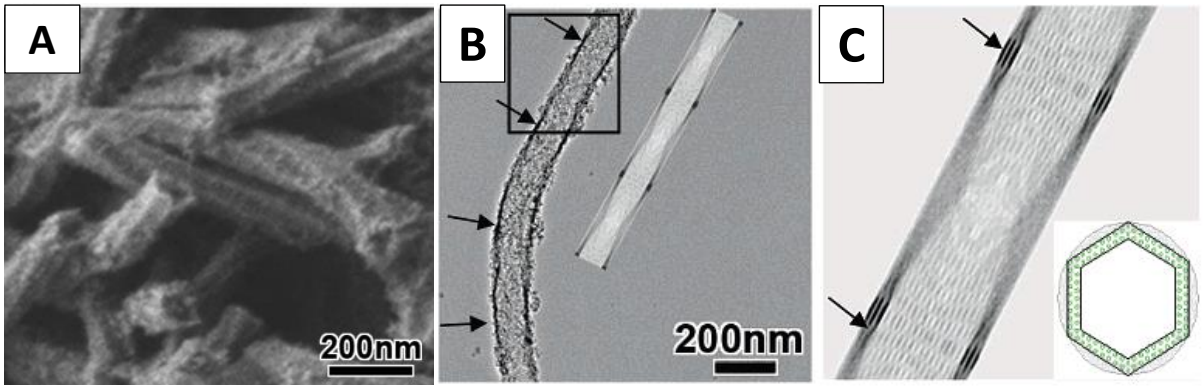

Figure 3.6-A: SEM images of calcined samples with different (R)-(+)-APP/SDS molar ratios of 0.8; B and C: low- and high-magnification TEM image with simulated chiral nanotubes of A.[18]

Later on they reported that via using N-miristoyl-l-alanine sodium salt (C_{14}-L-AlaS) and 3-aminopropyltriethoxysilane as structure- and co-structure-directing agents, mesoporous silicas with four different morphologies--helical ribbon, hollow sphere, circular disk, and helical hexagonal rod--were synthesized just by changing the synthesis temperature from 0 to 10, 15, or 20 ^{0}C. (Figure 3.7) They also pointed out the formation mechanism of helical ribbons that is at 0 ^{0}C, partially neutralized chiral amphiphilic carboxylate molecules can self-assemble into flat tapes with a bilayer structure, and then hydrogen bonding between the amide groups strengthens such bilayer arrangements, and the chirality of asymmetric carbon atoms demands a helical structure of bilayer strands or coiled ribbons, and finally APES and TEOS can easily penetrate into the ribbon from its surface and convert the lipid wall into a mesoporous one through reassembly as shown in the schematic illustration.[24]

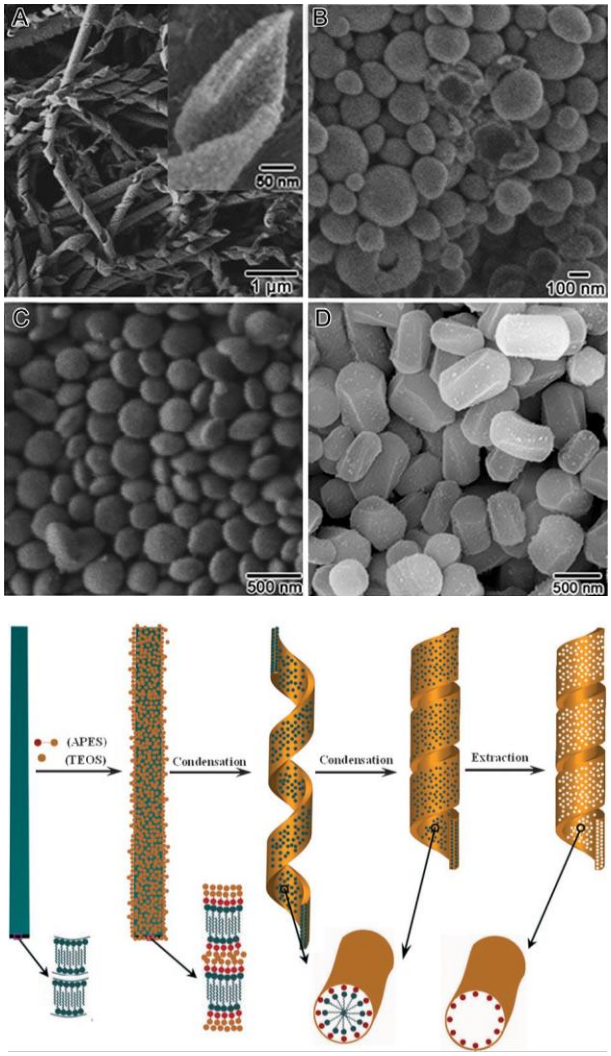

Figure 3.7-SEM images of extracted mesoporous silicas synthesized at different temperatures at 0 ^{0}C (A), 10^{0}C (B), 15^{0}C (C), and 20^{0}C (D). The synthesis molar composition was C_{14}-L-AlaS:APES:TEOS:HCl:H2O 1:1:7:0.1:1780. Insert image in the bottom is the schematic illustration of the mesoporous silica tape and helical ribbon formation processes.[24]

Alternatively, S. Che *et al.* also showed possibility to use natural DNA molecules as the templates for the synthesis of silica helical structures. In this case, by inducing APTMS, the cationic ammonium groups of APTMS can interact with phosphate groups of DNA and mediated DNA condensation in a similar way to polyamines and cationic surfactants[25, 26], and then the hydrolyzed APTMS can co-condensed with TEOS to form a silicatropic DNA liquid crystal phase as shown in the schematic representation in Figure 3.8. By adjusting APTMS/DNA molar ratios, different DNA packing states with various helical morphologies can be achieved and monitored in circular dichroism spectra.[27]

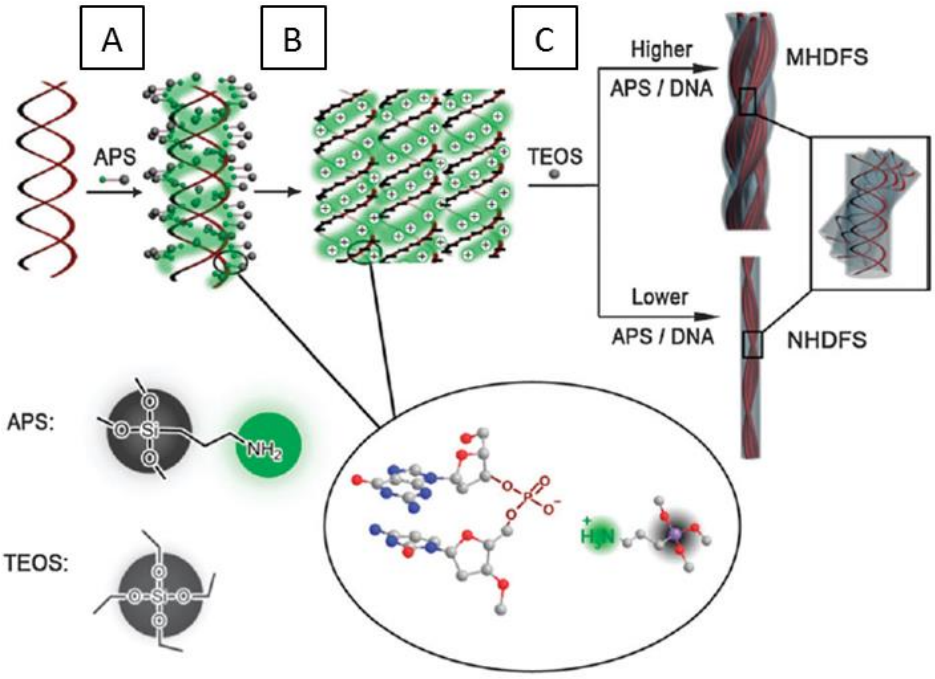

Figure 3.8-Schematic illustration of the formation of multi-helical DNA–silica fibers (MHDSFs) and non-helical DNA–silica fibers (NHDSFs).[27]

Unlike single- or double- walled silica nanotubes, Jung et al, for example, prepared sugar-based gelator **1** as a template, which, together with aminophenyl glucopyranoside **2**, can form a gel consisting of double-helical fibers that can be transcribed into double-helical silica nanotubes (Figure 3.9), where they believed this DNA like structure of silica materials was transcribed by hydrogen-bonding interactions between the amine moiety of **1** and the negatively charged oligomeric silica particles.[28]

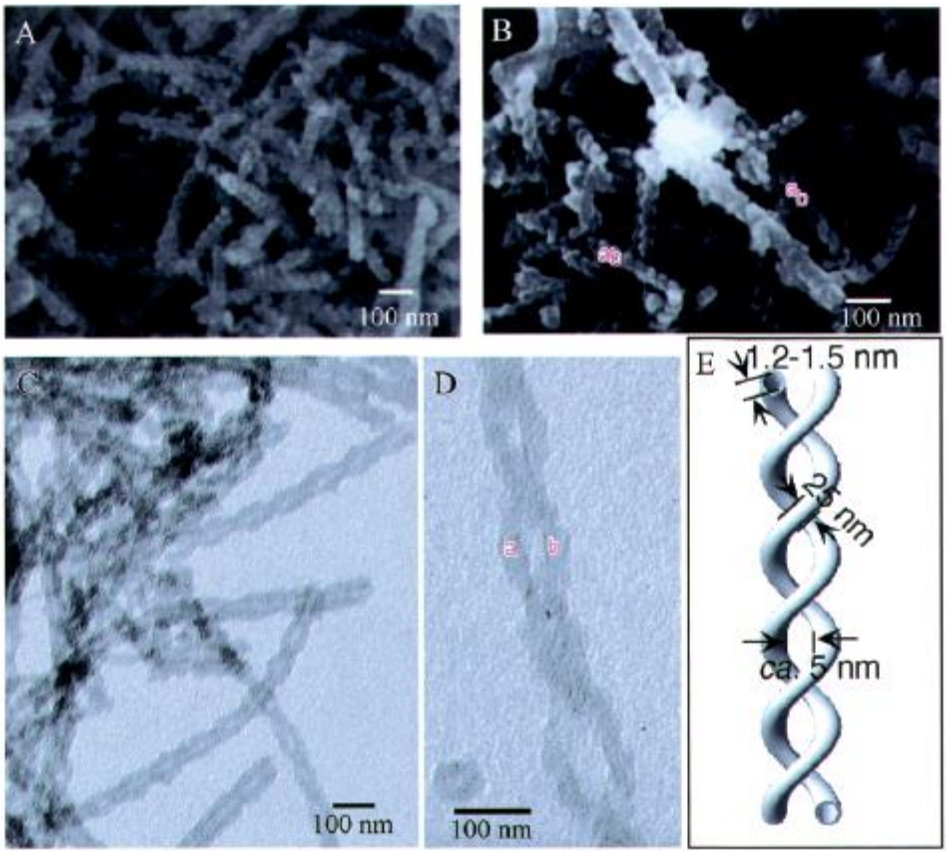

Figure 3.9-(A and B) FE-SEM and (C and D) TEM images of the double-helical silica nanotube obtained from the mixed gel of 1 and 2 (1:1 w/w) after calcination, and (E) schematic representation of the double-helical structure of the silica nanotubes through SEM and TEM observations. a and b indicate two silica nanotubes from which the double helixes are constructed (parts B and D). [28]

He also reported a highly enantioselective synthesis of right-handed and left-handed single chiral silica nanotubes by sol-gel transcription (Figure 3.10) of chiral diaminocyclohexane-based organogel systems **(1-4)** with different chirality.[14, 29] After calcination of the silica fibers, inner channels possess the same helicity as the fiber itself, thus proving the view that the organogel fibers had indeed been the template around which the silica structures had formed. These results showed that the chirality present in the gelator molecules is transcribed consistently into the macroscopic silica materials. This system is the most striking example of the potential of the organogel approach for the formation of inorganic materials.[19]

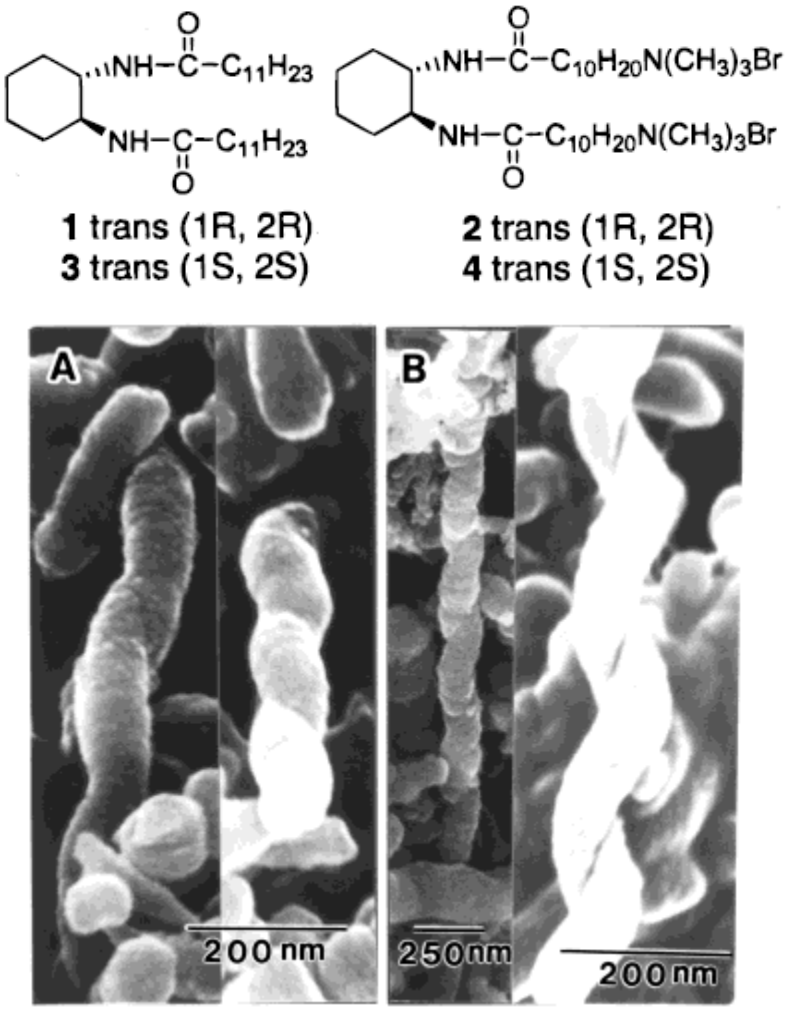

Figure 3.10-SEM pictures of the silica obtained by sol-gel transcription in (A) left-handed 1+2 (1:1 wt %), and (B) right-handed 3+4 (1:1 wt %) organogels. [19]

Oda's group has reported methods on synthesizing organic right-handed and left-handed helical nanostructures via chiral self-assembling of organic Gemini tartrate molecules the orientational order of the molecules within the membrane together with the chirality of the constituents provide a natural explanation for the observed twisted-ribbon shape and by finely controlling parameters such as aging time, concentration and pH, they are able to control the self-assembling process of these molecules to a desired morphology.[30] The synthesized chiral organic structures could be transcribed to inorganic silica via proper sol-gel chemistry as stated above.[31, 32] Basically, by controlling parameters such as the aging time for example (Figure 3.11), it was possible to finely tune the morphology of the inorganic nanostructures formed from organic templates. This fine-tuning has also been achieved upon

controlling the kinetics of both organic assembly formation and inorganic polycondensation by parameters like concentration of the gel, pH, and enantiomer excess amount.[32]

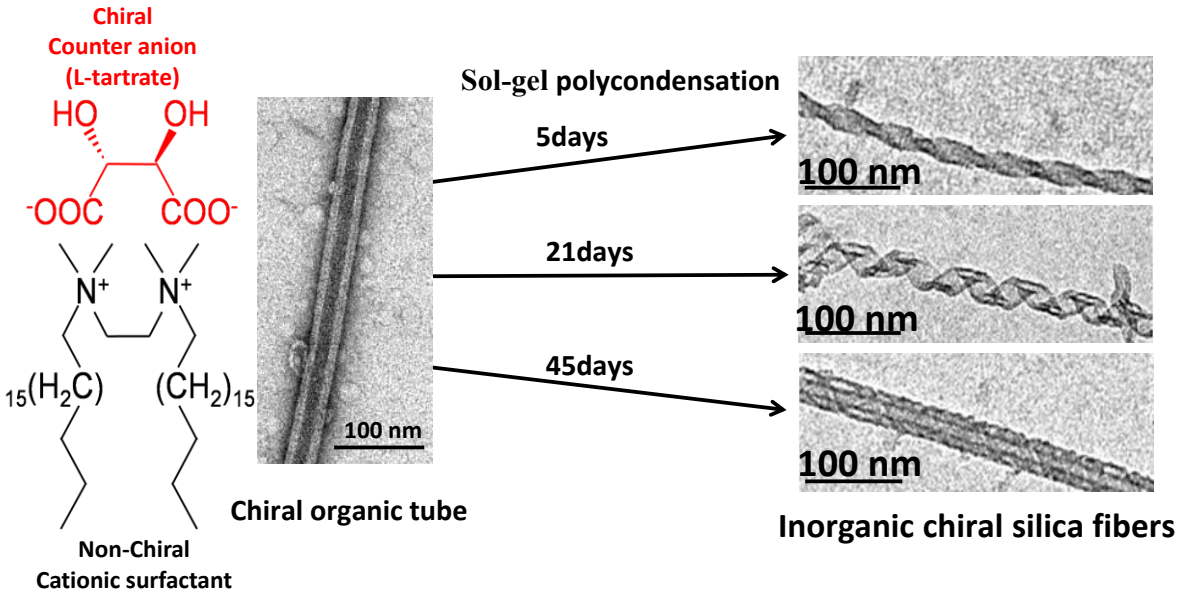

Figure 3.11- Typical example of aging time effect on sol gel transcription of organic tube formed by 5mM 16-2-16 Gemini tartrate. The organic gels need to be aged for 5 days to obtain silica twisted ribbons, 21 days for silica helical ribbons and 45 days for silica nanotubes.[30]

Unwinding of the organic fibers during the transcription procedure may be explained by replacing of chiral tartrate molecules, which induces supramolecular chirality in the system, with achiral silicate anion. If silica condensation occurs faster than the significant ion exchange the original morphology of organic fibers may be preserved (Figure 3.12a), otherwise unwound silica structures will be obtained (Figure 3.12b).[32]

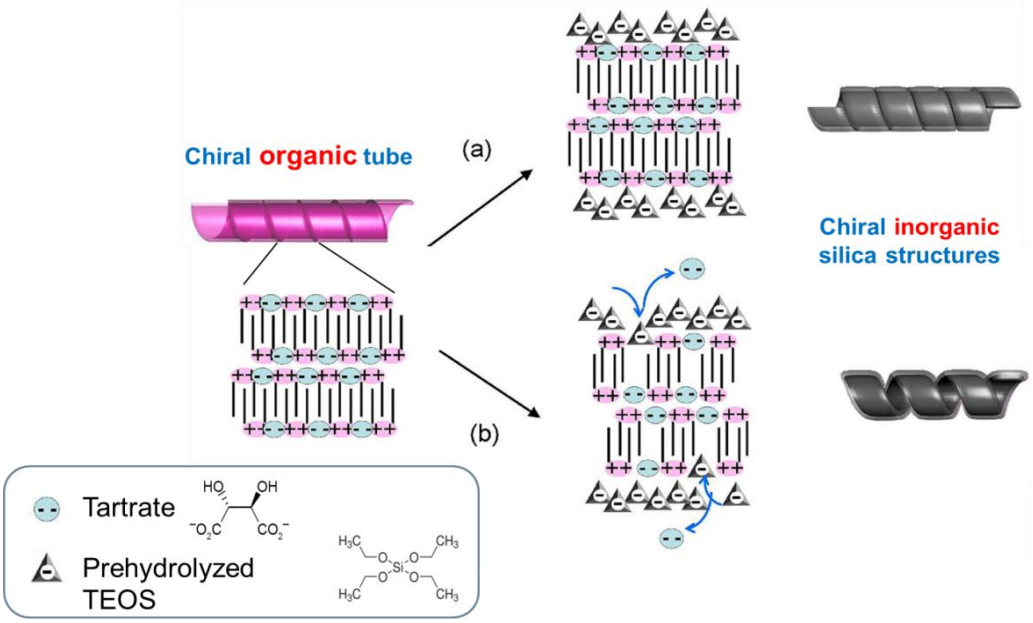

Figure 3.12– Schematic representation of dependence of the silica structure morphology on the replication conditions.[32]

Inspired by this idea, recently they showed a direct silica transcription approach to quickly obtain silica replicas by accelerating the hydrolysis of TEOS for the sol-gel reaction. With this method, they are able to produce various shapes of silica materials such as twisted ribbons and helical ribbons within 3 days, for the increasing amount of pre-hydrolyzed TEOS can greatly accelerate the polycondensation process and preserved the chirality from the organic template. (Figure 3.13) After polymerization, the synthesized silica materials can be widely used as template for a variety of applications such as optical materials and bio-tissue engineering for its high rigidity, nontoxicity and versatile functionality.[33]

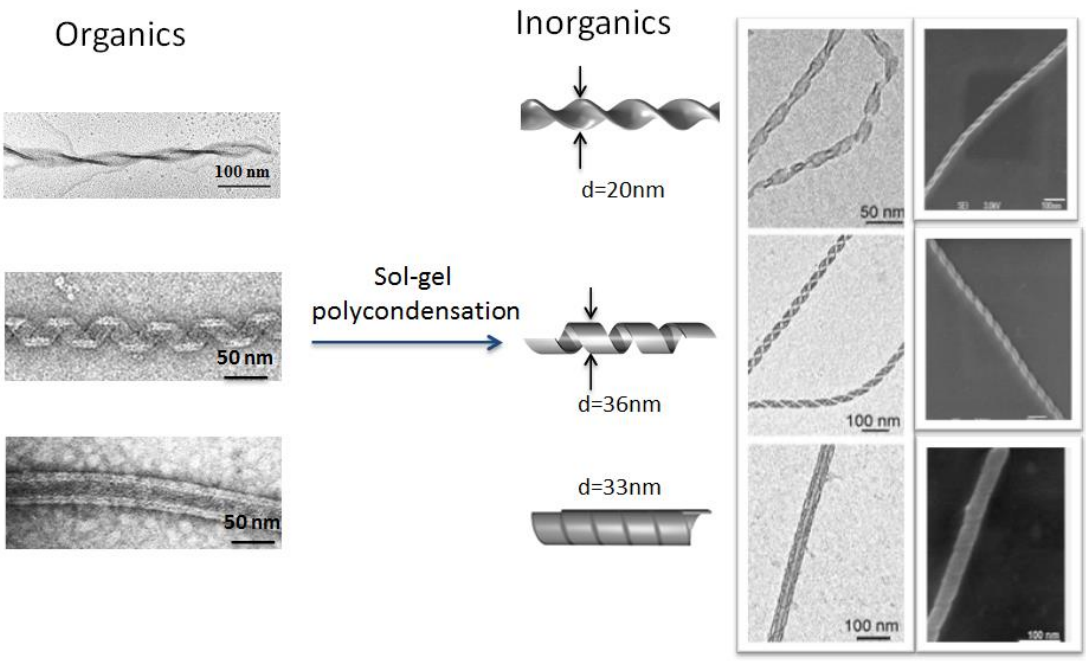

Figure 3.13- Silica sol-gel transcription. From organic twisted ribbons, helical ribbons and tubules to inorganic replicas. Basically, twisted ribbons formed with 2 hours aging at RT with a concentration of 1mM, and helical ribbons take 2-3days and tubules need 30-40 days. The diameters to the corresponding morphologies are around 20nm, 36nm and 33nm, respectively.[33]

Silica nanomaterials can be easily involved into optical and biomedical applications like SERS[34, 35], Plasmonics[36], MRI[37] with appropriate surface modification procedures. This is because these materials can be very easily functionalized by a wide range of silanes[38] and at the meantime, such surface treatments can allow changing hydrophilicity/hydrophobicity of the materials as well as functions for electrostatic and covalent grafting of small particles and molecules of interest.[39, 40] However, in view of engineering and material manufacturing, it requires rationally control on the morphology, dimensions and even dispersibility of the building blocks in order to obtain desired materials with controlled effective properties. Herein, in this chapter, morphology control of organic nanohelices by longer chain length will be introduced at the beginning. Subsequently, synthesis of silica nanohelices with controllable length, diameter, pitch length and well dispersibility will be discussed in details. Finally, the efficiency on surface functionalization of silica nanohelices will be investigated to reveal potential interactions between such silica nanohelices with other charged materials.

2. Morphology control of organic nanohelices by longer chain length

In our group, we have shown that nanometric helices different handedness can be formulated by using 16-2-16 acetate and L- or D- tartaric acid, respectively[30], *i.e.* silica twisted ribbons and helical ribbons can be fabricated with a certain dimension. (Basically, twisted ribbon exhibits a diameter of 20nm and pitch length around 100nm, and helical ribbons can have 35nm in diameter and 65nm in pitch length).

A critical issue concerning whether we can control the diameters and pitch value by simply changing the hydrophobic chain length of the organic Gemini tartrate (from 16 alkyl carbons to 18 or 20 carbons) quickly raised. Indeed, as we demonstrate below, the variation of hydrocarbon chain length is an efficient way to tune the dimension of the helices; however the elongation of carbon chain also results in variation of the properties of the compounds such as the Krafft temperature (Tk), surface tension, and particularly the kinetics of aggregates formation. Taking a simple and akin system to start with, the morphology of 1mM 18-2-18 Gemini tartrate was studied under observations at various aging time at room temperature. Figure 3.14(A-E) shows the typical TEM results on the evolution of the morphology from flat ribbons to twisted ribbons and helical ribbons. It shows that the longer carbon chain here has significantly increased both the Tk (~42 ℃ for 18-2-18 Gemini tartrate at 3mM[41]) and the gelation time. Similarly, in the case of 1mM 20-2-20 Gemini tartrate (here the compound was first heated up to 70 ℃, then cooled down to 20 ℃ because Tk is around 65 ℃ for 20-2-20 Gemini tartrate at 3mM[41]), even longer time was required for the formation of nanohelices, and it typically took more than 60 days to form nanohelical structures at room temperature as exhibited in Figure 3.14(F-J).

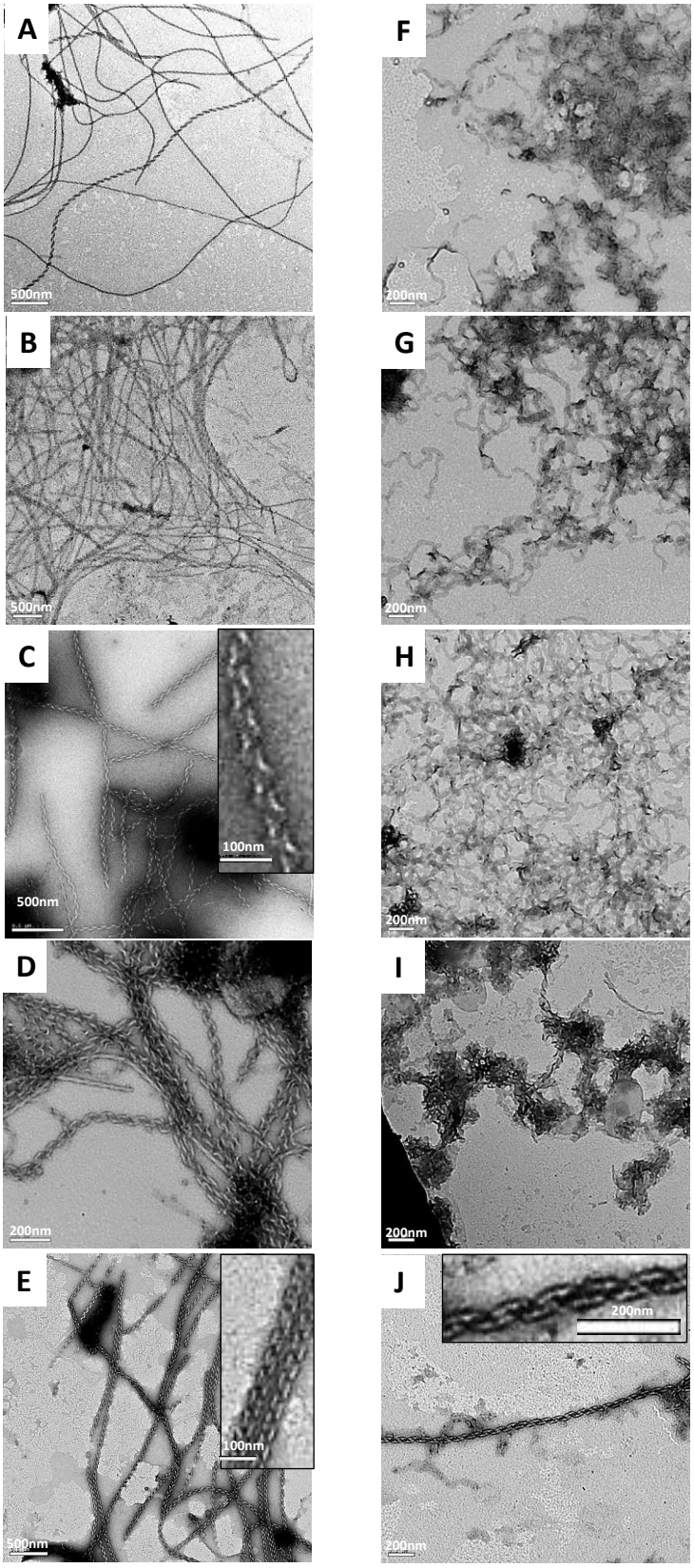

Figure 3.14- Morphology evolution of 18-2-18/20-2-20 Gemini gels. (A-E) represents for 18-2-18 Gemini with 7, 14, 28, 42, 49days of aging, respectively; (F-J) represents for 20-2-20 Gemini gel with 7d, 14d, 28d, 35d, and 63d of aging, respectively. The gels were incubated at 20 ℃ with a concentration of 1mM. Inserts are five times magnified images of the originals. The organogels have a pH=5.44.

Such a slow kinetics is clearly not practical for their use in nanomaterials formation. We therefore investigated how to optimize/accelerate the gel formation processes as shown hereafter. We first investigated the effect of parameters such as temperature and concentration during the aging procedure. We only investigated the temperature below Tk, since at the temperature higher than Tk, only micelles are formed, and helix formation was only observed below Tk. In Figure 3.15 and Figure 3.16 below, the typical TEM images show the kinetics of helix formation. It is observed that less time is needed for the formation of nanohelical ribbons in both of 1mM 18-2-18 (Figure 3.15) and 20-2-20 Gemini (Figure 3.16) at higher temperature (but below Tk), typically 5days at 35 ℃ compared to 7 days at 30 ℃ for 18-2-18 Gemini and 21days at 55 ℃ compared to 60 days at 40 ℃ for 20-2-20 Gemini. Clearly, the closer incubation temperature to the Tk, the observed mechanism of gel formation will be accelerated, which indicates a more efficient approach to obtain longer chain organic nanohelices.

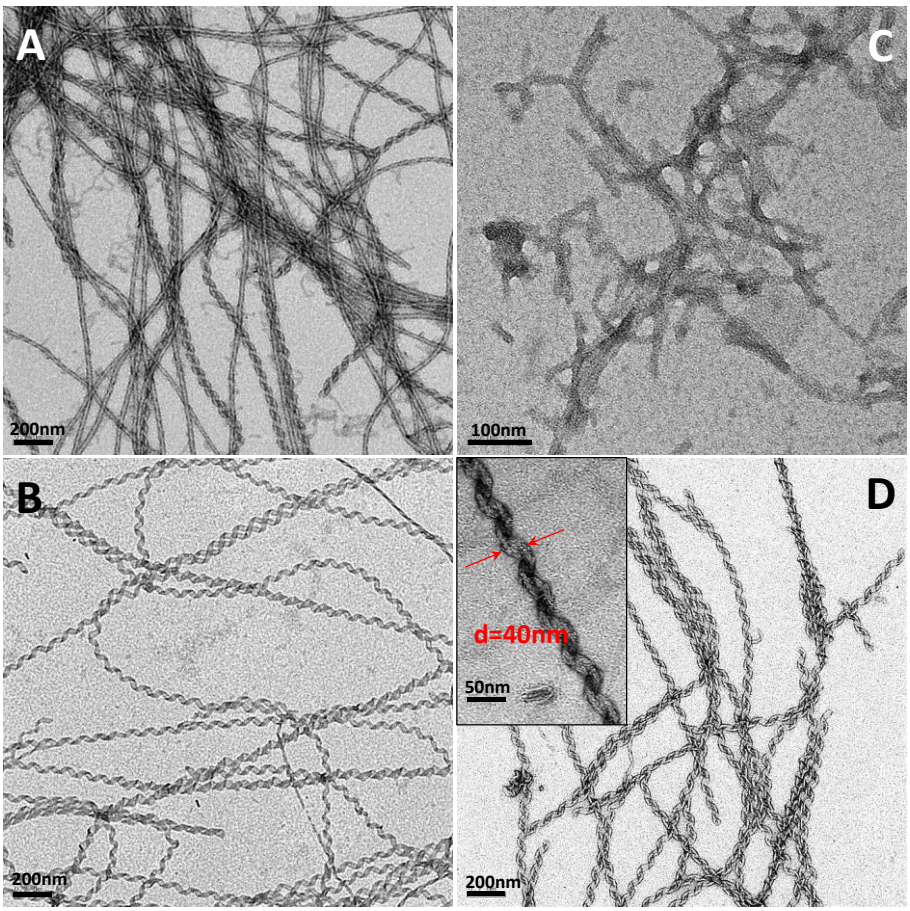

Figure 3.15- Typical TEM images of 18-2-18 organic helical ribbons. (A) and (B) Incubated at 30 ℃ for 3

and 7 days respectively, (C) and (D) incubated at 35 ℃ for 3days and 5days, respectively. The formed helical ribbons have an averaged diameter about 40nm and pitch length about 75nm. The concentrations of the organic gels are 1mM in both cases.

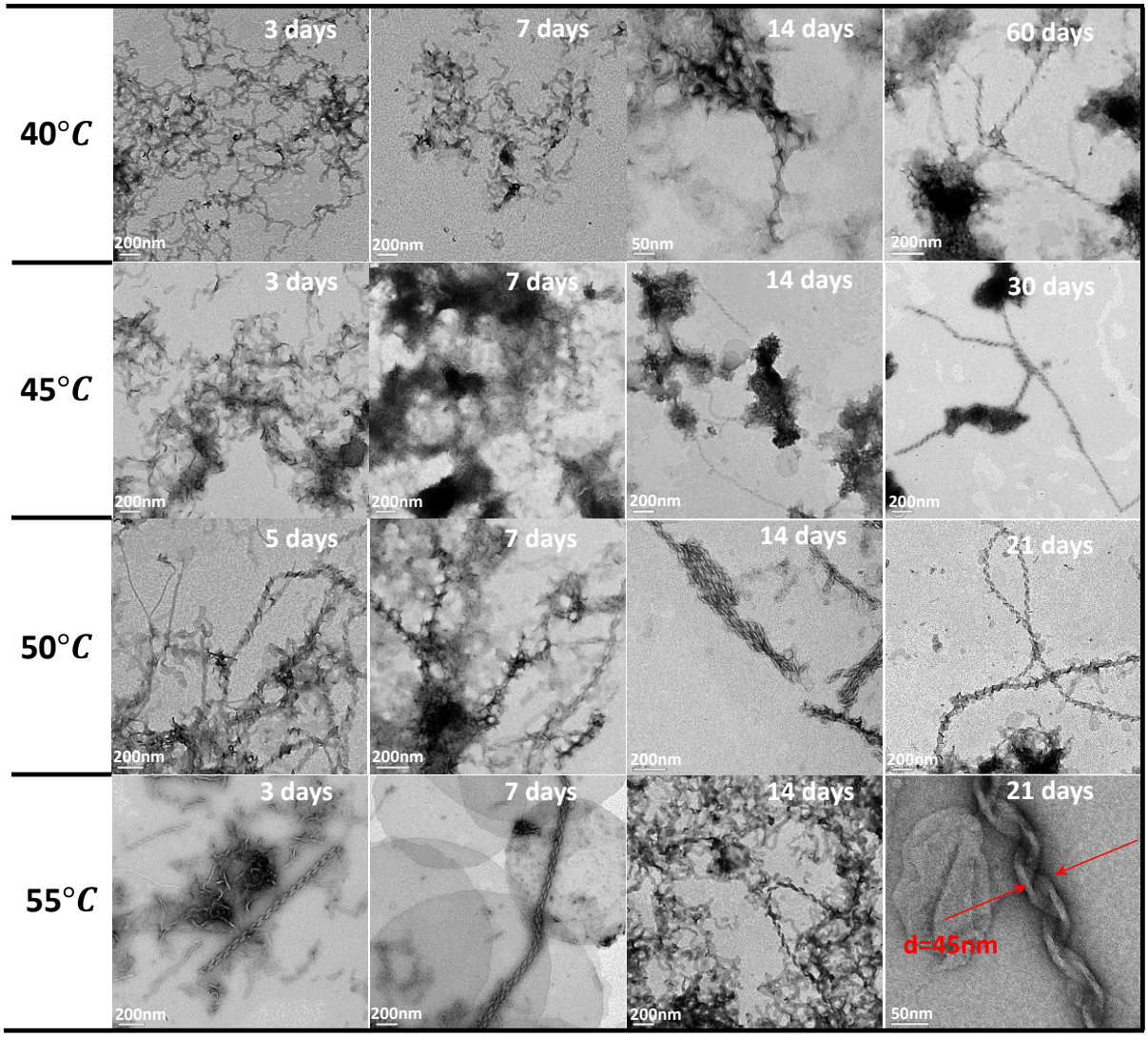

Figure 3.16- Temperature dependence on morphology evolution of 1mM 20-2-20 Gemini tartrate. The observed organic helical ribbons have a diameter around 45nm and pitch length around 107nm. The pH of the organogels is around 3.6.

On the other hand, another speedy formation of nanohelices can be established by simply increasing the concentration of organic compounds. As shown in Figure 3.17, when the concentration of 18-2-18 and 20-2-20 organogels is increased from 1mM to 5mM and 10mM while keeping other parameters unchanged, it still take at least 28days for 18-2-18 organogel and 56days for 20-2-20 organogel to make helices, showing the gelation rate would only increase in a small or even negligible scale in the above cases, however, to go up to a

concentration much higher than 10mM seems apparently not an economic choice.

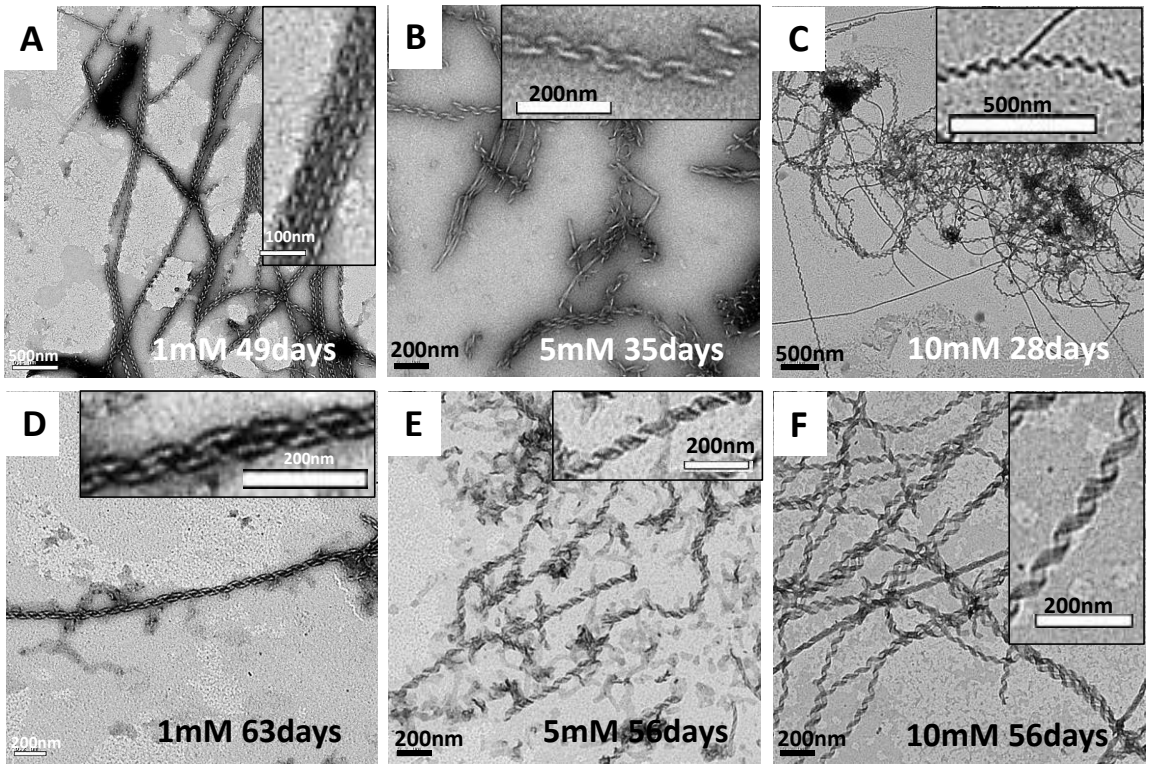

Figure 3.17- Typical TEM images of long chain Gemini tartrate aging at different concentrations. (A –C), 1nM, 5mM and 10mM 18-2-18 Gemini tartrate aging at 20 ℃ with 49days, 35days and 28days for the formation of helical nanoribbons, respectively; (D-F), 1mM, 5mM and 10mM 20-2-20 Gemini tartrate aging at 20 ℃ with 63days, 56days and 56days for the formation of helical nanoribbons, respectively.

Nonetheless, when the concentrations of 18-2-18 and 20-2-20 Gemini tartrate are increased from 1mM to 5mM and the incubation temperature set to 35 ℃ and 55 ℃ respectively, the helix formation time is shorten to 2 and 7 days respectively (Figure 3.18), indicating when increasing both the concentration and incubation temperature, the gel formation rate will drastically speed up, especially for 20-2-20 Gemini. This finding actually provides us an efficient way for controlled and accelerated fabrication of long chain nanohelices..

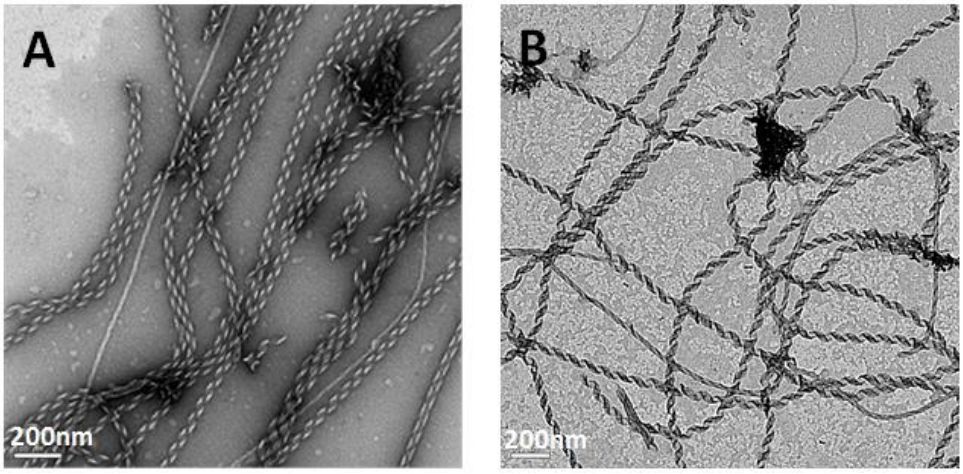

Figure 3.18- Helical ribbons formed by 18-2-18/20-2-20 Gemini tartrate. (A) 5mM 18-2-18 Gemini tartrate incubated in 35 ℃ for 2 days, (B) 5mM 20-2-20 Gemini tartrate incubated in 55 ℃ for 7 days.

It is worth noting that as the chain length increases, the overall kinetics of gel formation is overwhelmingly slowed down. This longer gelation time on the other hand gives us access to an intermediate product in the morphology transition that we name "bad helices" as described below (Figure 3.19) only observable with 18-2-18 and 20-2-20 Gemini tartrate with slow kinetics (5mM 18-2-18/20-2-20 incubated at 35 ℃/55 ℃ for 5days/7days). Their morphology is quite similar to the Archimedes screw found in Mississippian (Figure 3.19D), but they have a pitch length of 70nm and a maximum diameter about 50nm and a minimum diameter about 30nm in cone frustum as it is shown in Figure 3.19C.

In sum, the morphology transition rate of longer chain length Gemini tartrate can be accelerated by increasing concentration or incubation temperature, and the effect of incubation temperature plays a dominating role for accelerating the self-assembling procedures.

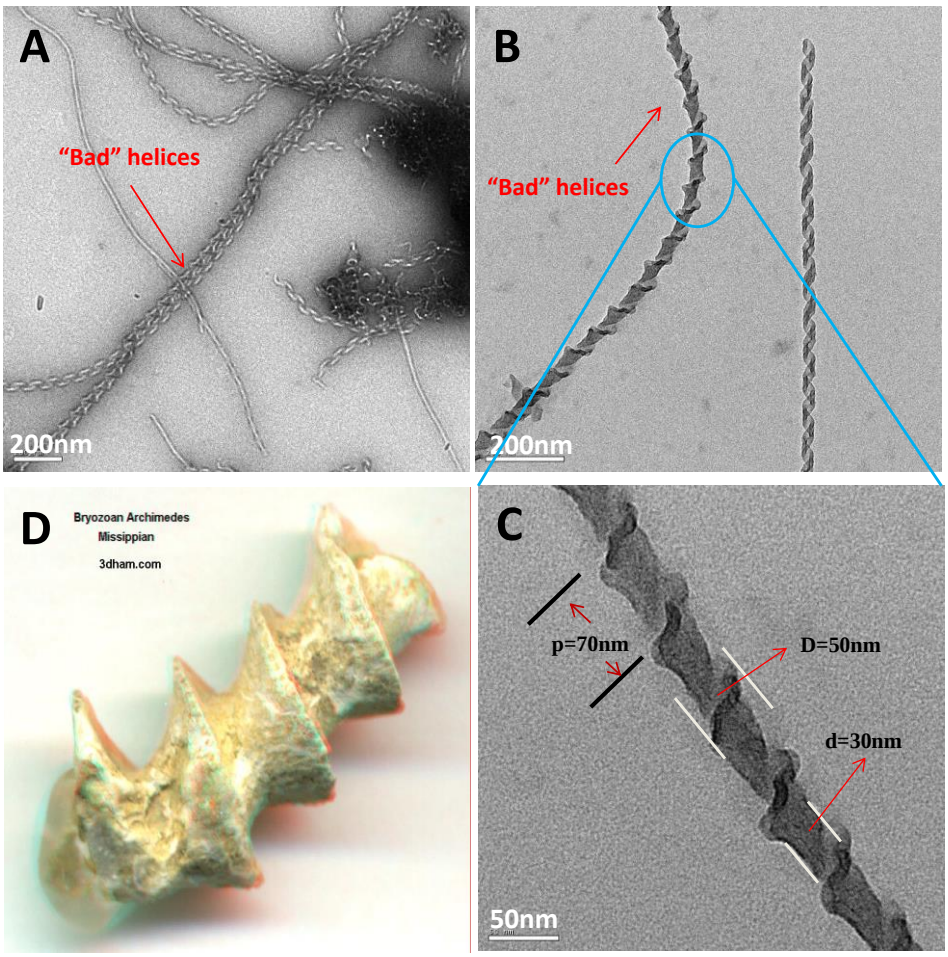

Figure 3.19- Typical TEM images of "Bad helices" formed by 18-2-18 Gemini tartrate. (A) Organic gel (B) silica replica of (A) after sol-gel transcripiton, (C) high maganification image of (B) and (D) is a Archimedes screw shape found in Mississippian.

3. Fabrication, fragmentation and functionalization of silica nanohelices

a) Quick silica transcriptions of organic Gemini tartrate to nanohelices

In this episode, optimization of the silica transcription from organic Gemini tartrate nanohelices is shown.[32, 34] Basically, 16-2-16 silica helical ribbons can be quickly produced from 2days aging instead of 21days aging of the organic gel, (and for twisted ribbons, 1-2 hours aging instead of 5 days aging of organic gel), followed by 7 hours pre-hydrolysis and 15 hours transcription at pH 3.8 instead of 12 hours pre-hydrolysis and 36 hours transcription at pH 6.0, where pH was adjusted by corresponding tartaric acid in order to ensure not to disturb the chiral environment at the organic nanohelices surface. Table 3.1 below shows the detailed information about the normal transcription at pH 6.0 and quick transcription at pH 3.8. When the transcription was completed, the mixture was thoroughly washed with isopropanol to remove the organic template and the potential byproducts.[1]

Table 3.1: The time required for obtaining 16-2-16 silica twisted and helical ribbons using TEOS prehydrolyzed at pH 6.0 and pH 3.8.

	prehydrolysis pH 6.0 for 12h		timing for overall process	prehydrolysis pH 3.8 for 7h		timing for overall process
	organic aging	Transcription time		organic aging	Transcription time	
helical ribbons	21d	1.5d	23d	1-3d	15h	2-4d
twisted ribbons	5d	1.5d	7d	1-2h	15h	1d

In the case of 18-2-18 or 20-2-20, the transcription procedure is affected by the slow kinetic aspects. As it was described previously[32] two major processes play important role during the transcription of Gemini tartrate: polycondensation of those pre-hydrolyzed TEOS on the surface of organics to freeze the overall structure; and ion exchange, in which counterion were replaced by pre-hydrolyzed TEOS alone with loss of chirality. The

competition between these two processes is the determining factor for the final morphology after the transcription. When the same sol-gel transcription is performed to the aggregates of 18-2-18/20-2-20 Gemini tartrate, with slow gelling kinetics, it often obtains some amount of "bad helices" in silica.

Therefore, studies on the amount of tartaric acid in pre-hydrolysis and transcription temperature were conducted systematically to investigate the relation between these parameters for the silica transcription of 18-2-18 and 20-2-20 organogels. Figure 3.20 below shows the silica nanohelices transcribed from 1mM 18-2-18 Gemini tartrate organic gels with 5 days incubation at 35 ℃. In Figure 3.20(A-C), with 0.1mM of corresponding tartaric acid used for pre-hydrolysis, it shows there is no significant difference for the transcription temperature at 20 ℃ and 35 ℃, but at 4 ℃, the polycondensation is not good. Afterwards, when the transcription temperature is fixed at room temperature with various concentrations of tartaric acid used for pre-hydrolysis; it shows that around 0.5mM of tartaric acid is better suitable for the case (Figure 3.20F). Here we assumed that when less tartaric acid is used for pre-hydrolysis (Figure 3.20D), the pre-hydrolyzed TEOS is not enough to make good polycondensation to have dense and homogenous silica nanohelices, however the concentration of pre-hydrolyzed TEOS should not be too high; otherwise it will unwind the organics and inevitably generate more deformed helices (Figure 3.20G).

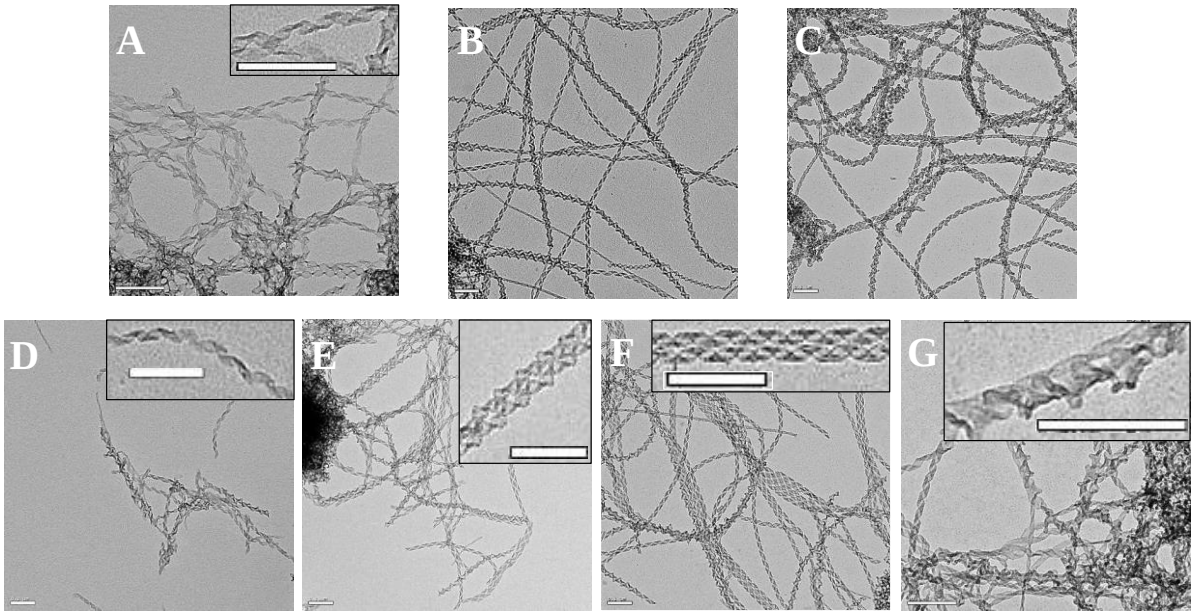

Figure 3.20- Study of temperature and concentration effect of tartaric acid on silica transcription of 18-2-18 Gemini tartrate: (A-C) transcription at 4 ℃, 20 ℃ and 35 ℃ with 0.1mM tartaric acid, respectively; and 0.1mM (D), 0.2mM (E), 0.5mM (F) and 1.0mM (G) of tartaric acid was used for silica transcription at 20 ℃. All the gels are incubated at 35 ℃ for 5days with a concentration of 1mM and the pH of organic gels is ~5.8. Inserts are magnified TEM images. All the scale bars = 200nm.

In the case of 20-2-20 Gemini, the transcription doesn't show too much difference between 20 ℃ and 55 ℃ (Figure 3.21(A-B)) and they all exhibit higher quantity of "bad helices" than 18-2-18 Gemini which is in line with expectation. The concentration effect of tartaric acid during pre-hydrolysis is investigated at 20 ℃ as well (Figure 3.21(C-F)), and this time less amount of tartaric acid during pre-hydrolysis is required to improve the yield of good helices (Figure 3.21C).

As shown here, delicate balance between a number of factors affect the rate of hydrolysis and condensation reactions, such as pH, temperature and time of reaction, reagent concentrations, catalyst nature and concentration, H_2O/Si molar ratio, aging temperature and time, and drying[42, 43] determines transcription procedure. The preliminary results shown here point out basic ideas of the effect of hydrocarbon chain length on the sol-gel interactions especially in transcriptions from chiral supramolecular assemblies. Moreover, the silica transcription of long chain Gemini tartrate do propose an interesting approach to rationally control the size of corresponding silica materials, which would provide an unique platform in nanotechnology and colloidal sciences.

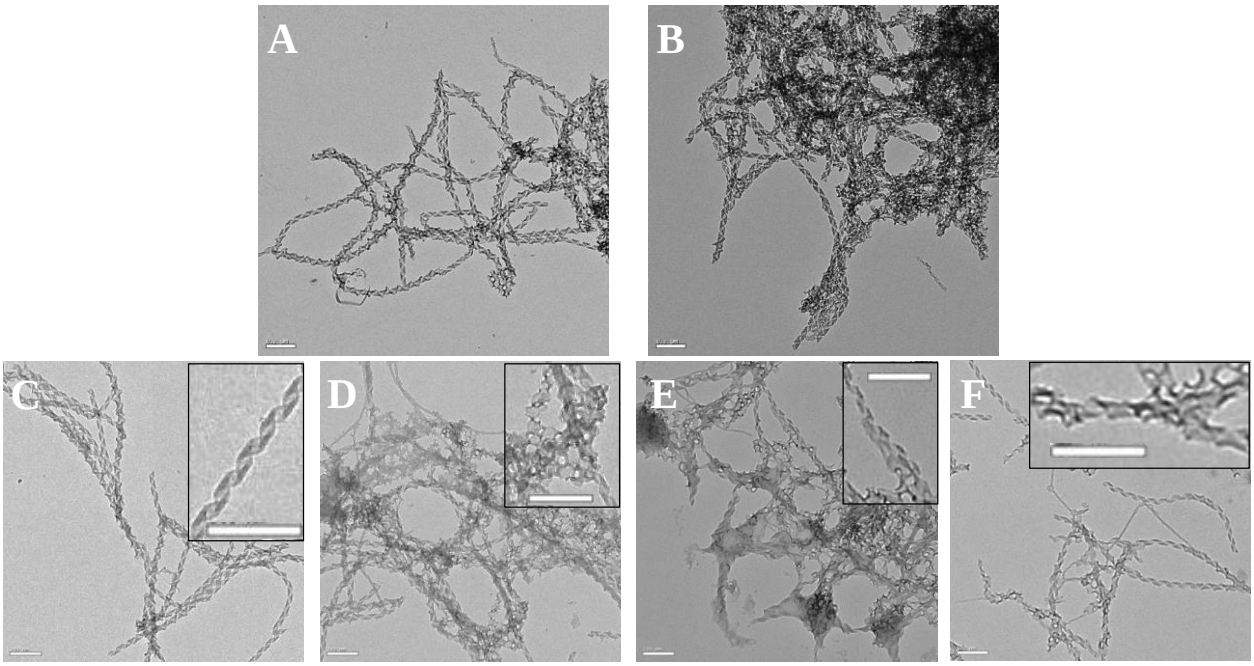

Figure 3.21- Study of temperature and concentration effect of tartaric acid on silica transcription of 20-2-20 Gemini tartrate: (A-B) transcription at 20 ℃ and 55 ℃ with 0.1mM tartaric acid, respectively; and 0.1mM (C), 0.2mM (D), 0.5mM (E) and 1.0mM (F) of tartaric acid was used for silica transcription at 20 ℃. All the gels are incubated at 55 ℃ for 7days with a concentration of 5mM. Inserts are magnified TEM images. All the scale bars = 200nm.

b) Cavitation effect and solvents on fragmentation efficiency

From previous discussion, silica helical nanoribbons can be easily obtained as illustrated in Figure 3.13. While the morphology of the final silica fibers is very well controlled in terms of diameter, pitches and handedness, these chiral fibers form knots and are entangled, resulting in a gel formation (Figure 3.22).

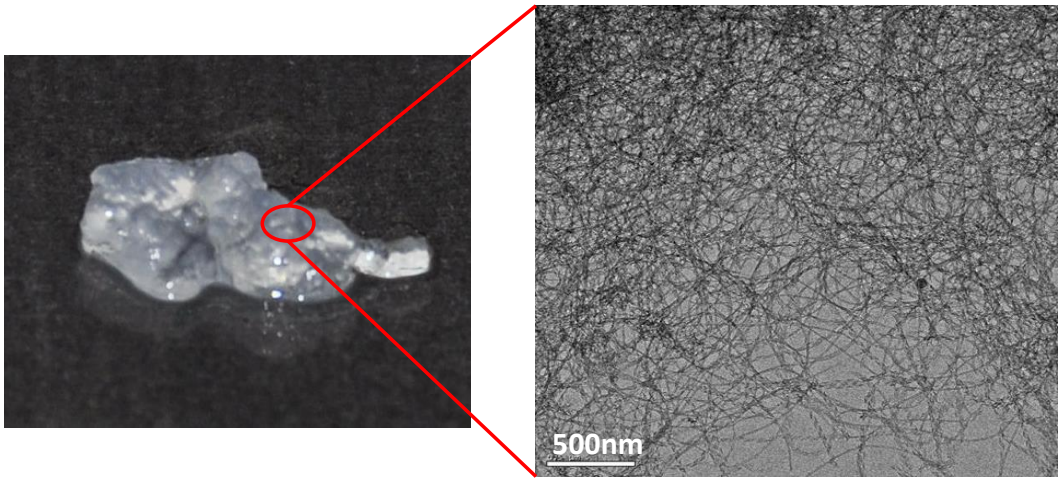

Figure 3.22- Typical entangled 3D network and macroscopically gel shape of silica nanohelices.

However, this causes problems for most of the potential applications which call for individualized chiral inorganic fibers. To achieve suspensions of such fibers, those fibers have to be disentangled and fragmented in a controlled way.

A number of reports have shown how carbon nanotubes can be fragmented and suspended in solution when submitted to a strong sonication. It was observed that the effect of sonication on the dispersion and de-bundling of the carbon nanotubes strongly depended on the physical properties of the solvent, including viscosity, surface tension, density, molecular weight and vapor pressure. These studies concerning the sonication effect on carbon nanotubes have shown that the nature of the solvent played an important role on their scission and dispersibility.[44] The high energy applied to the suspension during the sonication, induces the formation, growth, and collapse of bubbles which create a depression leading to the cavitation effect.[45, 46] While imploding, the bubble can produce a shock wave able to break or disentangle the silica structures. The efficiency of the cavitation process is then closely correlated to solvent parameters like vapor pressure, viscosity and surface tension. Moreover, the stabilization of the suspension is also directly linked to the nature of the solvents. Therefore, we performed a systematic study of the scission and stabilization of the silica nanohelices in various solvents. For this study, parameters such as the silica fibers concentration (1 mg/mL), the volume (2 mL), sonication time (15 min.) and power (130W) were fixed and only the solvents in which the helices were sonicated were varied from ethanol

by centrifugation and re-dispersion. We will refer to this method as "wet method", since the silica ribbons remain in solvents. Figure 3.23 shows the images of twisted nano-ribbons after sonication in solvents which are miscible with water (ethanol, dimethylsulfoxide (DMSO), dimethylformamide (DMF), acetonitrile, pyridine,) and others which are not miscible with water (hexane and toluene).

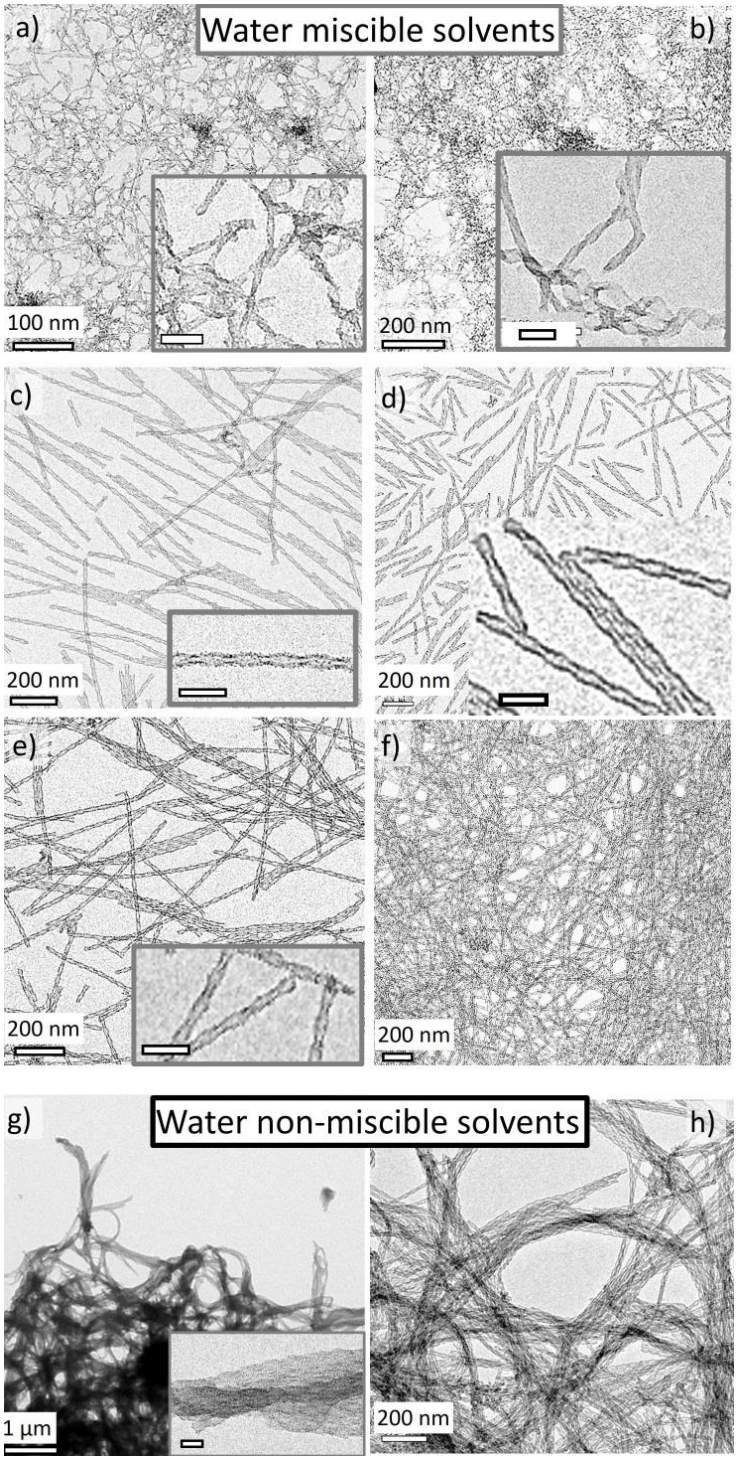

References – page 118

Figure 3.23- TEM images of silica twisted ribbons submitted to sonication in various solvents, a) water, and water miscible solvents such as b) ethanol, c) DMSO, d) DMF, e) pyridine, f) acetonitrile and water non-miscible solvent such as g) hexane and h) toluene. Bars in inserts: 50 nm.

The analysis of the TEM pictures shows that the nature of the solvent plays indeed a crucial role in the sonication process. In water (Figure 3.23a), the silica fibers are not fragmented or disentangled, but rather the high energy delivered when the cavitation bubbles implode induces the damage of the fine structure of the helical and twisted ribbons as it is observed in the higher resolution image (Figure 3.23a, insert). The damage is less pronounced in ethanol but a strong aggregation is still observed (Figure 3.23b). On the other hand, in other solvents such as DMSO, DMF or pyridine (Figure 3.23c-e) or in TFE (see Figure 3.24), much more clearly fragmented silica fibers with well-preserved chiral fine structure are dispersed in suspension. Interestingly, the fibers were relatively well disentangled in acetonitrile (decreased density of knots) but not fragmented (Figure 3.23f). This is probably due to the low viscosity of acetonitrile as it will be developed later in this article. In solvents which are not miscible with water such as hexane or toluene, silica fibers form aggregates with close-packed bundles. With this method, based on centrifugation and re-dispersion, there are still water molecules adsorbed on the silica surface which cannot be totally removed. This water layer seems to act as a glue between the fibers leading to the oriented aggregation in bundles.

c) Sonication power effects on length distribution and dispersion

We then evaluated the effect of sonication power, at fixed silica fibers concentration (1 mg/mL), the volume (2 mL) and sonication time (15 min.). For this study, trifluoroethanol (TFE) was chosen as the solvent in which nanoribbons were sonicated because it was identified as one of the best solvents in the previous section. The sonication power was varied from 0% to 100% of the maximum power (130 Watt). The size distribution of silica nanohelices submitted to various sonication powers was analyzed by transmission electron microscopy (TEM) as shown in Figure 3.24. The low magnification TEM pictures (Figure

3.24b and c inserts) show that at 26 Watt, the helices are still strongly aggregated whereas at 130 Watt, the helices are well dispersed and no aggregation is observed. At a higher magnification, we see that the helices are much shorter at 130Watt than at 26 Watt while preserving the well-defined helical morphology (Figure 3.24b-c). This indicates that in TFE it is possible to induce a scission of the silica helices and to disperse them in solvent without damaging the chiral structure.

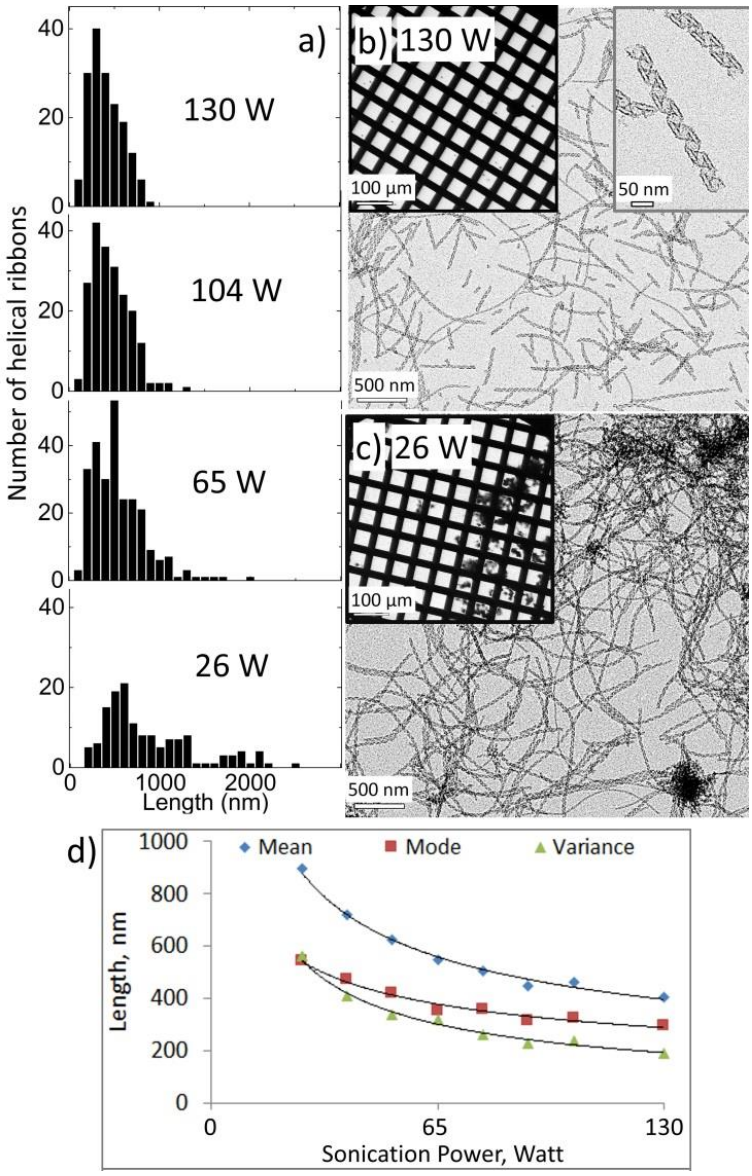

Figure 3.24- a) Size distribution of more than 150 helical ribbons sonicated in TFE as a function of the power of the sonication. TEM images of helices after the sonication at b) 130 Watt, and c) 26 Watt. Inserts are the low magnification images and another insert at high magnification for 130 Watt. d) The distribution of helices length is fitted with a lognormal law and analyzed by Kolmagorov-Smirnov algorithm showing the decrease in the Mean, Mode and Variance values with increasing sonication power.

To quantify this effect we measured the silica helices length as a function of the sonication power. Only the dispersed helices were taken into account as it is not possible to measure the length of the entangled ones. The length of more than 150 helices were measured for each sonication sample to obtain a length distribution with a sufficient precision (Figure 3.24a). We can clearly see that the higher the sonication power, the lower the maximum length, narrower the length distribution and lower the mode value (most frequent value) of the distribution of the resulting helices. At 26 Watt, we observed helices with the length ranging from 200 to 2500 nm whereas at 65 Watt, most of the helices were shorter than 1100 nm. At 104 Watt, most of the helices had lengths between 200 and 800 nm with the most frequently observed length of 400 nm. For 130 Watt, all the measured helices were shorter than 1000 nm whereas their overall length distribution was similar to the one observed for 104 Watt. The data were treated by Kolmagorov-Smirnov algorithm using a log normal distribution, and a clear decrease in the Mean, Mode and Variance values with increasing sonication power was observed (Figure 3.24d). The variance decreases from more than 500 nm for the helices submitted to 26 Watt sonication to less than 200 nm for those which were submitted to 130 Watt sonication. The mode value was also decreased from 900 nm to 400 nm respectively.

These results show that the sonication power is very important for disentanglement, fragmentation and suspension of silica fibers in solvents. The higher the sonication power, the lower is the polydispersity of the resulting fibers. In terms of morphologies and sizes of the helices, such as helical pitches and ribbon widths, they do not show notable variation before and after the fragmentation. When combined with the results of solvent variation in the previous section, it is interesting to note that the effect of sonication is observed either with the length (fragmentation) while their shapes are not affected or with their shapes destroyed while the length do not change.

d) Effect of drying and pH on dispersion of silica nanohelices

With the increasing demand for the integration of Green Chemistry, the production of

materials with limited use of hazardous substances, more benign to the environment has become one of the priorities. In this context, water, being environmentally sustainable, is an attractive alternative to organic solvents. Meanwhile, as shown above, the direct fragmentation of silica helices in water does not work well, since the cavitation effect in water drastically damages the chiral structures. In order to make them more robust against the cavitation effect during the sonication in water, we have developed a procedure called "dry method" as opposed to the previous wet one, including a freeze drying pre-treatment, in order to obtain silica walls with more consolidated structures. Freeze drying reinforces the silica wall as it induces the dehydration and reorganization of the silica and leads to more dense structures,[31] without causing the collapse of the network. Concretely, the silica helical and twisted nano-ribbons are washed thoroughly with ethanol just after the synthesis to remove the unreacted TEOS and organic templates, then washed with water and freeze-dried. The white powder obtained can then be dispersed in different solvents and treated by sonication. The sonication of the suspension in water resulted in fragmented silica helices which are well calibrated in length with a well preserved structure (Figure 3.25). The local chiral structures of helices obtained with this method were well conserved regardless of the solvents, compared to the "wet method" with which helices were destroyed after sonication in some of the solvents such as water or ethanol. This process also shows the advantage over the "wet method" because it allows easy quantification of silica before dispersing them in the solvent by weighing the powder when dry.

As also observed for the "wet method", the dispersibility of these dried helices also depended strongly on the nature of the solvents. In some solvents, they were well dispersed and the suspension was transparent whereas in others, they were strongly aggregated which led to precipitation. The "good" solvents were mostly the same as they were for "wet method", i.e. DMSO, Pyridine, DMF and TFE. An important difference was observed in between the two methods for water and ethanol. With the "wet method", the helices were deformed and aggregated in ethanol whereas with the "dry method", a good dispersion of helices with preserved morphology (helical or twisted ribbons) could be obtained. The aggregation

fraction (AF) as calculated and described in the experimental section was plotted as a function of solvent parameters such as viscosity, density, molecular weight and dielectric constants for all the solvents studied. The results on AF show a good agreement with previous report by Cheng et al.[44] on single wall carbon nanotube (SWNT); i.e. the aggregation fraction decreases with increasing viscosity, density, as well as molecular weight, suggesting the mechanisms of scission of both fibers are similar as reported for SWNT. As they have described, it can be suggested that it requires higher force and sonication intensity to create cavitation in more viscous liquid, once the cavitation bubbles are created, the temperature and pressure effect resulting from the bubbles collapse will be greater, thus more efficient fragmentation of the helices

In water non-miscible solvents such as hexane or toluene, silica fibers were totally aggregated as expected from their lipophobic and hydrophilic nature and strong hydrogen bonds which reinforce the cohesion between the silica surfaces in these solvents.

Attempts of dispersion in MQ water at pH 5.5 (typical pH when silica helices are dispersed in MQ water after solvent exchange) led to a strong aggregation. It however reveals to be strongly dependent on the pH of water. Indeed, because the silica surface charge varies with the pH, the dispersion of the silica colloids is strongly modified accordingly, i.e. the decrease of the pH induces protonation of the negatively charged surface oxygen and their conversion to OH. As a consequence, there is a strong decrease of the overall surface charge and an increase of affinity of the helices with their neighbors due to the hydrogen bonding, leading to their aggregation.

To evaluate the dispersibility of silica helices in water, we adjusted the pH to different values from 5.5 to 9 with sodium hydroxide 0.1N solution, and proceeded to the sonication at 130 Watt, for 15 min (Figure 3.25).

References – page 118

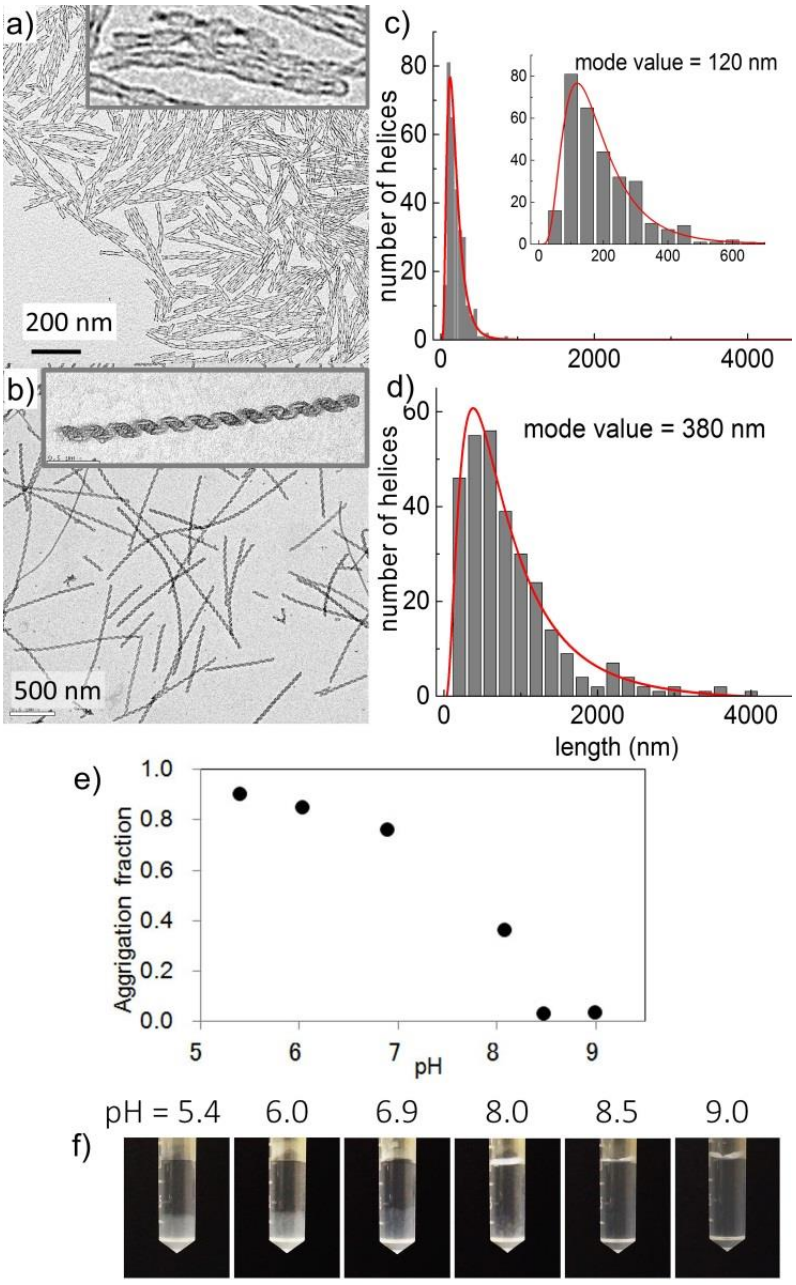

Figure 3.25- a) Twisted and b) helical ribbons made by dry method and redispersed in water at pH 8.5 with concentration of 5 mg/mL for twisted ribbons and 1.25 mg/mL for helical ones. The morphologies of the ribbons are well preserved and they are fully dispersed without aggregation. Size distribution of c) twisted and d) helical ribbons made by the dry method (on more than 200 helices). e) Aggregation fraction (AF) of the sonicated twisted ribbons in water as a function of pH. f) Silica helices dispersed in water with various pHs.

As it is well illustrated in Figure 3.25 a), b), e) and f) no aggregation is observed for pH higher than 8 after the sonication. The negative charge of the silica surface in this pH range stabilizes the colloidal suspension by electrostatic repulsions. For pH below 8, the helices

show strong aggregation. Again, the optimization of the choice of the parameters is of great importance. We observed that the optimal concentration of the twisted ribbons for the sonication process is 5 mg/mL whereas for the helical ribbons, the best results were obtained for 1.25 mg/mL. For higher concentration of helical ribbons, the helices are indeed very short but some of them are broken into small pieces which induce aggregation. The size distribution of both twisted and helical ribbons cut in the optimal conditions were analyzed and shown in Figures 3.25 c) and d). The results obtained with the helical ribbons are similar to those obtained with the wet method as the diagram shows a mode value of 380 nm and a long tail showing that some helices remain very long (variance is 880 nm). On the contrary, the sonication of the twisted ribbons induces short ribbons as the mode value is 120 nm, and mainly the length shows a real monodispersity with a variance of 68 nm. This monodispersity is crucial for potential application and above all for the hierarchical organization of the fibers as alignment or compact stacking.

In summary, we demonstrated that the sonication method inspired by the report on the carbon nanotubes can be extended to inorganic meal oxide structures such as silica fiber systems to disentangle, fragment them and get helical and twisted silica ribbons with well conserved nanometric morphologies of several hundreds of nanometers in length. We have shown that the power of sonication is an important parameter: for a maximum power of 130W, the higher the power of the sonication, the narrower the distribution of the fragmented helices, and the better the dispersion. The nature of the solvent is also crucial parameter. Solvents with high viscosity, high molecular weight, high density, and low dielectric constant such as TFE, DMSO, pyridine or DMF turned out to be the best ones for obtaining good dispersion of well fragmented helices with retained chiral morphology. The good agreement between these results with the previous report on carbon nanotubes indicates that this approach reported on SWNTs can be extended to metal oxide nanostructures, that the mechanism of fragmentation and dispersion of the nanoobjects follows the similar rule, the debundling and scission result from the cavitation collapse which is more efficient in viscous liquid than in less viscous liquid.

Freeze drying of the helices clearly consolidated the Si-O-Si bonds. The sonication of helices in water or in ethanol directly after the transcription destroyed the local chiral structures whereas the helices which were freeze dried first and only then dispersed in these solvents preserved their local chiral structure after sonication. In the case of water, the pH has a crucial effect on the dispersibility, and homogeneous dispersions of helices were obtained only for pH above 8. The application of sonication on the nanometric chiral fibrous structures, for which the local structures are consolidated by freeze drying, showed homogeneous colloidal suspension of individualized and size-controlled chiral nanometric silica fibers. This study describes for the first time scaled up synthesis and formation of stable chiral colloidal homogenous suspensions, based on self-organized chiral elongated structures, extremely promising for numerous applications.

*Study on the fragmentation of silica nanohelices was performed in collaboration with **Dr. Makoto Takafuji** and **Dr. Hirotaka Ihara** from Kumamoto University, Kumamoto, Japan.*

An article was published on the results of fragmentation of silica nanohelices:

Yutaka Okazaki, Jiaji Cheng, Dmytro Dedovets, Gregor Kemper, Marie-Helene Delville, Marie-Christine Durrieu, Hirotaka Ihara, Makoto Takafuji, Emilie Pouget, and Reiko Oda *Chiral Colloids: Homogeneous Suspension of Individualized SiO2 Helical and Twisted Nanoribbons.* Acs Nano, 2014. 8(7): p. 6863-6872

e) Evaluation on surface functionalization of silica nanohelices

The individualized and fragmented silica nanohelices with controlled size as described above could be further surface functionalized. Here, we describe in particular the functionalization with silane coupling agent—(3-Aminopropyl) triethoxysilane (APTES) to obtain the amine groups on the silica surface.[47] Zeta-potential measurement and X-ray photoelectron spectroscopy (XPS) analysis were employed to estimate the amount of amine

immobilized on the silica surface and their effect on adsorption by affecting surface charge density.

The existence of amine groups is confirmed in XPS by the presence of N1s peak with a binding energy at 399.8eV which is consistent with the great variation of ζ value from -15mV to +30mV before and after amine modification with pH around 5.0, suggesting a highly positively charged surface can be achieved after surface modification procedure. (Figure 3.26)

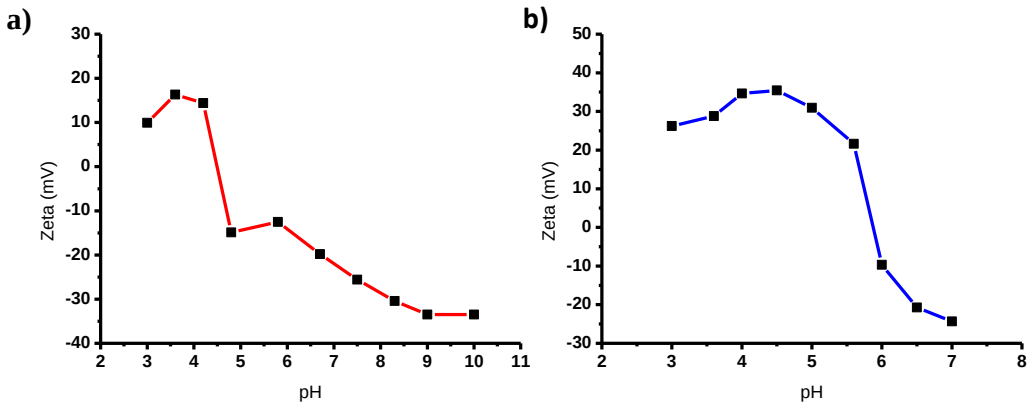

Figure 3.26- ζ potential study on surface charge density of silica nanohelices. (a) and (b), plots of the ζ potential measurements of silica helical ribbons before and after APTES functionalization, respectively.

However, to precisely quantify the effective amount of amine sites which are immobilized on the silica surface is difficult as the modification procedure neither leads to perfectly homogenous nor forms monolayer, then the amorphous three-dimensional structure of silica nanohelices renders it even harder to calculate the geometric properties of the nanohelices and the concentration of silica colloidal solutions in standard unit like molarity due to lack of applicable molar mass of silica nanohelices. Therefore, we used XPS measurement here in order to estimate the amount of amine groups in a given area. Basically, the structure of an amine functionalized silica nanohelices would be viewed as Figure 3.27 below:

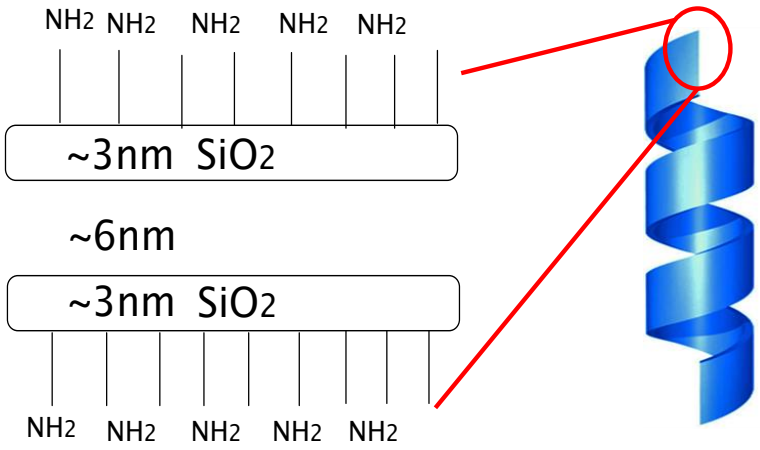

Figure 3.28- Schematic cross-section view of amine functionalized silica surface.

The thickness of the silica layer is around 3nm-5nm on both sides of the free space which was used to be occupied by the organic templates that has around 6nm thickness as is shown in Figure 3.27, meaning it can be studied by XPS which has a depth of penetration for ~10nm. In a typical area, if we assume that silica nanohelices has the same density as amorphous SiO_2 and from XPS analysis, the ratio between N to Si is known as $N_N : N_{Si} = 3.62 : 13.84$ in a typical measurement, the amount of amine groups can be estimated as: 17.2 to 28.7 amine groups per nm^2 depending on the thickness of the silica layers (3- 5nm). The relation between the amount of amine groups and the ratio of N to Si in a certain surface area can be expressed as below:

$$N_{NH_2} = \frac{d\,\rho_{SiO_2} N_A}{M_{SiO_2}} \times \frac{N_N}{N_{Si}}$$

Wherein $N_N : N_{Si}$ is the atomic ratio between N and Si measured by XPS. ρ_{SiO_2} is the density of amorphous SiO_2 (2.196 g/cm^3). d is the thickness of silica surface (in nm); M_{SiO_2} is the molecular weight of silicon dioxide (60.08 g /mol); N_A is Avogadro constant.

From this calculation, the amount of amine groups on the surface of silica is presented, however, the real value concerns the effective site of amine is still unclear. But, if we accept H-S Jung's estimation that around one fifth[48] of the amine groups would be effective amine sites on a glass surface, the estimated amount of effective amine sites in our case will be

around 3.4 to 5.7 amine groups per nm^2, which is actually higher than APTMS (0.44 amine groups per nm^2) and DETAS (1.3 amine groups per nm^2) modification presented in H-S Jung's work but still reasonable as a normal functionalization procedure on a silica substrate.[48, 49]

Conclusion

In this chapter, morphology control of organic nanohelices was done by elongating the hydrophobic chain length from 16 to 18 and 20 alkyl carbons. With longer carbon chain, the geometrical parameters such as diameters and pith length of the nanohelices would be increased while the helix formation kinetics is dramatically slowed down. To accelerate the gelation speed and transition rate for the helical structures, study on the concentration and incubation temperature effects was conducted and proved to be an effective way to obtain size controlled organic nanohelices.

The realization of fragmentation of silica nanohelices was accomplished by applying tip sonication to the silica suspensions with various parameters such as sonication power, pH and the solvents. The extent of dispersibility and fragmentation was quantified by aggregation fraction, which demonstrated the disentanglement of silica nanohelices. Finally, individualized and size-controlled silica nanohelices were prepared for further usage via surface functionalization with amine. The fulfillment of fabrication of such inorganic fibers in a controlled way will definitely broaden the scope of sol-gel chemistry and potential applications in hybrid materials and nanotechnology.

References – page 118

Experimental session

Gemini tartrate:

The synthesis of Gemini tartrate with different chain length was basically the same. Take 16-2-16 tartrate as a sample, the procedure for bromide to tartrate ion exchange for the synthesis was optimized from the procedure described previously to achieve exact stoichiometry.[50-52] First, 16-2-16Br was synthesized according to the procedure developed by R. Zana *et al*.,[53-56] by alkylation of tetramethylethylenediamine (TMEDA) with 1-bromohexadecane in acetonitrile.

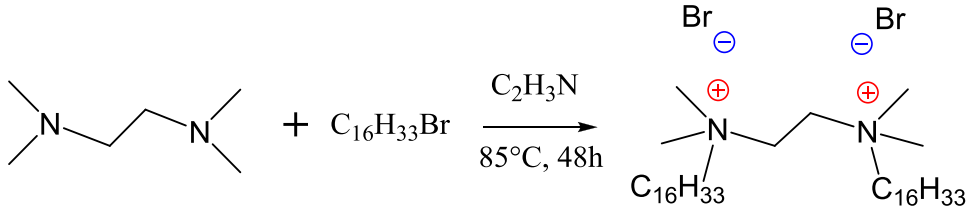

In typical synthesis 1 mL of TMEDA (1 eq.) was mixed with 16.5 mL of 1-bromohexadecane (3 eq.) in 50mL of acetonitrile in 250 mL round-bottom flask. Alkyl bromide was taken in excess in order to eliminate formation of monoalkylated by-product. Reaction was carried out for 48 hours under the reflux at 85 ℃ with continuous intensive stirring at 400rpm. Then reaction mixture was cooled down to the room temperature and stored in a fridge at 1 ℃ for 1 hour. White precipitate of Gemini bromide was formed on the bottom of the flask.

Product was filtered and purified by crystallization from acetonitrile in a follow manner. Powder was deposited in a 250 mL round bottom flask together with small quantity of acetonitrile and heated to 70 ℃ under continuous stirring. Acetonitrile was added with small portions until complete dissolution of Gemini Bromide. Then stirring and heating was stopped and solution was let to cool down to room temperature. Small white needle-like crystals of 16-2-16Br were formed within one hour. They were filtered, rinsed with acetone and dried under the vacuum.

References – page 118

Absence of start material and monoalkylated by-product in final product was proved by NMR analysis.

Typical example of 16-2-16Br ^{1}H NMR (300MHz, MeOD, 25°C, δ ppm, TMS): 4.04 (4H, s), 3.49 (4H, m), 3.27 (12H, s), 1.85 (4H, s), 1.29 (52H, m), 0.90 (6H, t, ^{3}J = 6.71)

^{13}C NMR (75MHz, MeOD, 25°C, δ ppm, TMS): 66.94, 57.10, 33.12, 30.84, 30.81, 30.72, 30.65, 30.52, 30.35, 27.34, 23.78, 14.48

Then, 16-2-16 acetate was synthesized from 16-2-16Br by ion exchange reaction with silver acetate as previously reported.[57] 16-2-16Ac was synthesized from 16-2-16Br by ion exchange reaction with silver acetate.

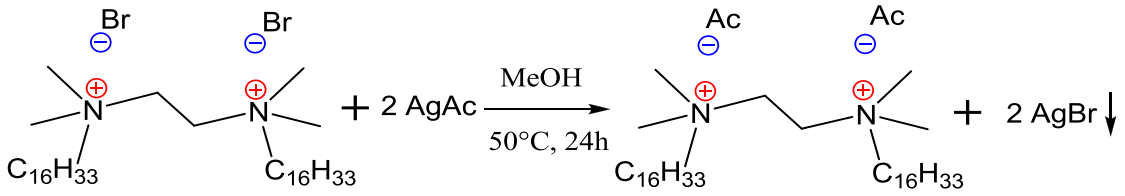

In a typical synthesis, 2g of 16-2-16Br (1 eq.) and 1.37g of silver acetate (3 eq.) were mixed in 250mL round-bottom flask with 50 mL of MeOH. Flask was covered with aluminium foil and reaction mixture was stirred at 50 ℃ for 24 hours. Then suspension was filtered on Celite to remove formed precipitate of silver bromide and unreacted silver acetate. Transparent solution was obtained after filtration. MeOH was evaporated on Rotary evaporator; product was dissolved in as small as possible amount of MeOH at 60 ℃ and precipitated by addition of ~100 mL of acetone. Fine white powder of Gemini acetate was formed. If presence of residual silver compounds was observed: formation of black particles of grey colour of final product then powder was dissolved in MeOH and filtered on Celite one more time. Finally, 16-2-16Ac was filtered, rinsed with acetone and dried under the vacuum.

Typical example of 16-2-16Ac ^{1}H NMR (300MHz, MeOD, 25°C, δ ppm, TMS):3.92 (4H, s), 3.42 (4H, m), 3.21 (12H, s), 1.90 (6H, s), 1.84 (4H, m), 1.29 (52H, m), 0.90 (6H, t, ^{3}J = 6.72Hz)

^{13}C NMR (75MHz, MeOD, 25°C, δ ppm, TMS): 65.48, 55.54, 50.35, 31.70, 29.41, 29.39, 29.36, 29.30, 29.24, 29.10, 28.95, 25.96, 23.03, 22.36, 22.30, 13.07

Finally, the acetate was replaced with tartrate by mixing the solution of 16-2-16 acetate in with the solution of 2 eq. of corresponding tartaric acid. Both L- and D- Gemini tartrates were synthesized in a similar way. Procedure is based on the difference in a solubility of 16-2-16Ac and 16-2-16Tartrate in a MeOH/Acetone mixture.

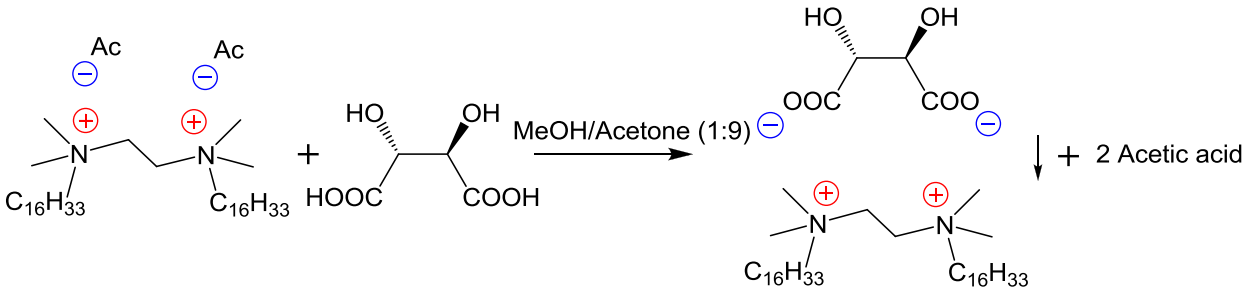

Typically, 16-2-16Ac was dissolved in MeOH/Acetone (1:9) mixture (10 mL for each 100mg of Gemini acetate) and the same amount of MeOH/Acetone mixture was used for dissolution of 2 eq. of corresponding tartaric acid. Tartaric acid solution was added drop wise to the 16-2-16Ac under stirring – white precipitate of 16-2-16Tartrate comes out. It was filtered and washed with several portions of acetone.

In order to obtain product with tartrate to Gemini ratio of 1 to 1 excess of tartaric acid was washed out in a follow way. Powder of 16-2-16 tartrate was dispersed in MilliQ water precooled to 1 ℃ (10 mL for each 100mg of starting Gemini acetate). Cooling is used to avoid solubilization and gelification of 16-2-16Tartrate. Suspension was sonicated for 5 minutes and centrifuged for 5 min at 4000 rpm (3076 g), 4 ℃ in swing out rotor. Supernatant was replaced with another portion of cold MilliQ water and procedure was repeated for 5 times. In the same way powder was washed 3 times with acetone and dried under the vacuum.

This method of synthesis was preferred over the one based on the reaction of 16-2-16Br with silver carbonate and tartaric acid because its allow obtaining 16-2-16 Tartrate with the lower residual 16-2-16Br content.

^{1}H NMR was carried out in MeOD to verify Tartrate (2H singlet at 4.28 ppm) to Gemini ratio and absence of acetate peak (6H singlet at 1.89 ppm).

Typical example of 16-2-16 Tartrate ^{1}H NMR (300MHz, MeOD, 25°C, δ ppm, TMS): 4.28 (2H, s), 3.90 (4H, s), 3.40 (4H, m), 3.19 (12H, s), 1.80 (4H, s), 1.28 (52H, m), 0.89 (6H, t, ^{3}J = 6.63Hz)

With the similar synthetic method as stated above, 18-2-18 and 20-2-20 tartrate can be also prepared by using corresponding bromide compounds in the beginning.

Organic gels:

Different concentration of Gemini tartrates are solubilized in MilliQ water (typically, 3.58 mg of 16-2-16, 3.87 mg of 18-2-18, and 4.17 mg of 20-2-20 L-tartrate powder are dissolved into 5 mL of MilliQ water, for a concentration of 1 mM tartrate, respectively), and next, the solutions of Gemini tartrate were heated up above the Krafft temperature for 15min, typically 60 ℃ for 16-2-16 and 18-2-18 tartrate while 70 ℃ for 20-2-20 tartrate, and then incubated at various temperature with adequate time as required. The morphology of self-assemblies was monitored with Transmission Electron Microscopy (TEM).

Inorganic transcription:

Once adequate ageing time of the gels is reached, these organic gels are used as templates to prepare silica nanostructures through a sol-gel transcription procedure. Basically, 500 µL of TEOS was added to the 10 mL of 0.1 mM aqueous solution of L-tartaric acid (pH 3.8) and pre-hydrolyzed at 20 ℃ by stirring on the roller-mixer for 7h. In parallel, a solution of 0.1 mM 16-2-16 Gemini surfactant with L-tartrate counterion is aged between 2 hours to 2 days for the formation of twisted or helical nano-ribbons respectively. Equal volumes of pre-hydrolyzed TEOS in 0.1 mM aqueous solution of L-tartaric acid and organic gels are mixed (typically, 2

mL of each) and stirred at 20 ℃ with a roller-mixer overnight. Once the transcription is completed, the mixture is washed thoroughly with isopropanol, in order to solubilize the organic byproducts and eliminate the excess of TEOS (washing 4 times with isopropanol by centrifugation (5 min., 2,000 G) and re-dispersing in isopropanol). Finally, the suspension of silica fibers is stored in isopropanol. On the other hand, similar method can be also applied to 18-2-18 and 20-2-20 tartrate with slightly modification. In order to study the effects of concentration, pH for pre-hydrolysis and incubation temperature on silica transcription, different concentration of Gemini tartrate, typically 1mM, 5mM and 10mM, are employed with different incubation temperature. Moreover, the pH effect on pre-hydrolysis of TEOS can be investigated by using 10 mL of 0.1 mM, 0.2 mM, 0.5 mM and 1.0 mM aqueous solutions of L-tartaric acid, respectively.

Sonication:

A high intensity ultrasonic processor "Vibra cell 75186" equipped with 6 mm microtip with variable power was used (maximum power, 130 W). A 20 kHz pulse mode was used for the dispersion and fragmentation of silica nano-helices and twisted nano-ribbons. For the study of the effect of the sonication power and nature of the solvent on the efficiency of scission and dispersion of the silica nano-objects with the wet method, the rest of the experimental parameters were kept constant: sample concentration (1 mg/mL), volume (2 mL), sonication time (15 min. with pulses of 1s separated by 1s pauses. Samples were cooled in an ice bath during the sonication process in order to avoid solvent evaporation and rising of the sample temperature which could influence the sonication effect. Two groups of solvents were used in this study: 1- v0020water miscible solvents: water, ethanol, trifluoroethanol (TFE), dimethyl sulfoxide (DMSO), N,N-dimethylformamide (DMF), acetonitrile, pyridine; 2- water immiscible solvents: hexane, and toluene. Sonication after freeze drying pre-treatment "dry method": The silica helices dispersion in ethanol was washed 4 times with MilliQ water using the centrifugation. The residue was freeze dried for 1 day to give a white powder you should give the exact conditions (temperature and vacuum) because they influence on the final result of

consolidation). 2 mL of MilliQ water was added to the x mg of the silica powder (x = 10 for twisted ribbons and 2.5 for helical ribbons), and this mixture was sonicated for 15 min. in the ice bath. The pH of this mixture was adjusted with a0.1 N-NaOH aq. w, and it was sonicated for another 15 min. in the ice bath.

Amine functionalization of fragmented silica nanohelices:

After fragmentation, the silica-nanohelices were then functionalized via a surface chemical modification with (3-aminopropyl) triethoxysilane (APTES).[34] Generally, 25 μmol of APTES were added to per 0.5 mg of short silica-nanohelices. The reaction mixture was submitted to ultrasonication for 5 minutes and then kept in oil bath overnight at 80 ˚C followed by three times precipitation with isopropanol. This modification procedure can be repeated one time to coat the surface of silica with more amine. As a result, approximately 0.8mg/mL amine modified silica nanohelices can be obtained.

The amount of APTES used was estimated as below.

In order to calculate the surface area of silica-nanohelices (*S*), density was assumed 1 in 5 mM of organic gels. *S* was calculated by:

$$l = V / \pi(R^2 - r^2), \text{with } R = 15\times10^{-7} cm,\ r = 10\times10^{-7} cm,\ V = 1.8\times10^{-3} cm^3$$

$$l = 4.60\times10^{6} m$$

$$S = 2\pi(R + r)l$$

$$S = 0.72 m^2$$

Generally, silane coupling agent was induced at least $15\mu mol / m^2$.

$$V_{APTES} = 15S \times M_{APTES}, (d_{APTES} \cong 1)$$

$$V_{APTES} = 2.4\mu L$$

Aggregation fraction:

1 mL of the pH adjusted-mixture (conc.: 5 mg/mL for twisted ribbons) was separated into precipitate part and supernatant part by centrifugation at 1000 rpm (192 G) for 2 min. and the

supernatant was removed. Then the pellet and the supernatant were freeze-dried. Weights of the supernatant ($W_{supernatant}$) and the precipitate ($W_{precipitate}$) were measured and the aggregation fractions were calculated according to eq (1).

$$\text{Aggregation Fraction} = \frac{\text{Aggregation part}}{\text{Total weight}} = \frac{W_{precipitate}}{W_{precipitate}+W_{supernatant}} \quad (1)$$

Characterization of silica nanohelices:

After each step of the synthesis, samples were characterized by Transmission Electron Microscopy (TEM). 400-mesh carbon-coated copper grids were used for the TEM. For the observation of the samples prepared in water hydrophilic grids were prepared. For this carbon-coated copper grids were treated in BioForce Nanosciences UV/Ozone ProCleaner 220 for 10 minutes. For the sample preparation, 5 μL of the silica suspension were drop-casted onto the grid and blotted after 1 minute. Samples were dried in air.

TEM observations were performed using a Philips EM 120 electron microscope operating at 120 kV and the images were collected by 2k × 2k Gatan ssCCD camera.

Zeta-potential measurement was done in a Wallis- ζ meter with a pH mode at 25 ℃. All the sample solutions are adjusted to reach proper scattering intensity (I_0~1000Kcp).

The measurement of the ribbon length was done with the ImageJ software and the analysis of the length distribution was performed using a log-normal low and confirmed with the Kolmagorov-Smirnov algorithm. From the histograms of the silica fiber length after the sonication we assumed log-normal distribution of this value. If some value X is log-normally distributed, then Y=ln(X) has a normal distribution. Therefore we calculated natural logarithm of the silica fiber lengths and subjected obtained data to the normality test using Kolmagorov-Smirnov algorithm in OriginPro 9 software. With the significance level of 0.05, the test confirms the normal distribution of the natural logarithm of the silica fiber lengths and so the log-normal distribution of the lengths themselves. Mean value (μ) and Standard deviation (σ) of normal distribution were obtained as parameters from the normality test. These parameters were used to calculate the Mean and Mode values as well as Variation of the silica

fibers length distribution (log-normal) according to the follow equations:

$$\text{Mode} = e^{\mu-\sigma^2}$$

$$\text{Mean} = e^{\mu+\sigma^2/2}$$

$$\text{Variance} = \left(e^{\sigma^2}-1\right)e^{2\mu+\sigma^2}$$

Typically the square root of the Variance is used to describe how far a set of values is spread out. Method described above was applied to the data obtained for various sonication powers. The values of Mode, Mean and square root of Variance showed power-law dependence on the sonication power.

Reference

1. Dedovets, D., *Cationic gemini amphiphiles: from chiral organic self-assembly towards functional composite micro-and nanomaterials*, 2014, Université de Bordeaux.
2. Che, S., et al., *Synthesis and characterization of chiral mesoporous silica.* Nature, 2004. **429**(6989): p. 281-284.
3. Ohsuna, T., et al., *Characterization of chiral mesoporous materials by transmission electron microscopy.* Small, 2005. **1**(2): p. 233-237.
4. Wu, X., et al., *Racemic helical mesoporous silica formation by achiral anionic surfactant.* Chemistry of Materials, 2006. **18**(2): p. 241-243.
5. Wang, B., et al., *Chiral Mesostructured Silica Nanofibers of MCM‐41.* Angewandte Chemie, 2006. **118**(13): p. 2142-2144.
6. Yang, S., et al., *On the origin of helical mesostructures.* Journal of the American Chemical Society, 2006. **128**(32): p. 10460-10466.
7. Wang, J., et al., *Hierarchically helical mesostructured silica nanofibers templated by achiral cationic surfactant.* Journal of Materials Chemistry, 2006. **16**(42): p. 4117-4122.
8. Han, Y., L. Zhao, and J.Y. Ying, *Entropy‐Driven Helical Mesostructure Formation with Achiral Cationic Surfactant Templates.* Advanced Materials, 2007. **19**(18): p. 2454-2459.
9. Qiu, H. and S. Che, *Formation mechanism of achiral amphiphile-templated helical mesoporous silicas.* The Journal of Physical Chemistry B, 2008. **112**(34): p. 10466-10474.
10. Wang, W., et al., *A novel method to fabricate silica nanotubes based on phase separation effect.* Journal of Materials Chemistry, 2010. **20**(41): p. 9068-9072.
11. Lin, G.-L., et al., *Synthesis of mesoporous silica helical fibers using a catanionic-neutral ternary surfactant in a highly dilute silica solution: Biomimetic silicification.* Langmuir, 2007. **23**(8): p. 4115-4119.
12. Qiu, H., et al., *Steric and temperature control of enantiopurity of chiral mesoporous silica.* The Journal of Physical Chemistry C, 2008. **112**(6): p. 1871-1877.
13. Yang, Y., et al., *Preparation of helical mesoporous silica and hybrid silica nanofibers using hydrogelator.* Chemistry of Materials, 2006. **18**(5): p. 1324-1329.
14. Ono, Y., et al., *Organic gels are useful as a template for the preparation of hollow fiber silica.* Chemical Communications, 1998(14): p. 1477-1478.
15. van Bommel, K.J., A. Friggeri, and S. Shinkai, *Organic templates for the generation of inorganic materials.* Angewandte Chemie International Edition, 2003. **42**(9): p. 980-999.
16. Tamaru, S.i., et al., *Sol‐Gel Transcription of Sugar‐Appended Porphyrin Assemblies into Fibrous Silica: Unimolecular Stacks versus Helical Bundles as Templates.* Angewandte Chemie International Edition, 2002. **41**(5): p. 853-856.
17. Jung, J.H., et al., *Helical ribbon aggregate composed of a crown-appended cholesterol*

derivative which acts as an amphiphilic gelator of organic solvents and as a template for chiral silica transcription. Journal of the American Chemical Society, 2001. **123**(36): p. 8785-8789.

18. Wu, X., et al., *A novel route for synthesizing silica nanotubes with chiral mesoporous wall structures.* Chemistry of Materials, 2007. **19**(7): p. 1577-1583.
19. Jung, J.H., et al., *Creation of both right-handed and left-handed silica structures by sol-gel transcription of organogel fibers comprised of chiral diaminocyclohexane derivatives.* Journal of the American Chemical Society, 2000. **122**(20): p. 5008-5009.
20. Kobayashi, S., et al., *Preparation of helical transition-metal oxide tubes using organogelators as structure-directing agents.* Journal of the American Chemical Society, 2002. **124**(23): p. 6550-6551.
21. Sugiyasu, K., et al., *Double helical silica fibrils by sol–gel transcription of chiral aggregates of gemini surfactants.* Chemical Communications, 2002(11): p. 1212-1213.
22. Seddon, A.M., et al., *Chiral templating of silica–lipid lamellar mesophase with helical tubular architecture.* Angewandte Chemie International Edition, 2002. **41**(16): p. 2988-2991.
23. Wu, Y., et al., *Composite mesostructures by nano-confinement.* Nature materials, 2004. **3**(11): p. 816-822.
24. Jin, H., et al., *Mesoporous Silicas by Self‐Assembly of Lipid Molecules: Ribbon, Hollow Sphere, and Chiral Materials.* Chemistry-A European Journal, 2008. **14**(21): p. 6413-6420.
25. Zhou, S., et al., *Nanostructures of complexes formed by calf thymus DNA interacting with cationic surfactants.* Biomacromolecules, 2004. **5**(4): p. 1256-1261.
26. Fang, Y. and J.H. Hoh, *Cationic silanes stabilize intermediates in DNA condensation.* FEBS letters, 1999. **459**(2): p. 173-176.
27. Cao, Y., et al., *Synthesis and characterization of multi-helical DNA–silica fibers.* Chemical Communications, 2013. **49**(11): p. 1097-1099.
28. Jung, J.H., K. Yoshida, and T. Shimizu, *Creation of novel double-helical silica nanotubes using binary gel system.* Langmuir, 2002. **18**(23): p. 8724-8727.
29. Jung, J., *Novel preparation method for multi-layered, tubular silica using an azacrown-appended cholesterol as template and metal-deposition into the interlayer space.* Journal of the Chemical Society, Perkin Transactions 2, 1999(7): p. 1289-1292.
30. Oda, R., et al., *Tuning bilayer twist using chiral counterions.* Nature, 1999. **399**(6736): p. 566-569.
31. Iler, R.K., *The chemistry of silica: solubility, polymerization, colloid and surface pro perties, and biochemistry*1979: Wiley.
32. Delclos, T., et al., *Individualized silica nanohelices and nanotubes: Tuning inorganic nanostructures using lipidic self-assemblies.* Nano Letters, 2008. **8**(7): p. 1929-1935.
33. Okazaki, Y., et al., *Chiral Colloids: Homogeneous Suspension of Individualized SiO2 Helical and Twisted Nanoribbons.* Acs Nano, 2014. **8**(7): p. 6863-6872.
34. Tamoto, R., et al., *Gold Nanoparticle Deposition on Silica Nanohelices: A New Controllable 3D Substrate in Aqueous Suspension for Optical Sensing.* Journal of

Physical Chemistry C, 2012. **116**(43): p. 23143-23152.
35. Zhang, S., et al., *Formation of Gold and Silver Nanoparticle Arrays and Thin Shells on Mesostructured Silica Nanofibers.* Advanced Functional Materials, 2007. **17**(16): p. 3258-3266.
36. Malassis, L., et al., *Bottom-up Fabrication and Optical Characterization of Dense Films of Meta-Atoms Made of Core–Shell Plasmonic Nanoparticles.* Langmuir, 2013. **29**(5): p. 1551-1561.
37. Pinho, S.L., et al., *Silica Nanoparticles for Bimodal MRI–Optical Imaging by Grafting Gd3+ and Eu3+/Tb3+ Complexes.* European Journal of Inorganic Chemistry, 2012. **2012**(16): p. 2828-2837.
38. Plueddemann, E.P., *Silane coupling agents*2013: Springer Science & Business Media.
39. Jung, J.H., M. Park, and S. Shinkai, *Fabrication of silica nanotubes by using self-assembled gels and their applications in environmental and biological fields.* Chemical Society Reviews, 2010. **39**(11): p. 4286-4302.
40. Han, L. and S. Che, *Anionic surfactant templated mesoporous silicas (AMSs).* Chemical Society Reviews, 2013. **42**(9): p. 3740-3752.
41. Manet, S., *Effet de contre-ion sur les propriétés d'amphiphiles cationiques*, 2007, Université Sciences et Technologies-Bordeaux I.
42. Brinker, C., *Hydrolysis and condensation of silicates: effects on structure.* Journal of Non-Crystalline Solids, 1988. **100**(1): p. 31-50.
43. Hench, L.L. and D.R. Ulrich, *Ultrastructure processing of ceramics, glasses, and composites*1984: Wiley.
44. Cheng, Q.H., et al., *Ultrasound-Assisted SWNTs Dispersion: Effects of Sonication Parameters and Solvent Properties.* Journal of Physical Chemistry C, 2010. **114**(19): p. 8821-8827.
45. Hennrich, F., et al., *The mechanism of cavitation-induced scission of single-walled carbon nanotubes.* The Journal of Physical Chemistry B, 2007. **111**(8): p. 1932-1937.
46. Lucas, A., et al., *Kinetics of nanotube and microfiber scission under sonication.* The Journal of Physical Chemistry C, 2009. **113**(48): p. 20599-20605.
47. Tamoto, R., *Chiral Nano/Micro Self-Assemblies of Cationic Surfactants: from dynamic behavior of supramolecular architectures towards hybrid nanomaterials.* Biophysical Chemistry, University of Bordeaux, Bordeaux, France, 2011: p. 222.
48. Jung, H.-S., D.-S. Moon, and J.-K. Lee, *Quantitative analysis and efficient surface modification of silica nanoparticles.* Journal of Nanomaterials, 2012. **2012**: p. 48.
49. Howarter, J.A. and J.P. Youngblood, *Optimization of silica silanization by 3-aminopropyltriethoxysilane.* Langmuir, 2006. **22**(26): p. 11142-11147.
50. Brizard, A., et al., *Counterion, temperature, and time modulation of nanometric chiral ribbons from gemini-tartrate amphiphiles.* Journal of the American Chemical Society, 2007. **129**(12): p. 3754-3762.
51. Brizard, A., R.K. Ahmad, and R. Oda, *Control of nano-micrometric twist and helical ribbon formation with gemini-oligoalanine via interpeptidic beta-sheet structure formation.* Chemical Communications, 2007(22): p. 2275-2277.

52. Oda, R., S.J. Candau, and I. Huc, *Gemini surfactants, the effect of hydrophobic chain length and dissymmetry.* Chemical Communications, 1997(21): p. 2105-2106.
53. Zana, R., *Dimeric (gemini) surfactants: effect of the spacer group on the association behavior in aqueous solution.* Journal of Colloid and Interface Science, 2002. **248**(2): p. 203-220.
54. Frindi, M., et al., *Alkanediyl-. alpha.,. omega.-bis (dimethylalkylammonium bromide) Surfactants. 4. Ultrasonic Absorption Studies of Amphiphile Exchange between Micelles and Bulk Phase in Aqueous Micellar Solution.* Langmuir, 1994. **10**(4): p. 1140-1145.
55. Zana, R., *Gemini (dimeric) surfactants.* Current Opinion in Colloid & Interface Science, 1996. **1**(5): p. 566-571.
56. In, M. and R. Zana, *Phase behavior of gemini surfactants.* Journal of dispersion science and technology, 2007. **28**(1): p. 143-154.
57. Manet, S., et al., *Counteranion effect on micellization of cationic gemini surfactants 14-2-14: Hofmeister and other counterions.* Langmuir, 2010. **26**(13): p. 10645-10656.

References – page 118

Chapter 4. Template-assisted synthesis and characterization of Goldhelix and its chiroptical properties

References – page 183

1. Introduction

The brief description offered in Chapter 1 showed how a media, especially those consisting of plasmonic nanoparticles can be used when they are assembled, in order to control the properties of light. Therefore the organization of metal nanoparticles on 2D and 3D surfaces has attracted a lot of attention due to its potential applications in nanoscale integrated photonics. The realization of fine tunability of 2D and 3D surfaces with chirality in Chapter 3 has clearly shown the promising properties for the fabrication of such structures via templated self-assembly of plasmonic NPs. In order to better understand how plasmonic nanoparticles can interact with surfaces and how the synthesized superstructures can affect the light propagation, in this chapter fine-tuned silica nanohelices were employed as a template and GNPs with different sizes were used as the building blocks. The relationship between surface ligands and the essential electrostatic interactions between NPs and silica nanohelices will be studied so as to discover the relationship between chiroptical properties and organizations of GNPs.

However, to obtain collective properties, especially chirality, via self-assembly of plasmonic NPs is an emerging area at its infancy, therefore we will first make a quick overview of the literature devoted to template-assisted self-assembly of plasmonic NPs with chiroptical activities in this introduction to give an idea about the origin of chirality and some of the cutting edge discoveries in this area, even if we can as well find some good examples which has already shown in Chapter 1.

First and foremost, as mentioned in Chapter 1, the idea of chiral self-assembly of plasmonic nanoparticles is often implemented via assistance of organic molecules such as DNA or peptides. A. P. Alivisatos and his coworkers[1] reported that nanostructures constructed from metal and semiconductor nanocrystals conjugated to and organized by DNA are an emerging class of materials with collective optical properties. As shown in Figure 4.1, the tetrahedral symmetry of DNA pyramids suggests the possibility of creating chiral nanostructures through rational controlled assembling of NPs.

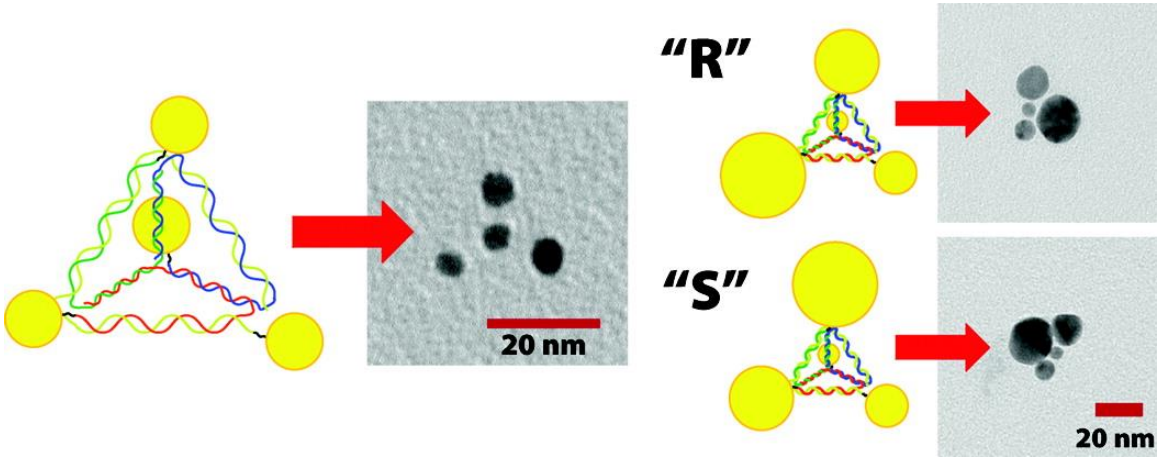

Figure 4.1- Schematic and TEM image of DNA-nanocrystal pyramids.[1]

In fact, many recent successes in using DNA as a molecular glue to direct GNPs into periodic 3D crystalline lattices further demonstrates the power of DNA as building blocks for 3D nanoengineering. H. Yan et al,[2] reported that by the attachment of single-stranded DNA to GNPs, nanotubes of various 3D architectures can form, ranging in shape from stacked rings to single spirals, double spirals, and nested spirals. The nanoparticles are active elements that control the preference for specific tube conformations through size-dependent steric and electrostatic repulsion effects, which in return will favor DNA tube formation. (Figure 4.2)

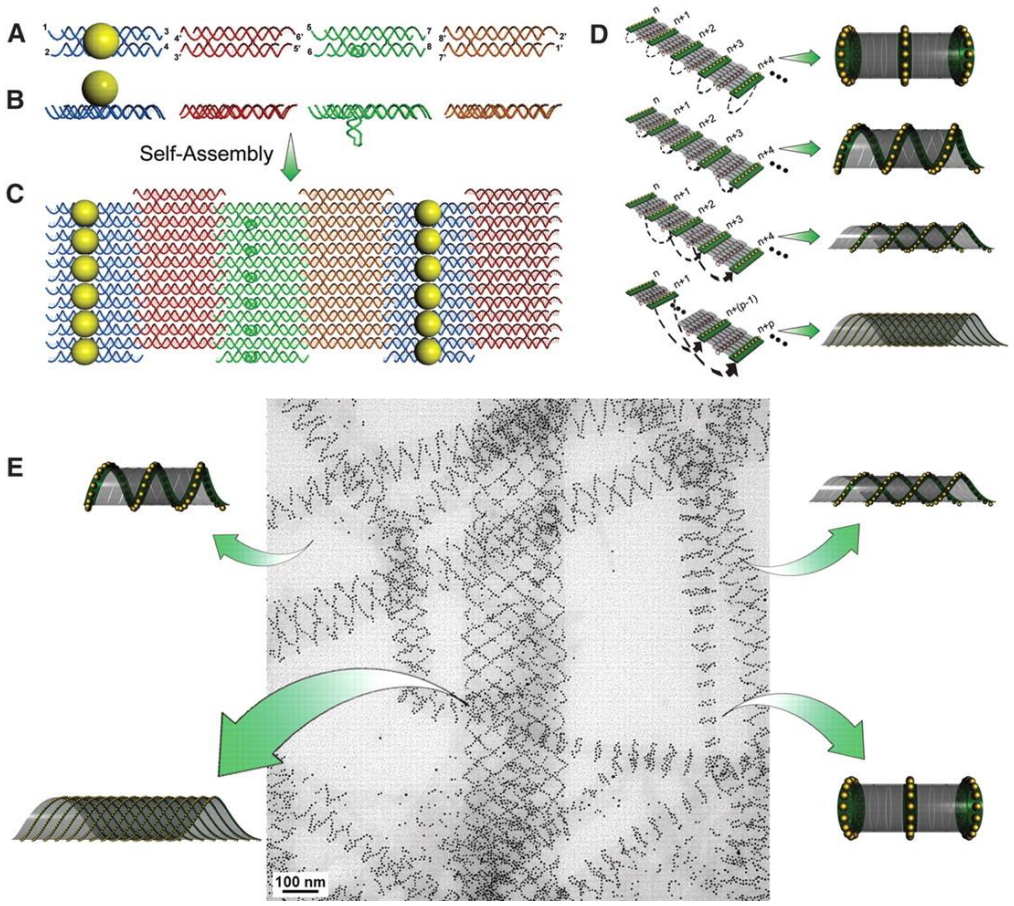

Figure 4.2-The design of a DNA tile system for the formation of a variety of tubular structures carrying 5-nm GNPs. (A and B) Top and side view of the four double crossover tiles (A tile, blue; B tile, red; C tile, green; and D tile, brown). The A tile carries a 5-nm GNPs on the top of the tile. The C tile carries a DNA stem loop pointing downward. (C) The four different tiles are designed to self-assemble into a 2D array displaying parallel lines of GNPs. (D) Possible ways for the corresponding edge tiles on opposite sides of the 2D array to associate and lead to formation of tubes displaying patterns of GNPs in stacked rings, single spirals, double spirals, and nested spiral tubes. (E) The different tube conformations were observed in a single TEM image.[2]

Different from using organic template, L. M. Liz-Marzán et al.,[3] showed that by using chiral silica fibers, a 3D organization of gold nanorods (GNRs) can be obtained and this 3D assembly of GNRs can have induced surface plasmon CD at the excitation wavelength of GNRs. The synthesized nanostructures have a record circular dichroism anisotropy factor for metal nanoparticles (> 0.02) across visible and near-infrared (Vis–NIR) wavelengths (600–900 nm) and these measurements are well in line with the theoretical approximations done via discrete dipole approximation (DDA) method.(Figure 4.3)

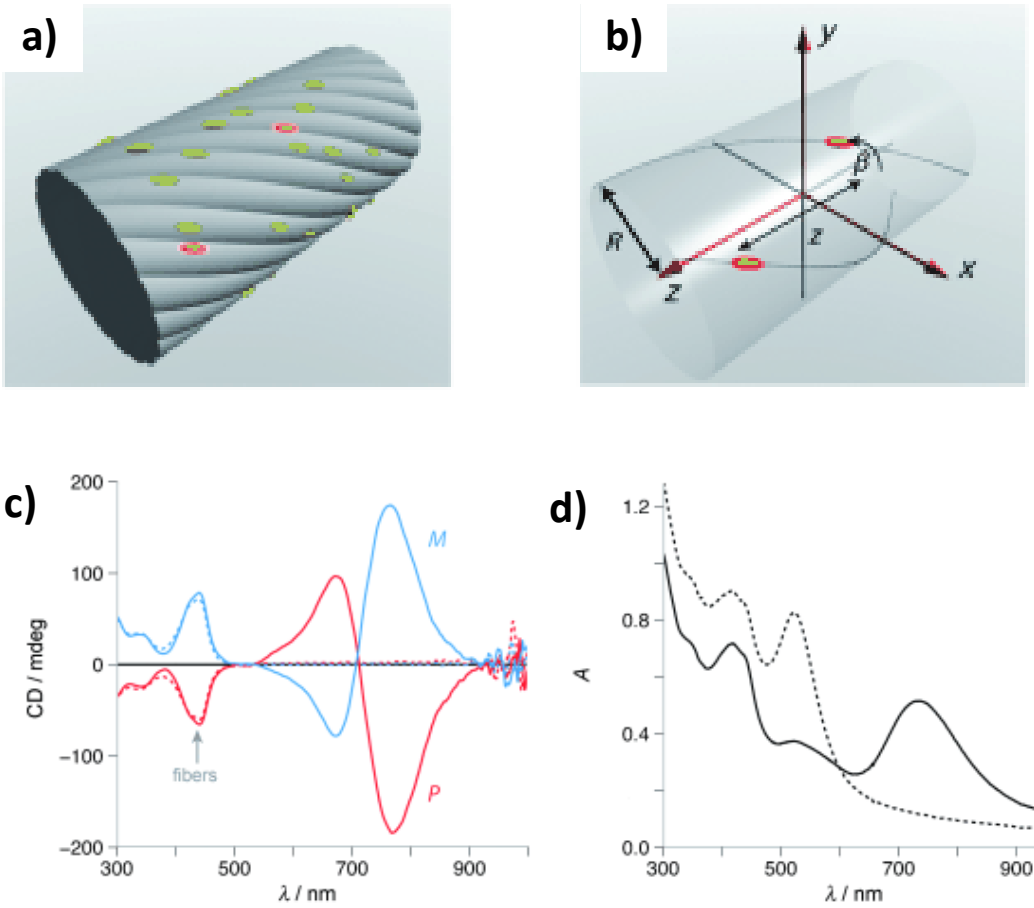

Figure 4.3-a) General sketch of the system. NRs are randomly positioned onto the surface of a cylinder of radius R=100 nm. The orientation of each particle is defined so that its long axis is tangential to a helical curve of 3 μm pitch. b) Same as in (a), but with only two particles. The parameters describing the relative position of the two NRs are the distance z along the cylinder axis and the rotation angle β around the cylinder. c) Experimental CD and d) UV/Vis spectra in fluid suspensions. Solid lines show the results for gold NRs (length 45 nm, width 17 nm); dashed lines show the results for gold nanospheres (average diameter 15 nm). CD spectra are shown for both P (red) and M nanocomposites (blue).[3]

Other than immobilized on the surface on the template, M. J. Maclachlan and coworkers demonstrated that silver nanoparticles can synthesized inside mesoporous chiral silica films with chiral nematic structure as illustrated in Figure 4.4. Further circular dichroism measurements of the silver NP-loaded silica films show NP-based optical activity in the vicinity of the surface plasmon resonance. By comparisons of CD spectra of different sizes of Ag NPs conjugated with different silica templates, they pointed out that the optical activities solely originate from the long-range organization of the Ag NPs in the chiral nematic silica host rather than from a property of the individual NPs.[4]

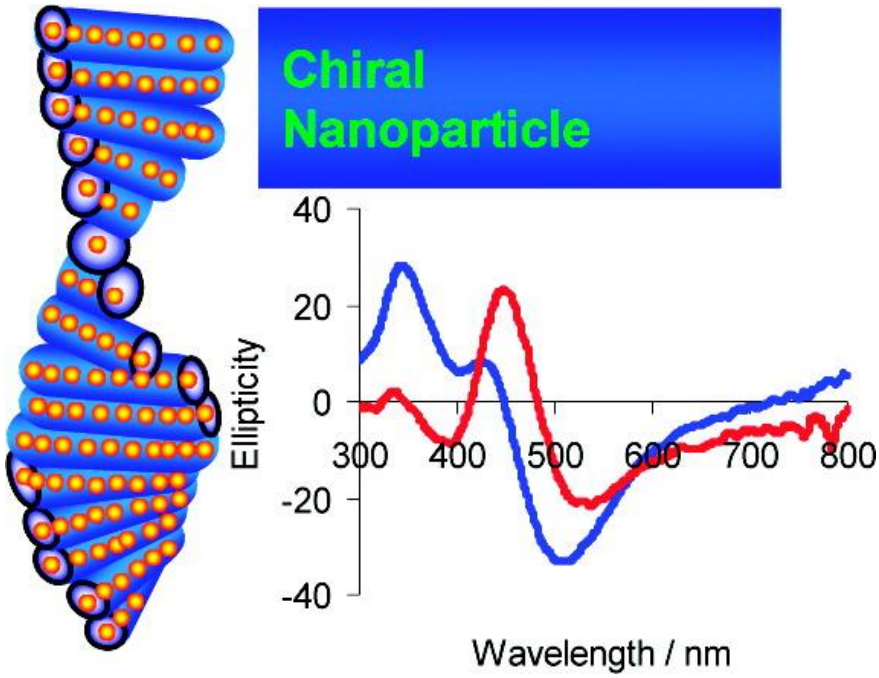

Figure 4.4- Schematic images of Ag NPs assembled inside chiral mesoporous silica films and its CD spectra.[4]

Moreover, if we broaden the scope of nanoparticles to larger scale building blocks such as nanowires (NWs), the idea of self-assembly can revolutionize the fabrication of chiral nanostructures. H. Chen and colleague reported a new type of water-soluble ultrathin Au-Ag alloy nanowire (NW), which exhibits unprecedented behavior in a colloidal solution. Upon growth of a thin metal (Pd, Pt, or Au) layer, the NW winds around itself to give a metallic double helix (Figure 4.5). They propose that the winding originates from the chirality within the as-synthesized Au-Ag NWs, which were induced to untwist upon metal deposition, indicating the chemistry of the NWs provides rich information for mechanistic inference and their chiral action is a dramatic display of the chirality at atomic scale.[5]

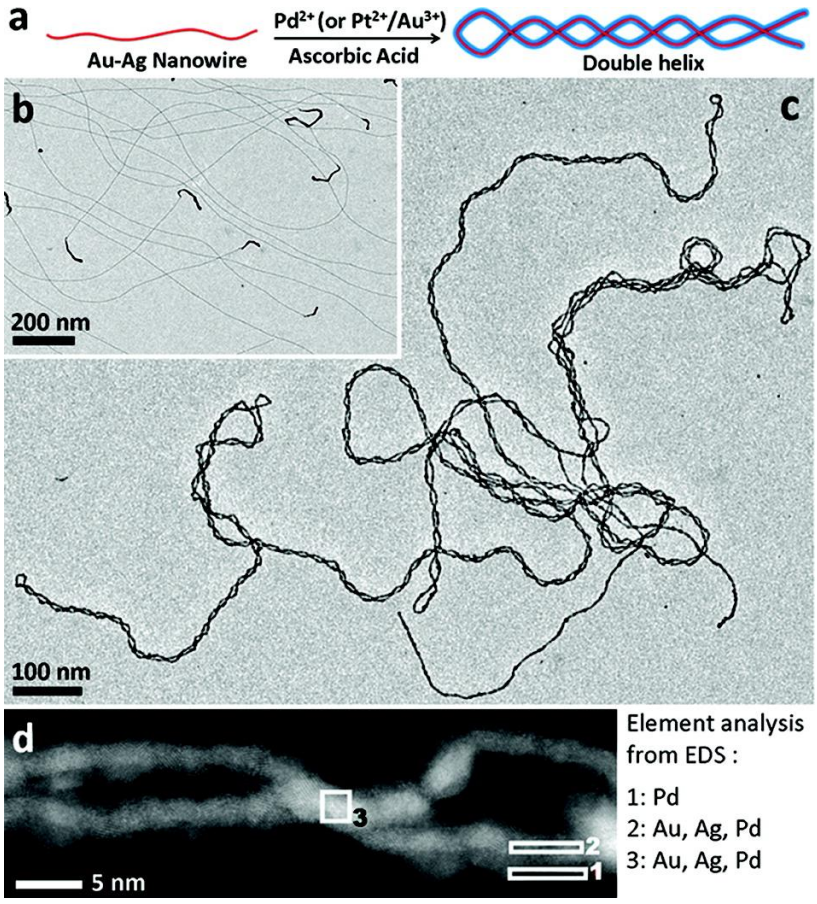

Figure 4.5-(a) Schematics illustrating the formation of double helix by growing a metal layer on Au-Ag alloy NW; TEM image of (b) the as synthesized Au-Ag NWs, and (c) a typical (Au-Ag)@Pd double helix; (d) HAADF-STEM image of a typical (Au-Ag)@Pd double helix, showing its core-shell NWs.[5]

In addition, other than metal nanoparticles, N. A. Kotov et al.,[6] proved that that illumination of dispersions of racemic CdTe NPs with right- (left-) handed circularly polarized light (CPL) induces the formation of right- (left-) handed twisted nanoribbons with an enantiomeric excess exceeding 30%, which is ~10 times higher than that of typical CPL-induced reactions. Linearly polarized light or dark conditions led instead to straight nanoribbons. CPL 'templating' of NP assemblies is based on the enantio-selective photoactivation of chiral NPs and clusters, followed by their photooxidation and self-assembly into nanoribbons with specific helicity as a result of chirality-sensitive interactions between the NPs. The ability of NPs to retain the polarization information of incident photons should open pathways for the synthesis of chiral photonic materials and allow a better understanding of the origins of biomolecular homochirality.(Figure 4.6)

References – page 183

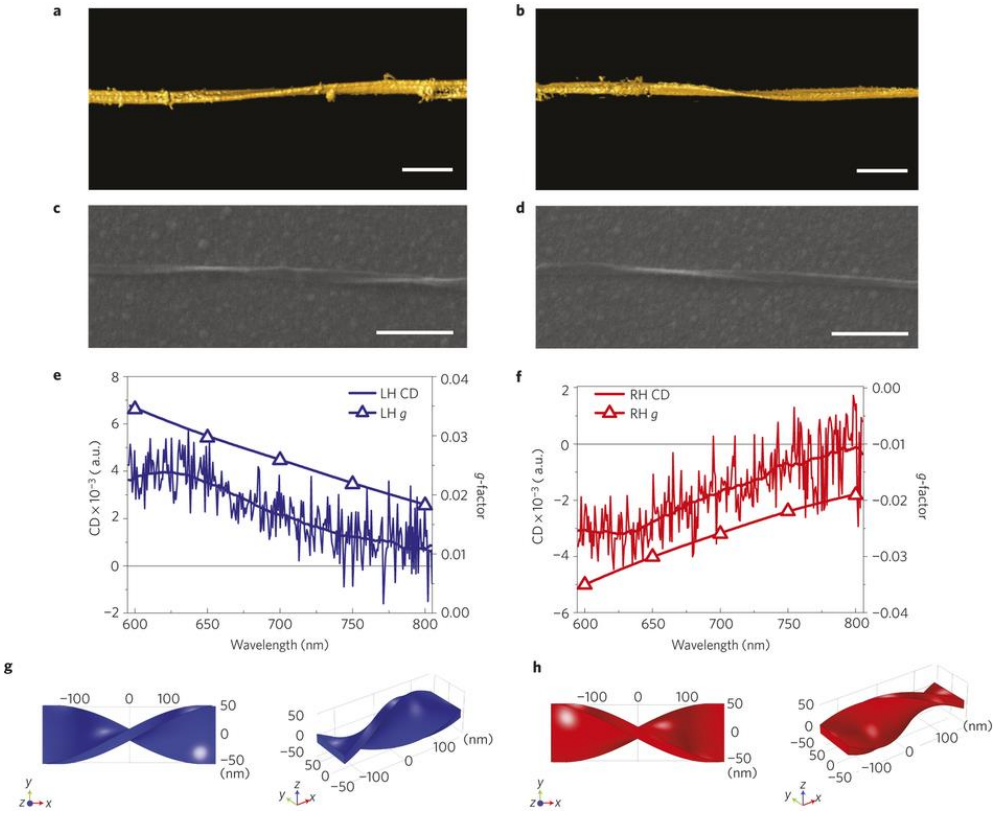

Figure 4.6-a,b, Surface rendering of the 3D TEM tomographic reconstruction of a LH (a) and a RH (b) nanoribbon. Scale bars, 100 nm. c,d, SEM images of single LH (c) and RH (d) nanoribbons. Scale bars, 500 nm. e,f, CD spectra and calculated g-factor spectra for the single LH (e) and RH (f) nanoribbons in c,d, respectively. g,h, Computational models of the LH (g) and RH (h) nanoribbons used in the FEM calculations of chiroptical properties on the basis of numerical solutions of the Maxwell equations.[6]

In short, the realization of chiral self-assembly of plasmonic particles can be done by many means such as organic and inorganic templating, photochemistry, steric and electrostatic interactions. Afterwards, the collective optical properties of the NPs can be used to enhance the optical activities such as chirality for applications in optical sensor, plasmonic rulers [1, 7-9] and metamaterials. In this chapter, the objective is to generate super-chiral materials exhibiting extreme values of chiral properties in visible light (i.e. optical rotatory power and optical circular dichroism). Therefore based on the silica nanohelices we introduced in Chapter 3, we will graft the surface of silica nanohelices with selected GNPs to obtain controllable circular dichroism activities.

Study on the time-resolved light scattering and magnetic dipole approximation was performed in collaboration with ***Dr. Virginie Ponsinet*** and ***Dr. Philippe Barois*** *from Centre de Recherche Paul Pascal (CRPP), CNRS, France.*

Study on 3D electron microscopic tomography was performed in collaboration with ***Dr. Ovidiu Ersen*** *from Institut de Physique et de Chimie des Matériaux de Strasbourg (IPCMS), CNRS, France*

Studies on the fundamental properties of NPs and characterizations were performed in collaboration with ***Dr. Marie-Helene Delville*** *from Institut de Chimie de la Matière Condensée de Bordeaux (ICMCB), CNRS, France.*

References – page 183

2. Synthesis and characterization of GNPs

2.1. Synthesis of GNPs with different stabilizers

The ability to study and understand the optical properties of metal nanoparticles relies on the ability to make metal nanoparticles with desired sizes and shapes. The most common way is based on bottom-up strategies which are built on the techniques of chemical synthesis and assembly. In a chemical synthesis of metal nanoparticles, it is commonly required careful selection of capping and reducing agents, where the metal salts are first reduced by the reducing agents to form gold clusters and then covered by the capping agents to prevent aggregation. One of the most popular such methods,[10] first developed in the mid-twentieth century, involves reaction of chloroauric acid ($HAuCl_4$) with tri-sodium citrate ($Na_3C_6H_5O_7$) in aqueous solution to make GNPs in which sodium citrate is used both as reducing and capping agents. Afterwards, many chemicals such as polymers, reducing acids, surfactants and ligands are used for the synthesis of GNPs for different size and shape.[11] In parallel, according to our previous research,[12] GNPs adsorbed onto silica nanohelices with diameters greater than 10nm or smaller than 4nm will either cause problems: too big GNPs regarding to the diameter of the silica nanohelices leads to inhomogeneous adsorption of GNPs, which ends in an uncontrolled adsorption of GNPs; or too small GNPs which can be homogeneously adsorbed but cannot show localized surface plasmon resonance (LSPR) peak in UV-vis extinction spectrum. Therefore, in order to preserve both LSPR effect and chiral organizations in the self-assembling process, in this thesis, we will typically investigate on three types of GNPs with diameters around 3.5-10nm, namely $NaBH_4$-GNPs[13] which is stabilized by tri-sodium citrate but reduced by sodium borohydride ($NaBH_4$), APTES-GNPs[14] which is both reduced and capped by (3-Aminopropyl)triethoxysilane (APTES), and TA-GNPs[15] which is reduced and capped by both tri-sodium citrate and tannic acid potassium. Additionally, depending on the properties of the ligands on the surface and requirements for the ongoing experiments, $NaBH_4$-GNPs and TA-GNPs can be further modified by using thiol

References – page 183

terminated ligand[16]: O-(2-Carboxyethyl)-O'-(2-mercaptoethyl), hereafter noted as HS-PEG$_7$-COOH. The modified GNPs are named as HOOC-PEG/NaBH$_4$-GNPs and HOOC-PEG/TA-GNPs, respectively (Figure 4.7). Details about the synthesis and modifications can be found in the experimental session in this chapter and several articles [11, 17, 18] are recommended here as additional reading materials for more information.

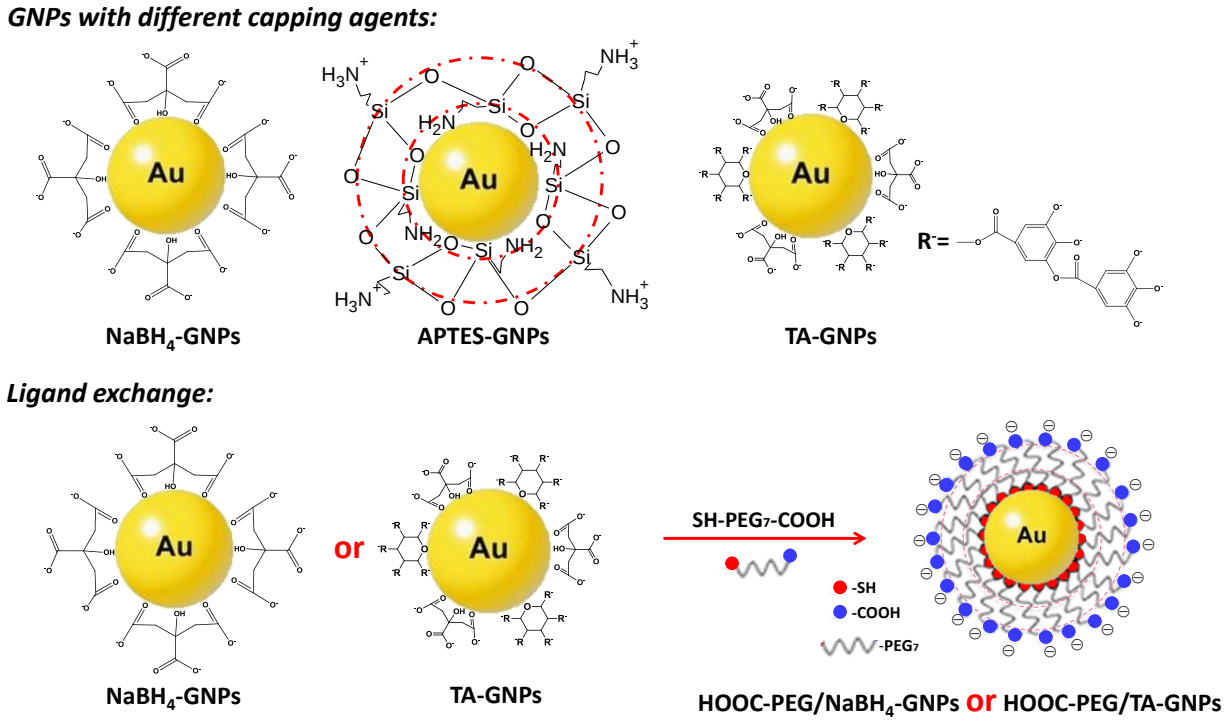

Figure 4.7- Top: schemes about the synthesized GNPs with different capping agents. From left to right: NaBH$_4$-GNPs (capped by tri-sodium citrate), APTES-GNPs (capped by APTES), and TA-GNPs (capped by tannic acid potassium, tri-sodium citrate), respectively; Bottom: schematic illustration of ligand exchange reactions of NaBH$_4$-GNPs/ TA-GNPs with SH-PEG$_7$-COOH. In a typical synthesis, 2mL of NaBH$_4$-GNPs and TA-GNPs (with different concentrations) were concentrated to 1mL and 0.5mL respectively to remove the unreacted capping agents before adding 0.5mL, 10mM SH-PEG$_7$-COOH for ligand exchange.

2.2. Characterization of GNPs via extinction spectrum and electron microscope

Before interacting with silica fibers, GNPs stabilized with different capping agents were first synthesized and characterized by UV-vis spectroscopy and transmission electron microscope (TEM). First of all, in case of NaBH$_4$-GNPs, an average size of 3.5±0.7 nm was measured by TEM, and after ligand exchange by HS-PEG$_7$-COOH, the size of the NPs only

slightly increased to 4.0±0.8nm as the red-shift observed in extinction spectrum confirmed which may be due to the solvent effect of ethanol[12]. (Figure 4.8A)

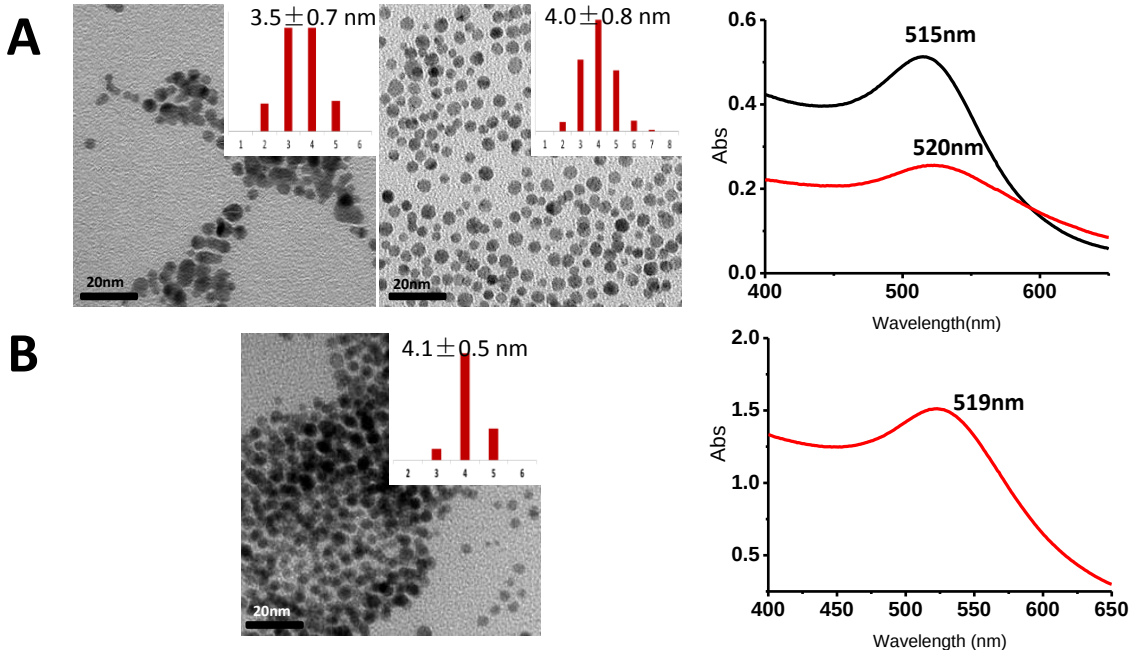

Figure 4.8-Characterization and surface modification of GNPs: A: Typical TEM images of as-synthesized $NaBH_4$-GNPs and ligand exchanged $NaBH_4$-GNPs plus their corresponding extinction spectrums, black line represents for bare $NaBH_4$-GNPs and red line represents for ligand exchanged $NaBH_4$-GNPs, B: TEM image of APTES-GNPs and its extinction spectra. All TEM statistics on NPs diameters are for >200 NPs.

Compared to $NaBH_4$-GNPs stabilized by charge repulsion, GNPs capped with (3-Aminopropyl)triethoxysilane is believed to be stabilized by the protection of the APTES bilayers and its surface charges created by protonation of amine groups on the surface.[14] The size of this type of GNPs is measured to be 4.1nm±0.5.7nm and the corresponding extinction spectrum shows a well-defined LSPR peak at around 519nm. (Figure 4.8B)

Finally, for TA-GNPs, the size can be controlled from 4 to 10nm via using different amount of tannic acid during the synthesis. The typical TEM images and corresponding extinction spectrums are shown in Figure 4.9. For around 4nm bare TA-GNPs and HS-PEG_7-COOH modified ones, there is no obvious LSPR peak as shown in the extinction spectrums meaning it may not be a good candidate to obtain LSPR effect, while for 5.4, 6.3, 7.4 and 9.4nm bare TA-GNPs, the UV-vis absorption peaks are shown clearly around 520nm, 525nm, 522nm and 520nm, respectively. After modification with HS-PEG_7-COOH, the

observed extinction absorption peaks are around 522nm, 525nm, 522nm, and 521nm respectively.

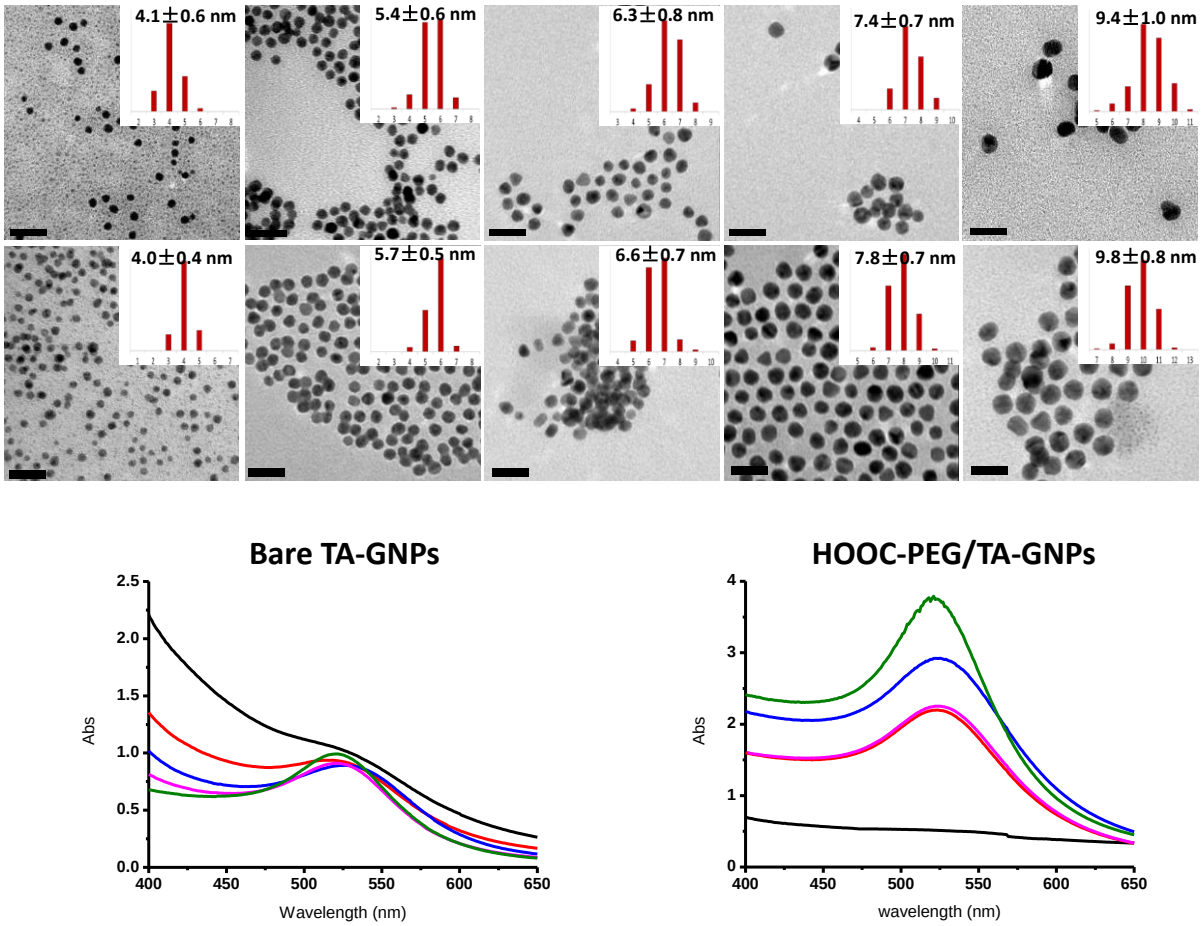

Figure 4.9- Preparation and surface modification of TA-GNPs. Top: representative TEM images of 5-10nm TA-GNPs and their size distribution before and after ligand exchange, respectively. Bottom: corresponding extinction spectrums of bare TA-GNPs (bottom left) and HOOC-PEG/TA-GNPs (bottom right). Black line: ~4nm TA-GNPs, red line: ~5nm GNPs, blue line: ~6nm GNPs, pink line: ~7.5nm GNPs and green line: ~9.5nm GNPs. All TEM statistics on NPs sizes are for >200 NPs. (All scale bars = 20nm)

We can then calculate the concentration of the GNPs colloids.[19] Basically, if we assume a set of spherical GNPs capped by different ligands on the surface, the average number of gold atoms per GNP ($N_{Au/GNP}$) is proportional to the diameters of the GNPs:

$$N_{Au/GNP} = \frac{\pi}{6}\frac{\rho D^3}{M_{Au}}$$

Wherein D is the average diameter of GNPs (in nm), ρ is the density for fcc gold (19.3 g/cm^3) and M_{Au} is the atomic weight of gold (196.97 g /mol) (CAS7440-57-5). Since the

concentration of gold chloride for the synthesis is known at the beginning, we can easily calculate the concentration of GNPs by simply dividing the concentration of gold chloride with $N_{Au/GNP}$. Moreover, since the surface charge density is greatly depending on pH values, the typical calculating results of concentration of GNPs together with pH values and sizes are shown in Table 4.1 below:

Table 4.1-corresponding concentration and pH value of GNPs before and after [#]modification:

GNPs	Size(nm)		Concentration(μM)		pH	
	bare GNPs	[#]Modified GNPs	bare GNPs	[#]Modified GNPs	bare GNPs	[#]Modified GNPs
$NaBH_4$-GNPs	3.5±0.7	4.0±0.8	0.25×10^{-3}	0.13×10^{-3}	6.04	4.88
APTES-GNPs	4.1±0.5	—	10.88	—	*10.12	—
TA-GNPs	4.1±0.6	4.0±0.4	0.13	0.05	6.39	4.37
TA-GNPs	5.4±0.5	5.7±0.5	0.067	0.26	6.27	4.47
TA-GNPs	6.3±0.8	6.6±0.7	0.04	0.23	6.10	4.40
TA-GNPs	7.4±0.7	7.8±0.7	0.02	0.19	6.15	4.43
TA-GNPs	9.4±1.0	9.8±0.8	0.01	0.15	6.33	4.39

***: the sample was 10 times diluted for pH measurement.**

[#]: GNPs after ligand exchanged with HS-PEG_7-COOH.

2.3. Zeta-potential, FTIR-ATR and XPS analysis on surface chemistry of GNPs

In previous section, surface ligand exchange effects on LSPR and size distribution of GNPs were studied. Here, characterizations on how the HS-PEG_7-COOH modification can affect surface charge density and stability will be discussed in details. Herein, we will start with zeta-potential measurements for it can provide fundamental information about the surface charges of the GNPs. As it is shown in Figure 4.10A, HOOC-PEG/$NaBH_4$-GNPs exhibits similar ζ values to bare $NaBH_4$-GNPs within pH ranging from 3 to 7, indicating this

ligand exchange procedure do not greatly change the surface charges. More importantly, in spite of slightly increasing the size of GNPs, the alkyl chain of HS-PEG$_7$-COOH can significantly improve the stability of the GNPs, which has been reported in many related literatures.[20-23]

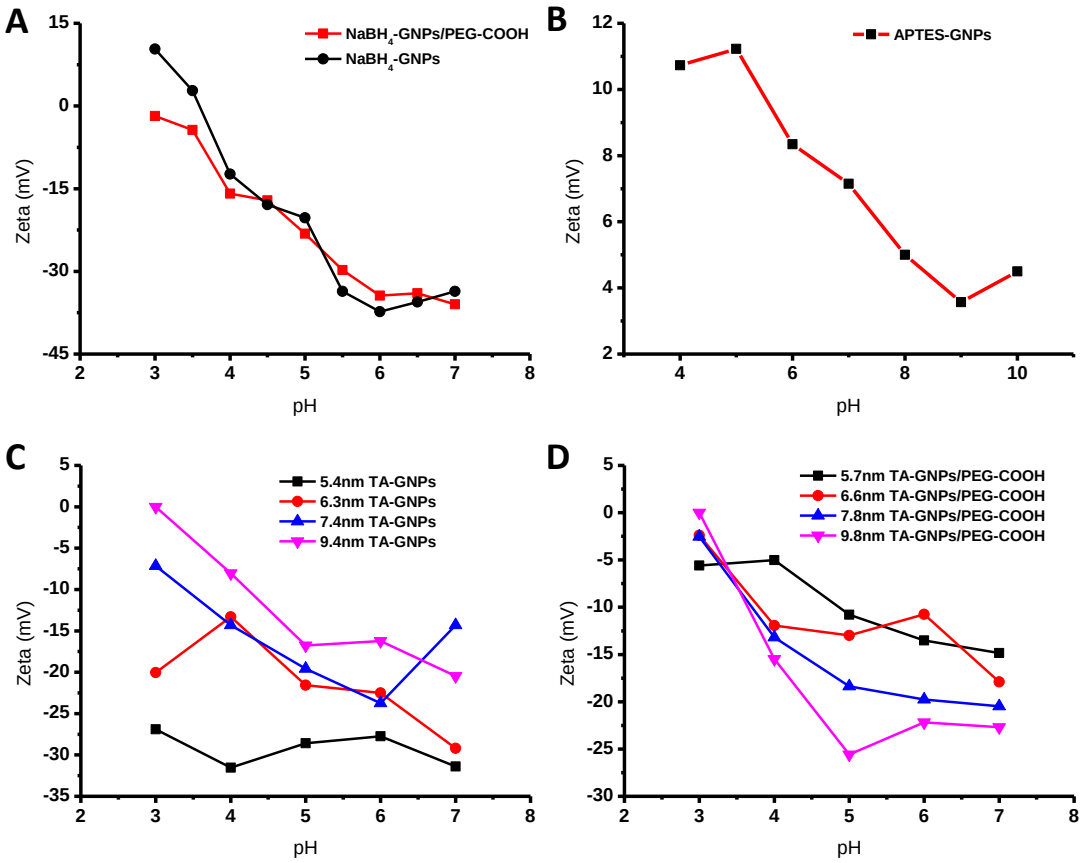

Figure 4.10- Zeta-potential measurement of GNPs with different ligands. (A) Black line: plots on zeta potential of bare NaBH$_4$-GNPs vs pH, red line: plots on zeta potential of HOOC-PEG/NaBH$_4$-GNPs vs pH; (B) plots on zeta potential of APTES-GNPs vs pH; (C) plots on zeta potential of bare TA-GNPs vs pH: 5.4nm (black), 6.3nm (red), 7.4nm (blue) and 9.4nm (pink), respectively; and (D) plots on zeta potential of HOOC-PEG/TA-GNPs vs pH: 5.7nm (black), 6.6nm (red), 7.8nm (blue) and 9.8nm (pink), respectively.

Subsequently, in terms of APTES-GNPs, the measured ζ value expresses slightly positive value within pH value ranging from 4 to 10, suggesting the NPs are only weakly positively charged due to the protonation of the amine groups on the surface. However, they do not aggregate and form bigger nanoparticles indicating that the bilayers of the APTES do keep the GNPs from merging with their neighbors and the whole system may be stabilized by the network of APTES which works like a scaffold to prevent the NPs to precipitate[14]. (Figure

4.10B)

Finally, in order to verify the efficiency of the ligand exchange reaction, bare TA-GNPs and HOOC-PEG/TA-GNPs are first characterized by dry FTIR-attenuated total reflectance (ATR) spectroscopy and XPS analysis. Figure 4.11 shows a typical measurement of ~9.5nm GNPs, in case of bare TA-GNPs ATR characteristic band at 3389cm^{-1} is associated to the stretching vibrations of O-H from tannic acid potassium and tri-sodium citrate, and the broad band around this wavenumber shows the existence of H-bonding. However, after ligand exchanged by HS-PEG$_7$-COOH molecule, this bond disappeared, indicating that tannic acid potassium and tri-sodium citrate are replaced by HS-PEG$_7$-COOH. The newly formed GNPs has characteristic bonds at 1101, 1729 and 2867cm^{-1}, which are the stretching vibrations of C-O-C, C=O and -CH_2 bonds, respectively. These three typical bonds imply the existence of –COOH and PEG chain. On the other hand, in the XPS analysis (Insert in Figure 4.11), the clear splitting of spin-orbit doublet in S2p spectrum at 161.5eV shows the existence of sulfur to metal bonding.[24] From these two techniques, we could assert that the ligand exchange reaction is completely accomplished in this protocol and the newly formed GNPs surfaces are capped by HS-PEG$_7$-COOH.

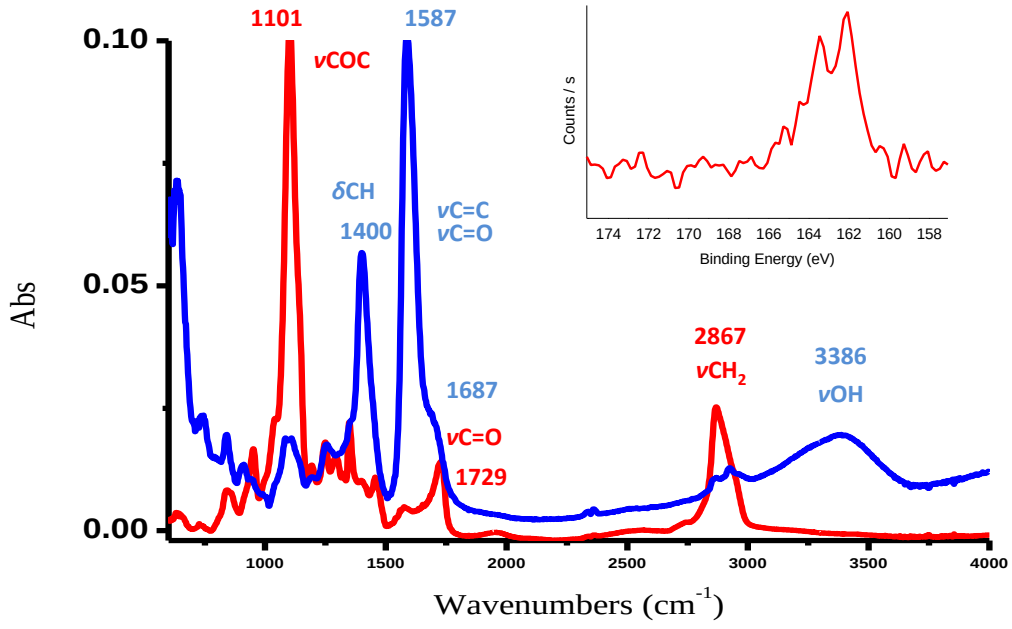

Figure 4.10-FTIR-ATR and XPS study on ligand exchange reaction of TA-GNPs. Blue line: bare 9.4nm TA-GNPs and Red line: 9.8nm HOOC-PEG/TA-GNPs. The spectrums are all collected in dry state

samples under dry CO_2 environment. Insert is the XPS spectrum of S2p spectrum of HOOC-PEG/TA-GNPs.

After studying on the ligand exchange efficiency, ζ potential measurement is conducted as shown in Figure 4.10(C and D) for investigation on surface electronegativity. An interesting observation is that when the NPs are not modified, it seems that the smaller size of the GNPs, the more negative ζ value could be achieved by the NPs, indicating that the surface charge density is in line with the amount of tannic acid (and K_2CO_3) used during the synthesis (Figure 4.10C). As an increasing amount of tannic acid is used during the synthesis, it means more tannic acid potassium salt would be on the surface of the NPs which in return, provides more negative charges. On the other hand, after they are ligand exchanged with SH-PEG_7-COOH, the overall surface charge decreases (Figure 4.10D). Here we assert that the ligand exchange procedure replaces the tannic acid salt and tri-sodium citrate on the surface of the NPs by SH-PEG_7-COOH which has a pKa~4.2, however, as an organic acid, SH-PEG_7-COOH can't provide as much negative charges as tannic acid salt in a pH range from 3-7. Moreover, since the surfaces of the GNPs are all covered by SH-PEG_7-COOH, the absolute ζ value depends on the density of the ligands on the surface. As shown in Figure 4.10D, the absolute zeta value increases when the size of GNPs increases indicating the packing density of SH-PEG_7-COOH is also increasing as the size of GNPs increases, however this stands in contradiction to the reports of M. Lammerhofer et al.,[19] who showed the packing density of SH-PEG_7-COOH molecules on GNPs surface is size-independent by using mass spectroscopy which indicates the zeta value should more or less remain unaffected as the size of GNPs increases. Here, we assume two possible explanations that may be related to the observations: one is that the packing density indeed increases as we observed due to the size effect considering that TA-GNPs has different capping agent when compared to the GNPs studied by Lammerhofer; another understanding can be explained by the asymmetry factors (defined as length-to-width proportion) of big nanoparticles which would be higher than that of small nanoparticles[25], indicating that more alternative binding sites (edges and corners) would be available for bigger nanoparticles to react with SH-PEG_7-COOH ligands, and in a

light scattering measurement it always considers the measured nanoparticles are perfect spheres meaning the packing density of SH-PEG$_7$-COOH may be artificially higher than its real value.[26, 27]

2.4. Synthesis of Goldhelix

After characterizations of GNPs, study on synthesis of Goldhelix based on interactions between GNPs and silica nanohelices will be investigated in this part. Typically, we can divide the synthesis of Goldhelix into two categories depending on whether there is a ligand exchange reaction on GNPs before adsorption: direct adsorption of GNPs on silica nanohelices and adsorption of GNPs onto silica nanohelices after ligands exchange. A schematic instruction about different types of interactions is presented in Figure 4.11. In the course of this section, details about these two approaches will be described and compared so as to set out a better understanding on the parameters that paly critical roles in the interactions between GNPs and silica surfaces.

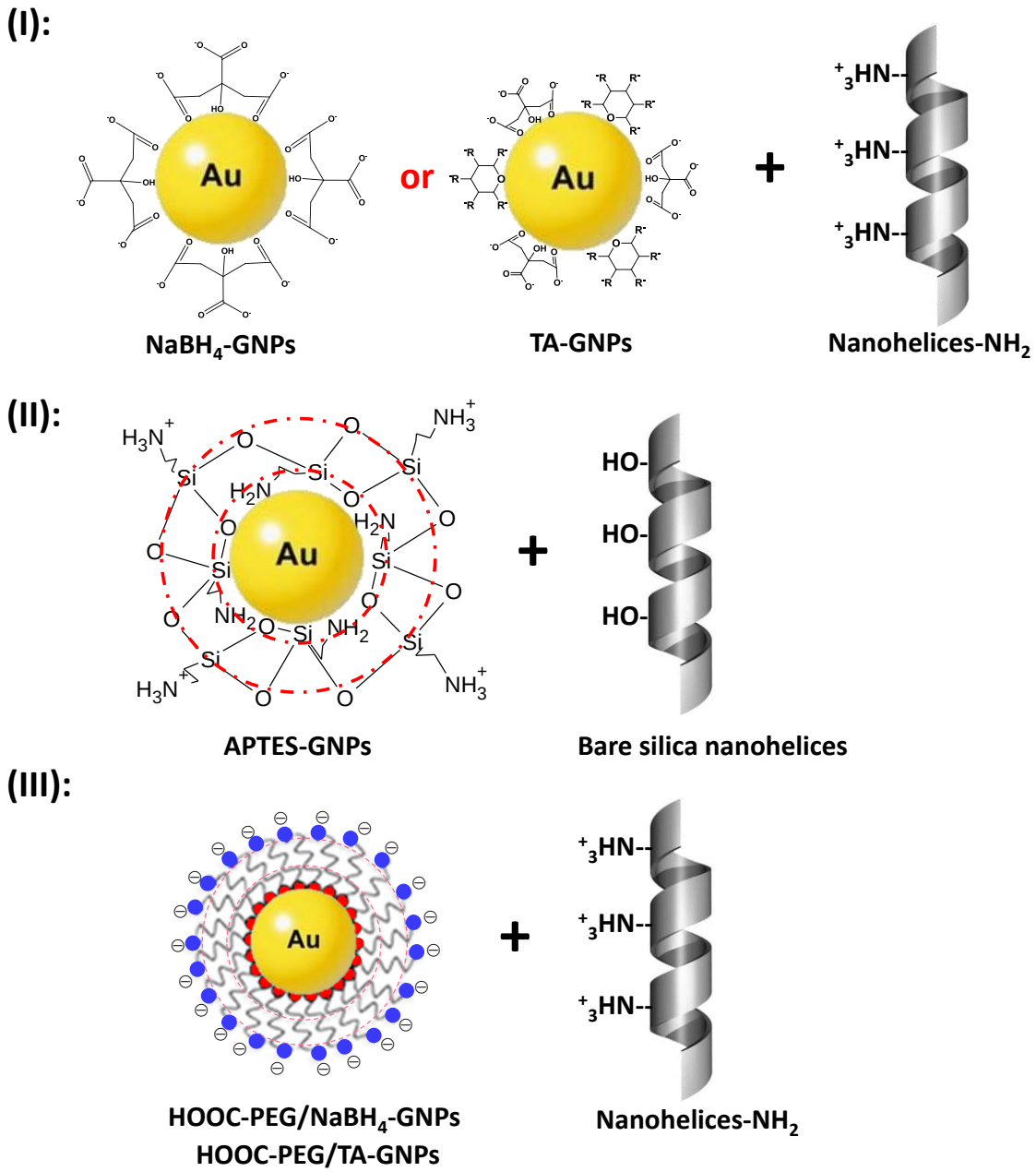

Figure 4.11-Schematic framework of different interactions between GNPs and silica nanohelices. (I): direct mixture of bare $NaBH_4$-GNPs or TA-GNPs with nanohelices-NH_2, (II): direct mixture of APTES-GNPs with bare silica nanohelices, (III): mixture of $NaBH_4$-GNPs or TA-GNPs with nanohelices-NH_2 after ligand exchange with SH-PEG_7-COOH.

2.4.1 Direct adsorption of GNPs on silica nanohelices

The interaction between silica nanohelices with/without amine functionalization to gold colloids with negative/positive charges is principally due to electrostatic attractions or repulsions. This interaction and resulting final organizations of GNPs adsorbed onto silica

surfaces depends strongly on the surface chemistry and surrounding physical environment such as surface ligands and pH values as well as geometrical properties like size of the GNPs and dimension of the silica nanohelices. To simplify the terminologies used in this thesis, we typically note that amine modified silica helical ribbons or amine modified silica twisted ribbons as naonohelices-NH_2.

$NaBH_4$-GNPs+nanohelices-NH_2

Figure 4.12 shows the typical results of direct adsorption of 3.5nm $NaBH_4$-GNPs and 5.4nm TA-GNPs onto fragmented nanohelices-NH_2 at a concentration of 0.8mg/mL. As shown in Figure 4.12(a and b), the silica surface was inhomogeneously but well covered by $NaBH_4$-GNPs, furthermore, as more GNPs were adsorbed onto the surface, large $NaBH_4$-GNPs and even big gold aggregations emerged (as highlighted in Figure 4.12) probably because the capping capability of citrate is insufficient when it applies to the very small gold colloids, and hydrophilic nanoparticles are normally stabilized by electrostatic repulsion by the equally charged ligand molecules on the particle surface. In the presence of high salt concentration in the interface of silica and GNPs, however, the electric field is shielded, attractive forces such as induced dipole interaction, i.e. Van der Waals force, or hydrogen bonds will cause the particles to agglomerate and finally, inhomogeneous adsorption of GNPs on the silica surface is formed as a consequence.[28]

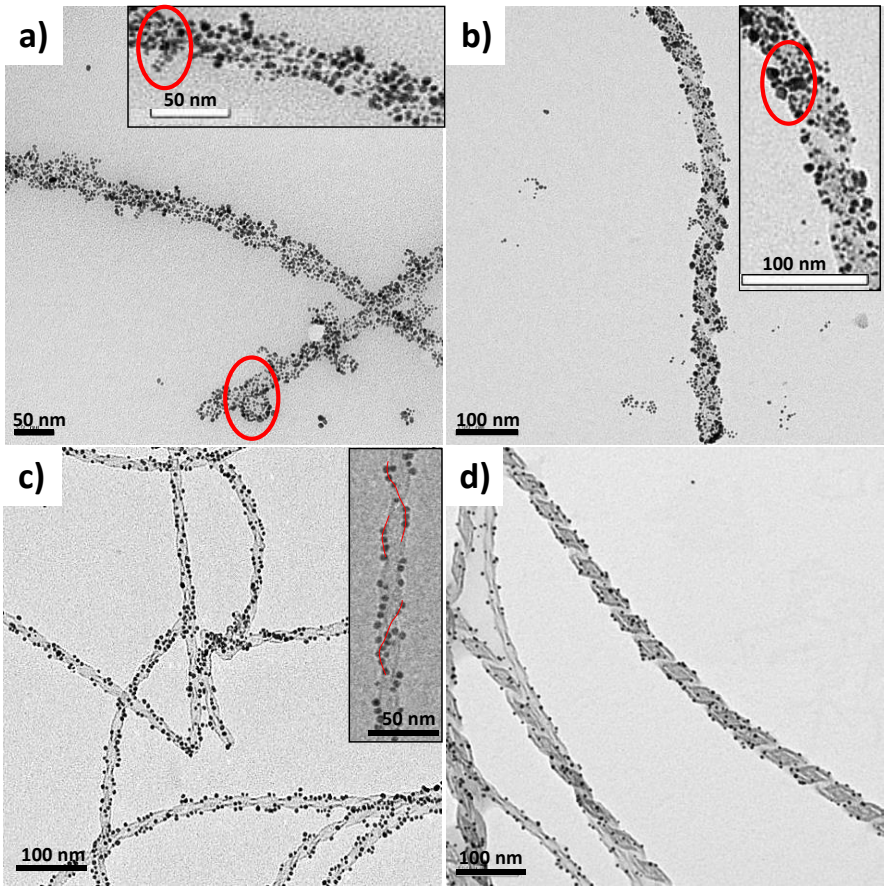

Figure 4.12-Typical TEM images of direct immobilization of GNPs on nanohelices-NH_2. a) and b), bare 3.5nm $NaBH_4$-GNPs+nanohelices-NH_2; c) and d), 5.4nm TA-GNPs+nanohelices-NH_2. 0.5mL GNPs (0.25.7nm for $NaBH_4$-GNPs and 0.125.7nm for TA-GNPs) and 50 µL of 0.8mg/mL nanohelices-NH_2 were used in each run. Insert are the magnified images of corresponding TEM images.

TA-GNPs+nanohelices-NH_2

Interestingly, in the case of TA-GNPs, shown in Figure 4.12(c and d), low attachment efficiency is observed which is probably due to the strong negative charges on the surfaces of small TA-GNPs as stated in ζ potential measurement. At early stage the adsorption of GNPs onto silica surfaces is mainly controlled by diffusion of NPs, but when they are immobilized or being immobilized onto the silica surface, the adsorption would be decided by the interparticle repulsion. Strong interparticle repulsion between two or more NPs will effectively inhibit additional particle immobilization in between, rendering the positive charged silica surface to be screened from external GNPs.[29] Additionally and interestingly, it seems that TA-GNPs are selectively adsorbed onto the edges of silica twisted ribbons (see

the insert in Figure 4.12c), which would be comprehended by the bending curvature of the silica nanohelices where a high density of amine groups is located and the geometrical convex on the curvature makes the GNPs more favorable to these regions so as to achieve a lower energy state for the NPs, however in case of silica helical ribbons, this phenomenon is not clearly observed. In order to better understand the adsorption mechanism concerning how GNPs interacts with silica surfaces, two mechanisms are proposed as to how GNPs are adsorbed onto an amine modified surface[26]: one is based on the electrostatic interactions between positively charged amine groups and negatively charged GNPs surfaces; the other theory concerns the bond formation between Au and N atoms, and replacement of citrate by this bond after GNPs are getting close to amine groups, which could explain why this attraction is strong enough to endure some drastic changes of the surface environment such as strong sonication, centrifugation and some pH changes. Lots of studies[30-32] have been conducted to clarify which of the two possible explanations dominates the adsorptions, but still no clear agreement is established.

APTES-GNPs+ bare nanohelices

Last but not least, in the case of APTES-GNPs, the GNPs capped by a bi-layer of APTES have positive net charges at their surface, and will interact with bare silica nanohelices which is negatively charged at pH>4 (Figure 3.26a). However, a considerable amount of APTES-GNPs clusters were observed as well in Figure 4.13(a and b), even the overall structures showed more or less a homogenous coverage of the GNPs. These aggregations may be formed by the polymerization of APTES on the surface of GNPs. The closely organized APTES-GNPs onto silica nanohelices with high APTES concentration at the interface may initiate APTES on the surface of neighboring NPs to polymerize. Additionally, an idea of pursuing a controllable homogeneous coverage of APTES-GNPs on the silica surfaces spontaneously prompts us to optimize parameters such as pH of the colloidal solution and the quantity of both APTES-GNPs and silica helical ribbons. As it is shown in Figure 4.13c, when the weight ratio between APTES-GNPs and silica helical ribbons decreases, a more

homogenously covered silica helical ribbons with APTES-GNPs could be observed, while an excess quantity of APTES-GNPs will lead to form gold clusters and small aggregations as mentioned before. We could also observe that a typical extinction spectrum slightly shifts from 519nm of bare APTES-GNPs to 525nm for silica helical ribbons grafted with APTES-GNPs as shown in Figure 4.13d. This small red shift probably results either from the aggregation of APTES-GNPs or the dipole-dipole coupling effect of neighboring APTES-GNPs, or both.

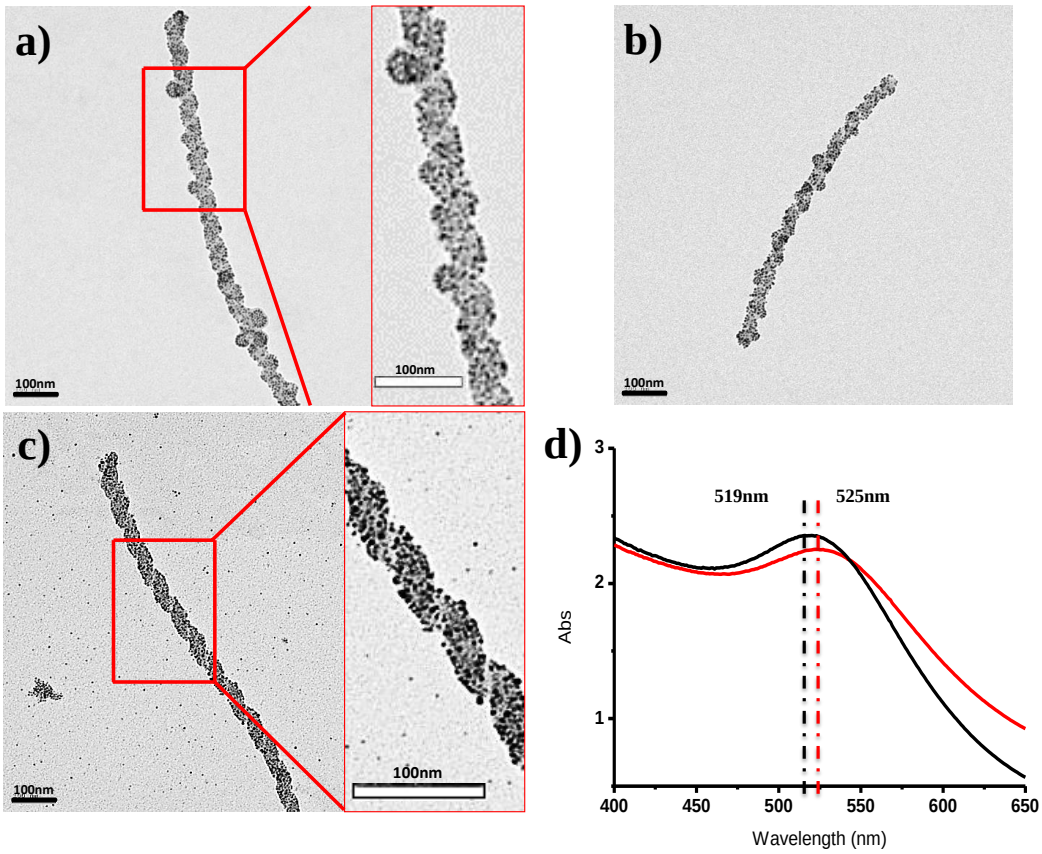

Figure 4.13- Immobilization of APTES-GNPs on silica helical ribbons. (a)-(c): Typical TEM image recorded from 0.84 mg (a), 0.63mg (b) and 0.42mg (c) APTES-GNPs (10.88µM) after mixing with silica helical ribbons, respectively. Inserts are magnified part from corresponding original images. (d): Corresponding extinction spectrum of bare APTES-GNPs (black line) and (c) (red line). All colloidal solutions were mixed with 0.05mg of fragmented silica helical ribbons (0.5mg/ml). The APTES-GNPs colloidals are all adjusted to pH=8 before mixing with silica helical ribbons. All the scale bars are 100nm.

At the same time, pH effect on the adsorption of APTES-GNPs is investigated. Figure 4.14 below presents the typical results. Since APTES-GNPs is only slightly positively charged at pH=4 to 10, the attraction between the NPs and the silica helical ribbons is mainly

determined by the surface charge of the silica helical ribbons. Figure 3.26 shows that silica helical ribbons are negatively charged only when pH>4, and when pH is around 4 or less, it exhibits quite positive zeta value. Indeed, as we observed in Figure 4.14a, almost no adsorption of APTES-GNPs is observed at pH=4, while at higher pHs the adsorptions are much more strengthened. However, disregarding the value of the pH (> 4), they all show gold clusters or aggregations (Figure 4.14-b to d).

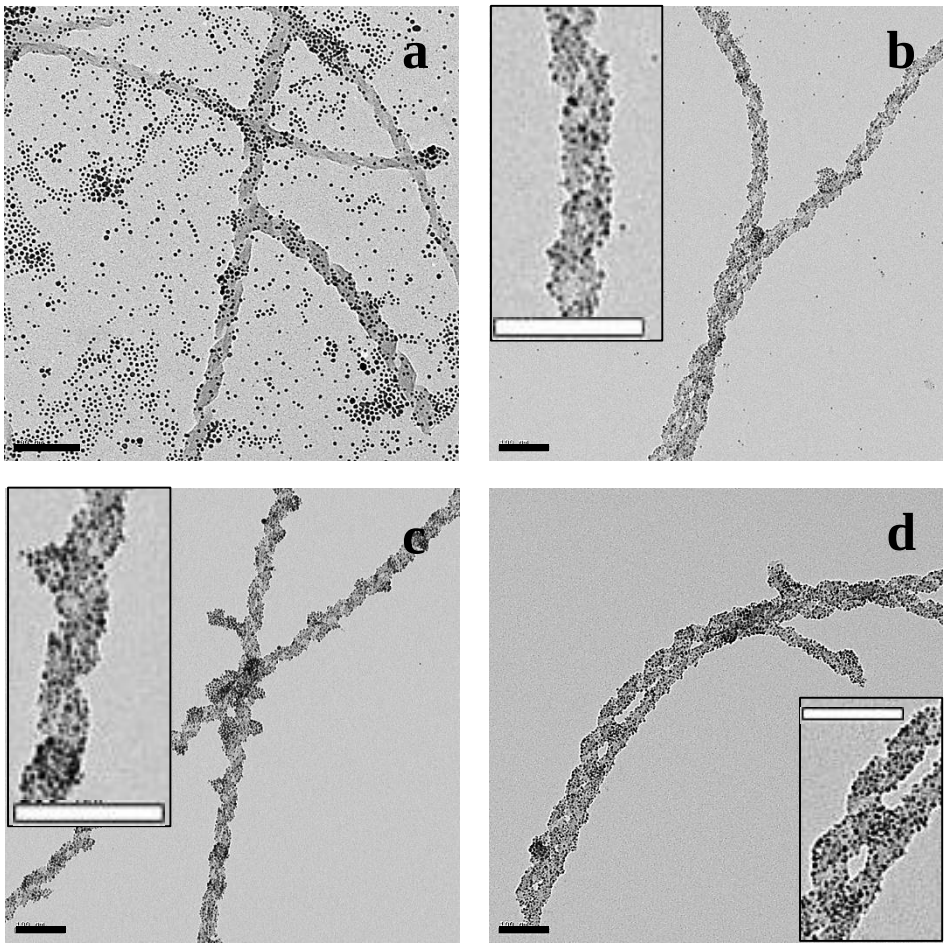

Figure 4.14-Image recorded from pH=4 (a), pH=5 (b), pH=7 (c) and pH=8 (d) APTES-GNPs after mixing with silica helical ribbons, respectively. In all mixtures, 0.05mg of fragmented silica helical ribbons (0.5mg/ml) was added to 0.42mg of 10.88 µM APTES-GNPs in 1mL Milli-Q H_2O. Inserts are magnified TEM images of corresponding samples. All the scale bars are 100nm.

2.4.2 Adsorption of GNPs onto silica nanohelices after ligands exchange

As it is shown in last section, when $NaBH_4$-GNPs and TA-GNPs are directly mixed with

nanohelices-NH_2, the adsorption procedures are very often limited by lack of stability of the NPs or not proper affinity between GNPs and silica nanohelices to obtain a homogenous surface covered with the GNPs. To improve the stability and versatile functionality[20] based on the properties of the ligands, GNPs were prepared with ligands exchange reaction to improve the adsorption and eliminate interactions between Au and amine groups. HS-PEG_7-COOH, which has a long chain of PEG with a length of 3.52nm for free molecules, is used as both exchanging ligands and stabilizer. The long chain of HS-PEG_7-COOH could bring in a steric effect to the nanoparticles, which is strongly chain length dependent[33] In the present case, the surface density at around 4.29 ± 0.45 molecules per nm^2 can be achieved by this ligand exchange method as stated in previous section.[19] This long chain could significantly screen the surface charges of the GNPs as well as the interaction of Au to the outside environment, and its own carboxyl groups provide a novel negatively charged surface that could further interact with positively charged materials like amine functionalized silica nanohelices mentioned before. The schematic framework is illustrated as Figure 4.7 and Figure 4.11C.

HOOC-PEG/$NaBH_4$-GNPs+nanohelices-NH_2

The negatively charged GNPs after ligand exchange could attach to nanohelices-NH_2 by employing electrostatic interactions as the driving force (as illustrated in Schematic framework Figure 4.11C). In the case of HOOC-PEG/$NaBH_4$-GNPs, shown in Figure. 4.15a, the GNPs exhibit a high coverage density at the surface of nanohelices-NH_2 in which no obvious aggregation is observed even strong mechanical treatments were applied during sample preparations, and due to the small diameter of the GNPs, the chiral organizations of the original silica would be entirely preserved. Here we assert that the steric stability derived from the long hydrophilic chain could stabilize the system against agglomeration during physical treatment or pH variation. At pH~5.0, the amount of effective amine groups is estimated as 3.4 to 5.7 amine groups per nm^2[34] Meanwhile, similar density of –COOH groups (4.29 molecules per nm^2) is observed at the surface of GNPs modified with

HS-PEG_7-COOH, implying a highly efficient electrostatic interactions between the GNPs and amine modified surfaces. Actually, this is supported by the zeta-potential measurement shown in Figure 4.10A. The fact that GNPs exhibit more or less the same negative ζ values after ligand exchange indicates that the ligand exchange reaction does not drastically affect the surface charge of the GNPs except that it can greatly induce the steric effect to increase the stability. Additionally, similar method is also applicable on silica twisted ribbons and bigger nanohelices. Figure 4.15(b and c) show that instead of using 16-2-16 silica helical ribbons, a high coverage density of GNPs could be obtained as well in case of 16-2-16 silica twisted ribbons and 18-2-18 silica helical ribbons. However, from the extinction spectrum of 16-2-16 silica helical ribbons grafted with HOOC-PEG/$NaBH_4$-GNPs in Figure 4.15d, a small red-shift of LSPR peak from 521nm (bare HOOC-PEG/$NaBH_4$-GNPs) was observed shift to 530nm after mixture. Since there are no clear aggregations observed in the TEM image, we believe the red-shift results from the coupling of these closely parked HOOC-PEG/$NaBH_4$-GNPs. Nonetheless, due to the fact that HOOC-PEG/$NaBH_4$-GNPs are still very small (less than 5nm), the coupling effect is considerably weak which is probably why only a small shift can be observed. Besides, it is worthy to note that in order to have enough coupling between closely packed GNPs, it basically requires the interparticle distance to be comparable to the diameter of the NPs,[35] but apparently from the 3D reconstruction image, the interparticle distance could be easily larger than 4nm as shown in Figure 4.15e below, which also helps explain why the observed red-shift is small.

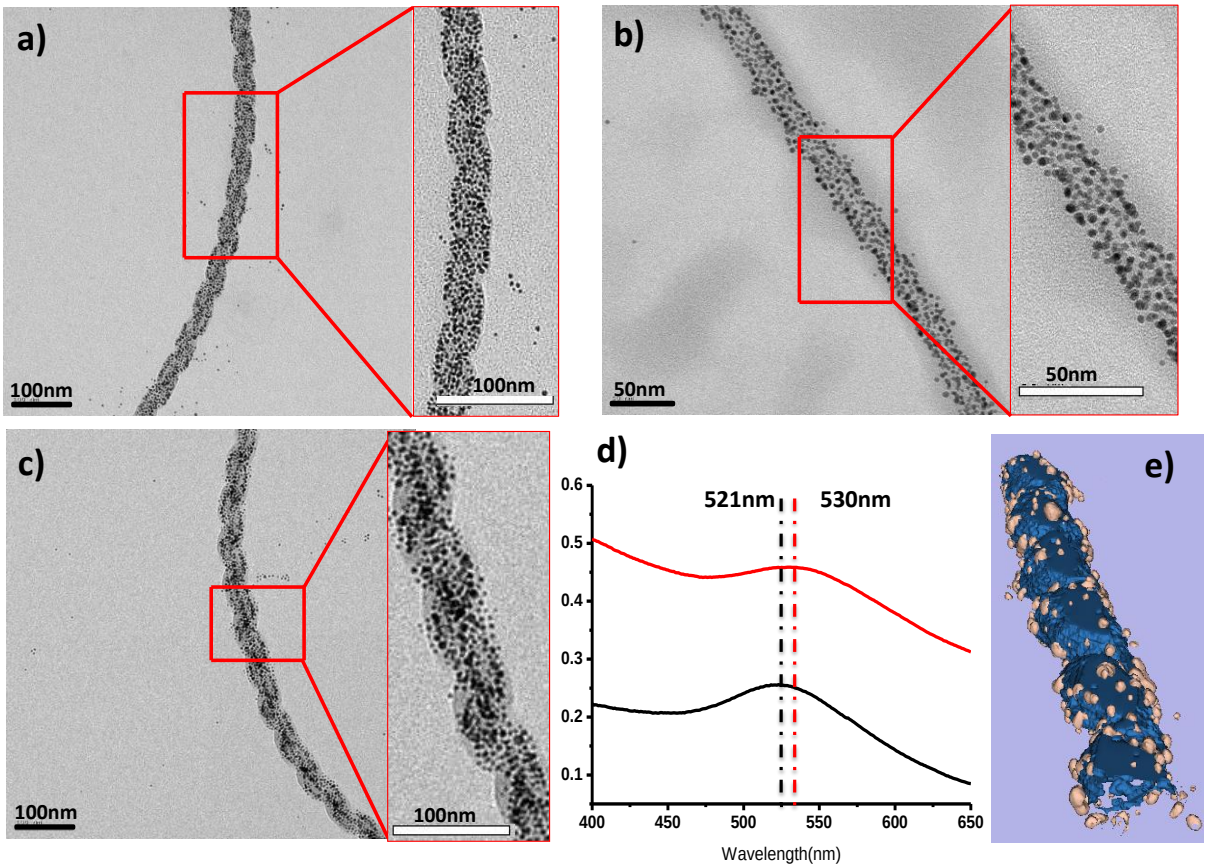

Figure 4.15- Study on the adsorption of HOOC-PEG/$NaBH_4$-GNPs on silica nanohelices. (a)-(c), Typical TEM image recorded from HOOC-PEG/$NaBH_4$-GNPs deposits on (a) 16-2-16 silica helical ribbons, (b) 16-2-16 silica twisted ribbons, and (c) 18-2-18 silica helical ribbons. Inserts are magnified part from corresponding original images. (d) Corresponding extinction spectrum of bare $NaBH_4$-GNPs/PEG (black line) and (a) (red line). (e) 3D reconstruction of the tomography of (a). The grey particles represent for HOOC-PEG/$NaBH_4$-GNPs and the blue helical substrate is the silica helical ribbons.

HOOC-PEG/TA-GNPs+nanohelices-NH_2

Figure 4.16 shows when the functionalization of TA-GNPs is done before grafting, better immobilization of HOOC-PEG/TA-GNPs onto the silica surfaces is observed. However, the surface electronegativity measured by zeta-potential suggested that bare TA-GNPs are generally more negatively charged than HOOC-PEG/TA-GNPs at pH~5. In fact, from the work reported by M. J. Natan[29], it is suggested that the coverage of charged GNPs on a surface is limited by repulsive interparticle interactions which can effectively inhibit additional particle immobilization, meaning when HOOC-PEG/TA-GNPs are immobilized or being immobilized on the silica surface, the charge repulsion will be weak enough to accept

additional HOOC-PEG/TA-GNPs to be located in between. Thus, at this condition, the HOOC-PEG/TA-GNPs cover the silica surface homogeneously and densely protected by the hydrophilic carbon chains. The overall structure would be stable for at least one month.

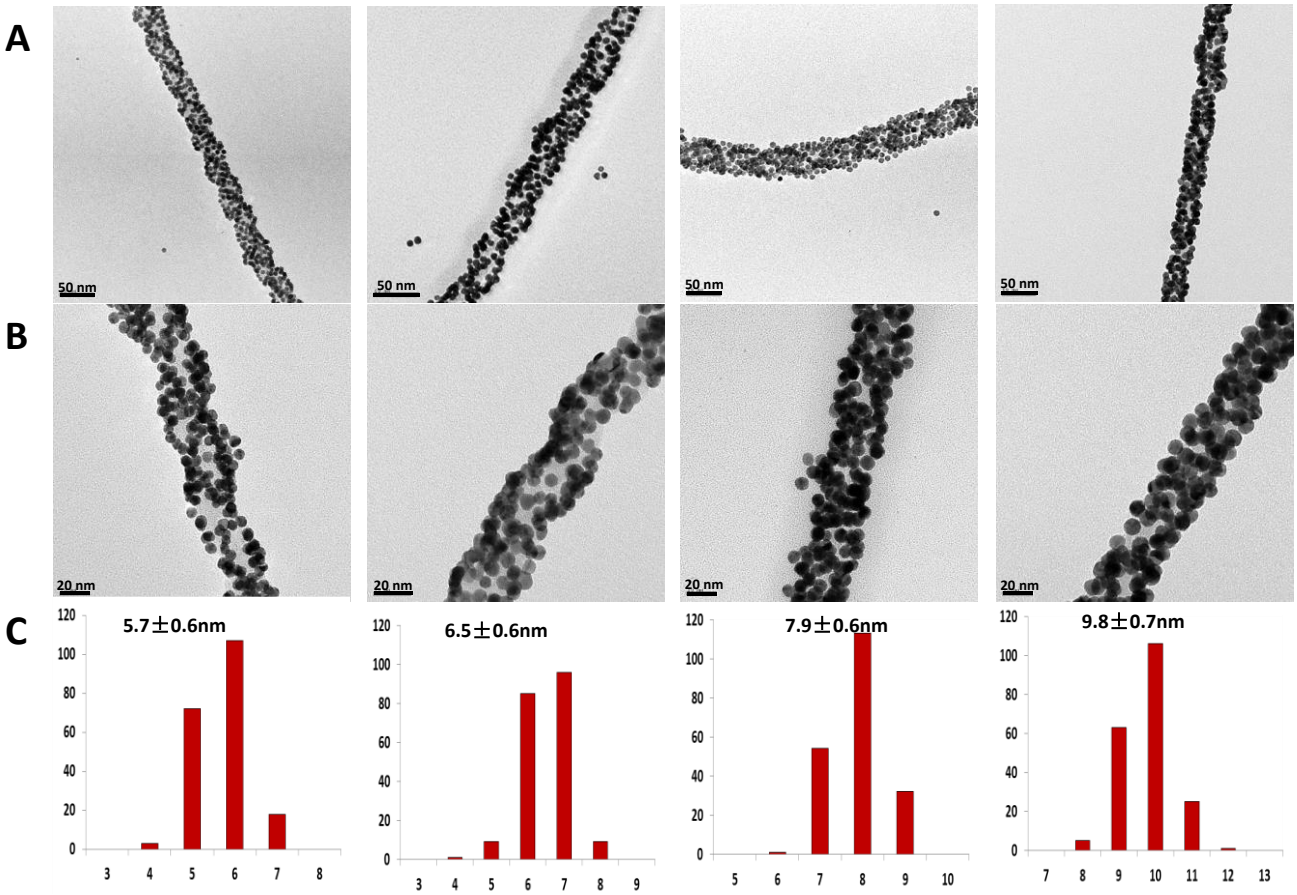

Figure 4.16-Adsorption of HOOC-PEG/TA-GNPs onto silica nanohelices. A and B: representative TEM images of 5-10nm HOOC-PEG/TA-GNPs + nanohelices-NH_2 and their high magnification images, respectively. C: corresponding size distribution of HOOC-PEG/TA-GNPs immobilized on silica surface based on TEM statistics for >200NPs. From left to right: 5.7±0.6nm, 6.5±0.6nm, 7.9±0.6nm, 9.8±0.7nm. All the scale bars are 20nm.

Interestingly, we found that the adsorption of smaller size HOOC-PEG/TA-GNPs (typically 4.0nm and 5.7nm) depends strongly on the amount of unreacted stabilizers (tannic acid potassium and tri-sodium citrate) that are remained after synthesis of bare TA-GNPs. Take 5.7nm HOOC-PEG/TA-GNPs for example, the TEM images in Figure 4.17-a) and b) show that, the adsorption of HOOC-PEG/TA-GNPs on the silica helical ribbons are quite different when 3/4 or 1/2 of the unreacted stabilizers is removed by centrifugation. When 3/4 of the stabilizer is removed (Figure 4.17 a)), a homogenous covered surface is observed while

1/2 of the unreacted stabilizers is removed, the TEM image shows that HOOC-PEG/TA-GNPs selectively follow the edges of the silica helical ribbons as it is shown in Figure 4.17-b). An illustrative scheme about these two observations is suggested as Figure 4.17e. Notably, a similar phenomenon can be observed as well in case of 4.0nm HOOC-PEG/TA-GNPs, in which more unreacted stabilizers have to be removed for the homogenous grafting (Figure 4.17c and d) but due to the weak excitation property, we will not focus on this type of GNPs for chiroptical study while it can be potentially useful for applications such as fluorescence, CT-imaging and biosensors.

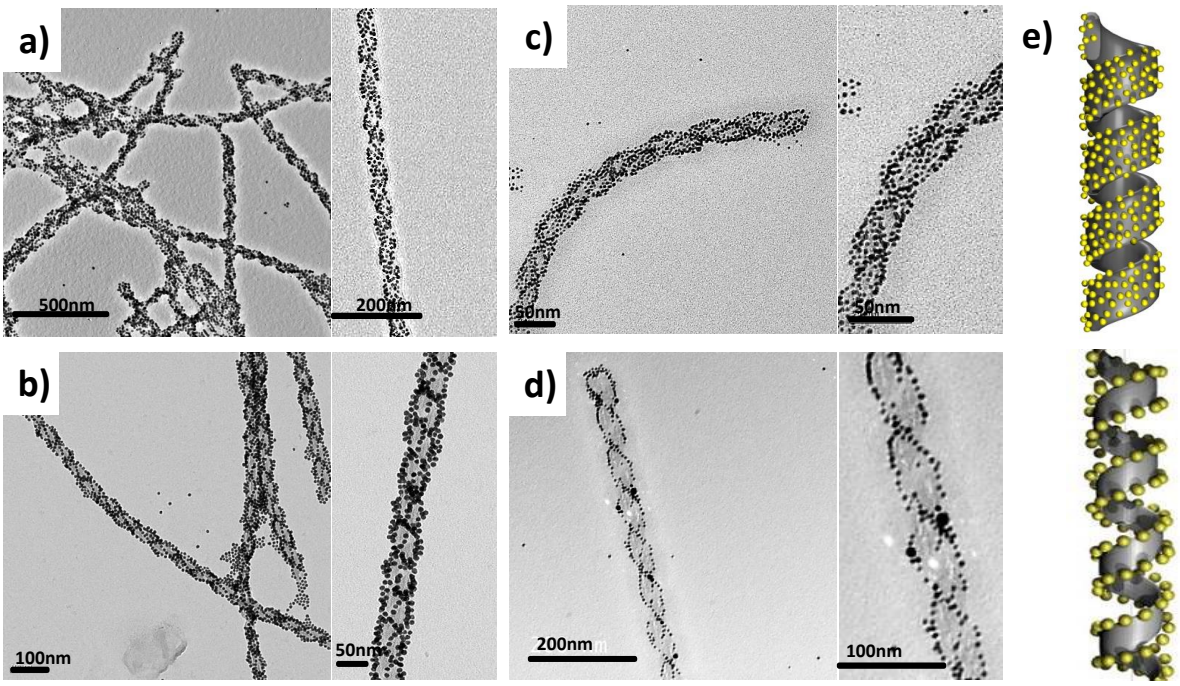

Figure 4.17-Stabilizer effects on adsorption of HOOC-PEG/TA-GNPs on silica helical ribbons. a): Adsorption of 5.7nm HOOC-PEG/TA-GNPs when 3/4 unreacted stabilizers are removed before ligand exchange; b): Adsorption of 5.7nm HOOC-PEG/TA-GNPs when 1/2 unreacted stabilizers are removed in advance; c): Adsorption of 4.0nm HOOC-PEG/TA-GNPs when 9/10 unreacted stabilizers are removed in advance and d): Adsorption of 4.0nm HOOC-PEG/TA-GNPs when 1/2 unreacted stabilizers are removed in advance. All inserts are the corresponding high magnified TEM images. e): illustrative frameworks of fully covered and edge-covered grafting of GNPs on silica nanohelices.

However, further investigation of these chiral nanostructures using 3D visualization with tomography technique (Figure 4.18) showed some of these images result from artifact during sample preparation. Indeed, Figure 4.19(b-d) shows that for the sample for which 1/2 of stabilizer are removed, HOOC-PEG/TA-GNPs are more likely to locate on the carbon film

close to the silica helical ribbons, not exactly on the edges. This phenomenon can be explained that the un-bonded GNPs move at the surface of silica nanohelices upon drying during sample preparation since there are only electrostatic interactions between NPs and amine modified silica nanohelices. The screening effect from the stabilizers on the surface of GNPs weakens the immobilization of NPs onto nanohelices-NH_2 surfaces.

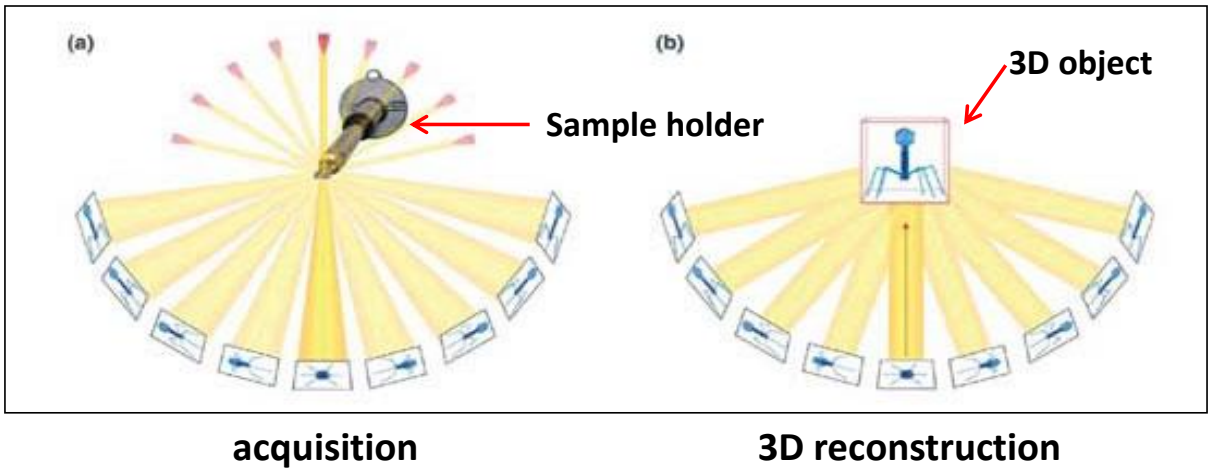

Figure 4.18-Illustration framework of 3D electron tomography. In a typical experiment, the sample holder (with specimen of interest) in (a) was tilted with certain angle (1 °) for multiple 2D projection acquisitions and then in (b), the collected 2D images from (a) was programed to rebuild the object in a 3D manner.

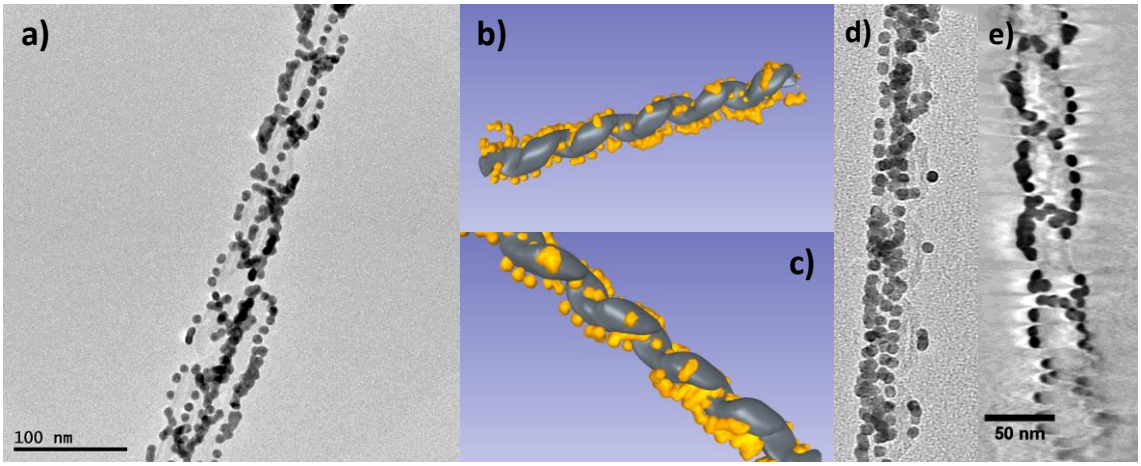

Figure 4.19-3D electron tomography of Goldhelix made from 5.7nm HOOC-PEG/TA-GNPs when 1/2 unreacted stabilizers are removed. a) Typical TEM image of the Goldhelix, b) and c), 3D modelling of a) with different incident angle, showing the non-homogeneity adsorption: the GNPs are located close to the helix at the surface of carbon film. Yellow particles are represented for HOOC-PEG/TA-GNPs and grey objects are the silica helical ribbons, d) a TEM image of a) at -75 °, indicating again the GNPs are on the

carbon film while not on the silica surface e) A lateral cross-section view of a).

Instead, when 3/4 stabilizers was removed (Figure 4.20), the observed nanostructures by the 3D reconstruction showed that the surface of silica surface is homogenously covered with TA-GNPs Figure 4.20-(B) to (F).

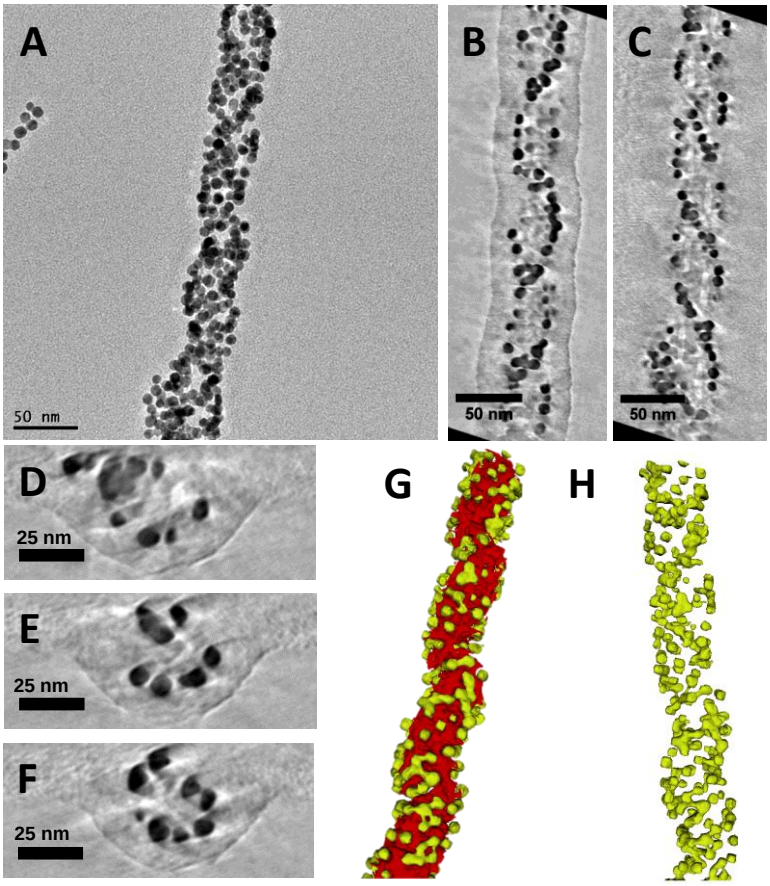

Figure 4.20-3D electron tomography of Goldhelix made from 5.7nm HOOC-PEG/TA-GNPs when 3/4 unreacted stabilizers are removed in the beginning. (A) Typical TEM image of the Goldhelix, (B) and (C), typical lateral cross-section views of (A), showing that GNPs are will organized on the silica surface at different lateral cross-section which confirms the homogeneity of the grafting; (D)-(F) transverse cross-section views of (A) at different height, (G) 3D reconstruction of the tomography of (A), showing the homogenous grafting of GNPs on silica nanohelices; (H) 180° rotation of (G) with peeling off the silica substrate. Yellow particles represent for 5.7nm HOOC-PEG/TA-GNPs and red objects are the silica helical ribbons.

3D electron tomography of Goldhelix made of 9.8nm HOOC-PEG/TA-GNPs is provided in Figure 4.21 as well. Apparently, when the size of the HOOC-PEG/TA-GNPs becomes bigger, the silica surface would be more densely covered in spite of the fact that the number of particles per surface area is decreased, meaning the packing density is not necessarily higher in

case of bigger HOOC-PEG/TA-GNPs. In addition, as illustrated from the cross-section views in Figure 4.21(B and C), with the increasing size of HOOC-PEG/TA-GNPs, the interparticle distance will become smaller and the overall nanostructure is more homogenous with respect to the helicity, which could be figured out easily when compare the 3D reconstruction images of Figure 4.20(G and H) with Figure 4.21(D and E).

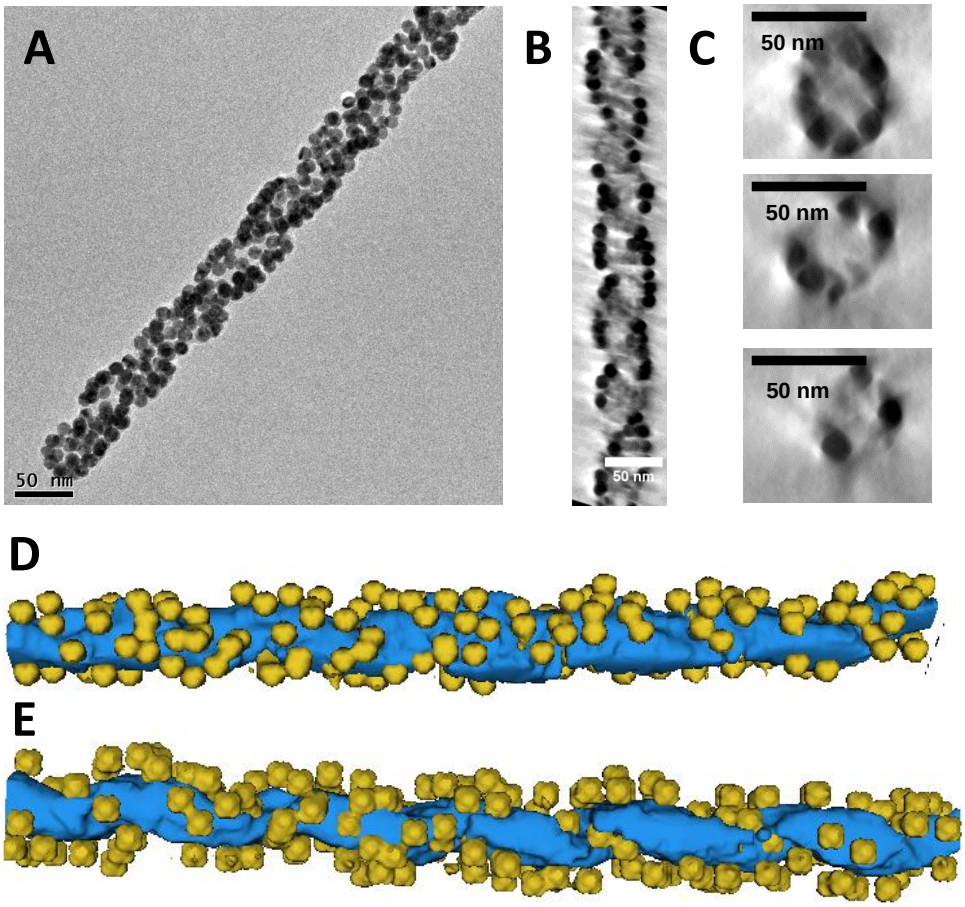

Figure 4.21-3D electron tomography of Goldhelix made from 9.8nm HOOC-PEG/TA-GNPs when 3/4 unreacted stabilizers are removed in the beginning. (A) Typical TEM image of the Goldhelix, (B) and (C), typical lateral and transverse cross-section views of (A), (D) 3D reconstruction of the tomography of (A), (E) 90 ° in plane rotation of (D). Yellow particles represent for 9.8nm HOOC-PEG/TA-GNPs and blue objects are the silica helical ribbons.

Now, if we look back to the question why the amount of unreacted stabilizers remained in colloids greatly affected the adsorption of GNP, a simple investigation on which of the substances (Tannic acid, K_2CO_3 and tri-sodium citrate) is the key factor for the difference was performed as it is shown in Figure 4.22. To find out the effects of each component separately, 0.5mL of these components with different combinations was added to the bare TA-GNPs

colloids instead of 0.5 mL Milli-Q water after centrifugation before adding SH-PEG_7-COOH. The concentration of each component (Tannic acid, K_2CO_3 and tri-sodium citrate) was finely adjusted to be equal to the initial solution. Intuitively, the tiny amount of K_2CO_3 from the protocol of synthesis is used for pH adjustment only and it would not significantly relate to the screening effect discussed above. As shown from the table in Figure 4.22, when tannic acid or tannic acid+ K_2CO_3 was used to replace the Milli-Q water, the gold colloids formed aggregations during purification. Whilst tri-sodium citrate was introduced, none of the three combinations (tannic acid+ tri-sodium citrate, tannic acid+ tri-sodium citrate+K_2CO_3 and tri-sodium citrate alone) aggregated during purification of GNPs after ligand exchange reaction, and particularly when tri-sodium citrate was used alone the GNPs could fully cover the silica surface as observed before. Given that tri-sodium citrate has less steric effect than tannic acid, when HS-PEG_7-COOH was added, it is easier to replace the tri-sodium citrate rather than tannic acid or its salt on the GNPs surface. Therefore, an intermediate negatively charged surface could be obtained, which accounts for the final immobilization onto nanohelices-NH_2. Moreover, as TEM observations indicated, when mixed stabilizers consisting of tannic acid and tri-sodium citrate were applied (see the cases of tannic acid+ tri-sodium citrate, tannic acid+ tri-sodium citrate+K_2CO_3), the adsorptions of GNPs are very inhomogeneous and only a few HOOC-PEG/TA-GNPs can be grafted on the silica surface. Here we envisaged that tannic acid or its counterions can inhibit the ligand exchange reactions, and itself can induce a strong interparticle repulsion effect which would decline further adsorptions of additional HOOC-PEG/TA-GNPs onto the surface of silica.[29]

References – page 183

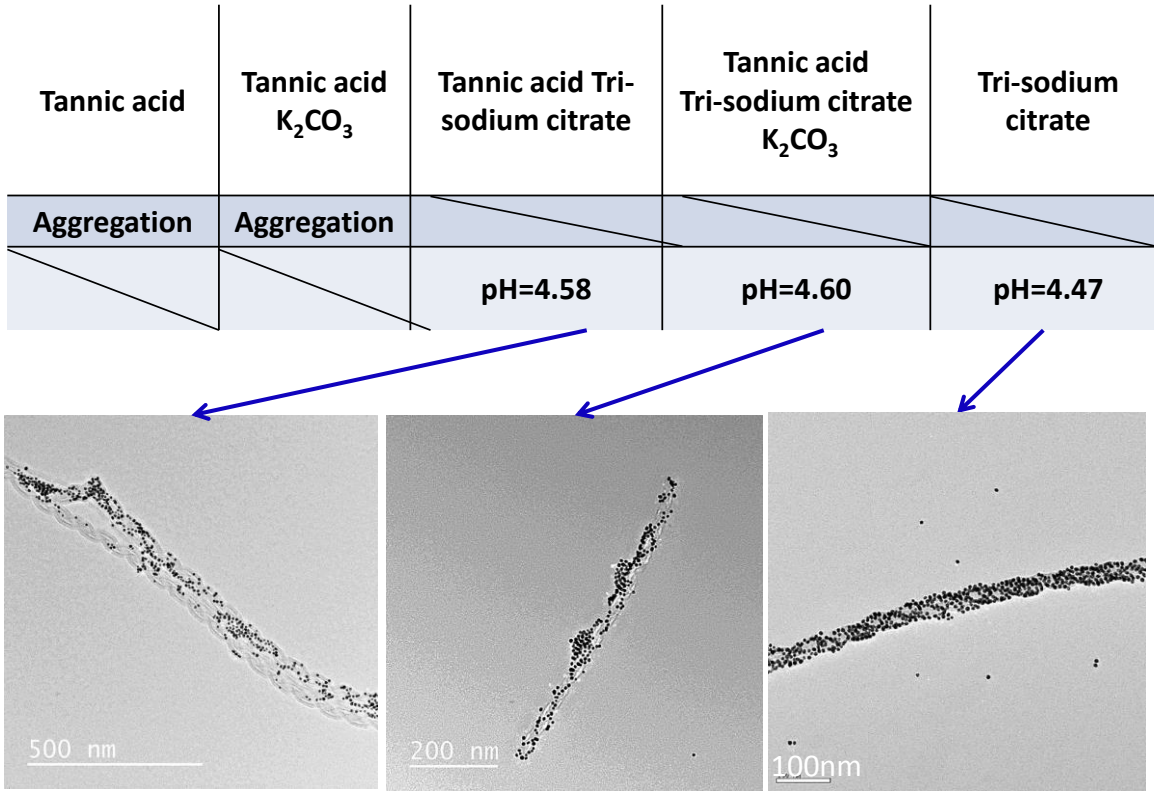

Figure 4.22-Stabilizers effects on the adsorption of HOOC-PEG/TA-GNPs. Top: a table of different combinations of stabilizers used for replacement of Milli-Q water in the protocol. Bottom: three typical TEM images of corresponding mixture results.

In summary, several routes for the synthesis of Goldhelix was presented in this section as summarized in Figure 4.23 below. Considering the homogeneity of the adsorption of GNPs and size effect for the optical properties, Goldhelix consisting of 5.7nm-9.8nm HOOC-PEG/TA-GNPs will be studied in the next section for chiroptical properties.

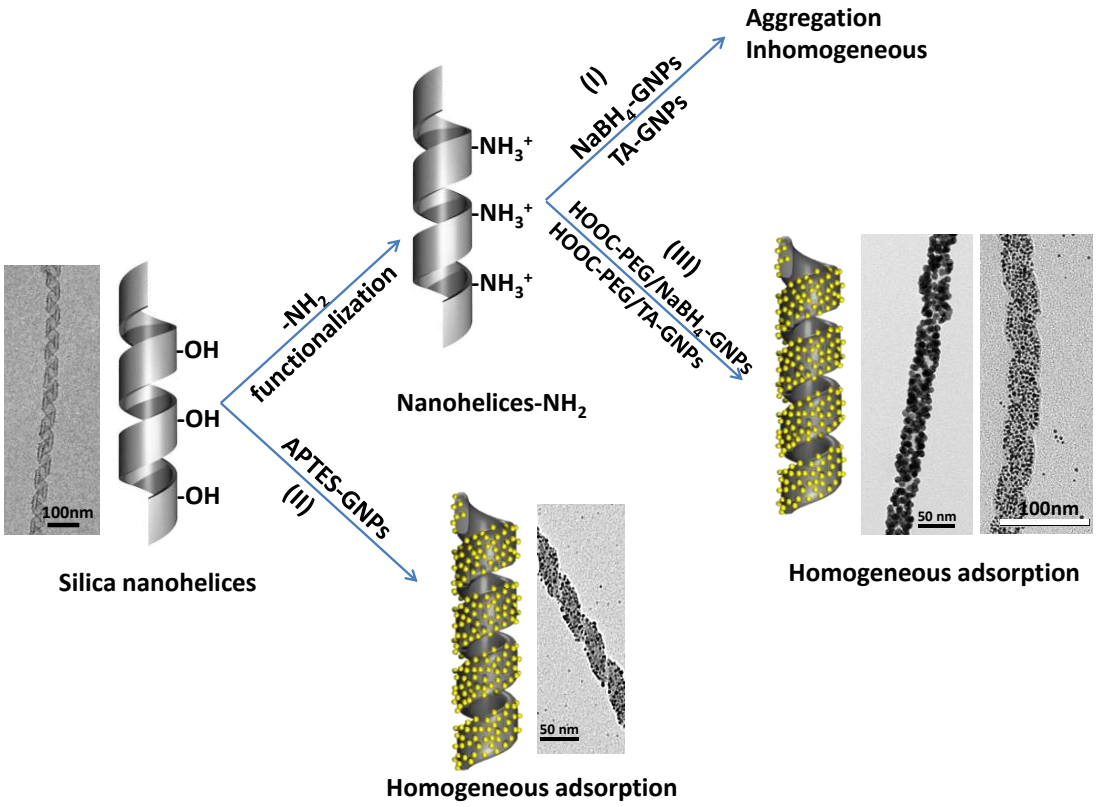

Figure 4.23- A summary of different approaches to the synthesis of Goldhelix.

References – page 183

3. Optical studies of Goldhelix

3.1 Chiroptical study and LSPR analysis of Goldhelix

Circular dichroism (CD) spectroscopy was employed to examine the optical activity of the as-synthesized Goldhelix in aqueous solution. In Figure 4.24-A to D, it shows that the Goldhelix with different sizes of HOOC-PEG/TA-GNPs adsorpted on silica helical ribbons can produce CD signals with a bisignate "dip–peak" shape around the plasmon resonance frequency of GNPs, these Goldhelix show opposite signals when assembled on left/right-handed silica helical ribbons; *i.e.* they generate negative-positive bisignate signal for right handed helices whereas with left handed helices, opposite signal is observed. Notice that there is no CD signal for free HOOC-PEG/TA-GNPs in visible range, therefore, if visible chiroptical activity at wavelengths corresponding to the collective surface plasmon resonance observed, it is due to the helical arrangement of the GNPs adsorbed on the silica surface. Indeed, when achiral GNPs are arranged in a chiral configuration with strong interparticle interaction (dipolar or multipolar), the chiroptical activity may occur at the electronic excitations of the GNPs with a magnitude depending on the strength of induced plasmonic coupling effect. Therefore, the bisignate CD signals is explained by the fact that the geometrical helical arrangement of the gold nanoparticles makes plasmonic coupling wave propagate along the helical directions, resulting in an enhanced adsorption to the incident light according to the handedness of the Goldhelix. The induced plasmonic CD (PCD) signal depends on particle size *a* and diameter of the helix *d*:[36-40]

$$\mathrm{CD}_{\text{plasmon-plasmon interaction}} \propto a^{12} / d^{8}$$

When the size of the GNPs is too small, *e.g.* less than 4nm (4.0nm HOOC-PEG/TA-GNPs and 4.0nm HOOC-PEG/$NaBH_4$-GNPs), the synthesized Goldhelix are silent in CD measurements. This is because too small GNPs will have no LSPR effect because they will behave more like molecules and lose the capability to produce surface plasmon resonance. Therefore, only results of 5.7nm-9.8nm HOOC-PEG/TA-GNPs are discussed here for the

induced plasmonic CD measurements. Furthermore, it is worthy to note that the interparticle distance is also an important factor. If this distance is too big with respect to the size of the NPs, the coupling effect between neighboring NPs would be negligible.[35]

In addition, when we compare the extinction spectrums of HOOC-PEG/TA-GNPs in Figure 4.9 with the absorption spectrums of Goldhelix shown in Figure 4.24(E and F), narrow extinction peaks were observed red-shifted and broadened from 520-525nm to around 550-580nm. Regarding that there is almost no red-shift observed in the surface ligand exchange process and the size of NPs remains basically the same before and after the adsorption on silica nanohelices, as seen from the TEM images in Figure 4.9, it ruled out that this big red-shift was due to the growth of the GNPs during ligand exchange reaction. Rather, as an increasing number of HOOC-PEG/TA-GNPs were added to the silica surface, the interparticle distance between neighboring GNPs became smaller, and nanoparticles were coupled when the distance between the particles was comparable to the nanoparticle size. Therefore, the localized surface plasmon resonance (LSPR) induced a red-shift at the surface plasmon wavelength, and this red-shift increased approximately exponentially as interparticle distance was reduced.[35] At the same time, the size of HOOC-PEG/TA-GNPs remain almost unchanged when adsorbed on the nanohelices-NH_2 (Figure 4.16C), and this excludes the possibility that GNPs can aggregate to form larger nonspherical asymmetric nanoparticles. [41]

References – page 183

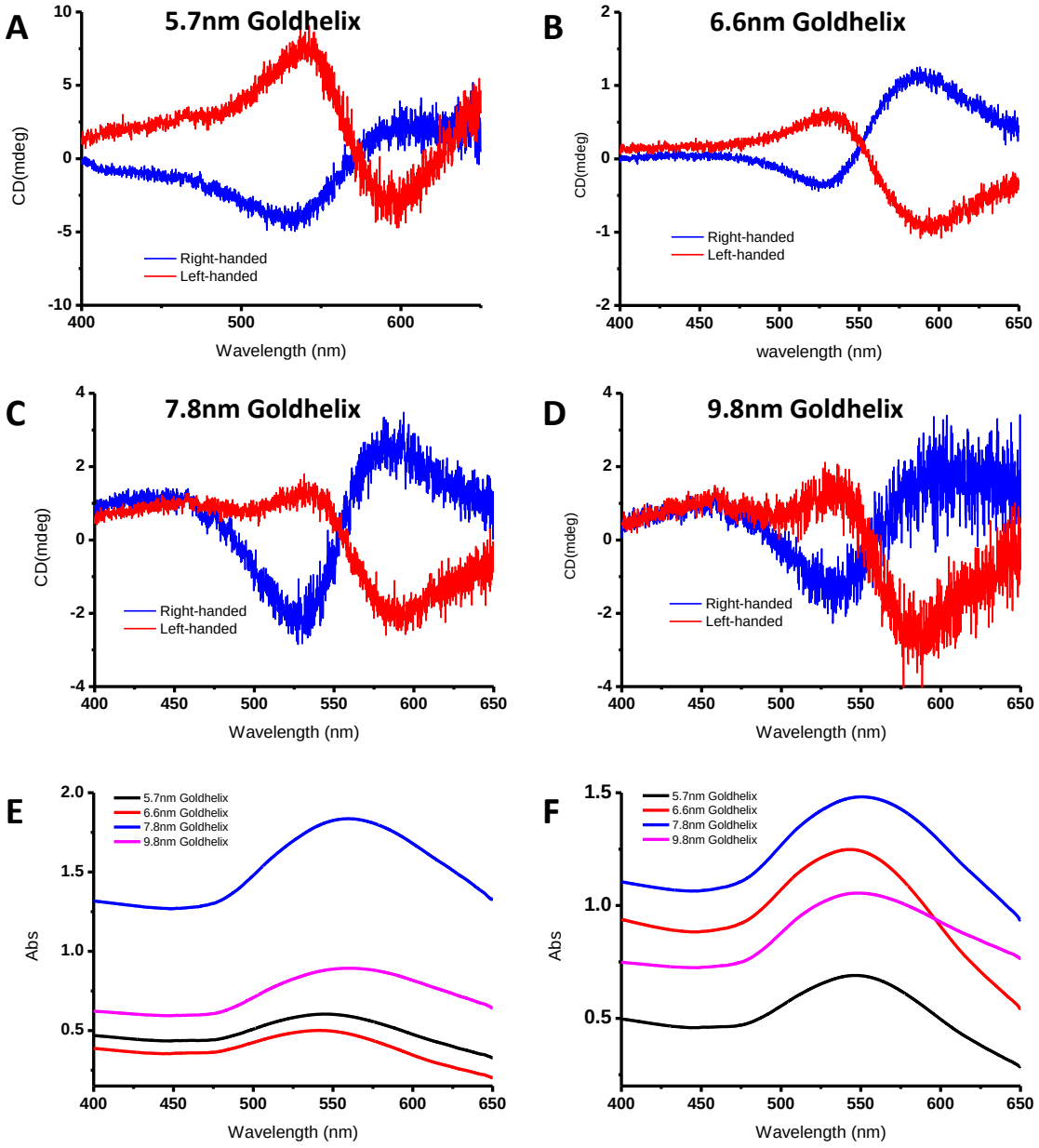

Figure 4.24- Chiroptical study on Goldhelix. (A)-(D): Typical raw electronic CD signals of Goldhelix made of 5.7nm, 6.6nm, 7.8nm and 9.8nm HOOC-PEG/TA-GNPs, respectively. Blue line represents for right-handed Goldhelix and red line represents for left-handed Goldhelix. (E) and (F): Corresponding extinction spectrums of right-handed Goldhelix and left-handed Goldhelix. Black line: 5.7nm HOOC-PEG/TA-GNPs, red line: 6.6nm HOOC-PEG/TA-GNPs, blue line: 7.8nm HOOC-PEG/TA-GNPs and pink line: 9.8nm HOOC-PEG/TA-GNPs. In (E), the absorption peaks are around 553nm, 548nm, 566nm and 574nm, respectively; and in (F), the absorption peaks are around 553nm, 554nn, 569nm and 563nm, respectively.

3.1.1. Size dependency of GNPs on plasmonic circular dichroism

Note that LSPR of metal NPs also depends strongly on the size of the NPs along with

their arrangement.[38, 39, 42-44] To date, much research has been done to investigate the effects of the size and arrangement of GNPs on PCD signal. N-L. Rosi and his co-workers for instance,[37] reported that peptide conjugated with GNPs could have chiral plasmonic optical behavior which can be carefully tuned by adjusting the size of GNPs and their arrangement. They pointed out in their simulation, based on discrete dipole approximation (DDA) method[45, 46], when the size of the GNPs increased from 7nm to 11nm, the magnitude of PCD signals could be amplified from 5 mdeg to over 40 mdeg and each 1nm increment on the diameter of GNPs would result in a great enhancement on the PCD activity, suggesting that GNPs smaller than 7nm could only have a very weak PCD signal with a magnitude no more than 5 mdeg. Generally, it is believed that when the size of GNPs is down close to 5nm, the dipole-dipole interactions between two closely located GNPs will be greatly vitiated, moreover, if it is smaller than 3nm, there will be no localized surface plasmon excitation. Here, we showed the optical activities of approximately 5-10nm GNPs with a well-defined PCD signal that is nearly consistent with the simulation based on peptides or DNA[47] for chiroptical behavior. It is however worthy to note that since the work presented by Rosi did not provide information about normalizations based on parameters such as concentration, we are not able to directly compare silica nanohelices to peptides or DNA in terms of capability of inducing plasmonic chirality as templates.

To understand the PCD signals produced by the plasmonic nanoparticles, it is important to quantify the signal in order to eliminate the concentration effect on the capability with respect to the observed PCD signals. Since induced electronic CD signal presents the power on light polarization of a certain medium in UV range and it is based on the adsorption by the substance. The absorption can be easily understood as Beer's law states. Circular dichroism (CD) is usually measured as the differential absorbance of left (A_{LCP}) and right circularly polarized (A_{RCP}) light, and so can be expressed as:

$$\Delta A = A_{LCP} - A_{RCP}$$

References – page 183

Using Beer's law to induce the concentration and pathlength of the incident light, we can obtain the molar circular dichroism ($\Delta\varepsilon$).

$$\Delta\varepsilon = \varepsilon_{LCP} - \varepsilon_{RCP} = \Delta A / (C \times l)$$

Where ε_{LCP} and ε_{RCP} are the molar extinction coefficients for LCP and RCP light respectively. C is the molar concentration and l is the pathlength in centimeters.

The degree of ellipticity (θ) is defined as the tangent of the ratio of the minor to major elliptical axis, and is illustrated as below:[48]

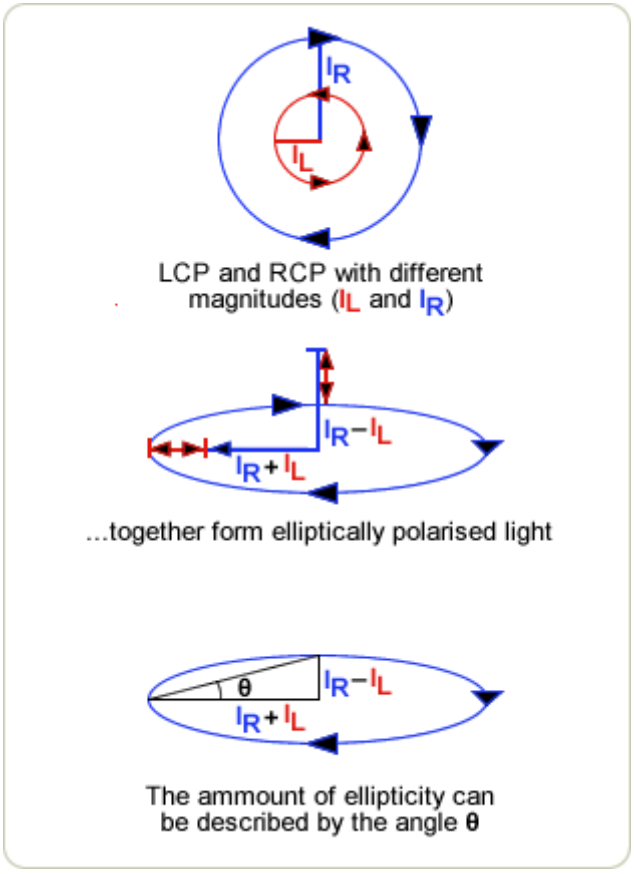

Where linear polarized light has zero degrees of ellipticity (θ), while fully LCP or RCP will have + or - 45 degrees respectively.

The merit of employing ellipticity as a measurement unit is because it can be easily related to optical rotation measurements and polarimetry. Both ellipticity and optical rotation are measurements of changes in polarization state of a linear polarized analyzer beam, and both have the same units and similar amplitudes for a given sample. With the unified unit, it is

therefore much more convenient to compare the optical rotation power of the system, which can be used to visualize the circular dichroism property of a given sample.[48]

On the other hand, it is very easy to make a conversion between θ and ΔA via mathematic tangent relation of ellipticity defined as above:

$$\tan\theta = \frac{E_R - E_L}{E_R + E_L},$$

$$\theta(radians) = \frac{\left(I_R^{1/2} - I_L^{1/2}\right)}{\left(I_R^{1/2} + I_L^{1/2}\right)} = \frac{e^{\Delta A\frac{\ln 10}{2}} - 1}{e^{\Delta A\frac{\ln 10}{2}} + 1},$$

$$\theta(\text{degrees}) = \Delta A(\frac{\ln 10}{4})(\frac{180}{\pi}),$$

which means:

$$\Delta A = \theta / 32.982,$$

Where θ is often quoted as millidegrees.

Similarly, Molar ellipticity can be also deduced in the same way as ΔA. According to Beer's law, we can derive a measurement of molar ellipticity [θ]. Following corresponding conventions, molar ellipticity is reported in degrees $cm^2\ dmol^{-1}$, or degrees $M^{-1}m^{-1}$ which are equivalent units.[48]

Then, molar ellipticity can be calculated using the following equation:

$$[\theta] = 100 \times \theta / (C \times l),$$

Where C is the concentration in molar, and l the cell pathlength in centimeter. The factor of 100 converts to pathlength into meters.

Thereby, molar Circular dichroism and molar ellipticity can be converted directly by:

$$\Delta\varepsilon = [\theta] / 3298.2.$$

References – page 183

With these conversions, the molar circular dichroism and molar ellipticity can be obtained provided the concentration of nanohelices-NH_2 that accounts for the PCD signal is known in advance. However, it is in fact not easy to measure the concentration (number/volume) of silica nanohelices in standard units. To overcome this problem, an estimation based on surface plasmon approximation was done via calculations on the concentration of HOOC-PEG/TA-GNPs on the silica surface and statistics analysis.[49-53] In general, the concentration of gold colloids can be determined by the UV-vis spectrum, therefore it is possible to obtain the total amount of HOOC-PEG/TA-GNPs grafted onto the surface of silica nanohelices by subtracting the unreacted HOOC-PEG/TA-GNPs from the original HOOC-PEG/TA-GNPs colloids. Then, if we consider the helical pitch as the smallest repeating unit of silica helical ribbon which is about 67nm and the average length of silica helical ribbons is known around 350nm, the average number of HOOC-PEG/TA-GNPs on one particular silica helical ribbon can be indirectly averaged by counting the number of HOOC-PEG/TA-GNPs in one helical pitch for >30 acquisitions. Afterwards, the concentration of nanohelices-NH_2 that accounts for the CD signal could be estimated by using the concentration of HOOC-PEG/TA-GNPs obtained from extinction spectrum divided by the number of HOOC-PEG/TA-GNPs nanoparticles on one helical ribbon estimated from TEM images (See Experimental session). The typical data is shown in Table 4.2 as below:

Table 4.2-Corresponding number of HOOC-PEG/TA-GNPs in one pitch from TEM images (More than 30 acquisitions are applied for each type of HOOC-PEG/TA-GNPs) and calculated concentrations of silica helical ribbons accounting for the observed CD signals with different sizes of HOOC-PEG/TA-GNPs:

Sizes of TA-GNPs/PEG-COOH on Goldhelix	N_{GNPs} per pitch	$C_{silica\text{-}L}$ for CD ($M10^{-10}$)	$C_{silica\text{-}D}$ for CD ($M10^{-10}$)
5.7nm	55	3.390	2.347
6.6nm	44	2.523	4.265
7.8nm	32	6.700	7.149
9.8nm	27	5.390	9.317

After obtaining the concentrations of the silica nanohelices that accounts for the PCD signals, the correlated PCD spectrums with molar circular dichroism and molar ellipticity can be calculated, respectively. If we assume that the grafting of GNPs are the same for left-handed and right-handed Goldhelix, the induced PCD signals should have the same background noise and the same magnitude of light rotation power with exactly mirrored positive and negative PCD signals. Thereby, it is possible to remove the background by mutually subtracting the measured PCD signals of left-handed and right-handed Goldhelix by:

$$CD_L^{measured} - CD_D^{measured} = 2CD_L^{real}$$

$$CD_D^{measured} - CD_L^{measured} = 2CD_D^{real}$$

In this way, after smoothing the obtained CD signals the size effect on the induced plasmon CD signal becomes clear as it is shown in Figure 4.25. As it is anticipated, the normalized CD signals show that the PCD signals as well as the extinction spectrums both shift to higher wavelength with increasing size of the HOOC-PEG/TA-GNPs. More interestingly, the observed bisignate cotton effects are also amplified due to the enhancement of dipole-dipole interaction between neighboring GNPs as increasing the size of HOOC-PEG/TA-GNPs. These observations simply assert that the induced PCD activities increase with increasing size of the HOOC-PEG/TA-GNPs, probably both due to the

enhancement of the LSPR effects of individual NPs and the amplification of plasmonic couplings between neighboring NPs.

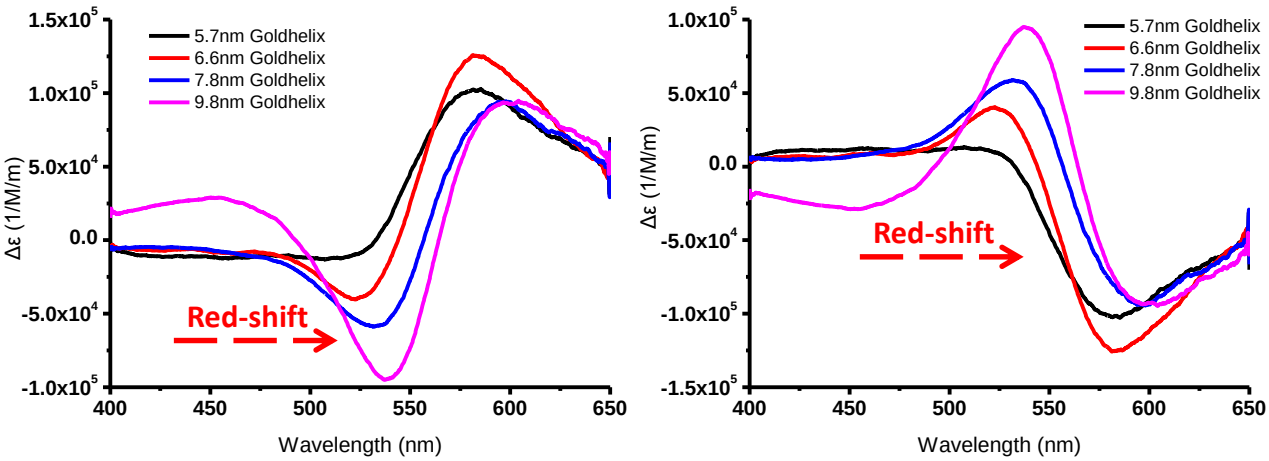

Figure 4.25- Size effects on PCD activities of Goldhelix. A and B, smoothed CD spectrums of right-handed and left-handed Goldhelix after removing the background noise, respectively. In all plots, black line: 5.7nm HOOC-PEG/TA-GNPs, red line: 6.6nm HOOC-PEG/TA-GNPs, blue line: 7.8nm HOOC-PEG/TA-GNPs and pink line: 9.8nm HOOC-PEG/TA-GNPs.

Since the induced PCD activity depends both on the structure of the individual GNP and their arrangement,[38] it is difficult to control the interparticle distance and the particle numbers in order to investigate the size-dependency or structural dependency separately. Therefore, very often simulations based on approximations such as DDA method concerning the arrangement of GNPs assemblies were employed for a theoretical modelling support. Govorov et al [38, 39, 44], for example, showed that helical arrangement of GNPs can be more efficient in terms of polarizing light than pyramid or tetrahedral organizations, and depending on the packing parameters, the molar circular dichroism of helical gold nanoparticles assemblies can vary from ~10^5 to 10^7 ($M^{-1}\bullet m^{-1}$), which is comparable to our system (~10^5 $M^{-1}\bullet m^{-1}$) meaning the synthesized Goldhelix could exhibit similar polarization capability. Another interesting point is in our case, the only resource for chirality is the morphology of silica itself and the induced organization if GNP at its surface. Unlike achiral metal particles in the presence of chiral ligands, where the induced chiral CD signal derives from $CD_{molecule}$ plus $CD_{plasmon}$[36], the observed CD signals here are completely attributed to interparticle electronic coupling. This finding may help reveal the mechanism of dipole-dipole

interactions between noble nanoparticles without the effect of substrates and provide an ideal model for study on induced chirality.

Furthermore, the optical activity of chiral systems is often measured through the dimensionless Kuhn factor (g-factor):[54]

$$g = \frac{\Delta\varepsilon}{\varepsilon}$$

Where $\Delta\varepsilon$ and ε are the molar circular dichroism and molar absorptivity, respectively.

With the help of g-factor, the optical activity of Goldhelix can be estimated without information on the molar mass, sample concentration, or sample path length. Figure 4.26A shows the typical relationship between g-factor of Goldhelix consisting of differed size of HOOC-PEG/TA-GNPs and the incident wavelength. First of all, the concomitant increase of g-factor maximal value (g_{max}) as the size of GNPs increased from 5.7nm to 9.8nm (Figure 4.26B), indicates the capability of the Goldhelix to polarize incident light increases with the size of GNPs. Secondly, when compared with other similar chiroptical systems with spherical nanoparticles in UV region, the capability of Goldhelix to generate circular polarization of light is much greater than gold nanoparticles with the same size(~10nm for example) bunched on organic molecules in which g_{max} is normally~10^{-5}[55, 56], this enhancement would be probably due to the accumulated dipole-dipole and multipole-multipole interactions between closely packed GNPs as stated before.

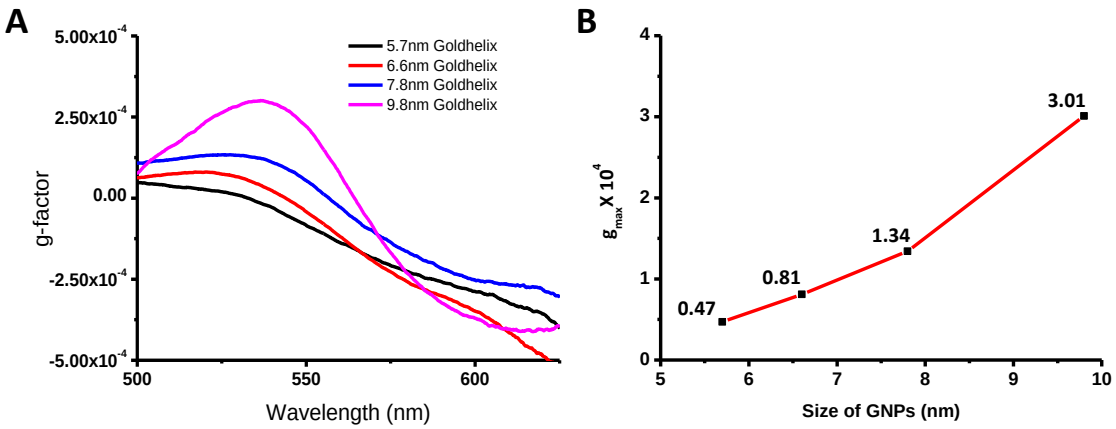

Figure 4.26-A: typical plot on g-factor spectrums of left-handed Goldhelix made by different sizes of HOOC-PEG/TA-GNPs. In the plot: black line represents for Goldhelix consisting of 5.7nm HOOC-PEG/TA-GNPs, red line: 6.6nm HOOC-PEG/TA-GNPs, blue line: 7.8nm HOOC-PEG/TA-GNPs

and pink line: 9.8nm HOOC-PEG/TA-GNPs; B: corresponding plot of g_{max} value to the sizes of HOOC-PEG/TA-GNPs used for the formation of Goldhelix.

3.1.2. Quantity and pH effects on PCD signal

After studying the size dependency on PCD signal, we then evaluated the quantity and pH effects on the CD signals so as to find out the optimal conditions for enhancing the power of light polarization induced by such systems. First, the relation between the PCD signal and the quantity of silica nanohelices used as self-assembling template was investigated. A typical experiment was conducted in which 500μL of 9.8nm HOOC-PEG/TA-GNPs was prepared, and different amount of nanohelices-NH_2 was added and kept on roller-mixer overnight followed by washing with Milli-Q water (See experimental session). The results of typical TEM images and PCD spectrums were shown in Figure 4.27. Obviously, when there is no silica template, no PCD signal is recorded. When excessive amount of silica helical fibers was added, *e.g.* weight ratio of 5.4:1 (silica to GNPs), again no PCD signal is observed. In this case all the GNPs will be absorbed and precipitated due to the scaling effect of nanohelices-NH_2. The PCD signal actually measures the supernatant which most probably consists of only water. When appropriate weight ratios of silica to the modified HOOC-PEG/TA-GNPs were used, between 1.35:1 to 4.05:1, bisignate PCD spectrums then can be obtained the optimal ratio being around 2.7:1, from which more amplified PCD signals were collected than any other cases no matter reacted with L- or D- silica helical ribbons.

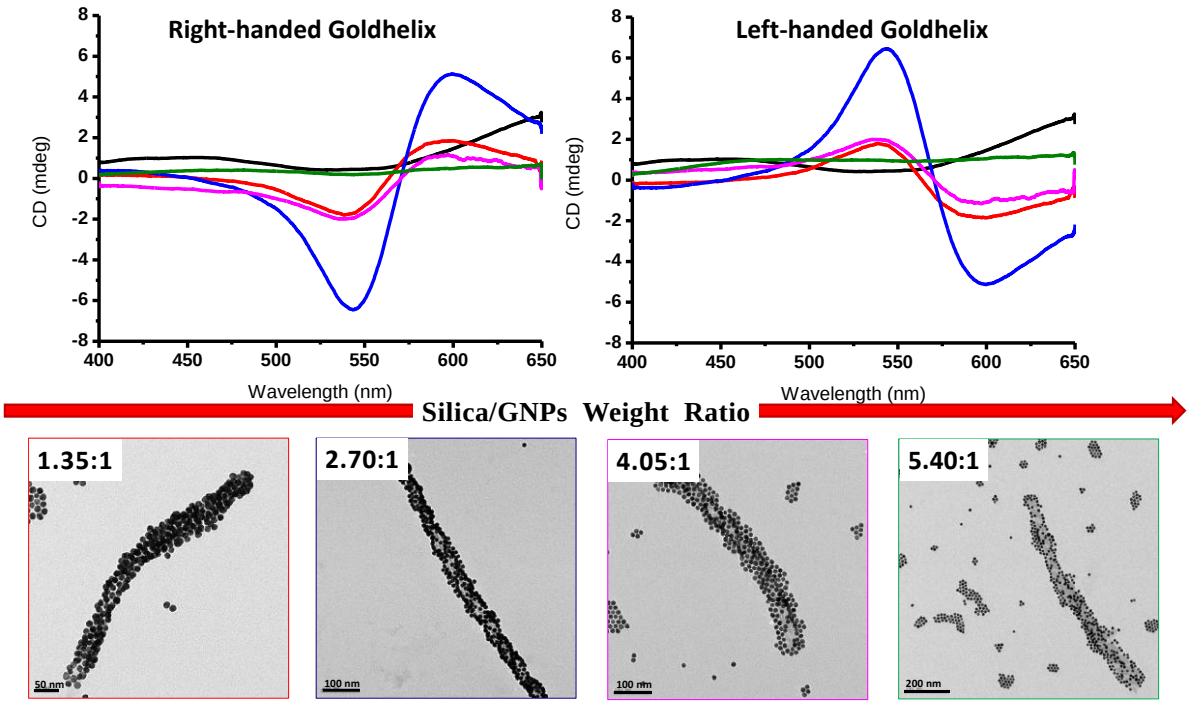

Figure 4.27-Study on quantity effects on PCD signals of Goldhelix. Top: normalized CD spectrums of right-handed and left-handed 9.8nm Goldhelix consisting of different weight ratios of silica helical ribbons to HOOC-PEG/TA-GNPs, respectively. Bottom: Corresponding TEM images of Goldhelix as increasing the weight ratio. The weight ratios between silica helical ribbons to 9.8nm HOOC-PEG/TA-GNPs are 0:1(black lines), 1.35:1(red lines), 2.70:1(blue lines), 4.05:1 (pink lines) and 5.40:1 (green lines).

We then study the pH effects on the adsorption and CD activity. Similarly, 500μL of 7.8nm HOOC-PEG/TA-GNPs was prepared at the beginning, and then 75μL of 0.8 mg/mL (right-handed/left-handed) nanohelices-NH_2 (when smaller GNPs was used, the optimal amount of silica would be slightly higher than the case for 9.8nm HOOC-PEG/TA-GNPs simply because the system is more stable than decorated with heavier NPs.) was injected. The mixture was incubated on roller-mixer overnight and followed by proper purification steps. To study the pH effect, 0.1M hydrochloride acid was used to adjust the pH of the suspension and monitored by pH meter. The normalized PCD signals are shown in Figure 4.28. As clearly observed both by TEM images and PCD signals, less GNPs adsorption is observed as the pH value goes down. This is probably because the surface charge of GNPs decreases due to the protonation of acid groups (pKa~4.2) on the surface of GNPs at lower pH. The results of both L- and D- Goldhelix show that at pH=4.0, the Goldhelix start to precipitate and give very weak PCD responses as the pink lines represent in the figure. This is well in line with

observed inhomogeneous coverage of the GNPs on silica surfaces from the TEM images. At higher pH value, around 5.0-5.5 (red and black lines) stronger PCD signals are observed as confirmed by the corresponding TEM images in which silica nanohelices are more homogenously covered by GNPs. These results support the above discussion and proved that the best condition is around pH=5.0 with the addition of strong acid. With this amount of hydrochloride acid, the interface between nanohelices-NH_2 and HOOC-PEG/TA-GNPs could have the most appropriate affinity and relatively stable environment for GNPs immobilization.

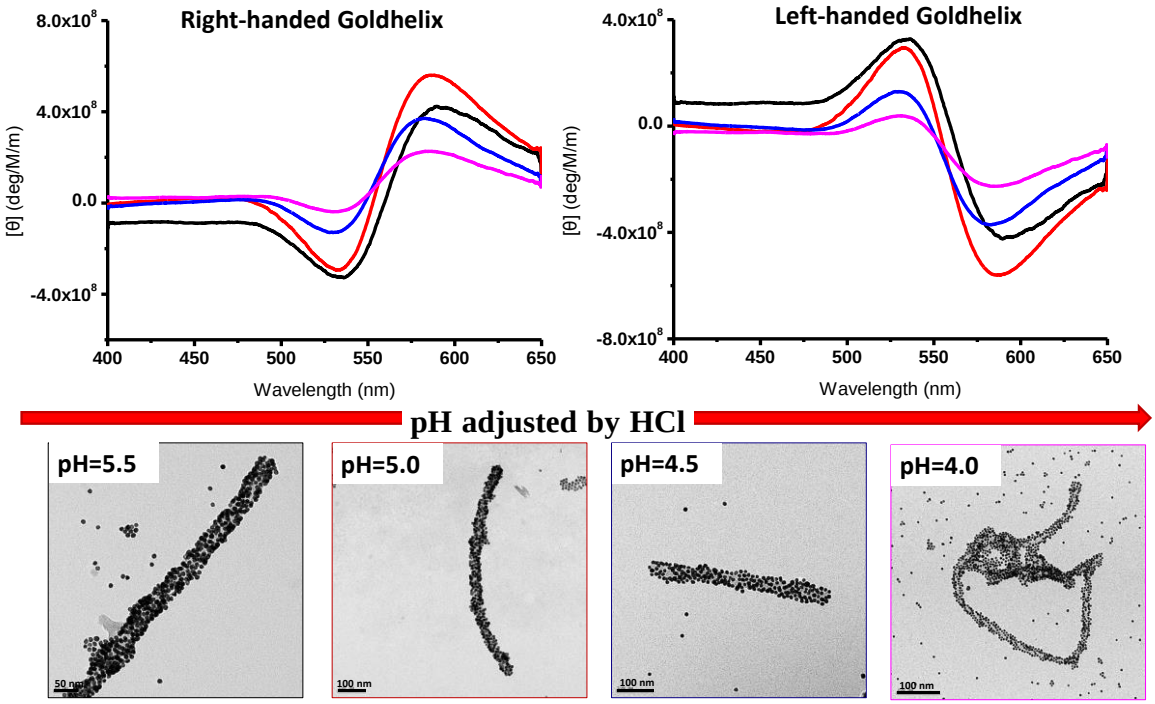

Figure 4.28-Study on ion effects on PCD signals of Goldhelix. Top: normalized CD spectrums of right-handed and left-handed 7.8nm Goldhelix with different pH adjusted by 0.1M HCl. Bottom: Corresponding TEM images of Goldhelix as decreasing the pH value by HCl. In all the spectrums and images, the black color represents for pH=5.5, red color: pH=5.0, blue color: pH=4.5 and pink color: pH=4.0.

3.2 Polarization-resolved light scattering study on magnetic properties

The scattering properties of such unique nanostructures are seldom studied from the point view of magnetism, whilst they would provide a lateral profile of the materials in a sense of induced magnetic dipole (MD) movement and its potential capability for

magnetization. At plasmon frequency, the GNPs on the Goldhelix are strongly polarized by plasmonic currents due to free electrons. From what we have observed in UV and electronic CD spectrometers, we expect this electromagnetic coupling of the GNPs to form a helical plasmonic current as the helical organization indicated. If so, such helical plasmonic current should generate magnetic moment along the helical axis which should generate corresponding MD mode in axial polarization. To verify such assumption, a static light scattering settlement was assembled with controlled polarized light source as illustrated in Figure 4.29 below:

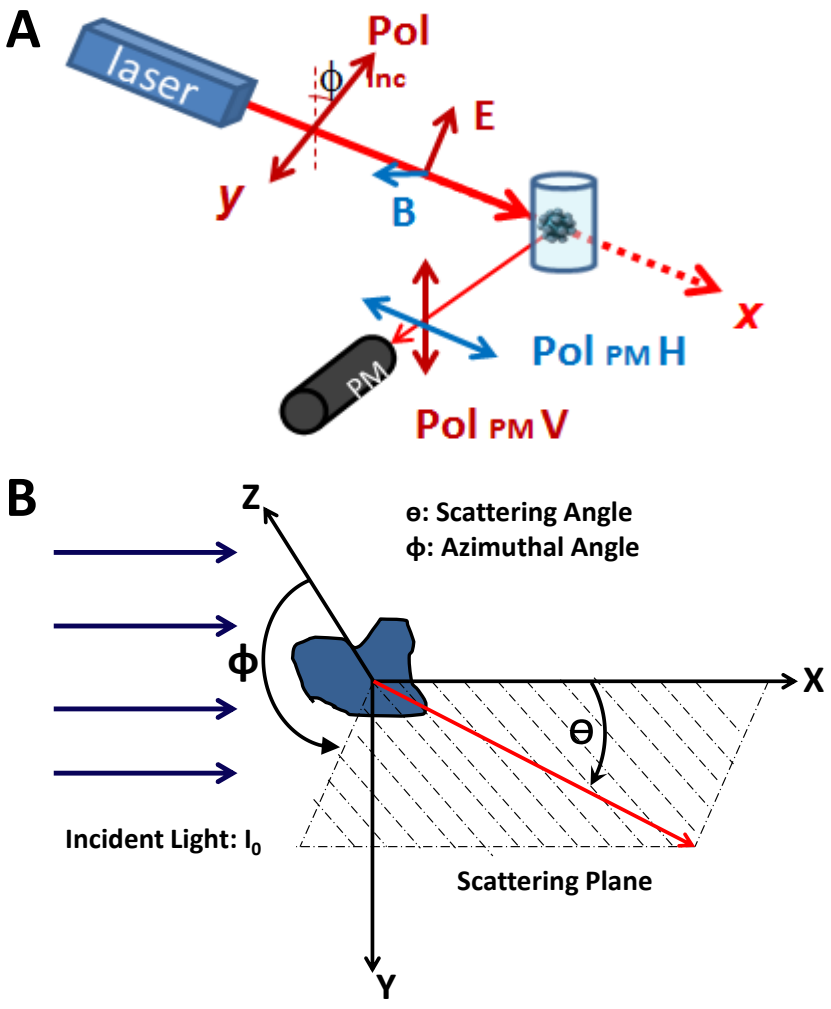

Figure 4.29- A: schematic illustration of polarization-resolved light scattering set up. The polarization and angular distribution of scattered light are illustrated in the transverse plane (perpendicular to the incident polarized laser beam); B: geometrical definitions of light scattering angle (ɵ) and azimuthal angle (ϕ).

As it is stipulated, the optical scattering measurements in atomic and molecular gases and anisotropic liquids have been adequately explained by isotropic and anisotropic response

of scatterers using the electric dipole (ED) approximation which is realized when (a) the absorption is negligible and (b) the radius a of the scatterer and the wavelength λ satisfy $ka \ll 1$, where $k = 2\pi / \lambda$. Nevertheless, further improved by inclusion of the induced MD contribution which can lead to a closer calculation to the exact results from Mie theory, N. L. Sharma[57] has proved that by observing the polarization and angular distribution of scattered light in the transverse plane, the plane perpendicular to the incident polarized laser beam it is possible to observe both ED scattering induced by the electric field of the incident light with its $\sin^2\phi$ angular distribution and transverse polarization, and a small fraction of scattering light that has an $\cos^2\phi$ angular distribution and axial polarization which could be understood either as the MD radiation produced by the magnetization induced in the target by the magnetic field of the incident light or as the induced electric quadrupole (EQ) radiation driven by the electric field gradient that exists along the direction of propagation of the incident light or a superposition of both of the above.

In particular, when scattering angle θ is 90 °, these relations could be extrapolated as[57]:

$$I_\phi(\phi) = I_{inc} \frac{\mu_0^2 \omega^4}{16\pi^2 r^2} \alpha_e^2 \sin^2\phi \quad \text{[Transverse]}$$

$$I_z(\phi) = I_{inc} \frac{\mu_0^2 \omega^4}{16\pi^2 r^2} \left[\frac{\alpha_m^2}{c^4} + \frac{\omega^2 \alpha_Q^2}{36c^2} \right] \cos^2\phi \quad \text{[Axial]}$$

Where $I_{inc} = (1/2)\varepsilon_0 c E_0^2$ is the intensity of the incident light and $\alpha_e, \alpha_m, \alpha_Q$, are, respectively, the induced electric, magnetic, and quadrupole polarizabilities of the scatterers. ϕ is azimuthal angle.

It then becomes possible to exploit this MD-EQ scattering to determine the magnetic response of a medium to incident light. In fact, as shown both experimentally and theoretically by S. L. Oliveira and S. C. Rand[58], the induced magnetic moment perpendicular to the electronic polarization can not only produce dipole radiation that is one fourth that produced by the electric field during linear optical interactions, but it can also result in intense nonlinear magneto-optic effects such as the magnetic dipole continuum emission. The existence of strong magnetic response at optical frequencies has important

implications for linear and nonlinear optics alike. Resonant response would offer the prospect of tunable magnetic dispersion and negative permeability as needed to synthesize low-loss, homogeneous liquid or solid optical materials with negative refractive indices for ‘‘perfect lenses’’[59, 60], magnetic mirrors[61, 62], nanolithography, and electromagnetic cloaking[63-66] in very simple ways. Therefore, based on both theories and practical results, a preliminary study on the light scattering properties of our Goldhelix will be conducted in this chapter and further discussions about how measured scattering phenomenon can associate to the magnetic properties and some useful comparisons between models will be introduced as well.

As described above, both ED and MD movements of a liquid sample can be observed by using light scattering resources, where the total scattering intensity consisting of ED ($\sin^2\phi$ dependence), and MD plus EQ radiation ($\cos^2\phi$ dependence). This means, as illustrated in Figure 4.29, if some special value of azimuthal angle were provided, for example 90 degree (scattering plane is vertical to the x-z plane), it is possible to get pure ED scattering intensity which can be denoted as I_{VV} afterwards, while if it is zero degree or the scattering plane is horizontal to the x-z plane, it is possible to get the intensity of MD together with EQ radiation (denoted as I_{VH}).[57] Therefore, it becomes possible to figure out the relation between scattering intensity of electric dipole and magnetic dipole plus quadrupole radiation.

Sparked by this idea, the measured scattering intensities of I_{VH} and I_{VV} of Goldhelix could be used to calculate the fraction of I_{VH} to I_{VV} (I_{VH}/I_{VV}) and plotted as function of wavelength. Figure 4.30 shows the value of I_{VH}/I_{VV} with different sizes of Goldhelix. The results shows that disregard the size of NPs (5-10nm), the MD+EQ scatterings in Goldhelix are clearly recorded. But when GNPs alone or silica helical ribbons alone the measured MD+EQ scatterings are nearly zero, suggesting that the assembling of GNPs induces not only electric dipole coupling as stated above but also magnetic and quadrupole couplings as well. Moreover, a maximum fraction of ~10% in I_{VH}/I_{VV} is obtained at a wavelength around 580nm in the case of 9.8nm Goldhelix.

References – page 183

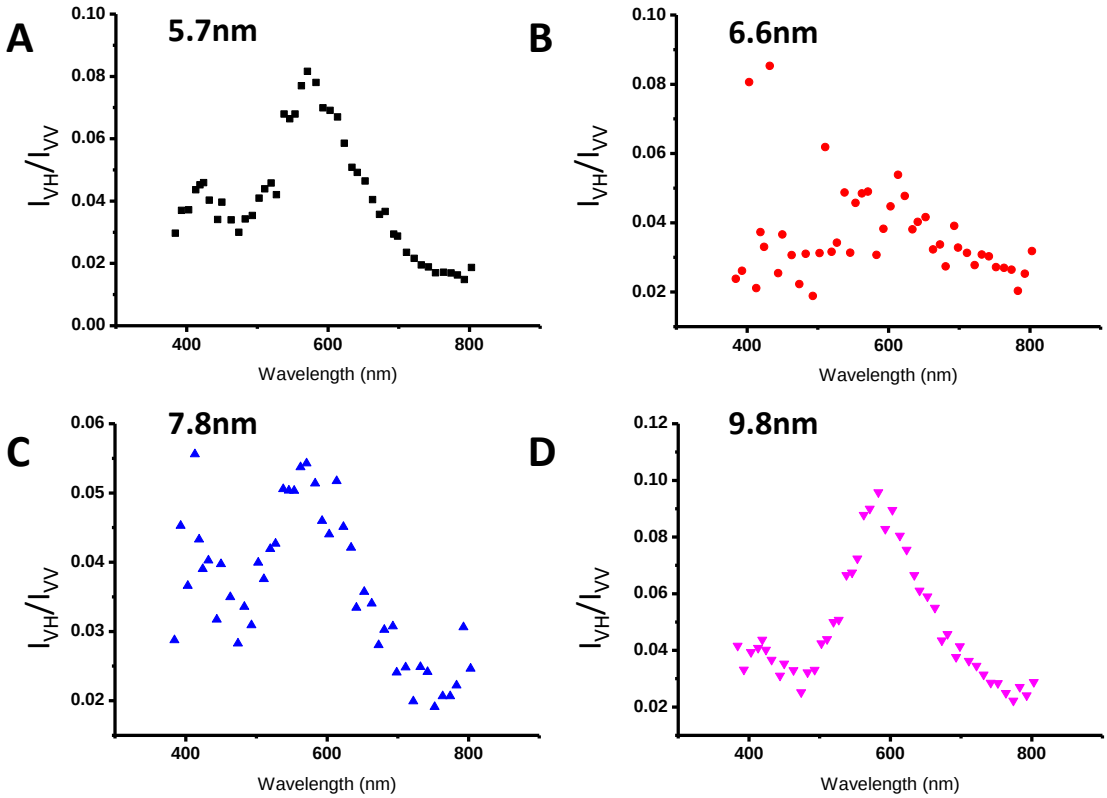

Figure 4.30- Polarization-resolved light scattering measurement of D-Goldhelix consisting of differed sizes of HOOC-PEG/TA-GNPs. A: 5.7nm TA-GNPs, B: 6.6nm TA-GNPs, C: 7.8nm TA-GNPs, and D: 9.8nm TA-GNPs.

Subsequently, in order to firmly compare the capability of Goldhelix system for light scattering and clarify the induction of magnetic scattering, we investigated a very interesting issue concerning parameters, typically scattering cross section, α, a parameter which describes how much light could be scattered by a sample. To do this, a normalization procedure is needed to eliminate the influence of the silica substrate. However, since such attempt is performed for the first time on a chiral helical silica substrate, there is actually no applicable reference. Therefore, measurements were carried out on various diameters of silica particles in water/ethanol at the beginning, and then compared with the theoretical predictions from Mie theory so as to establish a reasonable reference ready to use.

Basically, the raw data of the scattering from ED and MD+EQ of the sample can be interpreted as extrapolated:[57]

$$I^V(\phi) = I_0(\lambda)\delta\Omega f(\lambda,\delta\Omega)T(\lambda)N_{MNC}\sigma_{ED}^{90^0} \times \sin^2\phi = A^V(\lambda)\sin^2\phi$$

$$I^H(\phi) = I_0(\lambda)\delta\Omega f(\lambda,\delta\Omega)T(\lambda)N_{MNC}(\sigma^{0^0}_{MD+EQ}) \times \cos^2\phi = A^H(\lambda)\cos^2\phi$$

Where N_{MNC} is the number of target particles in the scattering volume for coupling, $\sigma^{90^0}_{ED}$ and $\sigma^{0^0}_{MD+EQ}$ are the scattering cross section at 90 and 0 degree for ED and MD+EQ radiation, respectively. $I_0(\lambda)\delta\Omega f(\lambda,\delta\Omega)T(\lambda)$ is the function which accounts for spectral sensitivity of the photomultiplier and optical transmission or reflection of all optical elements. Ω is the angular span of the detector.

Besides, the reference on electric dipole scattering of proper silica particles can be imported as:

$$I^V_{ref}(\phi) = I_0(\lambda)\delta\Omega f(\lambda,\delta\Omega)T_{ref}(\lambda)N_{ref}\sigma^{90^0}_{ref} \times \sin^2\phi = A^V_{ref}(\lambda)\sin^2\phi$$

After obtaining the electric dipole of silica particles, it becomes possible to deduce the scattering cross section of electric dipole radiation as:

$$\sigma^{sample}_{scat}(\lambda) \propto \frac{I^V_{sample}(\lambda)}{I^V_{silica}(\lambda)} \times \sigma^{silica}_{scat}(\lambda)$$

Where $\sigma^{silica}_{scat}(\lambda)$ is the scattering cross section of silica particles. It is exactly known from Mie theory and roughly proportional to $\frac{1}{\lambda^4}$ of incident light.

The scattering cross section of MD+EQ can be likewise expressed as:

$$\sigma^{sample}_{scat}(\lambda) \propto \frac{I^H_{sample}(\lambda)}{I^V_{silica}(\lambda)} \times \sigma^{silica}_{scat}(\lambda)$$

Based on what is discussed above, the scattering cross section of ED and MD+EQ can be calculated and Figure 4.31 below shows the calculated scattering cross section of ED radiation and MD+EQ radiation. As it can be seen from both ED cross section and MD+EQ cross section, the relation between the size of the Goldhelix and the corresponding scattering cross section is not straightforward, however, the strong ED and MD+EQ scattering cross section for 9.8nm Goldhelix exhibits a predominantly higher value in both measurements

proving that when the GNPs are considerably larger, the scattering radiation will be greatly enhanced. In fact, when the sizes of GNPs are much smaller than the wavelength of light (roughly <10nm diameter) the scattering property should be greatly reduced as indicated by Mie theory. Furthermore, for small GNPs the interparticle distance would be more comparable to their size, meaning the electromagnetic coupling would be weaker than large GNPs, indicating the measured ED and MD+EQ scattering cross sections should be smaller than big nanoparticles.[67]

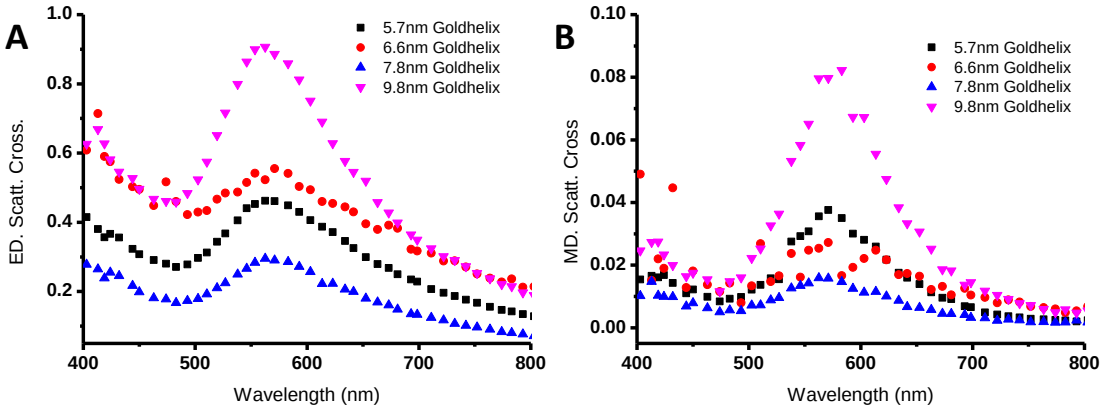

Figure 4.31- Calculated scattering cross section of D-Goldhelix in terms of ED scattering cross section (A) and MD+EQ scattering cross section (B). 5.7nm Goldhelix (black square dots), 6.6nm Goldhelix (red round dots), 7.8nm Goldhelix (blue triangle dots) and 9.8nm Goldhelix (pink triangle dots).

Admittedly, it is worthy to mention that the size of silica nanohelices is in fact comparable the wavelength of the laser beam, implying that EQ should be significant. However, the observed MD+EQ radiation and calculated scattering cross sections, as preliminary results, is still proven to be a reasonable evidence to confirm the presence of an axial (MD+EQ) mode with resonant property at plasmon frequency and introduce a feasible way for studying on magnetic issues of assembled nanoparticles. To deep it further, numerical simulations for plasmonic nanoparticles such as finite difference time domain (FDTD)[68], discrete dipole approximation (DDA)[45, 69], or finite element method (FEM)[11] should be applied for separation of MD radiation from MD+EQ radiation in this axial direction.

Experimental session

Synthesis of GNPs and Surface Ligands Exchange:

$NaBH_4$ reduced and tri-sodium citrate stabilized GNPs ($NaBH_4$-GNPs): Around 3.5nm GNPS were synthesized by using tri-sodium borohydride ($NaBH_4$) as the reducing agent and tri-sodium citrate as the capping agent through a modified method of Z. Jianming et al[31]. Typically, 0.23mL 0.1M $HAuCl_4 \cdot 3H_2O$ aqueous solution was added into 90mL of deionized water followed by injection of 2mL of 38.8mM tri-sodium citrate solution. And then 1mL of 0.075 wt% freshly prepared $NaBH_4$ solution (in 38.8mM tri-sodium citrated solution) was added after 5min of stirring, and then the reaction mixture was stirred overnight as room temperature.

APTES stabilized GNPs (APTES-GNPs): around 4nm APTES-GNPs was synthesized by using X. Sun's method with slightly modification.[14] Typically, 400μL of APTES was added to 0.84 mL of a 0.1M $HAuCl_4$ aqueous solution with 2.66mL Milli-Q water under vigorous stirring at room temperature to obtain supramolecular microstructures of the mixture. Then the colloidal soliton was heated up to 100˚C for 30 min and kept at room temperature for overnight, followed by centrifugation to remove unreacted APTES and other byproducts. The synthesized GNPs have an average diameter of 4.1nm in TEM measurement.

Tannic acid/citrate stabilized GNPs (TA-GNPs): Gold nanoparticles with approximately 5-10nm were synthesized by using both tannic acid and tri-sodium citrate as reducing and capping agent reported by J.W. Slot[15] with slightly modification. To make 100 ml of gold sol, two stock solutions have to be prepared. Solution A: 80 ml Milli-Q water and 1 ml 1% aqueous gold chloride. Solution B: 4 ml 1% tri-sodium citrate $\cdot 2H_2O$ + 16 ml H_2O + variable amount of 1% tannic acid (shown as Table 1). When 1 ml or more tannic acid is needed, add an equal amount of 25mM potassium carbonate for pH adjustment. Warm up solutions A and B to 60˚C and mix them while stirring. After the red color appeared heating up the mixture to 100 ˚C and cool the solution on ice. The larger particles (where lower concentrations of tannic acid are used) take longer to form and the red color can take up to 1 hour to develop.

Table 4.3-Relation between concentration of tannic acid and gold nanoparticle size:

Gold nanoparticle size	Amount of 1% Tannic acid
5.4nm	1mL
6.3nm	0.5mL
7.4nm	0.25mL
9.4nm	0.1mL

Surface Ligands Exchange: Surface ligands exchange reaction was done by using O-(2-Carboxyethyl)-O'-(2-mercaptoethyl) noted as HS-PEG_7-COOH. Briefly, in a typical preparation, 4×2mL of 0.067μM as-synthesized 5nm TA-GNPs for example, were first centrifuged to 1.0mL (~0.13 μM) or 0.5mL (~0.27μM) by precipitation to remove ½ or ¾ unreacted tannic acid salt and tri-sodium citrate. After that, 0.5mL of 10mM HS-PEG_7-COOH in ethanol was added to the colloidal solution (if ¾ unreacted tannic acid salt and tri-sodium citrate was remove, 0.5mL 1% tri-sodium citrate was add to equalize the concentration of GNPs and keep the GNPs from aggregation) and followed with 5min sonication and incubated in 4 ˚C overnight to reach equilibrium. After reaction, TA-GNPs with HS-PEG_7-COOH were precipitated by centrifugation and washed with water. (For each run, sample solutions were centrifuged to 0.5mL and mixed up to 1mL, and then 1mL of water was added before centrifugation.) Finally, TA-GNPs with HS-PEG_7-COOH (HOOC-PEG/TA-GNPs) were dispersed in water with a pH about 4.4 and kept in 20 ˚C overnight before any usage.

In the case of $NaBH_4$-GNPs, the ligand exchange reaction is basically the same with small modification. 4×2mL of 0.25nM as-synthesized $NaBH_4$-GNPs were first centrifuged to 1.0mL (~0.5nM) by precipitation to remove unreacted tri-sodium citrate and increase the concentration. After that, 0.5mL of 10mM HS-PEG_7-COOH in ethanol was added and followed with 5min sonication and incubated in 4 ˚C overnight to reach equilibrium. After reaction, $NaBH_4$-GNPs with HS-PEG_7-COOH (HOOC-PEG/$NaBH_4$-GNPs) were precipitated by centrifugation and washed with water. (For each run, sample solutions were centrifuged to

0.5mL and mixed up to 1mL, and then 1mL of water was added before centrifugation.) Finally, HOOC-PEG/TA-GNPs were dispersed in water with a pH about 4.4 and kept in 20 ˚C overnight before any usage.

Synthesis of Goldhelix:

Direct synthesis of Goldhelix without ligand exchange:

For APTES-GNPS: 0.1mL as synthesized GNPs were diluted and redispersed in 0.9mL Milli-Q water and then, the pH was adjusted to around 8 followed by adding 25 µL-100 µL of 0.5mg/mL bare silica nanohelices. The suspension was applied for 5min sonication and incubated at 20 ˚C overnight with roller-mixer. Afterwards, the suspension was washed 3 times by Milli-Q water to eliminate unreacted APTES-GNPs. The washing was done in a condition of 4000rpm and 5min for each run. To enhance the adsorption, the mixture can be repeated as stated. The final samples were kept in 20˚C before any characterizations and measurements.

For $NaBH_4$-GNPs and TA-GNPs: nanohelices-NH_2 were used as a template for GNPs immobilization. Basically, 25 µL-100 µL of 0.8mg/mL nanohelices-NH_2 was added to 0.5mL of as-synthesized GNPs with 10min sonication and then incubated at 20 ˚C overnight. The GNPs colloidal became clear suspension with dark red precipitate inside, and then followed by washing with three times of water to eliminate unreacted GNPs. The washing was done in a condition of 4000rpm and 5min for each run. To enhance the adsorption, the mixture can be repeated as stated. The final samples were kept in 20˚C before any characterizations and measurements.

Synthesis of Goldhelix after ligand exchange: After ligands exchange, 50 µL-150 µL of 0.8mg/mL nanohelices-NH_2 was added to 0.5mL of HS-PEG_7-COOH functionalized GNPs, respectively. 10min sonication was applied to the mixed solution to make it homogenous. Then, the suspension of GNPs with silica helices was washed by precipitation with water after 24h incubation at 20 ˚C in roller-mixer. The washing was repeated 5 times and the concentration of synthesized Goldhelix can be increased by condensation at the final stage of

washing. The final samples were kept in 20 ˚C before any characterizations and measurements.

Estimation of silica nanohelices grafted with HOOC-PEG/TA-GNPs

After immobilization of HOOC-PEG/TA-GNPs onto silica nanohelices, the amount of HOOC-PEG/TA-GNPs and the concentration of silica nanohelices which accounts for the chiroptical signals in CD are estimated by using UV-vis spectrometer.[49] The relation between the concentration of HOOC-PEG/TA-GNPs and absorbance in UV can be referred as:

$$c = \frac{\mathrm{A}_{450}}{\varepsilon_{450}}$$

With this relation, the amount of HOOC-PEG/TA-GNPs that is stayed for CD measurement can be obtained by simply subtracting the washed out HOOC-PEG/TA-GNPs from the original HOOC-PEG/TA-GNPs colloids. In a meanwhile, the number of HOOC-PEG/TA-GNPs per silica pitch can be counted from TEM images as well. Then the concentration of silica nanohelices covered with GNPs can be estimated by

$$C_{silica} = \left. \frac{L_{silica}}{L_{pitch}} \times N_{GNPs\ per\ pitch} \right/ (NA * V)$$

Where *NA* is the Avogadro's constant, L_{silica} and L_{pitch} are the length of silica nanohelices and length of helical pitch, respectively.

Characterizations

The study of localized surface plasmon resonance was performed with a Cary 300 UV-vis. spectrometer. The data were recorded with 1.0 nm data interval and 600 nm/min. scan rate. Quartz cuvettes with optical path length of 10 mm were used for measurements. TEM was performed at room temperature on a Philips EM 120 electron microscope operating at 120 kV and the images were collected by 2k × 2k Gatan ssCCD camera. Drops of diluted

dispersions of the hybrids were deposited on carbon films coated 200/400-mesh copper grids. The excess liquid was blotted with filter paper. Electron tomography (ET) experiments have been carried out on representative silica helices by using a JEOL 2100F TEM/STEM electron microscope operating at 200kV, equipped with a TRIDIEM post-column Imaging filter and a Cs probe corrector. Before observations, the samples were deposited on a holey carbon membrane copper grid which was previously cleaned using a H2/Ar plasma gas using a Solarus Plasma Cleaner. The acquisition of the tilt series was performed in the classical TEM mode with the Digital Micrograph software which provides an automated acquisition of the tilt series by varying the tilt angle step by step and by controlling the defocusing and the specimen drift at each tilt angle. Using a high tilt sample holder from the GATAN company, TEM tilt series were acquired between 75 °and -75 °, with a 1 °equal tilt increment. As a result, the total number of projections was about 150, for a recording duration of about 45 minutes. Once the acquisition of the tilt series completed, the images were roughly aligned using a cross correlation algorithm, followed by a fine alignment performed in the IMOD software 97 where the gold nanoparticles located on the silica helices were used as fiducial markers. The 3D reconstructions were computed by using algebraic reconstruction techniques (ART) 98 implemented in the TomoJ software 99 with 20 iterations. Visualization and quantitative analysis of the final volumes were carried out by using Slicer (http://www.Slicer3D.org) and ImageJ softwares. Circular dichroism measurements were conducted on a Jasco J-815 CD spectrometer. The scan rate was 20nm/min and 10-30 acquisitions were applied to each sample to eliminate the noise effect as much as possible. All CD experiments were carried out in Milli-Q water (pH=6.0±0.1) with a quartz cuvette (0.1 cm path length from Hellma) at 25 ℃. Zeta-potential measurement was done in a Wallis-ζ meter with a pH mode at 25 ℃. All the sample solutions are adjusted to reach proper scattering intensity (I_0~1000Kcp) with 6-9 acquisitions.

References – page 183

Reference

1. Mastroianni, A.J., S.A. Claridge, and A.P. Alivisatos, *Pyramidal and chiral groupings of gold nanocrystals assembled using DNA scaffolds.* Journal of the American Chemical Society, 2009. **131**(24): p. 8455-8459.
2. Sharma, J., et al., *Control of self-assembly of DNA tubules through integration of gold nanoparticles.* Science, 2009. **323**(5910): p. 112-116.
3. Guerrero‐Martínez, A., et al., *Intense Optical Activity from Three‐Dimensional Chiral Ordering of Plasmonic Nanoantennas.* Angewandte Chemie International Edition, 2011. **50**(24): p. 5499-5503.
4. Qi, H., et al., *Chiral nematic assemblies of silver nanoparticles in mesoporous silica thin films.* Journal of the American Chemical Society, 2011. **133**(11): p. 3728-3731.
5. Wang, Y., et al., *Chiral transformation: From single nanowire to double helix.* Journal of the American Chemical Society, 2011. **133**(50): p. 20060-20063.
6. Yeom, J., et al., *Chiral templating of self-assembling nanostructures by circularly polarized light.* Nature materials, 2014.
7. Anker, J.N., et al., *Biosensing with plasmonic nanosensors.* Nature materials, 2008. **7**(6): p. 442-453.
8. Jain, P.K., W. Huang, and M.A. El-Sayed, *On the universal scaling behavior of the distance decay of plasmon coupling in metal nanoparticle pairs: a plasmon ruler equation.* Nano Letters, 2007. **7**(7): p. 2080-2088.
9. Shen, X., et al., *Rolling up gold nanoparticle-dressed DNA origami into three-dimensional plasmonic chiral nanostructures.* Journal of the American Chemical Society, 2011. **134**(1): p. 146-149.
10. Turkevich, J., P.C. Stevenson, and J. Hillier, *A study of the nucleation and growth processes in the synthesis of colloidal gold.* Discussions of the Faraday Society, 1951. **11**: p. 55-75.
11. Pelton, M. and G.W. Bryant, *Introduction to metal-nanoparticle plasmonics*. Vol. 5. 2013: John Wiley & Sons.
12. Tamoto, R., et al., *Gold Nanoparticle Deposition on Silica Nanohelices: A New Controllable 3D Substrate in Aqueous Suspension for Optical Sensing.* Journal of Physical Chemistry C, 2012. **116**(43): p. 23143-23152.
13. Nikoobakht, B. and M.A. El-Sayed, *Preparation and growth mechanism of gold nanorods (NRs) using seed-mediated growth method.* Chemistry of Materials, 2003. **15**(10): p. 1957-1962.
14. Sun, X. and W. Wei, *Electrostatic-assembly-driven formation of micrometer-scale supramolecular sheets of (3-aminopropyl) triethoxysilane (APTES)-HAuCl4 and their subsequent transformation into stable APTES bilayer-capped gold nanoparticles through a thermal process.* Langmuir, 2010. **26**(9): p. 6133-6135.
15. Muhlpfordt, H., *THE PREPARATION OF COLLOIDAL GOLD PARTICLES USING TANNIC-ACID AS AN ADDITIONAL REDUCING AGENT.* Experientia, 1982. **38**(9): p. 1127-1128.

16. Brust, M., et al., *Synthesis of thiol-derivatised gold nanoparticles in a two-phase liquid–liquid system.* J. Chem. Soc., Chem. Commun., 1994(7): p. 801-802.
17. Saha, K., et al., *Gold nanoparticles in chemical and biological sensing.* Chemical Reviews, 2012. **112**(5): p. 2739-2779.
18. Daniel, M.-C. and D. Astruc, *Gold nanoparticles: assembly, supramolecular chemistry, quantum-size-related properties, and applications toward biology, catalysis, and nanotechnology.* Chemical Reviews, 2004. **104**(1): p. 293-346.
19. Hinterwirth, H., et al., *Quantifying Thiol Ligand Density of Self-Assembled Monolayers on Gold Nanoparticles by Inductively Coupled Plasma-Mass Spectrometry.* Acs Nano, 2013. **7**(2): p. 1129-1136.
20. Pillai, P.P., et al., *Controlled pH Stability and Adjustable Cellular Uptake of Mixed-Charge Nanoparticles.* Journal of the American Chemical Society, 2013. **135**(17): p. 6392-6395.
21. Manson, J., et al., *Polyethylene glycol functionalized gold nanoparticles: the influence of capping density on stability in various media.* Gold Bulletin, 2011. **44**(2): p. 99-105.
22. Wang, W., et al., *Role of thiol-containing polyethylene glycol (thiol-PEG) in the modification process of gold nanoparticles (AuNPs): Stabilizer or coagulant?* Journal of Colloid and Interface Science, 2013. **404**: p. 223-229.
23. Latham, A.H. and M.E. Williams, *Versatile routes toward functional, water-soluble nanoparticles via trifluoroethylester-PEG-thiol ligands.* Langmuir, 2006. **22**(9): p. 4319-4326.
24. ThermoScientific. *http://xpssimplified.com/elements/sulfur.php*.
25. Techane, S.D., L.J. Gamble, and D.G. Castner, *Multitechnique characterization of self-assembled carboxylic acid-terminated alkanethiol monolayers on nanoparticle and flat gold surfaces.* The Journal of Physical Chemistry C, 2011. **115**(19): p. 9432-9441.
26. Love, J.C., et al., *Self-Assembled Monolayers of Thiolates on Metals as a Form of Nanotechnology.* Chemical Reviews, 2005. **105**(4): p. 1103-1170.
27. Hostetler, M.J., et al., *Alkanethiolate gold cluster molecules with core diameters from 1.5 to 5.2 nm: core and monolayer properties as a function of core size.* Langmuir, 1998. **14**(1): p. 17-30.
28. Laaksonen, T., et al., *Stability and Electrostatics of Mercaptoundecanoic Acid-Capped Gold Nanoparticles with Varying Counterion Size.* ChemPhysChem, 2006. **7**(10): p. 2143-2149.
29. Grabar, K.C., et al., *Kinetic control of interparticle spacing in Au colloid-based surfaces: rational nanometer-scale architecture.* Journal of the American Chemical Society, 1996. **118**(5): p. 1148-1153.
30. Thomas, K.G., J. Zajicek, and P.V. Kamat, *Surface binding properties of tetraoctylammonium bromide-capped gold nanoparticles.* Langmuir, 2002. **18**(9): p. 3722-3727.
31. Zhang, J., et al., *Effect of Surface Oxidation on the Interaction of 1-Methylaminopyrene with Gold Nanoparticles.* Langmuir, 2012. **28**(5): p. 2858-2865.

32. Brewer, S.H., et al., *Probing BSA binding to citrate-coated gold nanoparticles and surfaces.* Langmuir, 2005. **21**(20): p. 9303-9307.
33. Xia, X., et al., *Quantifying the coverage density of poly (ethylene glycol) chains on the surface of gold nanostructures.* Acs Nano, 2011. **6**(1): p. 512-522.
34. Jung, H.-S., D.-S. Moon, and J.-K. Lee, *Quantitative analysis and efficient surface modification of silica nanoparticles.* Journal of Nanomaterials, 2012. **2012**: p. 48.
35. Su, K.-H., et al., *Interparticle coupling effects on plasmon resonances of nanogold particles.* Nano Letters, 2003. **3**(8): p. 1087-1090.
36. Ben-Moshe, A., et al., *Chirality and chiroptical effects in inorganic nanocrystal systems with plasmon and exciton resonances.* Chemical Society Reviews, 2013. **42**(16): p. 7028-7041.
37. Song, C., et al., *Tailorable Plasmonic Circular Dichroism Properties of Helical Nanoparticle Superstructures.* Nano Lett, 2013.
38. Fan, Z., H. Zhang, and A.O. Govorov, *Optical Properties of Chiral Plasmonic Tetramers: Circular Dichroism and Multipole Effects.* The Journal of Physical Chemistry C, 2013. **117**(28): p. 14770-14777.
39. Fan, Z.Y. and A.O. Govorov, *Plasmonic Circular Dichroism of Chiral Metal Nanoparticle Assemblies.* Nano Letters, 2010. **10**(7): p. 2580-2587.
40. Fan, Z.Y. and A.O. Govorov, *Chiral Nanocrystals: Plasmonic Spectra and Circular Dichroism.* Nano Letters, 2012. **12**(6): p. 3283-3289.
41. Zhang, S., et al., *Formation of Gold and Silver Nanoparticle Arrays and Thin Shells on Mesostructured Silica Nanofibers.* Advanced Functional Materials, 2007. **17**(16): p. 3258-3266.
42. Govorov, A.O., et al., *Chiral nanoparticle assemblies: circular dichroism, plasmonic interactions, and exciton effects.* Journal of Materials Chemistry, 2011. **21**(42): p. 16806-16818.
43. Govorov, A.O. and Z. Fan, *Theory of chiral plasmonic nanostructures comprising metal nanocrystals and chiral molecular media.* ChemPhysChem, 2012. **13**(10): p. 2551-2560.
44. Govorov, A.O., et al., *Theory of Circular Dichroism of Nanomaterials Comprising Chiral Molecules and Nanocrystals: Plasmon Enhancement, Dipole Interactions, and Dielectric Effects.* Nano Letters, 2010. **10**(4): p. 1374-1382.
45. Draine, B.T. and P.J. Flatau, *Discrete-Dipole Approximation For Scattering Calculations.* Journal of the Optical Society of America A, 1994. **11**(4): p. 1491-1499.
46. Brioude, A. and M.P. Pileni, *Silver Nanodisks: Optical Properties Study Using the Discrete Dipole Approximation Method.* The Journal of Physical Chemistry B, 2005. **109**(49): p. 23371-23377.
47. Tørring, T., et al., *DNA origami: a quantum leap for self-assembly of complex structures.* Chemical Society Reviews, 2011. **40**(12): p. 5636-5646.
48. Photophysics:. *http://www.photophysics.com/tutorials/circular-dichroism-cd-spectroscopy/7-cd-units-conversions*.

49. Haiss, W., et al., *Determination of Size and Concentration of Gold Nanoparticles from UV−Vis Spectra.* Analytical Chemistry, 2007. **79**(11): p. 4215-4221.
50. Amendola, V. and M. Meneghetti, *Size evaluation of gold nanoparticles by UV− vis spectroscopy.* The Journal of Physical Chemistry C, 2009. **113**(11): p. 4277-4285.
51. Khlebtsov, N.G., *Determination of size and concentration of gold nanoparticles from extinction spectra.* Analytical Chemistry, 2008. **80**(17): p. 6620-6625.
52. Scaffardi, L.B. and J.O. Tocho, *Size dependence of refractive index of gold nanoparticles.* Nanotechnology, 2006. **17**(5): p. 1309.
53. Scaffardi, L., et al., *Sizing gold nanoparticles by optical extinction spectroscopy.* Nanotechnology, 2005. **16**(1): p. 158.
54. Berova, N., L.D. Bari, and G. Pescitelli, *Application of electronic circular dichroism in configurational and conformational analysis of organic compounds.* Chemical Society Reviews, 2007. **36**(6): p. 914-931.
55. George, J. and K.G. Thomas, *Surface Plasmon Coupled Circular Dichroism of Au Nanoparticles on Peptide Nanotubes.* Journal of the American Chemical Society, 2010. **132**(8): p. 2502-2503.
56. Chen, W., et al., *Nanoparticle Superstructures Made by Polymerase Chain Reaction: Collective Interactions of Nanoparticles and a New Principle for Chiral Materials.* Nano Letters, 2009. **9**(5): p. 2153-2159.
57. Sharma, N.L., *Nondipole optical scattering from liquids and nanoparticles.* Physical Review Letters, 2007. **98**(21): p. 217402.
58. Oliveira, S.L. and S.C. Rand, *Intense nonlinear magnetic dipole radiation at optical frequencies: molecular scattering in a dielectric liquid.* Physical Review Letters, 2007. **98**(9): p. 093901.
59. Pendry, J.B. and D.R. Smith, *The quest for the superlens.* Scientific American, 2006. **295**(1): p. 60-67.
60. Pendry, J.B., *Negative refraction makes a perfect lens.* Physical Review Letters, 2000. **85**(18): p. 3966.
61. Schwanecke, A., et al., *Optical magnetic mirrors.* JOURNAL OF OPTICS A PURE AND APPLIED OPTICS, 2007. **9**(1): p. L1.
62. Roach, T., et al., *Realization of a magnetic mirror for cold atoms.* Physical Review Letters, 1995. **75**(4): p. 629.
63. Schurig, D., et al., *Metamaterial electromagnetic cloak at microwave frequencies.* Science, 2006. **314**(5801): p. 977-980.
64. Alu, A. and N. Engheta, *Plasmonic and metamaterial cloaking: physical mechanisms and potentials.* Journal of Optics A: Pure and Applied Optics, 2008. **10**(9): p. 093002.
65. Castaldi, G., et al., *Cloak/anti-cloak interactions.* Optics Express, 2009. **17**(5): p. 3101-3114.
66. Alù, A. and N. Engheta, *Cloaking a sensor.* Physical Review Letters, 2009. **102**(23): p. 233901.
67. Mayer, K.M. and J.H. Hafner, *Localized surface plasmon resonance sensors.* Chemical Reviews, 2011. **111**(6): p. 3828-3857.

68. Miller, E.K., *Time-domain modeling in electromagnetics.* Journal of Electromagnetic Waves and Applications, 1994. **8**(9-10): p. 1125-1172.
69. Purcell, E.M. and C.R. Pennypacker, *Scattering and absorption of light by nonspherical dielectric grains.* The Astrophysical Journal, 1973. **186**: p. 705-714.

References – page 183

Chapter 5. Hierarchical assembly of silica nanohelices

References – page 211

1. Introduction

After obtaining the silica nanohelices and Goldhelix with controllable optical behavior, we were naturally interested in hierarchical organization of such nanostructures in order to enhance these optical or mechanical properties in specific directions.

In this chapter, we will explore the possibility on the alignment of silica nanohelices by two very innovative techniques: 1) grazing incidence spraying (known as "the first step" towards layer-by-layer (LbL) oriented multilayer thin films, in which the same process repeats several times) and 2) controlled evaporation microfluidics in order to set up a basis for the future study on hierarchical assembly of silica nanohelices and Goldhelix.

Study on the alignment of silica helical ribbons by spraying layer-by-layer technique were performed in collaboration with ***Dr. Matthias Pauly*** *and* ***Dr. Gero Decher****, CNRS, Institut Charles Sadron, Strasbourg, France.*

Study on the alignment of silica helical ribbons by Microfluidics were performed in collaboration with ***Dr. Jacques Leng****, CNRS, Lab of the future, Bordeaux, France.*

1.1. Grazing incidence techniques in 2D assembling

Grazing incidence spraying (GIS) is a novel technique patented by the team of Gecher recently (not issued to public yet). As a method closely linking to traditional spraying LbL technique, GIS is capable to control the orientation of building blocks during the multilayered materials' fabrication via spraying LbL technique, which endows possibility to control the isotropy of multilayered materials by simply changing the incidence angle.

With the help of grazing incidence (GI) method, the realization of controlling multilayered materials' fabrication could be anticipated. It is a very new method that is suitable not only for spraying LbL deposition but also other deposition techniques, it is premature to write a very inclusive review with such a broad number of potential applications[1, 2]. We will therefore highlight some of the essential examples on the alignment of nano-objects via GI assisted LbL deposition techniques to shed light on the understanding of basic concepts and mechanism of GIS assembly.

1.1.1. Examples of GI assisted deposition techniques on flat substrate

To start with, LbL deposition techniques was first implemented in 1966[3] but revitalized by G. Decher in 1997[4] by the discovery of its applicability to a wide range of polyelectrolytes (Figure 5.1). Typically, LbL deposition technique is described as (1) immersing the substrate with the negatively charged surface in a solution of positively charged polyelectrolytes for layer number n = 1, (2) waiting for a sufficient time, (3) rinse the substrate (usually water), (4) immersing the substrate in a solution of positively charged polyelectrolytes, for layer number n = 2, (5) waiting for a sufficient time and rinse the substrate, and (6) repeating this procedure until the desired layer number of n is reached.

References – page 211

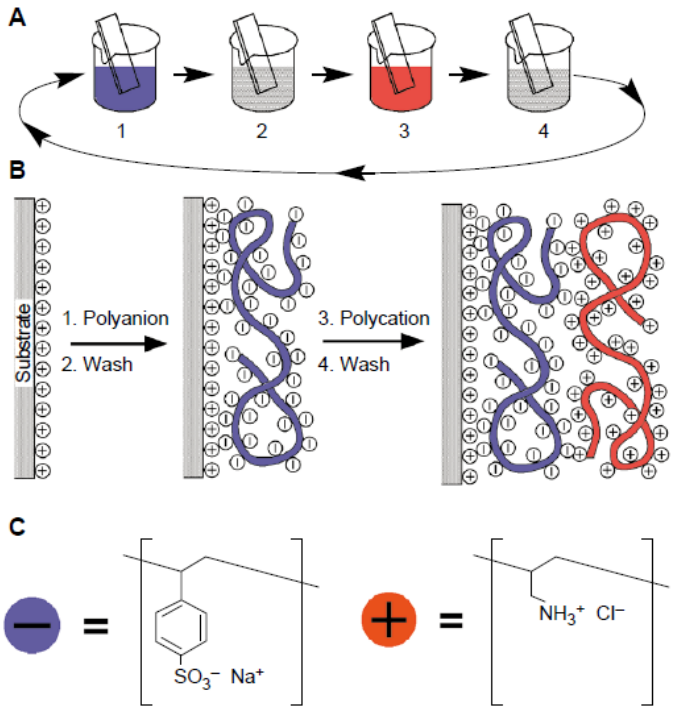

Figure 5.1- (A) Schematic of the film deposition process using slides and beakers. Steps 1 and 3 represent the adsorption of a polyanion and polycation, respectively, and steps 2 and 4 are washing steps. The four steps are the basic buildup sequence for the simplest film architecture, $(A/B)_m$. The construction of more complex film architectures requires only additional beakers and a different deposition sequence. (B) Simplified molecular picture of the first two adsorption steps, depicting film deposition starting with a positively charged substrate. Counterions are omitted for clarity. The polyion conformationand layer interpenetration is an idealization of the surface charge reversal with each adsorption step. (C) Chemical structures of two typical polyions, the sodium salt of poly(styrene sulfonate) and poly(allylamine hydrochloride).[4]

In particular, spraying LbL deposition is also known as an approach for functional materials processing. The experimental results from P. T. Hammond et al for example, suggested that the vacuum-assisted spray-LbL assembly technique can enable rapid, uniform electrostatic assembly of positively and negatively charged multi-walled carbon nanotubes (MWNTs) on individual electrospun (ES) fibers, creating highly porous networks of MWNT multilayers with controlled loading and electrical conductivity. As illustrated in Figure 5.2, their work offered a direct route for covalently attaching a receptor of interest to the MWNTs, tailoring the chemical specificity of the MWNT/ES fiber electrode for sensing applications with a means of greatly increasing properties such as selectivity and sensitivity in a modular fashion.[5, 6]

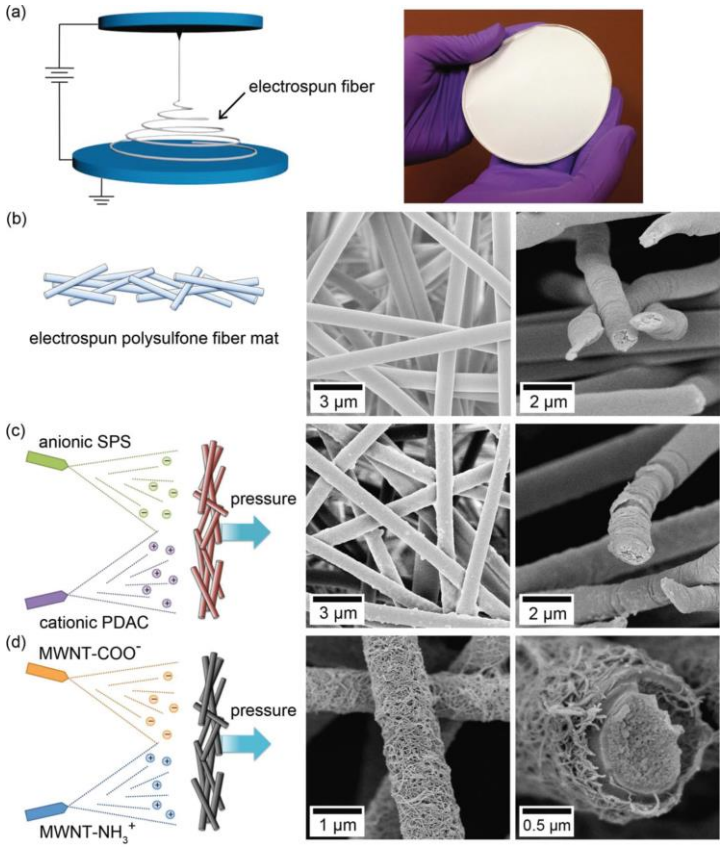

Figure 5.2- Illustration of layer-by-layer assembly on electrospun (ES) fiber mat. a) Parallel-plate electrospinning technique (diagram, left) is employed to create polysulfone ES fiber mats of 5–6 inch diameter (digital image, right). b) Schematic representation (left) and top-down (center) and cross-sectional (right) SEM images of the annealed polysulfone ES fiber mat. c) A spray-LbL deposition technique with a pressure imposed across the mat is demonstrated to create conformal coatings of $(SPS/PDAC)_{10}$ thin films on individual fibers. d) ($MWNT\text{-}COO^-/MWNT\text{-}NH_3^+$) 15 films are uniformly coated on ES fibers independent of spray direction, as shown in the cross-sectional SEM image.[6]

It is widely admitted when applying some control on the GI angle it is possible to obtain multilayered materials with controlled orientation. As it is reported by C.M. Lieber et al[7], by changing flow directions for sequential steps complex crossed nanowire arrays can be prepared with layer-by-layer assembly. They show that nanowires can be assembled into parallel arrays with control of the average separation and, by combining fluidic alignment with surface-patterning techniques (Figure 5.3). These studies provide a general and rational approach for hierarchical assembly of 1D nanomaterials into well-defined functional networks that can bridge the nanometer through millimeter size regimes.

References – page 211

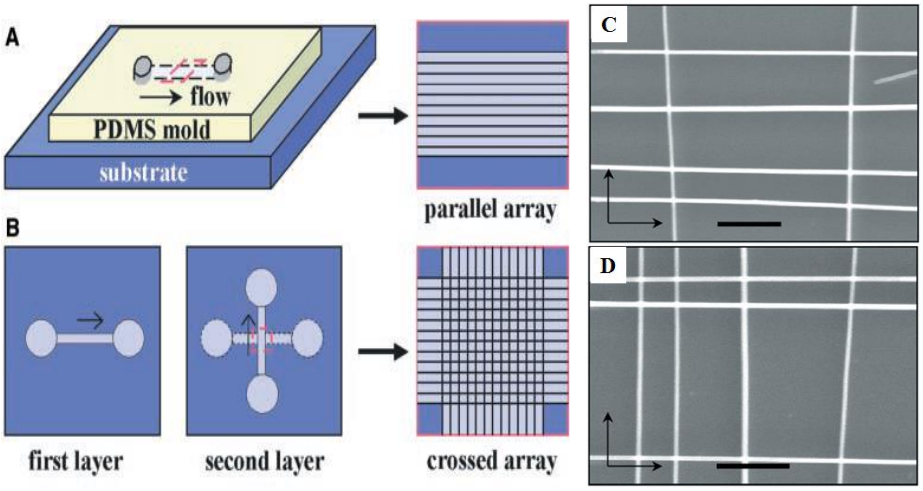

Figure 5.3- Schematic of fluidic channel structures for flow assembly. (A) A channel formed when the PDMS mold was brought in contact with a flat substrate. NW assembly was carried out by flowing an NW suspension inside the channel with a controlled flow rate for a set duration. Parallel arrays of NWs are observed in the flow direction on the substrate when the PDMS mold is removed. (B) Multiple crossed NW arrays can be obtained by changing the flow direction sequentially in a layer-by-layer assembly process. (C and D) Typical SEM images of crossed arrays of InP NWs obtained in a two-step assembly process with orthogonal flow directions for the sequential steps. Flow directions are highlighted by arrows in the images. The scale bars correspond to 500 nm.[7]

Their further studies showed that the degree of alignment can be controlled by the flow rate (Figure 5.4C). With increasing flow rates, the width of the NW angular distribution with respect to the flow direction narrows, furthermore, the average NW surface coverage can be controlled by the flow duration as shown in Figure 5.4D.

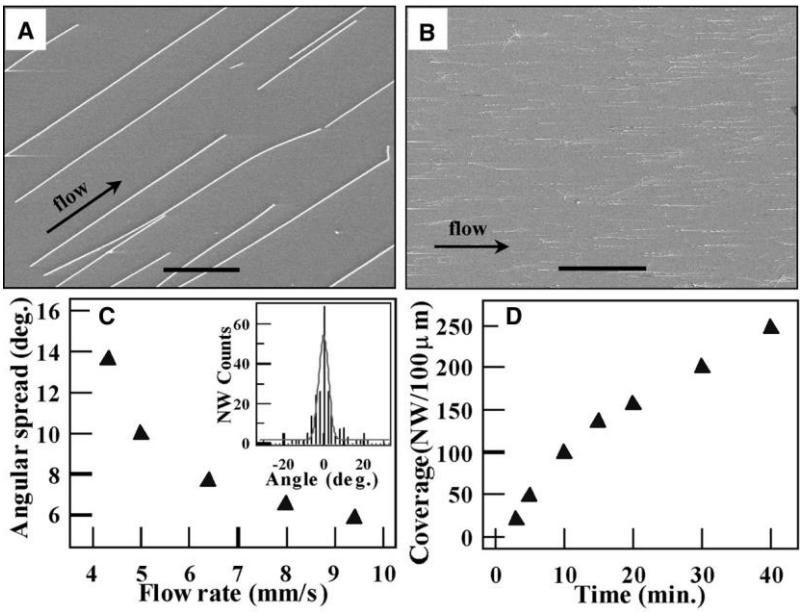

Figure 5.4. Parallel assembly of NW arrays. (A and B) SEM images of parallel arrays of InP NWs aligned by channel flow. The scale bars correspond to 2 mm and 50 mm in (A) and (B), respectively. (C) NW angular spread with respect to the flow direction versus flow rate. Each data point in the figure was obtained by statistical analysis of angular distribution of ~200 NWs (e.g., see inset). The inset shows a histogram of NW angular distribution at a flow rate of 9.40 mm/s. (D) The average density of NWs versus flow time. The average density was calculated by dividing the average number of NWs at any cross section of the channel by the width of the channel. All of the experiments were carried out with a flow rate of 6.40 mm/s.[7]

In fact, comparing to traditional deposition techniques such as LbL, GI assisted deposition methods can induce alignment and orientation control during the materials processing. With several steps deposition with controlled orientation, multilayered films with desired orientation or alignment of building blocks can be achieved. Inspired by these merits, a proof-of-concept experiment is provided in this chapter to show the feasibility of using grazing incidence spraying (GIS) for the alignment of silica nanohelices on a flat substrate, so that the alignment of Goldhelix or even multilayered films built by silica nanohelices or Goldhelix could be envisaged. Other depositions techniques such as electrospinning[8] and microfluidics are also capable for the alignment of small objects on a surface. The driving force for the alignment can vary among shear force, external electric field and flowing liquid each of them showing complementary property. The advantage of GIS is characterized by its convenience and capability for large scale production.

1.2. Microfluidics- Emerging technique for directed assembly in 3D motif

As claimed by *George M. Whitesides*, 2006[9] “The manipulation of fluids in channels with dimensions of tens of micrometers — microfluidics — has emerged as a distinct new field. Microfluidics has the potential to influence subject areas from chemical synthesis and biological analysis to optics and information technology. But the field is still at an early stage of development. Even as the basic science and technological demonstrations develop, other problems must be addressed: choosing and focusing on initial applications, and developing strategies to complete the cycle of development, including commercialization. The solutions to these problems will require imagination and ingenuity.” Indeed, the rapid flourishment of

microfluidics in areas like material science, biological applications and fundamental physics has witnessed this prediction to come true. Microfluidics has proven to have a wide range of applications in the fields such as molecular analysis, biodefence, molecular biology and microelectronics. These applications namely includes: i) to screen conditions (such as pH, ionic strength and composition, co-solvents, and concentration) for protein crystallization, ii) the manipulation of multiphase flows to generate and manipulate of monodisperse bubbles[10, 11], droplets[12, 13] of a dispersed gas or liquid phase in a continuous liquid stream, iii) cell biology for separations, iv) chemical synthesis and v) development of practical micro-analytical systems. Due to the rapid scientific and technologic development, new systems are emerging every year.[14]

All in all, the idea of employing microfluidics in this thesis is to make the alignment of our nano-objects so that we can study the optical properties of the synthesized systems in a 3D viewpoint. It is not in the scope of this thesis to include everything about the vast cross-disciplinary field of microfluidics or even a corner of the iceberg. We will only focus on some typical related researches in microfluidics to help understand some basic ideas of this cutting edge technique and specially its potential applications for the alignment of nano-objects in 3D motif.

1.2.1. Examples of microfluidics and its application on 3D assembly

An instructive example of microfluidics for the alignment of nano-objects can be found in carbon nanotubes. With patterned surfaces, ordered arrays of carbon nanotubes in bent and straight states were prepared by V. V. Tsukruk et al[15, 16] (Figure 5.5). Their modelling demonstrated that the alignment of CNTs is related to the rodlike molecule orientation by the contact liquid-air line observed in combing of DNA molecules. The contact line instabilities generates an array of microdroplets, and these size variable microdroplets did account for the shapes and orientations of the nanotubes.[17] The performance of thin-film transistors based on these densely packed and uniformly oriented CNT arrays are largely improved compared to random CNTs. The preparation of the ordered arrays of uniform nanotube loops or woven

nanotube stripes may be useful in microelectronic and microelectromechanical devices, where tunable electronic and surface properties result from different nanotube shapes, locations, and orientations.

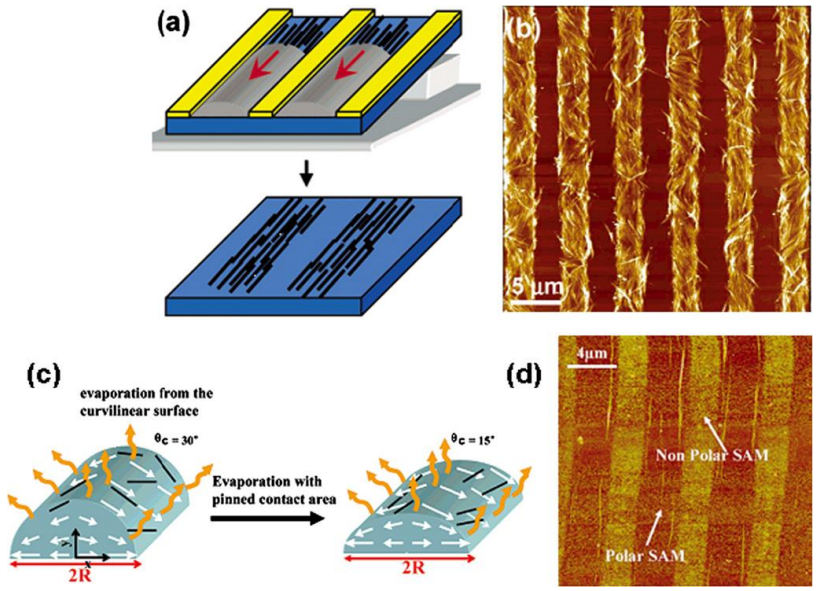

Figure 5.5– (a) Schemes for the tilted-drop fabrication of a thin film on an amine-terminated SAM surface micro-patterned with photoresist polymer stripes. (b) AFM topographical images of carbon nanotube films showing uniaxially oriented, densely packed CNT bundles. (c) Hydrodynamics in a cylindrical drop to align and place anisotropic nanoparticles. (d) AFM topographic images showing alignment and placement of individual SWCNT along the edges of the polar SAM (ovals highlight SWCNT).[15-17]

In parallel, microfluidics was proved useful for the preparation of two-dimensional ordered arrays of aligned lipid tubules as well. J. Fang et al, reported that lipid nano- and microtubules can be assembled into two-dimensional (2-D) parallel arrays with controlled separations by combining fluidic alignment with dewetting, which occurs within micro-channels (Figure 5.6a). They demonstrated that the lipid nanotubes can be bent into a well-defined shape at the channel entrance by the capillary pressure (Figure 5.6b). By using the aligned lipid tubules as a template, they were able to synthesize silica thin films controlled morphologies and patterns on solid substrates in a single-step process (Figure 5.6c).[18]

References – page 211

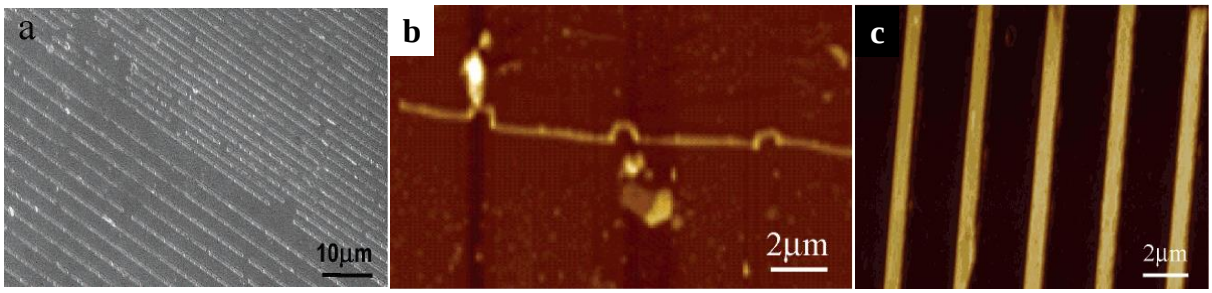

Figure 5.6-(a) Optical microscopy image of parallel arrays of the aligned lipid tubules with separations of 2 and 5 μm on a glass substrate (b) AFM image of a bent nanotubes on a glass substrate (C) AFM images of the deposition of silica particles on the aligned lipid tubules at pH 2.0.[18]

Another very interesting example of microfluidics for the alignment of nanoparticles is presented by P. Yang and his coworkers[19]. They reported that with the combination with microchannels, they are able to reproduce the aligned silicon NWs within the channel through traditional vapor-liquid-solid (VLS)- chemical vapor deposition (CVD) growth mechanism where patterned deposition of gold colloids led to confinement of the vertical nanowire growth to selected regions as illustrated in Figure 5.7, and afterwards, these microchannels (Figure 5.7c) can be resealed as a microfluidic device for applications such as macromolecular separation.

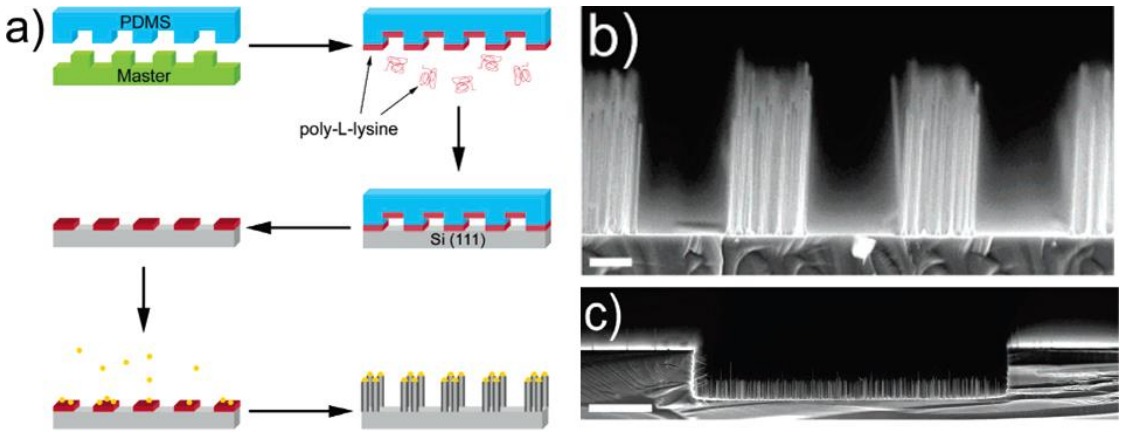

Figure 5.7-(a) Schematic of PDMS patterning of Au colloids. Briefly, a PDMS stamp is molded to the relief pattern of a photoresist master. After curing the polymer, the stamp is removed from the master and "inked" with a solution of poly-L-lysine. The stamp pattern is transferred to the Si (111) substrate, which is then immersed in the Au colloid solution. The colloid-patterned substrate is grown using the conventional VLS-CVD synthesis, resulting in a corresponding pattern of SiNW arrays. (b) Cross-sectional SEM image of PDMS patterned SiNW growth, and (c) A cross-sectional view SEM image of SiNWs grown directly in a microchannel. Scale bars are 1µm.[19]

To summarize, like GIS technique, the unlimited potential versatility of microfluidics has raised tremendous interests in both academic research and industry. Among those promising applications, this technique has been proved to be a useful tool for both 2D and 3D alignment of nano-objects such as nanoparticles and nanotubes. Therefore, inspired by those representative samples and applications, we believe that the idea of fabricating hierarchical assembling of silica nanohelices in 3D could also be realized by such way.

2. Assembling of silica nanohelices via GIS technique

Herein, we will show some proof-of-concept results about involving GIS for the alignment of silica nanohelices. A typical set up is schemed as Figure 5.9: After silica helical ribbons suspension in water is loaded into the spray jet, the suspension can be sprayed out at low angle on a subsrtate, which creates a liquid flow over the substrate surface. The nozzle is held at a distance of 1 cm from the substrate. The angle between the nozzle and the substrate plane is 20 °. The nozzle is fed by compressed air (air flow 30 L/min) and 0.25mg/mL silica nanohelices suspension in Milli-Q water is delivered by a liquid-handling pump (1 mL/min) in each run. The spraying time is 30 to 60 seconds, unless otherwise specified. Before spraying, the substrates are pre-coated with a PEI (poly(ethylene immine)) layer deposited by orthogonal spraying followed by a rinsing step with water to obtain a positively charged surface in aqueous solution. After deposition of the silica nanohelices, the substrate is rinsed with water and dried using a gentle air flow.[20]

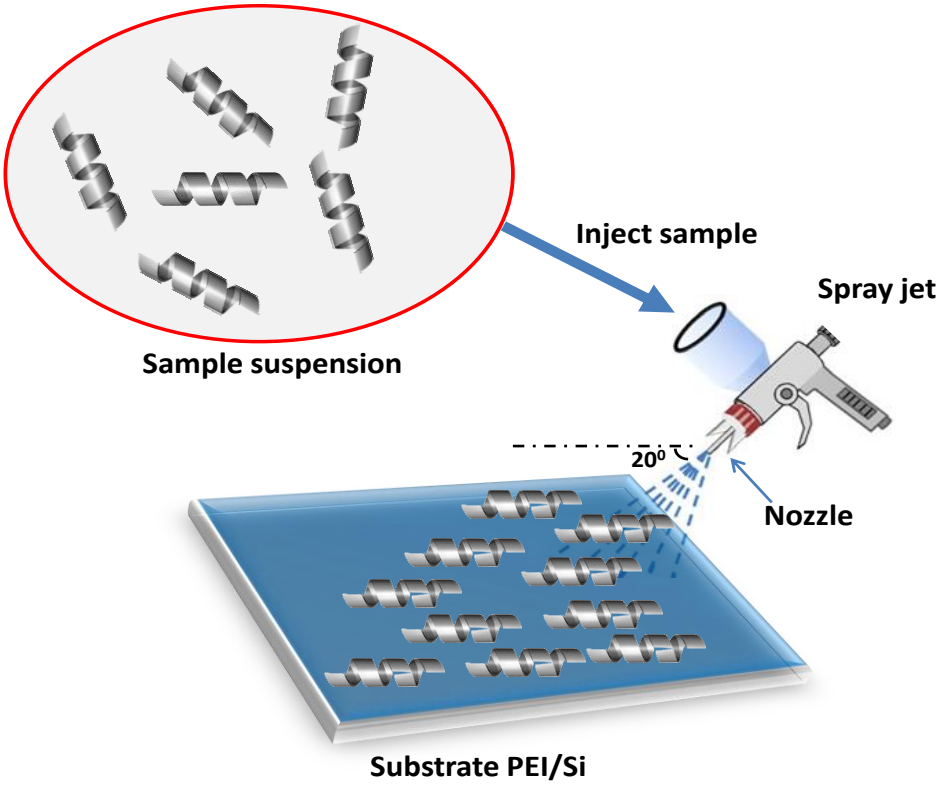

Figure 5.9- Schematic illustrations of the fabrication of aligned arrays of silica nanohelices on a PET/Si

substrate by GIS.

As it is shown in Figure 5.10, after spraying, the silica helical ribbons exhibited well aligned morphology compared to the drop casting samples. Note that this is a brand new technique in which the mechanism of the alignment is not well established yet, but we can still be inspired from the shear force theory suggested by H. Haick et al., They claimed that due to the fast moving nitrogen gas, the silica fiber suspension could produce microscopic droplets. The dynamics of the droplet formation is contributed by viscous shear forces together with capillary forces. By controlling the flow rate of the N_2 gas, the size of the droplets could be finely controlled and these droplets in the nozzle elongate in the direction of the fast gas flow due to the associated shear forces. When the size of the deposited droplet is comparable to the length of the silica fiber, its shear-driven elongation yields the alignment of the silica fibers with respect to the spraying direction. Then, these droplets with the encapsulated and flow-oriented silica fibers are adsorbed on the surface of the substrate via attractive intermolecular (van der Waals) forces, resulting in their immobilization on the PEI surface. They also showed a possible secondary mechanism of the alignment, where they suggested that after depositing the droplets on the PEI surface, the shear force exerted by the fast flow of the carrier gas over deposited droplets brings in the elongation and spreading of the microdrops in the spraying direction. The shear-induced elongation and possibly spreading of the deposited microdrops yields reorientation of the suspended silica fibers, resulting in their alignment in the flow direction before they are immobilized on the substrate that is due to solvent evaporation.[21] It is interesting to note that we can clearly observe the orientation of helices as observed in Figure 5.10 although we only have a continuously flowing liquid film which evaporates under room temperature compared to Haick's work, in which they heat the substrate, and thus the droplets evaporate upon landing.

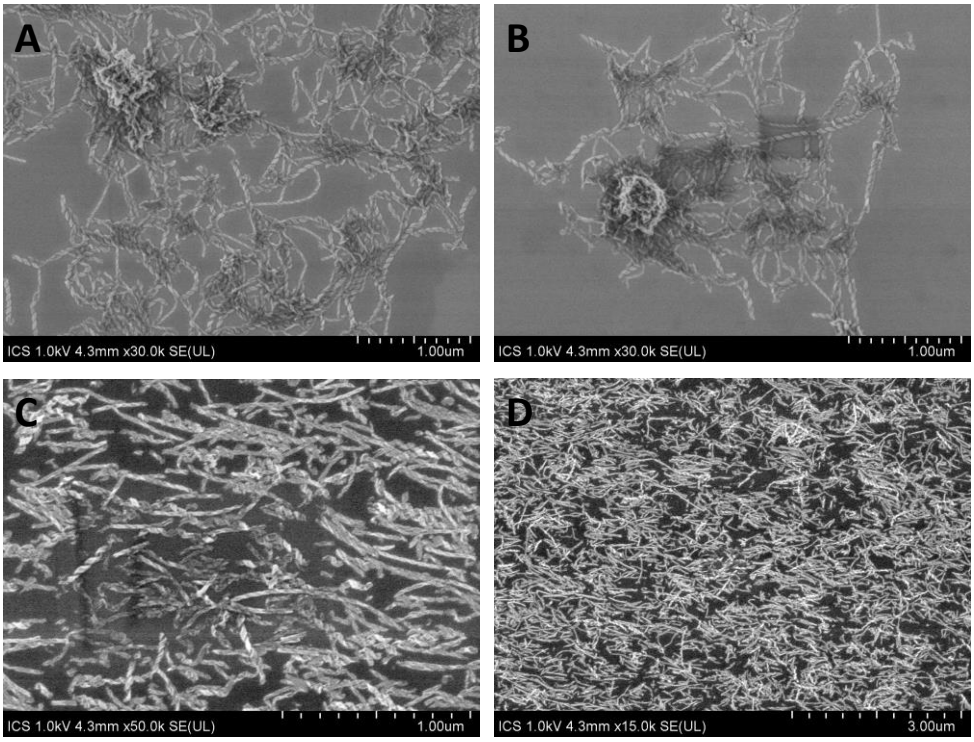

Figure 5.10- Typical SEM images of silica nanohelices. A and B: drop casting samples; C and D: silica nanohelices treated after GIS coating on the PEI/Si surfaces.

To quantify the degree of alignment, the nematic order parameter (*S*)[22] is used to quantify the degree of orientation:

$$S = \left\langle \frac{3\cos^2\theta - 1}{2} \right\rangle$$

Wherein θ is the angle between each nanoparticle and the main direction of orientation.

The variable (S) is directly related with the range of distribution of angles, such that S =0 for a group of completely disordered objects, and S = 1 for perfectly aligned objects. In Figure 5.11, the nematic order parameter was measured based on the spraying results on θ. The chromatic images were treated by ImageJ from the original SEM images, the color showed the angles of the fibers with respect to the spray direction which is set as the horizon. The following statistic study showed that the nematic order parameter *S* can be as high as 0.73 (Figure 5.11C), which mean highly ordered 2D arrays of silica nanohelices could be attained via this technique in an ultrafast way. Furthermore, extended deposition time (~60 s) produced silica nanohelices arrays with reduced spacing indicating we can control over the

density of the deposited silica fibers, while leaving the alignment of the silica fibers unaffected (S=0.77, Figure 5.11F), which agrees well with the study of H. Haick et al as well. Principally, parameters such as the flow rate, spraying angle, surface chemistry of the substrate and spraying duration will definitely affect the degree of alignment because they play a critical role for the droplets formation and interactions of silica fibers to the substrate surfaces.

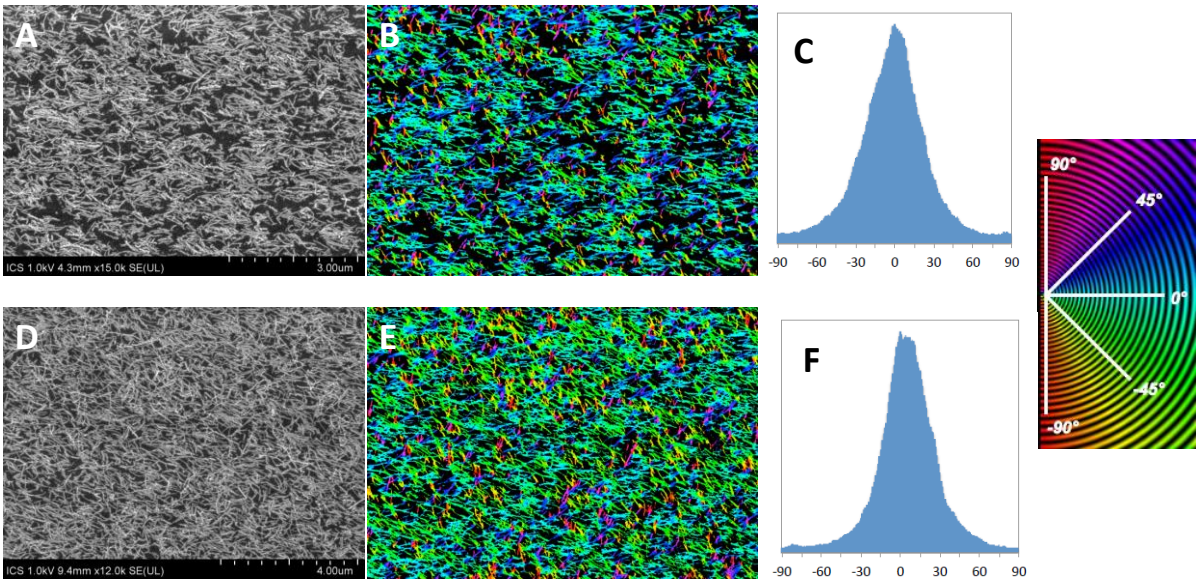

Figure 5.11- Study on spraying time effect on the alignment of silica nanohelices. A and B: typical SEM image and its treated version in ImageJ for statistics for a sample prepared with 30sec spraying, respectively. C: corresponding distribution plot of measured angle θ; D and E: SEM image and its treated version in ImageJ for statistics for a sample prepared with 60sec spraying, respectively. F: corresponding distribution plot of measured angle θ.

A multi-layer fabrication of such 2D arrays of nanohelices may be also done via GI assisted spraying LbL deposition by simply changing the spray directions, which provides a versatile way for the materials design and fertilizes the top-down fabrication techniques towards chiral film structures for optical applications as illustrated in Figure 5.12.

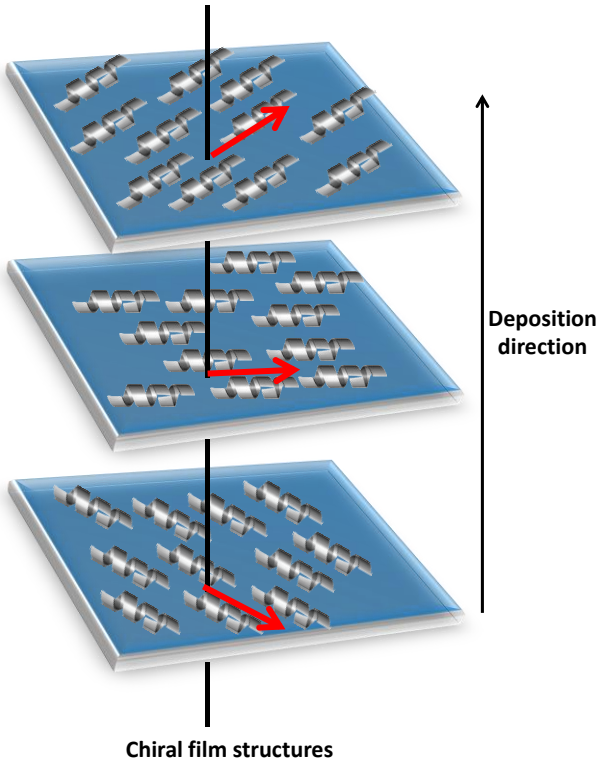

Figure 5.12- Schematic illustration of GI assisted spraying LbL technique for chiral film fabrication.

Other intrinsically important parameters[20] such as concentration, pH, surface chemistry of the substrate, spray angle should also be investigated individually to elucidate the alignment mechanism. However, these preliminary but promising results have already shown the possibility of using GIS for the fabrication processes for uniaxially alignment of 2D arrays of these nanohelices enhancing the versatility of GIS for developing multifunctional materials such as biomedical materials and optical materials.[23-25]

3. Assembling of silica nanohelices via microfluidics

The microfluidic device was prepared as described in the literature.[26] Figure 5.13 shows the typical set up for the device for alignment of silica twisted ribbons. The microfluidic channels are made from Polydimethylsiloxane (PDMS). In a typical fabrication, the dimension and the routes of the channels are all editable by controlling the photolithography and spin coating procedures. The size of the channel can be controlled in a range from several microns to hundreds of microns in height h: 5-50μm and width w: 10-500μm. To make it comparable in all parallel experiments, the microfluidic devices are produced with a PDMS thin film (thickness e=10μm) in the bottom, and the typical dimensions are: h= 20μm, w=100-500μm. In parallel, fragmented silica twisted ribbons are prepared via dry method as mentioned in chapter 3. Typically, 2mL 5mg/mL fragmented silica twisted ribbons are adjusted to pH=8.5 after freeze dry, and then the suspension in water is fragmented at 135Watt by tip sonication, afterwards the pH of the suspension can drop down to pH=6-7, then the pH of the suspension was readjusted to pH=8.5 and followed by another cycle of tip sonication at 135Watt and pH adjustment to 8.5. In any case, before injected to the reservoir, the suspension can be sonicated 5min in sonication bath in order to avoid possible aggregation between the silica nanohelices.

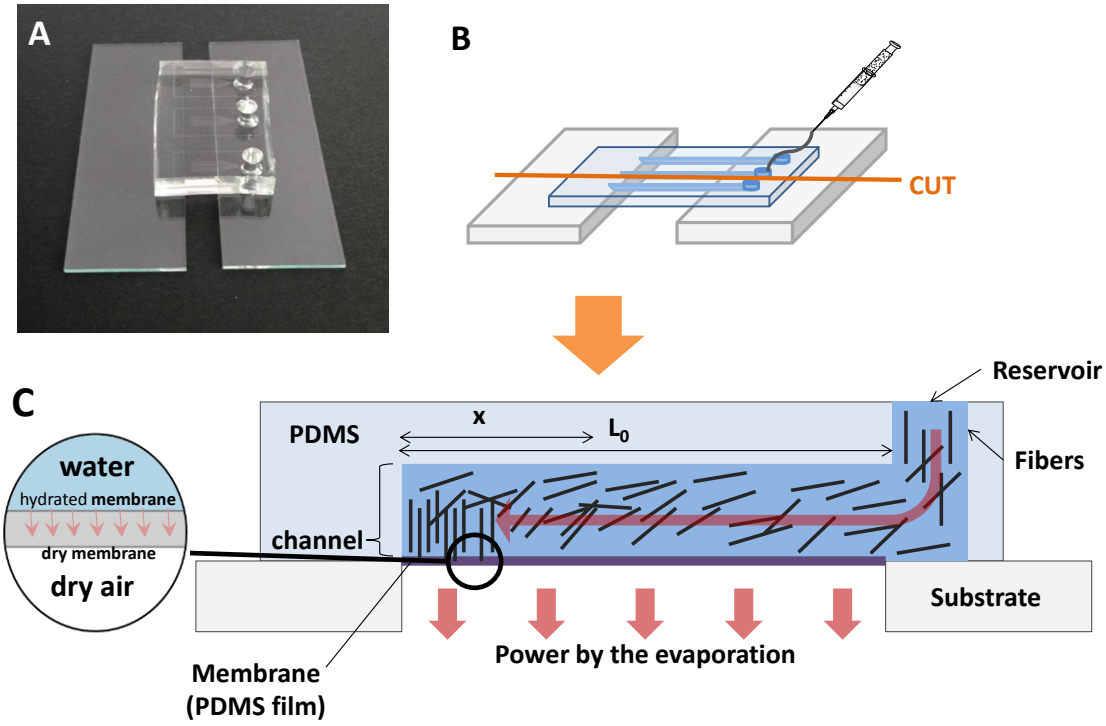

Figure 5.13- Schematic illustration of alignment of silica nanohelices via microfluidic channels. A: Photograph of microfluidic device; B and C: Sketch of the microfluidic channel geometry: general and side view showing the gas and liquid layers and the thin PDMS membrane in between.

The operation principle is simple as stated by P. Tabeling[26]: during continuously filling with the solution of interest, water in the bottom channel pervaporates through the thin PDMS membrane, which induces a compensating flow from the reservoir and concentration of the convected solutes at the tip of the finger[27, 28]. This is similar to concentration at the boundary of a drying droplet[29], without the motion and shear of the concentration zone due to the recess of the liquid-air interface, and without spurious convective flows, because of the confinement. The small dimensions lead to thermal regulation much faster that typical kinetics involved in our studies (milliseconds vs hours), which permit isothermal studies. The compensating flow could direct the silica twisted ribbons towards the dead end where it accumulates. If we define the current of solute injected into the channel is steady $J_0 = c_0 v_0$. Backwards thermal diffusion against the flow controls the width of the accumulation zone[28], which is $p = (Dh/v_e)^{1/2} = (D\tau_e)^{1/2} < L_0$ for strong flows or long fingers $v_0 L_0 / D \gg 1$ (D is the diffusion coefficient). The concentration of the colloidal particles can be expressed as:

$$c(x,t) \simeq c_0 v_0 t \sqrt{\frac{2}{\pi p^2}} \exp(-\frac{x^2}{2p^2}) + c_0 R(x)$$

With $R(x) \simeq L_0 / x$ for $p \ll x \ll L_0$. Where x is the distance from the edge of accumulation zone to the dead end.

The geometrical parameters such as *h, w, e* and L_0 (which affect the evaporation speed v_e) will play a significant role on the control of the concentration at the tip and decide where the frontline of max concentration will be located. From the preliminary results done on bare silica twisted ribbons in Figure 5.14, we observe that narrower the finger channels are, the more densely assembled silica twisted ribbons are formed (Figure 5.14A). And interestingly, the magnified SEM images show that at the end of the channel, the densely packed silica twisted ribbons exhibit kind of needle like shapes with uneven topography (Figure 5.14C), while outside the dense area, the silica twisted ribbons are well dispersed and randomly oriented (Figure 5.14D). These observations prompt us to assume that the silica ribbons are perpendicularly oriented to the thin PDMS membrane at the tip of the channels. Here, the evaporation is so slow that there is no gradient of concentration over the height of the channel. Alignment probably arises from increased concentration at the tip of the channel, where ribbons or helices undergo a phase transition, from random to oriented (like an isotropic-nematic phase transition[30]). The overall concentration mechanism is based on convection induced by evaporation. At the tip of the channel, the concentration increases with time, which triggers the isotropic-ansotropic phase transition.

References – page 211

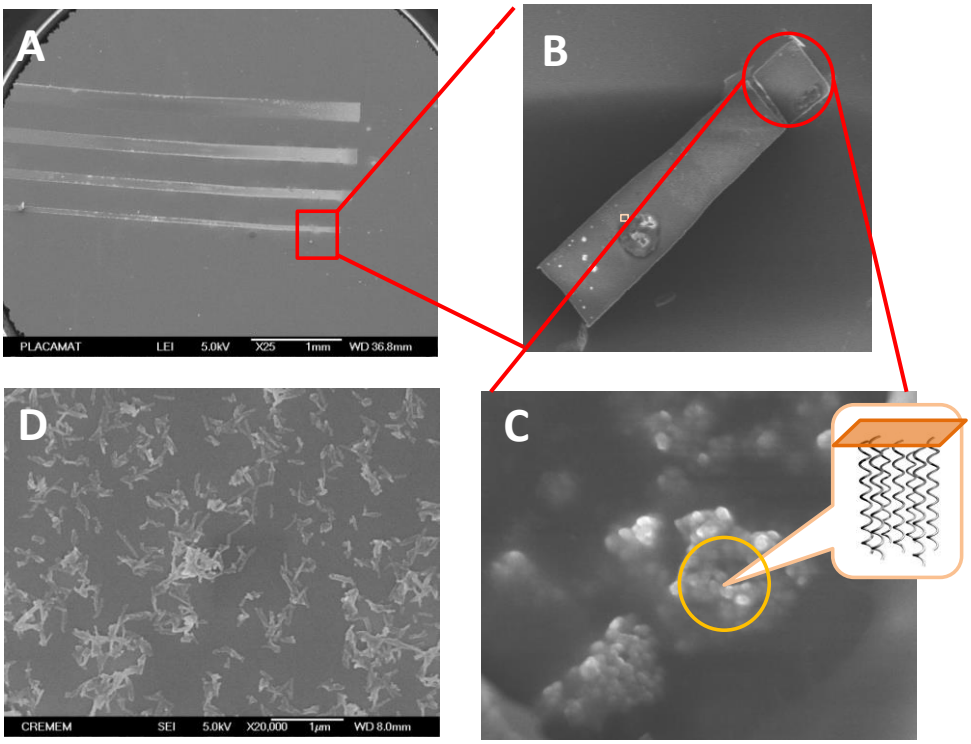

Figure 5.14- Typical alignment result of silica twisted ribbons based microfluidics. A, B and C are the SEM images of the silica twisted ribbons that located in the end of the channel. D is a typical SEM image of the silica twisted ribbons that are outside of the dense area. Insert in C shows the schematic illustration of the 3D bundles formed by silica twisted ribbons.

Admittedly, further investigations concerning the observations on lateral cross-sectional views are needed to provide in-situ information for the alignment processing, but the tilted SEM models are restricted by the dimension of the silica twisted ribbons, which makes it very difficult to be visualized and quite fragile for many possible mechanical treatments for sample preparations. Nonetheless, the idea of employing microfluidics for the alignment of non-spherical chiral nano-objects in a direction perpendicular to the flow is first performed here, which definitely broadens the boundary of such technique in microfluidics control and paves a way for further investigations on more complicated systems such as Goldhelix and other hybrid nanoparticles for applications in areas like optics and biomedical devices.[31-35]

Conclusion

To conclude, a first step for the alignment of silica nanohelices for developing mesoscopic anisotropic materials was fulfilled and discussed in this chapter. Two methodological trials based on GIS technique and microfluidic devices were proved effective for the alignment of silica nanohelices in 2D arrays and 3D bundles. The mechanism could be different in these two approaches however the fundamental idea concerning the alignment of silica fibers here could be both understood as the fine manipulation of microfluids, which has been well known as a key issue for many applications in materials processing. As proof-of-concept results, our work showed that GIS technique can not only contribute to 2D films fabrication, but also induce fine control for the alignment of nanometric helical fibers which can be identified as nematic organization. On the other hand, microfluidics was also demonstrated to be an efficient way for the alignment of nano-sized materials or assemblies, seldom used as here for a first step to smectic type 3D assembly of twisted fibers. Notably, more incisive studies should be done in order to better understand and optimize the alignment systems, in the meantime cross-disciplinary characterization techniques are also needed to broaden the scope of applications in both of the two techniques for materials design.

References – page 211

Reference

1. Moeller, M. and K. Matyjaszewski, *Polymer Science: A Comprehensive Reference, 10 Volume Set*2012: Newnes.
2. Borges, J.o. and J.F. Mano, *Molecular interactions driving the layer-by-layer assembly of multilayers.* Chemical Reviews, 2014. **114**(18): p. 8883-8942.
3. Iler, R., *Multilayers of colloidal particles.* Journal of Colloid and Interface Science, 1966. **21**(6): p. 569-594.
4. Decher, G., *Fuzzy nanoassemblies: toward layered polymeric multicomposites.* Science, 1997. **277**(5330): p. 1232-1237.
5. Krogman, K.C., et al., *Spraying asymmetry into functional membranes layer-by-layer.* Nature materials, 2009. **8**(6): p. 512-518.
6. Saetia, K., et al., *Spray‐Layer‐by‐Layer Carbon Nanotube/Electrospun Fiber Electrodes for Flexible Chemiresistive Sensor Applications.* Advanced Functional Materials, 2014. **24**(4): p. 492-502.
7. Huang, Y., et al., *Directed assembly of one-dimensional nanostructures into functional networks.* Science, 2001. **291**(5504): p. 630-633.
8. Li, D., Y. Wang, and Y. Xia, *Electrospinning nanofibers as uniaxially aligned arrays and layer‐by‐layer stacked films.* Advanced Materials, 2004. **16**(4): p. 361-366.
9. Whitesides, G.M., *The origins and the future of microfluidics.* Nature, 2006. **442**(7101): p. 368-373.
10. Gañán-Calvo, A.M. and J.M. Gordillo, *Perfectly monodisperse microbubbling by capillary flow focusing.* Physical Review Letters, 2001. **87**(27): p. 274501.
11. Garstecki, P., et al., *Formation of monodisperse bubbles in a microfluidic flow-focusing device.* Applied Physics Letters, 2004. **85**(13): p. 2649-2651.
12. Link, D., et al., *Geometrically mediated breakup of drops in microfluidic devices.* Physical Review Letters, 2004. **92**(5): p. 054503.
13. Anna, S.L., N. Bontoux, and H.A. Stone, *Formation of dispersions using "flow focusing" in microchannels.* Applied Physics Letters, 2003. **82**(3): p. 364-366.
14. Nguyen, N.-T. and S.T. Wereley, *Fundamentals and applications of microfluidics*2002: Artech House.
15. Ko, H., S. Peleshanko, and V.V. Tsukruk, *Combing and bending of carbon nanotube arrays with confined microfluidic flow on patterned surfaces.* The Journal of Physical Chemistry B, 2004. **108**(14): p. 4385-4393.
16. Ko, H. and V.V. Tsukruk, *Liquid-crystalline processing of highly oriented carbon nanotube arrays for thin-film transistors.* Nano Letters, 2006. **6**(7): p. 1443-1448.
17. Sharma, R., et al., *Nanometer positioning, parallel alignment, and placement of single anisotropic nanoparticles using hydrodynamic forces in cylindrical droplets.* Nano Letters, 2007. **7**(9): p. 2693-2700.
18. Mahajan, N. and J. Fang, *Two-dimensional ordered arrays of aligned lipid tubules on substrates with microfluidic networks.* Langmuir, 2005. **21**(7): p. 3153-3157.
19. Hochbaum, A.I., et al., *Controlled growth of Si nanowire arrays for device integration.*

Nano Letters, 2005. **5**(3): p. 457-460.
20. Decher, G.B., R.; Hu, H.; Pauly, M.; Felix, O.; Martel, D.; Lin, X.; Sekar, S.; Diabang, S.; Baer, J, *Preparation of coatings containing at least one in-plane oriented layer of anisotropic shaped objects*, 2014.
21. Assad, O., et al., *Spray-coating route for highly aligned and large-scale arrays of nanowires.* Acs Nano, 2012. **6**(6): p. 4702-4712.
22. Rezakhaniha, R., et al., *Experimental investigation of collagen waviness and orientation in the arterial adventitia using confocal laser scanning microscopy.* Biomechanics and modeling in mechanobiology, 2012. **11**(3-4): p. 461-473.
23. Decher, G. and J.B. Schlenoff, *Multilayer thin films: sequential assembly of nanocomposite materials*2006: John Wiley & Sons.
24. Schmitt, J., et al., *Metal nanoparticle/polymer superlattice films: fabrication and control of layer structure.* Advanced Materials, 1997. **9**(1): p. 61-65.
25. Lvov, Y., G. Decher, and G. Sukhorukov, *Assembly of thin films by means of successive deposition of alternate layers of DNA and poly (allylamine).* Macromolecules, 1993. **26**(20): p. 5396-5399.
26. Leng, J., et al., *Microevaporators for kinetic exploration of phase diagrams.* Physical Review Letters, 2006. **96**(8): p. 084503.
27. Verneuil, E., A. Buguin, and P. Silberzan, *Permeation-induced flows: Consequences for silicone-based microfluidics.* EPL (Europhysics Letters), 2004. **68**(3): p. 412.
28. Randall, G.C. and P.S. Doyle, *Permeation-driven flow in poly (dimethylsiloxane) microfluidic devices.* Proceedings of the National Academy of Sciences of the United States of America, 2005. **102**(31): p. 10813-10818.
29. Clément, F. and J. Leng, *Evaporation of liquids and solutions in confined geometry.* Langmuir, 2004. **20**(16): p. 6538-6541.
30. Song, W. and A.H. Windle, *Isotropic-nematic phase transition of dispersions of multiwall carbon nanotubes.* Macromolecules, 2005. **38**(14): p. 6181-6188.
31. Witzenrath, M., et al., *The NLRP3 inflammasome is differentially activated by pneumolysin variants and contributes to host defense in pneumococcal pneumonia.* The Journal of Immunology, 2011. **187**(1): p. 434-440.
32. Martinez, A.W., et al., *Diagnostics for the developing world: microfluidic paper-based analytical devices.* Analytical Chemistry, 2009. **82**(1): p. 3-10.
33. Whitesides, G.M., *The'right'size in nanobiotechnology.* Nature biotechnology, 2003. **21**(10): p. 1161-1165.
34. Weibel, D.B., W.R. DiLuzio, and G.M. Whitesides, *Microfabrication meets microbiology.* Nature Reviews Microbiology, 2007. **5**(3): p. 209-218.
35. Chabinyc, M.L., et al., *An integrated fluorescence detection system in poly (dimethylsiloxane) for microfluidic applications.* Analytical Chemistry, 2001. **73**(18): p. 4491-4498.

- General conclusion –

In this thesis, we proposed a simple and unique approach to fabricate Goldhelix by using inorganic chiral (silica) nanohelices as scaffold for the GNPs grafting. To fulfil this goal, chiral superstructures of organic assemblies formed via bottom-up approach are employed as templates for the fabrication of inorganic silica materials through sol–gel chemistry, where the combination of cooperative self-assembly and the chiral templating process favors the formation of inorganic chiral materials with highly ordered meso-structures. Specifically, organic self-assembly of achiral Gemini surfactant with chiral counterions was used for the synthesis of organic helical fibers. Afterwards, silica replicas were templated by using the as-synthesized organic helices as molds. Then, with proper surface functionalization, plasmonic GNPs are grafted on the silica surface to obtain chiroptical properties. Furthermore, hierarchically assembly of Goldhelix to create 2D or 3D structures was investigated based on proof-of-concept attempts on the alignment of silica nanohelices by using grazing incidence spraying (GIS) and controlled evaporation microfluidics techniques. The three dimensional aspect and the nanometric size of the Goldhelix enabled novel applications such as new unusual refractive index materials, chiro-optical sensors circular polarizers, heterogonous catalysts and even metamaterials.

In Chapter 1, a bibliography study on the light and matter interactions was done by specifically focusing on plasmonic metal nanoparticles, especially gold and silver, which are proved to be promising candidates for the design of optical resonators due to the LSPR effect that can greatly enhance the resonance effect close to the surface plasmon frequencies. The beauty of asymmetric materials is discussed as well and it has been proved that chiral nanostructures have the capability to rotate light propagation planes, indicating uncommon materials such as near-zero or even negative index materials can be realized with positive constitution parameters. These interdisciplinary fields actually inspire the interest of designing

chiral metal nanostructures to manipulate and enhance light polarizations in an unusual manner.

In Chapter 2, a detailed description of this project was introduced. First of all, synthesis of 3D Goldhelix via bottom up approach was proposed by using silica nanohelices as the platform and GNPs were used as the building blocks. Furthermore, grazing incidence spraying associated with LbL technique and controlled evaporation microfluidics technique are proposed for the realization of hierarchical organizations of Goldhelix in 2D and 3D motif. Some of the typical cutting edge characterization techniques were introduced as well for further instructive interpretations and investigations.

In Chapter 3, a brief overview on the sol-gel transcription of organogels to mesoporous silica replicas was introduced at the beginning. Then, morphology control of organic nanohelices was done by elongating the hydrophobic chain length from 16 to 18 and 20 alkyl carbons. With longer carbon chain, the geometrical parameters such as diameters and pith length of the nanohelices would be increased while the helix formation kinetics is dramatically slowed down. To accelerate the gelation speed and transition rate for the helical structures, study on the concentration and incubation temperature effects was conducted and proved to be an effective way to obtain size controlled organic nanohelices.

The realization of fragmentation of silica nanohelices was accomplished by applying tip sonication to the silica suspensions with various parameters such as sonication power, pH and the solvents. The extent of dispersibility and fragmentation was quantified by aggregation fraction, which demonstrated the disentanglement of silica nanohelices. Finally, individualized and size-controlled silica nanohelices were prepared for further usage via surface functionalization with amine. The fulfillment of fabrication of such inorganic fibers in a controlled way will definitely broaden the scope of sol-gel chemistry and potential applications in hybrid materials and nanotechnology.

In Chapter 4, we first made a quick review about current study on chiral self-assembly of GNPs for optical applications. Then, Goldhelix with different types of GNPs grafting were synthesized. We found that only when GNPs are larger than 5nm, *i.e.* Goldhelix consisting of

HOOC-PEG/TA-GNPs. The synthesized Goldhelix could exhibit CD activities in the vicinity of the wavelength of HOOC-PEG/TA-GNPs. Further study on the size of the GNPs and handiness of the silica template proved these CD signals resulted from the plasmon-plasmon coupling between neighboring GNPs. Then, the normalized PCD signals and calculated g factors were compared with simulated CD signals and other related systems provided in literature. The results are well in line with the simulations and comparable to other organic systems with GNPs assembly, showing that silica nanohelices could be a feasible template for induced plasmonic chirality for metal nanoparticles and they are good models for studying on induced PCD activities. Next, optimization on the adsorptions of HOOC-PEG/TA-GNPs on Goldhelix was investigated through quantity and pH effect, the results proved that the adsorptions of GNPs as well as the PCD activities could be dramatically varied based on the conditions of quantity ratio and pH value of the Goldhelix suspension. In addition, a polarization--resolved light scattering experiment was conducted to prove the induced chiral plasmon interactions in the view of magnetism. The preliminary results proved the existence of an axial (MD+EQ) mode with resonant property at plasmon frequency and introduce a feasible way for studying on magnetic issues of assembled nanoparticles.

In Chapter 5, we introduced the first step for the alignment of silica nanohelices for developing mesoscopic anisotropic materials. Two methodological trials based on GIS technique and microfluidic devices were proved effective for the alignment of silica nanohelices in 2D arrays and 3D bundles. As proof-of-concept results, our work showed that GIS technique can not only contribute to 2D films fabrication, but also induce fine control for the alignment of nanometric helical fibers which can be identified as nematic organization. On the other hand, microfluidics was also demonstrated to be an efficient way for the alignment of nano-sized materials or assemblies, seldom used as here for 3D assembly of twisted fibers.

Appendix:

Basic theories on light-matter interaction

References – page 242

Classical fields in matter*

Coulomb's force law between two electric point charges q, q' with a distance of r can be expressed as:

$$\mathrm{F}=\frac{1}{4\pi\varepsilon_0}\left(\frac{qq'}{r^3}\right)\mathrm{r}$$

And Ampere's force laws of magnetic induction between two infinitely long wires carrying electric currents I, I' with a distance of r can be written as:

$$\frac{d|\mathrm{F}|}{dl}=\frac{\mu_0}{2\pi}\left(\frac{II'}{r}\right)$$

Where ε_0 and μ_0 are the permittivity and the permeability of free space, respectively. Therefore, the time-independent vector fields issuing from these force expressions are the electric filed, E, and the magnetic field, B. The E-field is the Coulomb force per unit charge,

$$\mathrm{E}=\frac{1}{4\pi\varepsilon_0}\frac{q}{r^3}\mathrm{r}$$

And the magnetic induction B-field is given by the Biot-Savart law,

$$\mathrm{B}=\frac{\mu_0}{4\pi}\int\frac{\mathrm{I}\times\mathrm{r}}{r^3}dl=\frac{\mu_0}{4\pi}I\int\frac{d\mathrm{I}\times\mathrm{r}}{r^3}$$

Where I is the current and $d\mathrm{I}$ is an element of the wire length. The Lorentz force law succinctly summarizes the effect of the E- and B-fields on a charged particle moving the velocity *v*,

$$\mathrm{F}=q\left(\mathrm{E}+\mathrm{v}\times\mathrm{B}\right)$$

In addition to these two fields, the displacement field D and magnetic field H are needed to describe the modification of force fields in dielectric or conductive matter. In linear, isotropic materials these two additional fields are linked to E and B by the "constitutive relations":

* Weiner, J. and F. Nunes, *Light-matter interaction: physics and engineering at the nanoscale* 2012: Oxford University Press

$$\mathrm{D} = \varepsilon \mathrm{E}$$

$$\mathrm{H} = \frac{1}{\mu}\mathrm{B}$$

Where ε and μ are the permittivity and permeability of the material. These material parameters are related to those of free space by

$$\varepsilon = \varepsilon_0 \varepsilon_r$$

$$\mu = \mu_0 \mu_r$$

Where ε_r and μ_r are the relative (and unitless) permittivity and permeability respectively. The relative permittivity e is often called the dielectric constant, but the relative permeability rarely finds application and does not have a common alternative name. However, many researchers use ε for the dielectric constant so there is a danger of confusion between permittivity and the unitless dielectric constant.

In free space, the relation among E,B,D,H can be described by:

$$\mathrm{D} = \varepsilon_0 \mathrm{E}$$

$$\mathrm{B} = \mu_0 \mathrm{H}$$

When these force fields act on a materials medium, however, the D and H fields take on added terms. Matter consists of positively charged core nuclei surrounded by distributions of negatively charged electrons. If the core nuclei are arranged according to some symmetric spatial extension the materials is crystalline; if not, the materials may be a glassy solid, a liquid or a gas. The electric charge distribution may be bound to the nuclei or delocalized throughout the crystal structure. In any case, if E and B are present, the Lorentz forces acting on the electric charge distribution will clearly modify it. These modifications can be characterized by the introduction of two new fields, the polarization P and the magnetization M. In the presence of matter the displacement and magnetic fields now are expressed as:

$$\mathrm{D} = \varepsilon_0 \mathrm{E} + \mathrm{P}$$

$$\mathrm{B} = \mu_0 \mathrm{H} + \mathrm{M}$$

For E- and B- fields that are not P and M fields themselves are proportional to E and H.

References – page 242

$$\mathrm{P} = \varepsilon_0 \chi_e \mathrm{E}$$

$$\mathrm{M} = \mu_0 \chi_m \mathrm{H}$$

Where χ_e, χ_m are electric and magnetic susceptibility. Then:

$$\mathrm{D} = \varepsilon_0 (1 + \chi_e) \mathrm{E}$$

$$\mathrm{B} = \mu_0 (1 + \chi_m)\ \mathrm{H}$$

Which means the relative permittivity and permeability can be written in terms of the corresponding susceptibilities as

$$\varepsilon_r = 1 + \chi_e$$

$$\mu_r = 1 + \chi_m$$

The relative permittivity and permeability are unitless but may be complex, the imaginary parts reflecting absorptive loss.

$$\varepsilon_r = \varepsilon' + i\varepsilon'' = 1 + \chi_e' + \chi_e''$$

$$\mu_r = \mu' + i\mu'' = 1 + \chi_m' + \chi_m''$$

Maxwell equations in microscopic and macroscopic scale

The Maxwell equations are the fundamental equations for the understanding of all electromagnetic and optical phenomena.[1, 2] In their different form, these equations are written as

Gauss' law for electricity $\nabla \cdot \mathrm{E} = \frac{\rho}{\varepsilon_0}$

Gauss' law for magnetism $\nabla \cdot \mathrm{B} = 0$

Faraday's law of induction $\nabla \times \mathrm{E} = -\frac{\partial B}{\partial t}$

Ampere's law $\nabla \times \mathrm{B} = \mu_0 J + \varepsilon_0 \mu_0 \frac{\partial E}{\partial t}$

References – page 242

Where E and B are the electric field and the magnetic induction, respectively, and ρ and J are the volume charge and current densities, respectively. These equations are called microscopic Maxwell equations because ρ and J here represent the actual microscopic charge and current densities. In a material medium, for example, ρ would describe the electronic and nuclear charge distributions. Thus ρ and J would necessarily be complicated and vary extremely fast on very small length scales. Most often, however, we are not interested in the correspondingly fast variation of the electric and magnetic fields over atomic length scales and a macroscopic description is sufficiently accurate. The fundamental Maxwell equations are therefore rewritten at the macroscopic level as:

$$\nabla \cdot \mathrm{D} = \rho_{free}$$

$$\nabla \cdot \mathrm{B}=0$$

$$\nabla \times \mathrm{E}=-\frac{\partial B}{\partial t}$$

$$\nabla \times \mathrm{H}=J_{free}+\frac{\partial D}{\partial t}$$

Where E and H are the macroscopic electric and magnetic fields, ρ_{free} is the macroscopic net charge density. Here the microscopic field quantities wherein the fast variations over small length scale are not observable. Thus, the underlying medium appears homogeneous and shows a homogeneous response to the applied fields. The first two equations make statements about field sources. The first states that the source of the displacement field D is the "free" electric charge density ρ_{free}. In fact, the charge density is composed of two terms: the free charge density and the "bound" charge, ρ_{bound},

$$\rho = \rho_{free} + \rho_{bound}$$

The bound charge density is defined as the negative divergence of the polarization field,

$$\rho_{bound} = -\nabla \cdot \mathrm{P}$$

So that from the first Maxwell equation, we can see that

$$\nabla \cdot \mathrm{E} = \frac{\rho}{\varepsilon_0}$$

The second source equation states that the magnetic induction field B does not originate from a magnetic charge density, ρ_m. In fact, this equation implies that magnetic source "charges" do not exist; and magnetic monopoles have never been found in nature. The second pair of equations, termed Faraday's law and the Maxwell-Ampere law respectively, describes the spatial and temporal behavior of the fields. The Ampere's law introduces another field, the charge current density J_{free}. Similarly, the total current density J is composed of the sum of free and bound current densities.

$$J = J_{free} + J_{bound}$$

Refractive index and polarization

Light travelling in vacuum has a velocity $c = 3 \times 10^8$m/s which is obtained from the constants ε_0 and μ_0 as $c = 1/\sqrt{\varepsilon_0 \mu_0}$. Interaction between electromagnetic field and matter occurs because atoms have charged species like the negatively charged electron and the positively charged ion cores. One important consequence of this interaction is a change in the velocity of light in a medium from its value in vacuum. This new velocity is represented as: $v = 1/\sqrt{\varepsilon\mu}$, where the permittivity and permeability now differ from that of vacuum. To characterize this change, an important dimensionless quantity known as the refractive index (n) is used and its magnitude is given by:

$$n = \frac{c}{v} = \sqrt{\frac{\varepsilon\mu}{\varepsilon_0 \mu_0}}$$

An important property of the index of refraction n is that, for a given material, the index varies with the frequency of the light passing through the material. This behavior is called dispersion. Because n is a function of frequency, Snell's law of refraction indicates that light

of different wavelengths (frequencies) is refracted at different angles when incident on a material. By using the results of Maxwell equation and trial solution, the relation of refractive index to frequency can be expressed by:

$$n^2 = 1 + \frac{Nq^2}{m\varepsilon_0}\left(\frac{1}{\omega_0^2 - \omega^2}\right)$$

This important equation is known as the dispersion relation as it shows how light of a given frequency ω behaves when it is incident in a material with *N* dipoles each having resonant frequency ω_0 .[3]

As it is known to all, when light interacts with matter, the outcome of the interaction can be all common phenomena such as transmission, reflection, refraction and scattering. Since light is an electromagnetic wave (Figure 1) and it is produced by vibrating electric charges and it has both an electric and a magnetic component, a light wave that is vibrating in more than one plane is referred to as unpolarized light. Light emitted by the sun or by a flame is unpolarized light. Such light waves are created by electric charges that vibrate in a variety of directions, thus creating an electromagnetic wave that vibrates in a variety of directions. It is possible to transform unpolarized light into polarized light. The process of transforming unpolarized light into polarized light is known as polarization. There are a variety of methods of polarizing light.

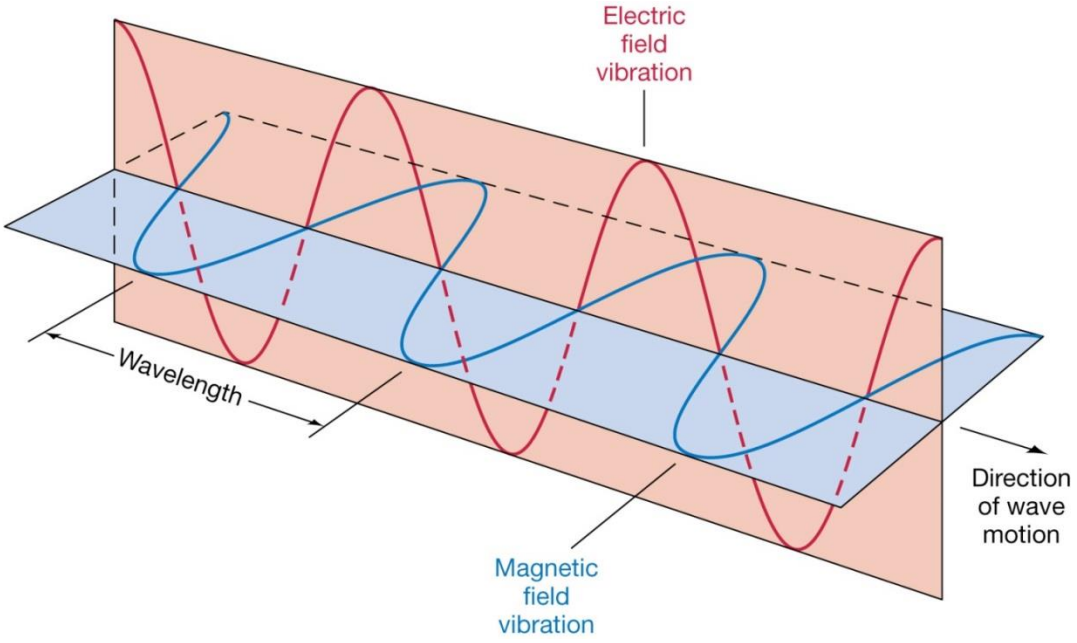

References – page 242

Figure 1- A plane linearly polarized electromagnetic radiation wave propagation.[4]

The most common method of polarization involves the use of a Polaroid filter (Figure 2). Polaroid filters are made of a special material that is capable of blocking one of the two planes of vibration of an electromagnetic wave. In this sense, a Polaroid serves as a device that filters out one-half of the vibrations upon transmission of the light through the filter. When unpolarized light is transmitted through a Polaroid filter, it emerges with one-half the intensity and with vibrations in a single plane; it emerges as polarized light.[5]

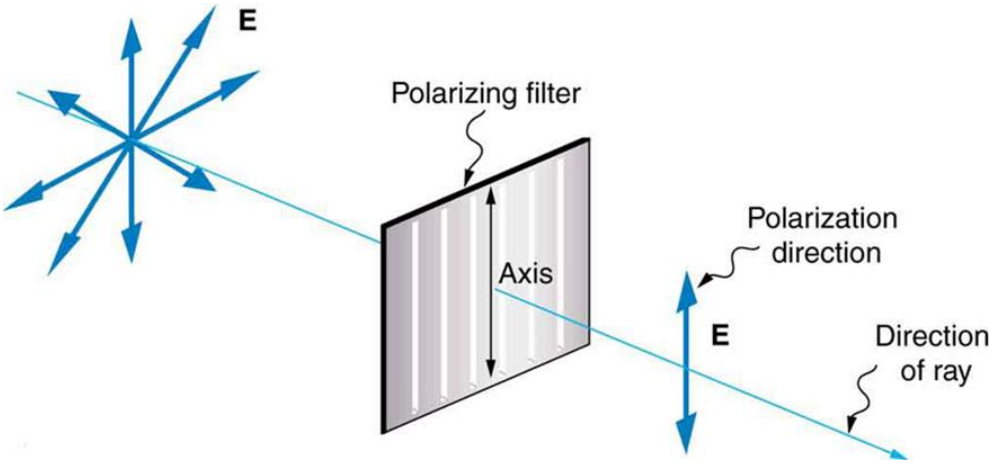

Figure 2- Schematic illustration of light polarization by polaroid filter.[6]

Unpolarized light can also undergo polarization by reflecting from nonmetallic surfaces or refraction upon penetrating into the medium. As shown in Figure 3, at the interface, light is separated to reflected and refracted light. The amount of polarization of the reflected light depends on the indices of refraction of the media involved and the angle of the incident light with interface. It can be shown that reflected light is completely polarized at a angle of reflection θ_b, given by

$$\tan\theta_b = \frac{n_2}{n_1}$$

Where n_1 is the medium in which the incident and reflected light travel and n_2 is the index of refraction of the medium that forms the interface that reflects the light. This equation is known as Brewster's law, and θ_b is known as Brewster's angle.

Meanwhile, metallic surfaces reflect light with a variety of vibrational directions; such reflected light is unpolarized. However, nonmetallic surfaces such as water reflect light in a way that there is a large concentration of vibrations in a plane parallel to the reflecting surface.

Refraction occurs when a beam of light passes from one material into another material. At the surface of the two materials, the path of the beam changes its direction. The refracted beam acquires some degree of polarization. Most often, the polarization occurs in a plane perpendicular to the surface.

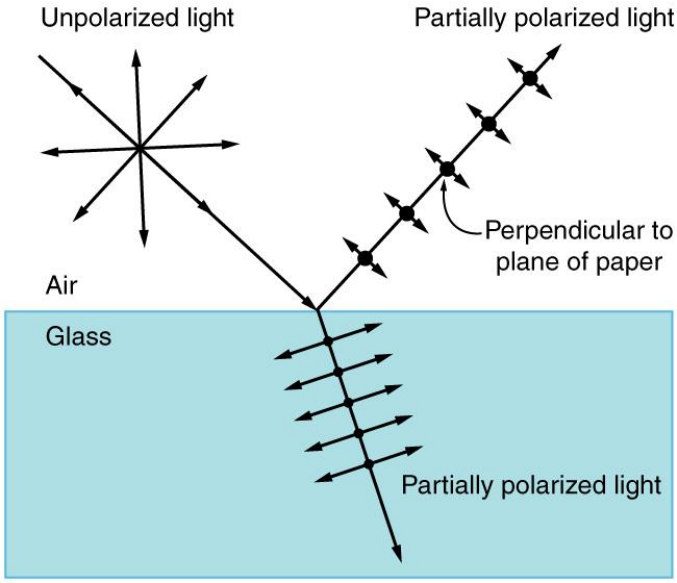

Figure 3- Polarization by reflection. Unpolarized light has equal amounts of vertical and horizontal polarization. After interaction with a surface, the vertical components are preferentially absorbed or refracted, leaving the reflected light more horizontally polarized. This is akin to arrows striking on their sides bouncing off, whereas arrows striking on their tips go into the surface.[6]

The radiant power of the reflected and refracted light depends on the angle of incidence, the refractive indices of the two media and the polarization of the incident beam. The Fresnel equations[7] describe the dependence of the reflected light on these quantities. In the case of normal incidence, the incident beam polarization doesn't appear. The reflectance $\rho = E_r / E_0$ is

$$\rho = \left[\frac{n_i - n_t}{n_i + n_t} \right]^2,$$

Where n_i and n_t are the refractive index of incident and transmitted medium.

The reflectance is thus related to the difference in refractive indices between the two media. When polarized light encounters a dielectric interface, the polarization of the reflected and or refracted beams may be impacted. This is described by using Fresnel equations that refer to the reflection coefficient (related to beam amplitude) of the EMR beams rather than the reflectance (related to beam power) and include the polarization of the beam. If the electric vector oscillates in the plane of incidence, the reflection coefficient is denoted $r_{\|}$

$$r_{\|} = \left[\frac{\tan(\theta_i - \theta_t)}{\tan(\theta_i + \theta_t)} \right],$$

Where θ_i and θ_t are the angle of incidence and refraction.

If the electric vector vibrates in the direction perpendicular to the plane of incidence, the reflection coefficient is $\rho_{\perp}$.

$$r_{\perp} = -\left[\frac{\sin(\theta_i - \theta_t)}{\sin(\theta_i + \theta_t)} \right].$$

Polarization also occurs when light is scattered while traveling through a medium (Figure 4). When light strikes the atoms of a material, it will often set the electrons of those atoms into vibration. The vibrating electrons then produce their own electromagnetic wave that is radiated outward in all directions. Due to the scattering direction, the light can be divided into unpolarized light along the incident direction, polarized light at 90 degree and partially polarized light in between.[8, 9]

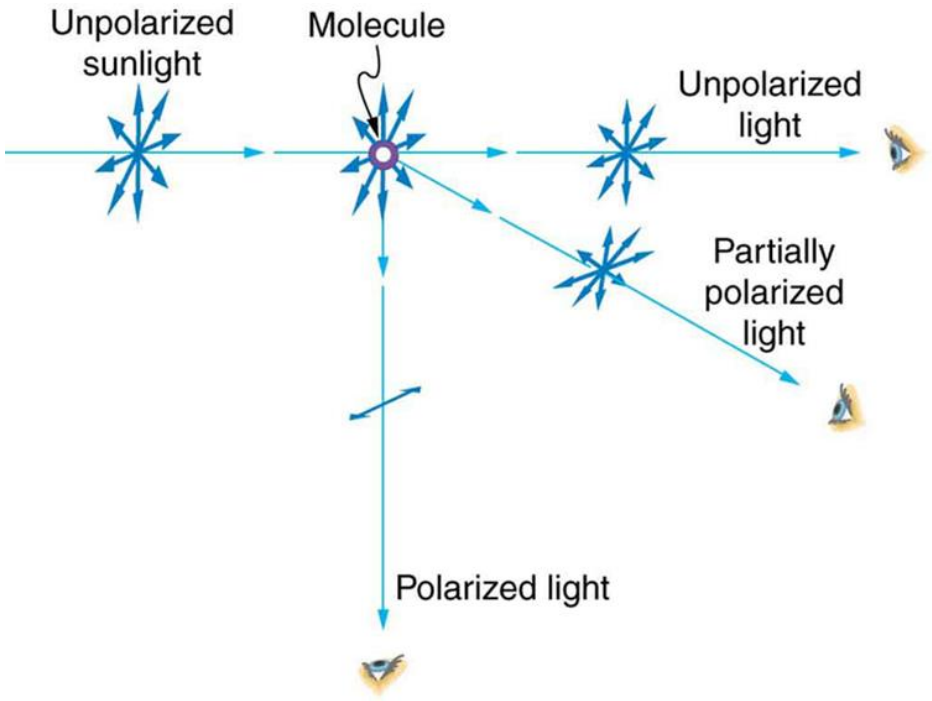

Figure 4- Polarization by scattering. Unpolarized light scattering from air molecules shakes their electrons perpendicular to the direction of the original ray. The scattered light therefore has a polarization perpendicular to the original direction and none parallel to the original direction.[6]

Polarization of light is best understood as a sum of pure polarized light described by coherent sinusoidal waves at a given optical frequency as it shows in Figure 5, the electric and magnetic fields oscillate in the x-y plane, with the wave propagating in the z direction, perpendicular to x-y plane. The first diagram traces the electric field vector over a complete cycle for linear polarization at two different orientations with an angle of 45 ° to both electric field and magnetic field. When a phase shift is introduced between those horizontal and vertical polarization components, one would generally obtain elliptical polarization[10] as is shown in the third figure. When the phase shift is exactly ±90 °, then circular polarization is produced. Circular polarization may be referred to as right-handed (clockwise) or left-handed (anti-clockwise) depending on the direction in which the electric field vector rotates. However, depending on the point view of the source or the receiver, the terms left- and right- handed can be oppositely defined, and unfortunately, these two opposing historical conventions exist together. Circular dichroism (CD), which is very often referred to the differential absorption of left- and right-handed light of a medium, is widely used in structural biology and chemistry. Left-hand circular (LHC) and right-hand circular (RHC) polarized light represent two

possible spin angular momentum states for a photon, and so circular dichroism is also referred to as dichroism for spin angular momentum.[11] This phenomenon was discovered by Jean-Baptiste Biot, Augustin Fresnel, and Aimé Cotton in the first half of the 19th century[12] and has a wide range of applications in many different fields.[13]

Fundamentally, the interaction of light and matter is based on the interactions of light to electrons within the molecules of a medium; as the consequences of different transitions of electrons between atomic states depending on the incoming light's polarization linked to the effective parameters or the natural properties of materials, Particularly optical index is a crucial parameter used to depict the optical properties of a medium. Investigation of the basic theories concerning on dielectric permittivity and magnetic permeability will therefore be central.

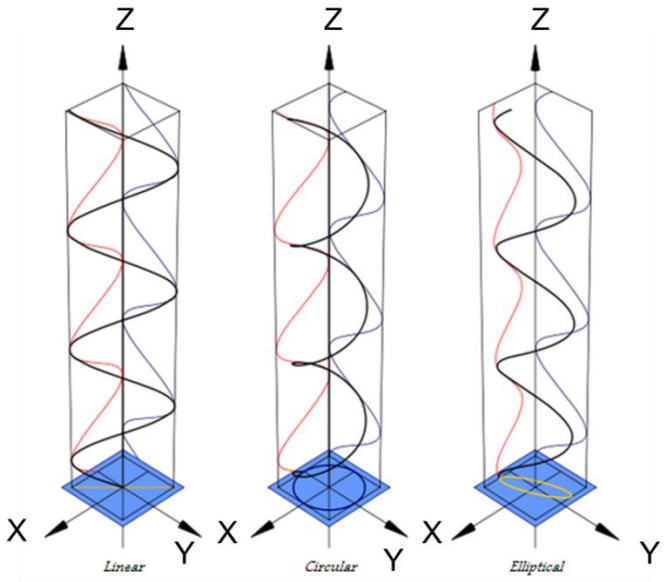

Figure 5- Typical polarization states of light. Red: electric field vibration, blue: magnetic field vibration.[13]

Dispersive models and mixing rules for properties of hybrid materials

Modelling of resonances in permittivity and permeability

The dielectric function $\varepsilon(\omega)$ is determined by the properties of the matter and its interaction with a light wave propagating through that matter. The exact solution of this

problem requires a quantum mechanical treatment of the properties of solids and their interaction with light which is quite complicated. The basic features, however, can be seen already a classical treatment within the frame of the electromagnetic theory of light propagation and electron theory by Lorentz, Drude and others. This classical theory is frequently used instead of more sophisticated quantum mechanical theories to interpret the results of laboratory measurements of optical constants of materials of practical interest. The basic concepts of the classical approach are described in this section.

Lorentz dispersion model for dielectric permittivity

One widely used dispersive model for the dielectric permittivity is first introduced by H.A. Lorentz.[1] As the frequency dispersive nature of a medium is related to the polarizability of its basic units, an easy and adequate description of dispersion of a medium can be established by simply concerning the properties of atoms and molecules. Note that an applied electric field will cause charge separation of the positively charged nuclei and negatively charged electrons in an atom or molecule, the induced dipole moments can be determined by the displacements of the charges from their equilibrium positions. The force on the electrons is given by the Lorentz force:

$$\mathrm{F} = -e\left(\mathrm{E} + v \times \mathrm{B}\right),$$

Where v is the velocity of the electrons. The electron in an atom or molecule can be assumed to be bound to the equilibrium position through an elastic restoring force. Thus, if m is the mass of the electron, the equation of motion becomes

$$m\ddot{\mathrm{r}} + m\gamma\dot{\mathrm{r}} + m\omega_0^2\mathrm{r} = -e\mathrm{E}_0 \exp\left(-i\omega t\right),$$

Where r is the displacement vector, ω_0 is the resonance angular frequency characterizing the harmonic potential trapping the electron to the equilibrium position, and ω is the angular frequency of the light.

Using a trail solution for stationary state: $\mathrm{r} = \mathrm{r}_0 \exp\left(-i\omega t\right)$, the displacement of the electron is obtained as

References – page 242

$$\mathrm{r}_0 = \frac{-e\mathrm{E}_o / m}{\omega_0^2 - \omega(\omega + i\gamma)}.$$

The dipole moment due to each electron is P=-er and the polarization* defined as the total dipole moment per unit volume, P, is given by the vectorial sum of all the dipoles in the unit volume. Assuming on dipole per molecule and an average number density of *N* molecules per unit volume, one can obtain

$$\mathrm{P}=N\mathrm{p} = \frac{Ne^2\mathrm{E} / m}{\omega_0^2 - \omega(\omega + i\gamma)} = \varepsilon_0 \chi_e \mathrm{E},$$

Where χ_e is the dielectric susceptibility. Hence one can write for the dielectric permittivity as

$$\varepsilon(\omega) = 1 + \chi_e(\omega) = 1 + \frac{Ne^2 / m\varepsilon_0}{\omega_0^2 - \omega(\omega + i\gamma)}.$$

The quantity $f^2 = Ne^2 / m\varepsilon_0$ is often called the oscillator strength. This equation is called the Lorentz formula for the dispersion of ε. The imaginary part, Im(ε), is seen to strongly peak at ω_0 and the real part, Re(ε), changes in a characteristic manner near ω_0 which is consistent with the Kramers-Kronig relations[14]

$$\mathrm{Re}(\varepsilon(\omega)) - 1 = \frac{1}{\pi}\mathrm{PV}\int_{-\infty}^{\infty} \mathrm{d}\omega' \frac{\mathrm{Im}(\varepsilon(\omega'))}{\omega' - \omega},$$

$$\mathrm{Im}(\varepsilon(\omega)) = \frac{1}{\pi}\mathrm{PV}\int_{-\infty}^{\infty} \mathrm{d}\omega' \frac{\mathrm{Re}(\varepsilon(\omega'))}{\omega' - \omega}.$$

Remember, the dielectric permittivity here is only valid for a dilute gas of the polarizable objects.

Drude model for metals

A special case of the Lorenz model is the Drude model,[15] which considers the harmonic oscillator model without restoration force, treating the elections in conduction band as

* The term "polarization" here is dielectric polarization referring to the dipole moment caused by charge separation while light polarization means the process of transforming unpolarized light into polarized light as stated in previous section.

non-interacting electron gas and yields a fairly accurate description of metals like silver, gold or aluminum. For a bulk crystal of a simple metal, one can describe electron motion in the lattice using a simple classical model of a free-electron gas:

$$m\frac{d^2x}{dt^2} = -\frac{m}{\tau}\frac{dx}{dt} - qE_{tot}(t)$$

Where *m* is the electron effective mass, *q* is the charge of the electron, τ is a decay time to account macroscopically for electron scattering, and $E_{tot}(t)$ is the total electric field acting on the electron, including any internal and external field generated by the electron motion. Here, we describe one-dimensional motion defined by the direction of the driving field, where *x* is the displacement of the electron relative to the fixed background of atomic cores. For an oscillatory applied field with frequency ω, the spatial displacement and any induced field will oscillate at the same frequency ω, so that $E_{tot}(t) = \mathrm{Re}\left[E_{tot}(\omega)\exp(-i\omega t)\right]$ and $x(t) = \mathrm{Re}\left[x(\omega)\exp(-i\omega t)\right]$. This gives

$$x(\omega) = \frac{qE_{tot}(\omega)}{m\left(\omega^2 + i\omega/\tau\right)}$$

The induced polarization *P* arising when a two-dimensional sheet of conducting electrons is displaced by a distance *x* is:

$$P(\omega) = -qx(\omega)n,$$

Where *n* is the conduction electron density.

The dielectric function ε connects the displacement field and the polarization:

$$D(\omega) = \varepsilon(\omega)E_{tot}(\omega) \equiv \varepsilon_0(\omega)E_{tot}(\omega) + 4\pi P(\omega),$$

Where $\varepsilon_0(\omega)$ includes any dielectric response other than the polarization *P* from the conduction electrons. We thus get the following Drude form for the dielectric function of a free-electron metal:

$$\varepsilon(\omega) = \varepsilon_0(\omega) - \frac{\varepsilon_0(\omega)\omega_p^2}{\omega^2 + i\omega/\tau},$$

References – page 242

Where the bulk plasmon frequency is

$$\omega_p = \sqrt{\frac{4\pi q^2 n}{\varepsilon_0 m}}$$

Debye model for dielectric fluids

The Debye model is often used in aquametric applications[16, 17] as it describes well the dielectric response of fluids with permanent electric dipole moments. These dipole moments feel a torque in the electric field the polarization requires time to reach its equilibrium state. The permittivity in the frequency domain reads

$$\varepsilon(\omega) = \varepsilon_\infty + \frac{\varepsilon_s - \varepsilon_\infty}{1 + j\omega\tau},$$

Where ε_s and ε_∞ are the low-frequency and optical permittivities of the materials. The material is lossy, and the dissipativity of the material is described from the fact that the imaginary part of $\varepsilon(\omega)$ is negative for all frequencies. The magnitude of the imaginary part is maximum at the relaxation frequency $f_r = 1/(2\pi\tau)$.[18]

Brendel model for amorphous material

For amorphous materials, the density and the type of the inter atomic bonding is similar to that in the crystals, therefore one expects the number and the type of the vibrations that contribute to the dielectric function remains essentially unchanged, except that the resonance frequencies ω_0 and possibly the damping constants γ change because bond lengths and bond angles are modified.

While in a crystalline state there exists for each type of oscillator a very big numbers of individual oscillators of a given type with identical resonance frequencies, one would expect that in the corresponding amorphous material the resonance frequencies of the individual oscillators are now spread over a certain range of values around that of the corresponding

crystalline materials. A simple model for this has been proposed by Brendel (1992). The model accounts for the amorphous structure of a material by assuming that the different lattice vibrational modes in the infrared can be represented by Lorentz-oscillators with randomly shifted resonance frequencies that are distributed according to a Gaussian probability distribution.

The dielectric function in the infrared spectral region where it is determined by the lattice vibrations then is assumed in this model to be given by

$$\varepsilon(\omega) = \varepsilon_\infty + \sum_{j=1}^{N} \frac{1}{\sqrt{2\pi\sigma_j}} \int_0^\infty dz e^{-(z-\omega_{0,j})^2/2\sigma_j^2} \frac{\omega^2{}_{p,j}}{z^2 - \omega^2 - i\gamma_j\omega}$$

It consists of a dielectric background ε_∞ accounting for the contribution of modes with resonance frequencies at much higher frequencies and *N* distributions of Lorentz oscillators with resonance frequencies $\omega_{0,j}$, damping constants γ_j, and plasma frequencies $\omega_{p,j}$ with standard deviations σ_j of the Gaussian probability distributions.

In practical this model is fitted to measured data. It is then often not possible to determine the damping constants γ_j with any precision because of the large widths σ_j of the Gaussian probability distribution. Then it seems to be a good compromise to fix γ_j at some fixed value to fit the remaining parameters.[19]

Resonance in magnetic permeability*

For magnetic materials, the constitutive equation giving the relation between M and H such as Landau-Lifshitz equation[20] describes the equation of motion. In the case of single domain ferromagnetic ellipsoidal sample, static magnetic moments of all atoms are parallel to each other and the static magnetization vector M is directed along the effective static

* Liu, Y., D.J. Sellmyer, and D. Shindo, *Handbook of Advanced Magnetic Materials: Vol 1. Nanostructural Effects. Vol 2. Characterization and Simulation. Vol 3. Fabrication and Processing. Vol 4. Properties and Applications*2008: Springer Science & Business Media.

magnetic field H. If the dimensions of the samples are small, they can be analyzed the precession of an isolated magnetic moment using Landau-Lifshitz equation. As it will be seen from the further consideration, two parameters-the static permeability and the ferromagnetic resonance frequency are crucial and can be treated neglecting the dissipation of energy. In this case the Landau-Lifshitz equation is written as

$$\frac{d\mathrm{M}}{dt} = -\gamma \mathrm{M} \times \mathrm{H},$$

Where γ is the gyromagnetic factor.

If no external static field is applied, then the precession of the magnetic moment in a uniaxial material induced by the anisotropy field H_k (k refers to Kittel, 1946) that must be used in Landau-Lifshitz equation instead of H. Let the external high frequency magnetic field be small compared to H_k. Then the frequency dependence of permeability is readily obtained by the linearization of Landau-Lifshitz equation. In this case, the diagonal components of the permeability tensor can be simplified as

$$\mu_{xx} = 1 + \frac{4\pi \mathrm{M}_0 \left[\mathrm{H}_k + \left(N_y - N_z \right) \mathrm{M}_0 \right]}{\left[\mathrm{H}_k + \left(N_x - N_z \right) \mathrm{M}_0 \right] \left[\mathrm{H}_k + \left(N_y - N_z \right) \mathrm{M}_0 \right] - \left(\omega / \gamma \right)^2}$$

$$\mu_{yy} = 1 + \frac{4\pi \mathrm{M}_0 \left[\mathrm{H}_z + \left(N_x - N_z \right) \mathrm{M}_0 \right]}{\left[\mathrm{H}_k + \left(N_x - N_z \right) \mathrm{M}_0 \right] \left[\mathrm{H}_k + \left(N_y - N_z \right) \mathrm{M}_0 \right] - \left(\omega / \gamma \right)^2}$$

$$\mu_{zz} = 1$$

Where ω represents the circular frequency of the incident wave, and the demagnetization factors of the sample N_x, N_y, N_z are normalized so that $N_x + N_y + N_z = 4\pi$, M_0 is the saturation magnetization. A wave having the magnetic field vector parallel to the easy axis does not introduce into the resonance. The frequency dependency of two other principal permeability components, μ_{xx} and μ_{yy}, is of Lorentzian form

$$\mu(\omega) = 1 + \frac{\mu_s - 1}{1 - \left(\omega / \omega_\tau \right)^2}$$

With the same resonance frequency

References – page 242

$$\omega_\tau = \gamma\sqrt{\left[\mathrm{H}_k + \left(N_x - N_z\right)\mathrm{M}_0\right]\left[\mathrm{H}_k + \left(N_y - N_z\right)\mathrm{M}_0\right]}$$

But different static permeability μ_s:

$$(\mu_s)_{xx} = 1 + \frac{4\pi\mathrm{M}_0}{\mathrm{H}_k + \left(N_x - N_z\right)\mathrm{M}_0}, \quad (\mu_s)_{yy} = 1 + \frac{4\pi\mathrm{M}_0}{\mathrm{H}_k + \left(N_y - N_z\right)\mathrm{M}_0}$$

In reality, oscillations of magnetization result in the dissipation of energy. This can be accounted for by adding an empirical damping term to the right part of Landau-Lifshitz equation, which leads to

$$\frac{d\mathrm{M}}{dt} = -\mathrm{M} \times \left(\gamma \mathrm{H} - \frac{\alpha}{\mathrm{M}_0} \bullet \frac{d\mathrm{M}}{dt} \right),$$

Where α is the damping factor. And in practice, the solution of the frequency dependence of permeability can be written in a Lorentzian form:

$$\mu(\omega) = 1 + \frac{\mu_s - 1}{1 + i\omega/\omega_\alpha - \left(\omega/\omega_\tau\right)^2},$$

This dispersion law is closely related to the standard resonance dispersion law for permittivity that is commonly accepted in the theory of dielectrics.[21, 22]

Mie Scattering for Particles*

Mie theory[23, 24] describes the scattering of light by particles. "Particles" here means an aggregation of material that constitutes a region with refractive index n_p that differs from the refractive index of its surroundings n_{med}. The dipole reradiation (radiation resulting from the previous absorption of primary radiation) pattern from oscillating electrons in the molecules of such particles superimposes to yield a strong net source of scattered radiation. Also, the reradiation patterns from all the dipoles do not cancel in all but the forward direction of the incident light as is true for homogenous medium, but rather interfere both constructively and destructively in a radiation pattern. Hence, particles "scatter" light in various directions with varying efficiency (Figure 6).

* http://omlc.org/education/ece532/class3/mie.html

Gustav Mie in 1908 published a solution to the problem of light scattering by homogeneous spherical particles of any size. Mie's classical solution is described in terms of two parameters, n_r and *x*. The magnitude of refractive index mismatch between particle and medium expressed as the ratio of the n for particle and medium,

$$n_r = \frac{n_p}{n_{med}}$$

The size of the surface of refractive index mismatch which is the "antenna" for reradiation of electromagnetic energy, expressed as a size parameter *x* which is the ratio of the meridional circumference of the sphere ($2\pi a$, where radius = a) to the wavelength $\frac{\lambda}{n_{med}}$ of light in the medium,

$$x = \frac{2\pi a n_{med}}{\lambda}$$

A Mie theory calculation will yield the efficiency of scattering which relates the cross-sectional area of scattering, σ_s (cm^2), to the true geometrical cross-sectional area of the particle, $A = \pi a^2$ (cm^2):

$$\sigma_s = Q_s A$$

Finally, the scattering coefficient is related to the product of scatterer number density, ρ_s (cm^{-3}), and the cross-sectional area of scattering, σ_s (cm^2),

$$\mu_s = \rho_s \sigma_s$$

Noto that when electromagnetic waves fall on a dielectric sphere, Maxwell's equations will show that at certain frequencies of the incident wave field the light will be strongly scattered and/or absorbed. Such frequencies are resonance frequencies and the modes associated to the excitation are called Mie resonances.

References – page 242

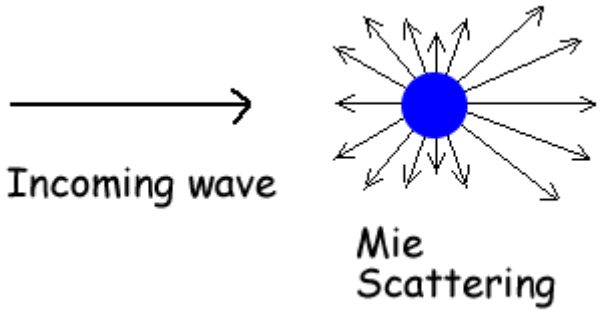

Figure 6- Typical schematic illustration of Mie scattering.[25]

Theories on optical properties of mixed materials

In this section, theoretical background concerning the macroscopic dielectric properties of mixed materials such as composites and hybrid materials is provided. By assuming that the mixture of materials can be viewed as homogeneous inclusions of an element in another homogeneous matrix, the concept of effective or macroscopic permittivity can be applied to the mixture. To find out the relation of effective permittivity to the constituent permittivities and other parameters of the constituent, theoretical issues have been studied since early 1800s and some of dielectric mixing models are available from early twentieth century. Basically, Maxwell Garnett formula, Rayleigh mixing formula and Bruggeman rule will be briefly discussed here for a quick look at how mixed materials can be modeled and effective parameters can be settled in order to give a theoretical base for innovative material design.

Clausius-Mossotti formula and Maxwell Garnett mixing rule

From the polarizability of a single sphere, the effective permittivity of a mixture can be calculated as a function of the density of the spheres in the background medium with permittivity ε_e and ε_i for the background and inclusions, respectively.

The effective permittivity is the relation between the external field and the average electric flux density D:

$$\mathrm{D} = \varepsilon_{eff}\,\mathrm{E}_e = \varepsilon_e \mathrm{E}_e + \mathrm{P}\,,$$

Where the average polarization P is connected to the dipole moment density in the mixture:

$$\mathrm{P}=n\mathrm{p}\,,$$

Where n is the density of dipole moments p in the mixture.

In a mixture, especially when it is dense, one cannot assume the field exciting one inclusion to be the external field E_e. The surrounding polarization increases the field effect and has to be taken into account. The field that excites one inclusion E_L is often called the local field or the Lorentzian field. It is dependent on the shape of the inclusion, and for a sphere it is

$$\mathrm{E}_L = \mathrm{E}_e + \frac{1}{3\varepsilon_e}\mathrm{P}\,,$$

Where the coefficient 1/3 corresponds to the depolarization factor of the sphere. Combining this equation with $\mathrm{p}=\alpha\mathrm{E}_L$ leaves us with the average polarization, and then the effective permittivity can be written as :

$$\varepsilon_{eff} = \varepsilon_e + \frac{n\alpha}{1-\frac{n\alpha}{3\varepsilon_e}}\,.$$

The equation is often seen in the form

$$\frac{\varepsilon_{eff}-\varepsilon_e}{\varepsilon_{eff}+2\varepsilon_e} = \frac{n\alpha}{3\varepsilon_e}$$

This relation carries the name Clausius-Mossotti formula[26], although it deserves the label Lorentz-Lorentz formula as well.[27] The dilute-mixture approximation can be written by taking the limit of small n:

$$\varepsilon_{eff} \approx \varepsilon_e + n\alpha\,.$$

In practical application, we can combine the Clausius-Mossotti formula with the polarizability expression

References – page 242

$$\alpha = V(\varepsilon_i - \varepsilon_e)\frac{3\varepsilon_e}{\varepsilon_i + 2\varepsilon_e},$$

Then we can have

$$\frac{\varepsilon_{eff} - \varepsilon_e}{\varepsilon_{eff} + 2\varepsilon_e} = f\frac{\varepsilon_i - \varepsilon_e}{\varepsilon_i + 2\varepsilon_e},$$

Where f=nV is a dimensionless quantity, the volume fraction of the inclusions in the mixture. This formula is called the Rayleigh mixing formula. Note that, because only the volume fraction and the permittivities appear in the mixing rule, the spheres need not be of the same size if all of them are small compared the wavelength.

The most common mixing rule is the Maxwell Garnett formula[28-30], which is the Rayleigh rule written explicitly for the effective permittivity:

$$\varepsilon_{eff} = \varepsilon_e + 3f\varepsilon_e\frac{\varepsilon_i - \varepsilon_e}{\varepsilon_i + 2\varepsilon_e - f\left(\varepsilon_i - \varepsilon_e\right)},$$

This formula is in wide use in diverse fields of applications. The beauty of the Maxwell Garnett formula is in its simple appearance combined with its broad applicability. It satisfies the limiting processes for the vanishing inclusion phase $f \to 0$, giving $\varepsilon_{eff} \to \varepsilon_e$, and for a vanishing background $f \to 1$ we have $\varepsilon_{eff} \to \varepsilon_i$.

The perturbation expansion of the Maxwell Garnett rule gives the mixing equation for dilute mixtures ($f \ll 1$):

$$\varepsilon_{eff} = \varepsilon_e + 3f\varepsilon_e\frac{\varepsilon_i - \varepsilon_e}{\varepsilon_i + 2\varepsilon_e} + 3f^2\varepsilon_e\left(\frac{\varepsilon_i - \varepsilon_e}{\varepsilon_i + 2\varepsilon_e}\right)^2.$$

Bruggeman mixing rule

As we have already discussed in the last section, the effective permittivity can be estimated using the Maxwell Garnett formula. However, this rule may not apply for dense materials, for it considers the interaction of scatterers to be small enough to be treated as an inclusion with the average polarization. In this case, another mixing rule called Bruggeman

References – page 242

mixing formula is often induced in material modeling studies.

This basic form of this formula for spherical scatterers is

$$(1-f)\frac{\varepsilon_e-\varepsilon_{eff}}{\varepsilon_e+2\varepsilon_{eff}}+f\frac{\varepsilon_i-\varepsilon_{eff}}{\varepsilon_i+2\varepsilon_{eff}}=0.$$

This Bruggeman formula has the special property that it treats the inclusions and the environment symmetrically. The interpretation of this rule shows that this formula balances both mixing components with respect to the unknown effective medium, using the volume fraction of each component as weight (*f* for inclusions and 1-*f* for the environment). This symmetry property makes the radical distinction between the Maxwell Garnett rule and the Bruggeman rule. The Maxwell Garnett approach is inherently nonsymmetric.

The Bruggeman formula for the case when the inclusions are randomly oriented ellipsoids is

$$\varepsilon_{eff}=\varepsilon_e+\frac{f}{3}(\varepsilon_i-\varepsilon_e)\sum_{j=x,y,z}\frac{\varepsilon_{eff}}{\varepsilon_{eff}+N_j\left(\varepsilon_i-\varepsilon_{eff}\right)},$$

Where now N_j are again the depolarization factors of the inclusion ellipsoids in the three orthogonal directions.[26]

References – page 242

Reference

1. Ramakrishna, S.A. and T.M. Grzegorczyk, *Physics and applications of negative refractive index materials*2008: CRC press.
2. Weiner, J. and F. Nunes, *Light-matter interaction: physics and engineering at the nanoscale*2012: Oxford University Press.
3. Hecht, E., *Optics 4th edition.* Optics, 4th Edition, Addison Wesley Longman Inc, 1998, 1998. **1**.
4. Website:, http://physics.stackexchange.com/questions/88976/can-we-draw-analogy-between-em-power-flow-through-free-space-and-ac-power-flow-t.
5. Ivanoff, A. and T.H. Waterman, *Factors, mainly depth and wavelength, affecting the degree of underwater light polarization.* J. mar. Res, 1958. **16**(3): p. 283-307.
6. Website:. http://philschatz.com/physics-book/contents/m42522.html.
7. Obukhov, Y.N. and G.F. Rubilar, *Fresnel analysis of wave propagation in nonlinear electrodynamics.* Physical Review D, 2002. **66**(2): p. 024042.
8. Lovesey, S.W., *Theory of neutron scattering from condensed matter.* 1984.
9. Bethe, H., *Scattering and polarization of protons by nuclei.* Annals of Physics, 1958. **3**(2): p. 190-240.
10. Chandrasekhar, S., *Radiative transfer*2013: Courier Corporation.
11. Park, D., *Introduction to the quantum theory*2012: Courier Corporation.
12. Fasman, G.D., *Circular dichroism and the conformational analysis of biomolecules*2013: Springer Science & Business Media.
13. Website:, https://en.wikipedia.org/wiki/Polarization_(waves).
14. Lucarini, V., *Kramers-Kronig relations in optical materials research*2005: Springer Science & Business Media.
15. Pelton, M. and G.W. Bryant, *Introduction to metal-nanoparticle plasmonics*. Vol. 5. 2013: John Wiley & Sons.
16. Kraszewski, A., *Microwave aquametry: electromagnetic wave interaction with water-containing materials*1996: IEEE.
17. Kupfer, K., *Methods of density-independent moisture measurement*2005: Springer.
18. Baas, A.F.d., *Nanostructured Metamaterials*, P.B. S. Tretyakov, T. Scharf, V. Kruglyak and I. Bergmair, Editor 2010, European Union.
19. Quinten, M., *Optical properties of nanoparticle systems: Mie and beyond*2010: John Wiley & Sons.
20. Landau, L.D., et al., *Electrodynamics of continuous media*. Vol. 8. 1984: elsevier.
21. Lagarkov, A., et al., *Dielectric properties of fiber-filled composites.* Journal of Applied Physics, 1998. **84**(7): p. 3806-3814.
22. Usov, N., A. Antonov, and A. Lagar'kov, *Theory of giant magneto-impedance effect in amorphous wires with different types of magnetic anisotropy.* Journal of magnetism and magnetic materials, 1998. **185**(2): p. 159-173.
23. Hergert, W. and T. Wriedt, *The Mie Theory: basics and applications*. Vol. 169. 2012: Springer.

24. Maier, S.A., *Plasmonics: fundamentals and applications*2007: Springer Science & Business Media.
25. Website:, http://www.daviddarling.info/encyclopedia/M/Mie_scattering.html.
26. Capolino, F., *Theory and phenomena of metamaterials*2009: CRC Press.
27. Sihvola, A., *Lorenz-Lorentz or Lorentz-Lorenz?* Antennas and Propagation Magazine, IEEE, 1991. **33**(4): p. 56-56.
28. Sihvola, A.H. and I.V. Lindell, *Chiral Maxwell-Garnett mixing formula.* Electronics Letters, 1990. **26**(2): p. 118-119.
29. Mallet, P., C.-A. Guerin, and A. Sentenac, *Maxwell-Garnett mixing rule in the presence of multiple scattering: Derivation and accuracy.* Physical Review B, 2005. **72**(1): p. 014205.
30. Sihvola, A.H., *Electromagnetic mixing formulas and applications*1999: Iet.